THÈSE

En vue de l'obtention du

DOCTORAT DE L'UNIVERSITÉ DE TOULOUSE

Délivré par : *l'Institut National Polytechnique de Toulouse (INP Toulouse)*

Présentée et soutenue le 15/12/2015 par :

Tarik BENADDI

Sparse Graph-Based Coding Schemes for Continuous Phase Modulations

JURY

Pierre DUHAMEL	Directeur de recherche CNRS, Supélec, Gif-sur-Yvette	Président
David DECLERCQ	Professeur des Universités, ENSEA, Cergy-Pontoise	Rapporteur
Christophe JEGO	Professeur des Universités, ENSEIRB, Bordeaux	Rapporteur
Abdel Nour CHARBEL	Maître de conférence, Télécom Bretagne, Plouzané	Examinateur
Guy LESTHIEVENT	Ingénieur de recherche, Centre National d'Etudes Spatiales, Toulouse	Invité
Benjamin GADAT	Ingénieur de recherche, Thales Alenia Space, Toulouse	Invité
Nicolas VAN WAMBEKE	Ingénieur de recherche, Thales Alenia Space, Toulouse	Invité
Charly POULLIAT	Professeur des Universités, ENSEEIHT, Toulouse	Directeur de thèse
Marie-Laure BOUCHERET	Professeur des Universités, ENSEEIHT, Toulouse	Codirectrice de thèse

École doctorale :
Mathématiques, Informatique et Télécommunications de Toulouse (MITT)
Spécialité :
Réseaux, Télécoms, Systèmes et Architecture (RTSA)
Unité de Recherche :
Institut de Recherche en Informatique de Toulouse (IRIT)
Directeur(s) de Thèse :
Charly POULLIAT et *Marie-Laure BOUCHERET*
Rapporteurs :
David DECLERCQ et *Christophe JEGO*

À ma grand-mère ...

Remerciements

Je tiens tout d'abord à remercier mes directeurs de thèse, Charly Poulliat et Marie-Laure Boucheret, auprès desquels j'ai passé trois formidables années. Leur confiance en moi, leurs encouragements et leurs conseils ont été déterminants dans l'avancement et le bon déroulement de cette thèse. Plus précisément, je remercie Charly pour ses éclairages, sa disponibilité et son enthousiasme, avec lui j'ai appris beaucoup de chose, et sans lui, cette thèse n'aurait pas été possible. J'adresse aussi un grand merci à Marie-Laure pour sa bonne humeur, ses encouragements et ses conseils. Mes remerciements vont aussi à mes encadrants industriels Benjamin Gadat, Guy Lesthievent et Nicolas Van Wambeke.

Je remercie le Centre National d'Études Spatiales (CNES) et Thales Alenia Space (TAS) pour avoir financé cette thèse et le laboratoire Telecommunications for Space and Aeronautics (TéSA) pour m'avoir offert un cadre de travail exemplaire.

Je souhaite remercier Pierre Duhamel pour m'avoir fait l'honneur de présider mon jury de thèse. Mes remerciements vont aussi à Christophe Jego et David Declercq pour avoir rapporté ma thèse. J'adresse également un grand merci à Abdel Nour Charbel pour avoir accepté d'examiner ma thèse.

Durant ces trois dernières années, j'ai eu la chance de côtoyer beaucoup de personnes formidables. En commençant par le Gang TéSA, un grand merci à Amina, Corinne, David, Fabio, Fany, Isabelle, Jean-Adrien Réunionmann, Jorge Creepy, Marie-Josée Lartiste, Phillipe Firstalbumonly, Rami, Raoul Who .... Du côté de l'IRIT, je pense à Aziz Cuisinier, Bilel Trader, Buchstabieren, Farouk, Olivier Zitoun, Pierre-Antoine Derleser, Qi et Ningning Lesmagnifiques, Sebastien, ... Et enfin, merci à mes nouveaux collègues de Télécom Bretagne, merci à Laurent et Geneviève pour leur sympathie et leur accueil très chaleureux.

Et les meilleurs pour la fin, comment ne pas remercier mes parents qui ont fait de moi ce que je suis aujourd'hui, je leur suis éternellement reconnaissant pour leurs sacrifices et leur éducation, merci maman, merci maman, merci maman et merci papa. Un énorme merci à mon formidable grand petit frère Tibilah qui s'est intéressé à ma recherche et à mes conférences. Il en a fait du chemin, de hatitoune aux équations différentielles stochastiques, je lui souhaite tout le bonheur du monde, Yo! J'exprime mes sincères remerciements à ma chère Narjiss qui a dû affronter toute seule les traumatismes post-Enquête-Criminelle la veille de mes deadlines. Je ne saurais comment te remercier pour ta patience, tes encouragements, ta présence, tes bons petits plats et ta manière si particulière de gérer mon stress: en stressant plus que moi je me retrouve entrain de te rassurer...Et pour finir, un grand merci à toutes les autres personnes (la grande famille et les amis) que je ne vais pas nommer au risque d'en oublier certains.

Tarik

O
/|\o
||

Résumé

L'utilisation de la modulation à phase continue (CPM) est particulièrement intéressante lorsque le canal de communication comporte une forte non-linéarité et un support spectral limité, en particulier pour la voie aller, lorsque l'on dispose d'un amplificateur par porteuse à bord du satellite, et pour la voie retour où le terminal d'émission travaille à saturation. De nombreuses études ont été effectuées sur le sujet mais les solutions proposées reposent sur la démodulation/décodage itératif des CPM couplées à un code correcteur d'erreur de type convolutif ou bloc. L'utilisation de codes LDPC n'a pas été à ce jour abordée de façon précise. En particulier, il n'existe pas à notre connaissance de travaux sur l'optimisation des codes basés sur des graphes creux adaptés à ce type de schémas. Dans cette étude, nous proposons d'effectuer l'analyse asymptotique et le design d'un schéma Turbo-CPM basé sur des graphes creux. Une étude du récepteur associé comportant les fonctions de démodulation sera également effectuée.

Abstract

The use of the continuous phase modulation (CPM) is interesting when the channel represents a strong non-linearity and in the case of limited spectral support; particularly for the uplink, where the satellite holds an amplifier per carrier, and for downlinks where the terminal equipment works very close to the saturation region. Numerous studies have been conducted on this issue but the proposed solutions use iterative CPM demodulation/decoding concatenated with convolutional or block error correcting codes. The use of LDPC codes has not yet been introduced. Particularly, no works, to our knowledge, have been done on the optimization of sparse graph-based codes adapted for the context described here. In this study, we propose to perform the asymptotic analysis and the design of turbo-CPM systems based on the optimization of sparse graph-based codes. Moreover, an analysis on the corresponding receiver will be done.

Contents

List of Figures

List of Tables

Introduction (French)

Contexte de la thèse

Les véhicules aériens sans pilote ou drones sont devenus très populaires et représentent aujourd'hui une solution rentable dans de nombreux nouveaux domaines autres que militaires (la surveillance des forêts, les situations d'urgence, l'inspection des pipelines, le divertissement, la communication, l'observation ...). En raison de ces applications très hétérogènes, les drones doivent envisager d'assurer une communication par satellite car ils ne peuvent pas toujours compter sur la présence d'infrastructures terrestres pour être commandés (régions éloignées, catastrophes naturelles, catastrophes industrielles ...). En effet, pour des raisons de sécurité dans l'espace aérien civil, il faut s'assurer que nous pouvons toujours garantir le contrôle de l'UAV. Un scénario typique est représenté dans Fig. 4.

Aujourd'hui, les drones utilisent principalement la bande Ku du service fixe par satellite (FSS) pour communiquer avec la station de pilotage à distance (RPS) quand il n'y a pas de trajet direct. Sinon, ils peuvent utiliser une plus grande gamme de solutions (C, Ku, S et UHF bandes). Dans le cadre de la future augmentation de l'utilisation des communications drones-satellites civiles, les drones auront besoin d'accéder aux bandes de fréquences des services de l'aviation civile dans les zones de l'espace aérien non-distincts ou au moins à certaines positions de leur trajectoire de vol. Afin de parvenir à une intégration complète et sûre dans le système du trafic aérien existant, un déploiement sur les fréquences du système d'atterrissage micro-ondes de l'aviation civile (MLS) est prescrit par l'Organisation Internationale de l'Aviation Civile (ICAO) et l'Union Internationale

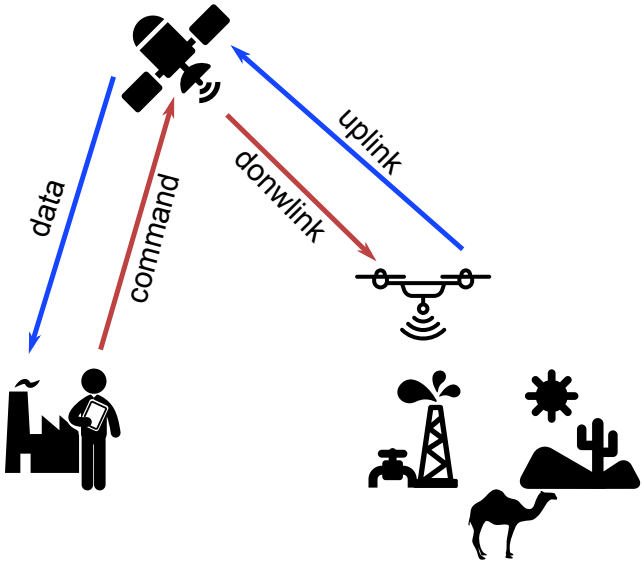

Figure 1: Context communication drone-satellite

des Télécommunications (ITU). D'autre part, aucun système de communication par satellite n'est actuellement déployé dans la bande du service aéronautique en-route mobile-satellite (AMS (R) S). Aujourd'hui, la bande de 5GHz n'est pas utilisé mais elle est allouée pour le système d'atterrissage (MLS), le système de satellite et le système terrestre [IR10, IR11, CNE12]. Afin de répondre à la forte augmentation de la demande, la première bande apparaît comme une opportunité unique pour un déploiement futur. Par ailleurs, en termes de propriétés de transmission, la bande 5GHz est relativement immunisée contre l'atténuation causée par la pluie ou d'autres conditions météorologiques. La figure 5 illustre un exemple de liens de communication entre le drone et le RPS. La même bande est prévue pour le futur standard de normalisation STANAG 4660.

La Conférence mondiale de la radio de l'ITU (WRC) de 2012 a inclus un point à l'ordre du jour couvrant ce contexte: nous devrons être en mesure, d'ici 2020, de définir un schéma de communication complet à la fois pour la commande et l'acquisition de données sur la bande de fréquence de 5030-5091MHz, en particulier pour le service mobile aéronautique en-Route (AM (R) S). Ce nouveau lien de communication ne doit pas interférer avec l'infrastructure déjà existante. La figure 6 résume les principales attributions de fréquences dans la bande 5GHz ciblée.

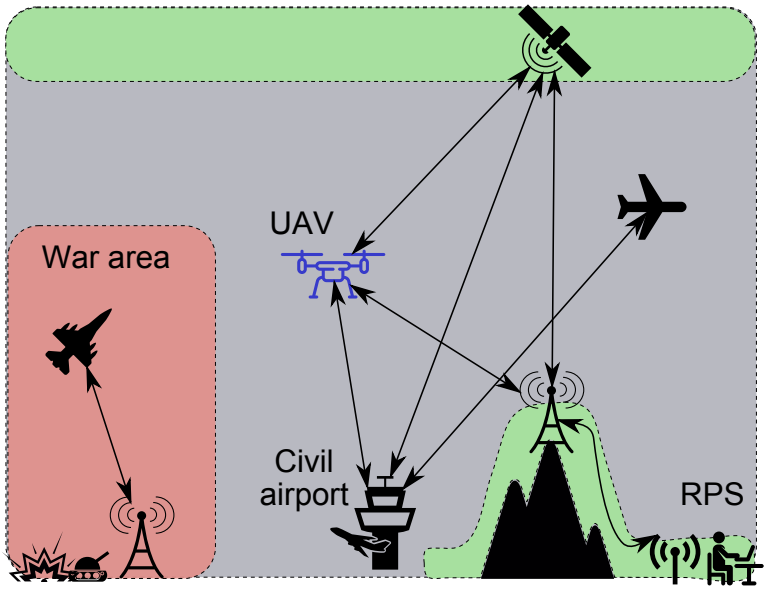

Figure 2: Environnement typique d'un drone. La zone rouge correspond à une zone militaire contrôlée par l'OTAN, la zone grise est civile mais contrôlée par l'ICAO et la zone verte correspond à un espace civil non contrôlé.

D'autre part, le signal transmis est soumis à de fortes distorsions en raison du modèle du canal. Enfin, les satellites visés sont supposés transparents (ils répètent seulement le signal reçu). Par conséquent, les amplificateurs intégrés induisent une distorsion du signal supplémentaire surtout quand ils travaillent près du régime de saturation. Dans la littérature, plusieurs techniques ont été proposées pour palier à cette dégradation:

Prédistortion

Cette technique est effectuée du côté de l'émetteur. Elle consiste à prédistordre le signal transmis de telle sorte qu'elle compense l'effet des amplificateurs à haute puissance embarqués (HPA). Ceci peut être effectué en inversant simplement la fonction de transfert de ces distorsions. L'expansion Volterra [BBD79] est largement utilisé pour décrire ces non-linéarités ainsi que leur inverse. Cette technique, ainsi que quelques autres connexes plus avancées (prédistorsion de données [SS83]), ont été utilisées dans le standard de la diffusion de la vidéo numérique de deuxième génération (DVB-S2) [ETS06].

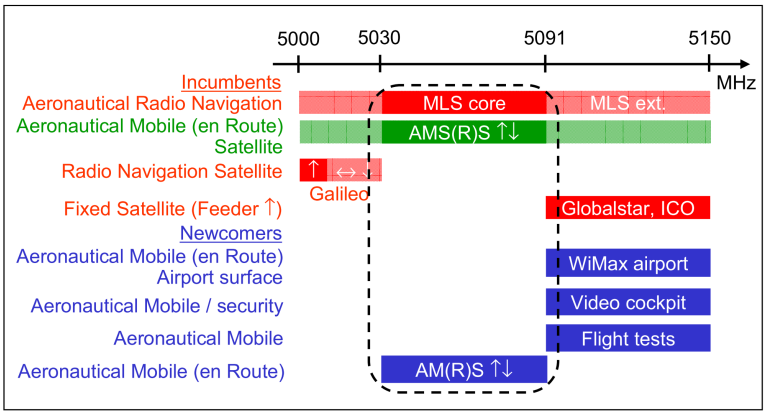

Figure 3: Vue d'ensemble du spectre à 5GHz. Cette figure a été prise de [GHGZ12]

Égalisation

Dans certaines applications, la complexité de la caractéristique des amplificateurs HPA et la non invertiblité de la fonction de transfert ne permettent pas une bonne correction des non-linéarités. Dans ces cas, on peut considérer une prédistorsion à l'émetteur associée à une égalisation à la réception. Cette égalisation va contrebalancer les résidus des non-linéarités restants ou d'autres termes d'interférence de canal. Généralement, cette approche est basée sur les symboles pilotes: chaque message dispose d'un nombre fixe de symboles connus utilisés pour estimer le canal. Comme dans l'approche précédente, les égaliseurs basés sur la décomposition de Volterra sont largement utilisés [BB83, BTP+13].

Schémas de modulations avancées

Une autre alternative consiste à utiliser des schémas de modulations avancées relativement immunisés contre les non-linéarités, comme les modulations à enveloppe constante. Différents schémas ont été proposés dans la littérature:

- La modulation Interplex [BT72]: une sous-classe des modulations de phase qui multiplexe plusieurs signaux dans un seul signal modulé en phase.

- La modulation Intersymbol-interference et jitter-free offset quadrature phase shift keying

(IJF-0QPSK) [LNF81]: cette modulation est obtenue en introduisant une proportion contrôlée de l'interférence inter-symboles (ISI) dans un signal IJF.

• Modulation à phase continue (CPM): une modulation de phase où les transitions de phase sont maintenues continues durant la transmission. Cette classe est très intéressante non seulement d'un point de vue occupation spectrale mais aussi pour sa structure facilement adaptable à des schémas de concaténation en série.

Modulations à phase continue

Dans ce contexte, les modulations à phase continue (CPM) représente un très bon candidat pour ces contraintes. Tout d'abord, elles ont une enveloppe constante qui les rend robustes face aux non-linéarités des amplificateurs intégrés. Du point de vue du satellite, ceci permet de travailler avec des puissances plus élevées sans aucun back-off, ce qui améliore le budget global de la liaison. Deuxièmement, les modulations à phase continue ont une meilleure occupation spectrale (des lobes secondaires bas) en comparaison avec les modulations linéaires classiques (QPSK, PSK, ...) pour des raisons qui vont être exposées plus tard.

Les signaux CPM ont bénéficié d'un grand nombre de recherches depuis leur introduction et leur performance dans le canal Gaussien a été bien étudiée. Dans des schémas codés concaténés, plusieurs travaux ont été effectués sur les concaténations en série avec des codes convolutifs binaires/non-binaires et différents codes en blocs de courte taille: [XA05, GiAND09, MA01] pour ne citer que quelques-uns. Il a été souvent stipulé que la concaténation série avec des codes Low Density Parity Check (LDPC) implique un système doublement itérative difficile à analyser et donc à optimiser. Étonnamment, aucune étude complète n'a été menée sur la conception de bons codes LDPC pour la CPM. Cette classe de codes correcteurs d'erreur présente de nombreux avantages: elle présente une performance compétitive par rapport aux turbo-codes, elle peut offrir une certaine flexibilité des rendement pour différents schémas de modulation et elle présente une complexité de décodage faible. En outre, si bien optimisés, on a montré que les codes LDPC peuvent opérer à des seuils très proches de la capacité pour un large éventail d'applications [MN96, tBKA04, YRL04, LSL06, VNND11] ...

Dans les quelques contributions traitant des systèmes concaténés faisant intervenir les LDPC et la CPM, les approches proposées manquent de généralité. Le premier travail est dû à [NAN01] où une étude basée sur l'évolution de densité du code LDPC concaténé avec une modulation Minimum Shift Keying (MSK) a été réalisée. Dans [NAN03], les mêmes auteurs ont proposé un code LDPC pour le MSK récursive, optimisé en utilisant une évolution différentielle avec quelques noeuds de variables de degrés 1. Dans [Gan03], l'auteur a étudié l'optimisation de modulation CPFSK M-aire selon une approche de modulation codée à bits entrelacés (BICM) en utilisant des techniques d'évolution de densité. Non seulement l'auteur n'a pas envisagé l'insertion d'une proportion de noeuds de variables de degré 1, mais aussi la démarche proposée mène à un problème d'optimisation non-linéaire. L'auteur a utilisé une évolution différentielle pour optimiser le code, toutefois, cet algorithme repose sur différentes heuristiques et ne garantit pas l'obtemption d'une solution optimale. Finalement, les auteurs dans [XA05] ont considéré un Irregular Repeat Accumulate(IRA) comme code externe et ont remplacé la partie accumulateur de l'IRA par la CPM. Comme ils ont considéré un code IRA non systématique, les auteurs ont remarqué qu'une introduction (à optimisée) de noeuds de parité dits de dopage est inévitable. Dans tous les systèmes concaténés introduits ici, on a considéré un entrelaceur global entre le CPM et le code externe, et on a toujours utilisé la représentation de la CPM découlant de la décomposition de Rimoldi [Rim88].

Structure du manuscrit et principales contributions

Dans cette thèse, nous visons à étudier et à concevoir des schémas CPM avec des codes basés sur des graphes creux. L'application principale sera le canal aéronautique pour le futur déploiement de drones dans le domaine civil. L'organisation de cette thèse et les principales contributions sont résumées ci-dessous:

Chapitre 1: Ce chapitre présente une introduction de la CPM, définit ses principaux paramètres et décrit les principales notations. Nous passons en revue les décompositions de la littérature les plus importantes et leurs récepteurs correspondants (la décomposition d'Anderson *et al*

[AAS86], la décomposition de Rimoldi[Rim88] et la décomposition de Laurent [AAS86]). Enfin, nous présentons les principaux codes basés sur des graphes creux qui vont être pris en compte dans cette thèse.

Chapitre 2: Dans ce chapitre, nous dérivons une méthode générique pour optimiser des codes LDPC non structurés pour la CPM. Notre méthode est basée sur une analyse EXIT Chart et peut être vu comme une généralisation des résultats dans [tBKA04]. Contrairement aux méthodes existantes et en tenant en compte les propriétés de la CPM, nous allons introduire une proportion de noeuds de variables de degré 1 afin d'améliorer le seuil de décodage itératif. Pour assurer un décodage réussi, cette proportion est soumise à une condition de stabilité qui est une généralisation de [RU01] dans le sens où elle prend en compte les degrés 1 et 2 et qu'elle peut être appliquée à tout autre détecteur. Differemment de [RSU01], nous dériverons cette condition de stabilité généralisée à partir d'une analyse EXIT Chart. Enfin, les résultats de simulation et les divers codes LDPC optimisés sont fournis. Nous allons voir qu'on est en mesure de trouver des codes LDPC qui fonctionne à seulement 0.01dB du seuil de décodage minimal théorique. Dans ce chapitre, nous nous concentrons sur la performance asymptotique et l'évaluation du rendement maximal atteignable, les résultats de cette famille seront utilisés le long de la thèse et comparés avec d'autres codes plus pratiques.

Les résultats de ce chapitre ont été présentés dans:

- Papier: "*Asymptotic Analysis and Design of LDPC Codes for Laurent-based Optimal and suboptimal CPM Receivers*", T. Benaddi, C. Poulliat, M.-L. Boucheret, B. Gadat, G. Lesthievent, *IEEE Int. Conf. Acoust., Speech, and Signal Proc. (ICASSP), 2014*.

Chapitre 3: Dans ce chapitre, nous menons une analyse asymptotique pour concevoir des codes LDPC plus pratiques pour le CPM. Tout d'abord, nous étudions les codes IRA en raison de leur performance et de leur encodage facile. Comparés aux codes LDPC non structurés, ils ont de bons seuils et sont facilement encodable grâce à leur partie structurée. Par ailleurs, nous généralisons cette famille aux codes Generalized IRA (GIRA). Contrairement à la méthode de

design proposée dans [XA05] pour les codes LDGM et afin de s'affranchir de l'optimisation des noeuds de dopage, nous proposons d'étudier les codes GIRA systématiques. Cette considération implique un ordonnancement de décodage particulier.

Deuxièmement, nous étudions la performance des codes LDPC basés sur des protographes [Tho03]. Cette classe bénéficie d'une représentation compacte, d'une analyse des performances plus simple et d'une implémentation facilement parallélisable. Nous allons montré qu'on peut optimiser des codes LDPC-protographe qui opèrent à 0.5dB seulement des LDPC non-structurés. Les résultats de simulation et la comparaison avec les protographes optimisés du canal Gaussian, ARJA et AR3A [LC07, DDJ06], sont fournis. Les protographes conçus ont été optimisés pour minimiser le seuil de décodage. Par conséquent, ils ne disposent pas nécessairement de bonnes propriétés de distances minimales en raison de l'introduction d'une grande proportion de noeuds de variables de degré 1 et 2. Toutefois, étant donné le contexte de nos applications, avec des trames de données longues, notre méthode donne de très bons résultats à 10^{-3} en terme de taux d'erreur paquet.

Finalement, afin d'obtenir des protographes avec de bonnes performances à la fois dans la région *waterfall* et la région du plancher d'erreur, nous étudions les codes LDPC spatialement couplés basés sur des protographes [MLCJ14] parce qu'il a été démontré que cette famille de code atteint universellement de bons seuils sur une large variété de canaux. En plus de tous les avantages des codes LDPC basés sur des protographes, ces codes présentent un *gain de convolution* qui améliore les performances de la famille précédente. Nous allons montrer que par couplage de protographes simples tel que le $(3, 6)$ régulier, nous atteignons déjà des seuils satisfaisants et par construction, une bonne distance minimale. En outre, pour remédier à la perte de rendement inhérente à la terminaison des codes LDPC spatialement couplés, nous introduisons une nouvelle terminaison qui préserve le rendement du protographe sous-jacent indépendamment de la longueur de couplage, tout en présentant un gain de convolution. C'est la première fois à notre connaissance qu'on envisage la possibilité d'utiliser un seul *effet de vague* pour les LDPC spatialement couplés. Cette nouvelle terminaison nous permet de concevoir un couplage du $(3, 6)$ qui donne le même seuil et le même rendement que le code LDPC optimisé

au chapitre 3 avec une longueur de couplage égale à 4 seulement.

Enfin, afin de concevoir de très bons codes LDPC spatialement couplés en terme de seuil de décodage pour le CPM, nous introduisons une technique d'optimisation en deux étapes: après avoir trouvé un bon protographe, nous optimisons le couplage afin d'obtenir de très bons seuils. Cette stratégie conduit à des codes très compétitifs qui fonctionnent à des seuils de seulement $0.1 - 0.15$ dB des codes LDPC non structurés.

Les différent résultats de ce chapitre ont été publiés dans:

- Papier: "*Protograph-based LDPC Convolutional Codes for Continuous Phase Modulation*", T. Benaddi, C. Poulliat, M.-L. Boucheret, B. Gadat, G. Lesthievent *IEEE International Conference on Communications (ICC), 2015.*
- Papier: "*Design of Unstructured and Protograph-based LDPC Coded Continuous Phase Modulation*", T. Benaddi, C. Poulliat, M.-L. Boucheret, B. Gadat, G. Lesthievent *IEEE International Symposium on Information Theory (ISIT), 2014.*
- Papier: "*Design of Systematic GIRA Codes For CPM*", T. Benaddi, C. Poulliat, M.-L. Boucheret, B. Gadat, G. Lesthievent, *IEEE International Symposium on Turbo Codes and Iterative Information Processing (ISTC), 2014.*

Chapitre 4: Dans ce chapitre, nous nous concentrons sur certains aspects des récepteurs CPM et le design de codes LDPC pour les récepteurs CPM à faible complexité. Une des deux décompositions les plus utilisées a été introduite par Pierre-André Laurent [Lau86] en 1986. Cette décomposition rend les techniques de synchronisation plus efficace et permet la conception de récepteurs à faible complexité. Le récepteur maximum de vraisemblance basés sur l'algorithme de Viterbi a été introduit par Kaleh dans [Kal89]. Malheureusement, aucun récepteur maximum *a posteriori* (MAP) *exacte* n'a été proposé dans la littérature: les récepteurs proposés ne prennent pas en compte "l'interférence inter-symbole" inhérente à la décomposition de Laurent et souffrent de la non-blancheur des statistiques de bruit après filtrage. Cette approximation est d'autant plus pénalisante pour le décodage itératif, la détection non-cohérente, l'égalisation

ou les applications multi-porteuses. Dans ce chapitre, après avoir discuté les récepteurs existants, nous dérivons un nouveau récepteur MAP qui résout le problème de l'ISI sans introduire des traitements supplémentaires, de type filtres de blanchiment. D'autre part, sur la base de l'autre décomposition CPM [Rim88], nous explicitons le lien entre les deux représentations et nous proposons une méthode analytique pour calculer le nouveau banc de filtre de réception. En appliquant la méthode d'optimisation du chapitre 2, nous optimisons des codes LDPC pour les récepteurs à faible complexité basé sur la décomposition de Laurent et montrons que les codes optimisés restent très efficaces pour le récepteur à faible complexité pour peu qu'on considère suffisamment de composantes. Enfin, nous comparons la performance du récepteur MAP proposé avec le récepteur classique en termes d'EXIT Chart et de taux d'erreur pour la CPM non codée et codée.

Les différents résultats de ce chapitre ont été publiés dans:

- Brevet: "*Procédé de génération d'un banc de filtre pour la réception d'un signal modulé par une modulation à phase continue et procédé de réception du dit signal*".
- Papier: *Récepteur Exact pour la Décomposition de Laurent pour les CPM*", T. Benaddi, C. Poulliat, M.-L. Boucheret, B. Gadat, G. Lesthievent, *Colloque GRETSI, 2015.*
- Papier: "*Asymptotic Analysis and Design of LDPC Codes for Laurent-based Optimal and suboptimal CPM Receivers*", T. Benaddi, C. Poulliat, M.-L. Boucheret, B. Gadat, G. Lesthievent, *IEEE Int. Conf. Acoust., Speech, and Signal Proc. (ICASSP), 2014.*

Chapitre 5: Dans ce chapitre, nous appliquons notre méthode de design dans le contexte qui est derrière la motivation de cette thèse: communication pour les drones sur des liens satellites. Ce type de communication est modélisé par le canal satellite aéronautique [B+63, B+73, SLPF+08, ser09]. En outre, nous évaluons la performance des CPM codées lorsque nous considérons une égalisation par minimisation de l'erreur quadratique moyenne (MMSE) dans le cas d'un canal séléctif en fréquence générique. Le but de ce chapitre est de montrer la faisabilité d'une *simple* égalisation dans le cadre du canal aéronautique. Les schémas proposés ne sont

pas la solution ultime, mais une approche directe parmis les techniques d'égalisation. Divers résultats de simulation sont fournis. Des résultats qui montrent que l'égalisation peut être très efficace dans ces canaux pour la CPM et que les schémas concaténés LDPC proposés sont très compétitifs par rapport à certains systèmes proposés, comme celui du DVB-S2 [ETS05].

Introduction

Context of this thesis

Unmanned aerial vehicles (UAV) become very popular and a cost effective solution in many new domains outside of the military areas (forest surveillance, emergency situations, pipelines inspection, entertainment, communication, observation ...). Due to these heterogeneous contexts, the UAVs should consider satellite communications since they cannot always count on the presence of terrestrial infrastructures and so we have to be able to command the UAV even if there is no line of sight (LOS) such as in remote areas, natural disasters, industrial disaster ... Indeed, for security reasons, one need to ensure that we can always guaranty the control of the UAV if we aim to introduce UAVs in the civilian area. This would be mandatory. A typical scheme is depicted in Fig. 4.

Today's UAVs use principally the Ku-band Fixed Satellite Service (FSS) to communicate with the remote pilot station (RPS) when they are beyond radio line of sight. Otherwise, they can use a larger range of solutions (C, Ku, S and UHF bands). In the scope of the future increasing use of the civil UAVs-satellite communications, UAVs will require more access to the frequency bands of the civil aviation services in non-segregated airspace areas or at least at some positions of the flight trajectory. In order to achieve a complete and safe integration in the existing air traffic aircraft system, a deployment on the civil aviation microwave landing system (MLS) frequency range is prescribed by the International Civil Aviation Organization (ICAO) and the International Telecommunication Union (ITU). Moreover, no satellite communication system is nowadays deployed in the Aeronautical Mobile Satellite en-Route Service (AMS(R)S) band. The 5GHz band is not used today but it is

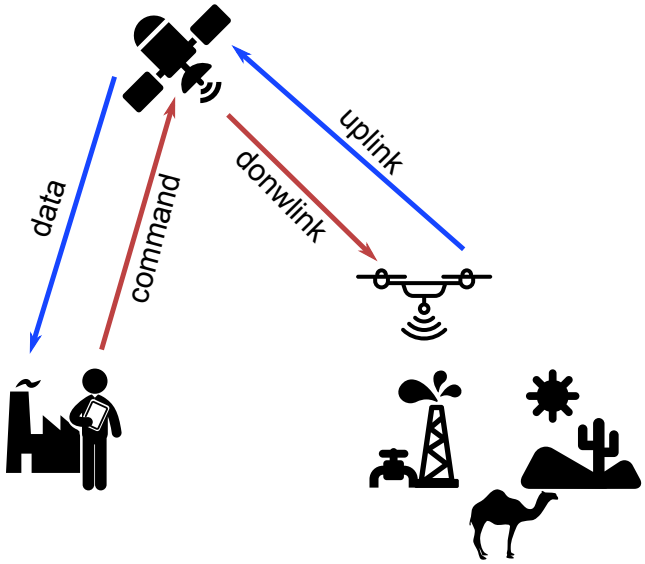

Figure 4: Typical satellite-UAV context

allocated for Microwave Landing Systems (MLS), the satellite system and the terrestrial system [IR10, IR11, CNE12]. To meet the increasing capacity demand, the first band appears as a unique opportunity for future development. Besides, in terms of transmission properties, the 5GHz band is relatively immune to rain attenuation and other weather conditions. Figure 5 illustrates an example of principle communication links between the UAV and the RPS. The same band is planned for the future standardization agreement STANAG 4660.

The ITU World Radio Conference (WRC) 2012 included an agenda item 1.3 covering this context: we should be able, by 2020, to define a complete communication scheme for both the command link and the data retrieving link on the 5030-5091 MHz frequency band especially for the Aeronautical Mobile en-Route Service (AM(R)S). This new established communication link should not interfere with the existing infrastructure. Figure 6 summarizes the main frequency allocations within the targeted 5GHz band.

Moreover, the transmitted signal is subject to strong distortions because of the channel model. Finally, the so-called satellites are assumed transparent (they only repeat the received signal). Consequently, the embedded amplifiers induce an additional signal distortion when they work in or near

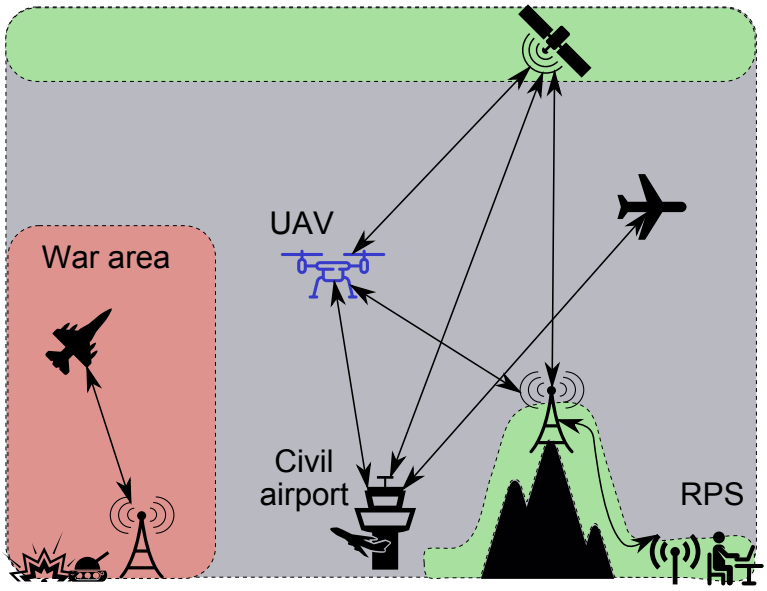

Figure 5: Typical UAV environment. The red area corresponds to a segregated and NATO controlled zone, the gray area to an non segregated but ICAO controlled zone and the green area to an uncontrolled zone

the saturation regime. In the literature, several mitigation techniques were proposed to solve this non-linearity degradation:

Predistortion

This technique is performed on the transmitter side. It consists in predistorting the transmitted signal in such way that it compensates the High Power Amplifiers (HPA) effets. This can be done by simply inverting the transfer function of the distortions. For this purpose, Volterra expansion [BBD79] is widely used to describe the non-linearity as well as its inverse. This technique and some other advanced related methods (data predistortion [SS83]) have been used in the Digital Video Broadcasting Second generation (DVB-S2) [ETS06].

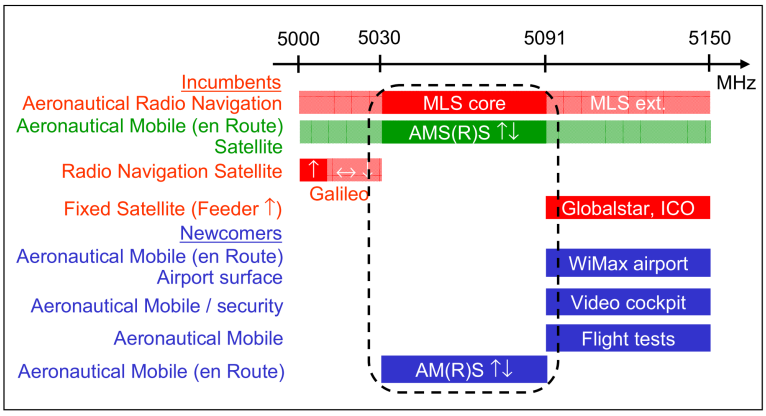

Figure 6: Overview of the 5GHz spectrum. This figure was taken from [GHGZ12]

Equalization

In some applications, the complexity of the HPA characteristic and the non-invertiblity of the transfer function do not allow a prefect recovery from the non-linearities. For these cases, one can consider a predistortion at the transmitter coupled with an equalization at the receiver side. The equalization will counterbalance the remaining non-linearity residues or other channel interference terms. Generally, this approach is based on training symbols: each message has a fixed number of known symbols used to estimate the non-linearity terms of the channel. Like in the previous approach, Volterra-based equalizers are widely used [BB83, BTP+13].

Advanced modulation schemes

Another alternative of these mitigation techniques is to use some advanced modulation schemes that are relatively immune to non-linearities, such as having a constant-envelope property. Various schemes were proposed in the literature:

- The Interplex modulation [BT72], a subclass of phase modulations, that multiplexes multiple signals into one phase modulated signal.

- Intersymbol-interference and jitter-free offset quadrature phase shift keying modulation (IJF-0QPSK) [LNF81]: this modulation is obtained by introducing a controlled proportion of

intersymbol-interference (ISI) signal into a binary IJF signal.

• Continuous phase modulation: a phase modulation where the phase transitions are kept continuous during the transmission. This class is very interesting not only for its power and spectral efficiency but also for its structure easily adaptable for serially concatenated schemes.

Continuous phase modulations schemes

In this context, the continuous phase modulations (CPM) represents a very good candidate for these constraints. Firstly, they have a constant envelope which make them immune to embedded amplifiers non-linearities happening at the saturation regime. From a satellite point of view, this allows to work with higher powers without any back-off, a fact that improves the overall link budget. Secondly, continuous phase modulations have better spectral occupation (lower side lobes) in comparison to classical linear modulation (QPSK, PSK, ...) for reasons that are going to be apparent later. In particular, it enables to increase the system capacity by avoiding too large frequency band guard intervals.

CPM signals have benefited from a large amount of research since their introduction, and their performance in the Gaussian channel has been well studied. When considering concatenated coded schemes, several works were conducted on serial concatenated schemes with binary/non-binary convolutional codes or other short block codes [XA05, GiAND09, MA01] to cite only a few. It has been often argued that serial concatenation with low density parity check (LDPC) codes implies a doubly iterative system which is difficult to analyse and thus to optimize. Surprisingly, no real complete study have been dedicated to designing good LDPC codes for CPM. This class of forward error correction code has many advantages: they exhibit competitive performance in comparison to turbo-codes, they can offer some rate flexibility for different modulation schemes and they have low decoding complexity. Moreover, if properly designed, one can achieve close to capacity performance for a wide range of applications [MN96, tBKA04, YRL04, LSL06, VNND11] ...

In most contributions dealing with concatenated schemes with LDPC and CPM, the proposed

approaches lack generality. The first related work is due to [NAN01] where a study of the concatenated LDPC code and the Minimum Shift Keying (MSK) modulation has been performed using density evolution framework. In [NAN03], the same authors proposed an LDPC code optimized with differential evolution program for the recursive MSK with some degree-1 variables nodes. In [Gan03], the author studied the optimization of M-ary Continuous-Phase Frequency-Shift Keying (CPFSK) schemes from a bit interleaved coded modulation (BICM) approach using density evolution techniques. Not only the author did not discuss the insertion of degree-1 variable nodes, but also the proposed scheduling leads to a non-linear optimization problem. They used differential evolution but this algorithm relies on different heuristics and does not guarantee an optimal solution. Finally, authors in [XA05] have considered an irregular-repeat accumulate (IRA) like concatenated scheme. They replace the IRA accumulator part by the CPM encoder. Because they considered an non-systematic IRA code, more caution should be taken in the optimization and the introduction of doping check nodes turns to be unavoidable. All the introduced concatenated schemes consider a full interleaving between the CPM and the outer code, and the CPM representation was always considered within the Rimoldi's decomposition framework [Rim88].

Dissertation outline and principle contributions

In this thesis, we aim to study and design sparse graph based coded CPM schemes. The main application will be the aeronautical channel for future UAV's deployment in the civil area. The dissertation outline and the principle contributions are summarized bellow:

Chapter 1: This chapter gives an introduction to the CPM, defines its main parameters and describes the main notations. We review the main decompositions in the literature and their related receivers (Anderson's *et al* decomposition [AAS86], Rimoldi's decomposition [Rim88] and Pierre-André Laurent's decomposition [AAS86]). Finally, we introduce the main sparse graph based codes that are going to be considered in this thesis.

Chapter 2: In this chapter, we derive an a general framework to design unstructured LDPC

codes for CPM detectors. Our method is based on an EXIT chart analysis and can be seen as a generalization of the results in [tBKA04]. Unlike the existing methods and by taking an advantage of the properties of the CPM, we will allow a proportion of degree-1 variable nodes in order to improve the iterative decoding threshold. To insure successful decoding, this proportion is subject to a stability condition which is a generalization of [RU01] in the sense that it takes into account degree-1 and degree-2 variable nodes and that it can be applied to any other detector. Unlike [RSU01], we will derive this generalized stability condition from an EXIT chart analysis. Finally, simulation results and various optimized LDPC codes of different rates concatenated with several CPM schemes are provided. We were able to design LDPC codes that operates at only 0.01dB from the capacity. In this chapter, we focus on the asymptotic performance and the evaluation of the maximum achievable rates, the results of this family will be used along the thesis to compare with other more practical codes.

The results of this chapter were published in:

- Paper: "*Asymptotic Analysis and Design of LDPC Codes for Laurent-based Optimal and suboptimal CPM Receivers*", T. Benaddi, C. Poulliat, M.-L. Boucheret, B. Gadat, G. Lesthievent, *IEEE Int. Conf. Acoust., Speech, and Signal Proc. (ICASSP), 2014.*

Chapter 3: In this chapter, we derive an asymptotic analysis to design more functional LDPC codes for the CPM. Firstly, we investigate IRA codes because of their performance and implementation advantages. Compared to the unstructured LDPC codes, they have good thresholds and are easily encodable thanks to their *step-function-like* structured part. Moreover, we generalize this family to Generalized IRA (GIRA) codes, this class includes, *inter alia*, Low Density Generator Matrix (LDGM) and IRA codes. Unlike the design method proposed in [XA05] for LDGM codes and in order to avoid the optimization of doping check nodes, we propose to study systematic GIRA codes. This consideration involves to consider an uncommon iterative decoding scheduling.

Secondly, we study the performance of protograph-based LDPC codes [Tho03]. This class

benefits from a compact representation (copy-and-permute generation), an easy performance analysis (same performance as the underlying small protograph) and an efficient implementation (the decoding can be easily parallelized). We provide an optimization method to design protograph-LDPC codes that operate 0.5dB from the unstructured LDPC codes threshold. Simulation results and comparison with the AWGN optimized protographs, ARJA and AR3A [LC07, DDJ06], are provided. The designed protographs were optimized with threshold performance in mind. Consequently, they do not have necessarily good minimum distance properties due to the introduction of large proportion of variable node of degree 1 and 2. However, since the context of our application deals with long data frames, this method gives very good results down to 10^{-3} in terms of frame error rates.

Finally, in order to obtain protographs with good performance in both the water fall and the error floor region, we study protograph-based spatially coupled LDPC codes [MLCJ14] since this class achieves universally good performance over a wide variety of channels. Besides all the advantages of the protograph-based LDPC codes, these codes exhibit a *convolution gain* that improves greatly the performance of the previous family. We will show that by coupling simple protographs such as the $(3, 6)$-regular LDPC code, we already achieve satisfactory thresholds and by construction, good minimum distance. In addition, to remedy the rate loss inherent to the termination of the spatially coupled LDPC codes, we introduce a new termination that preserves the rate the of underlying protograph independently on the coupling length, still shows a convolution gain and, depending on the coupling, leads to very good thresholds. This is the first time to our knowledge that the possibility of using only one *wave* effect is investigated. This new termination allows us to design a coupling of the $(3, 6)$-regular spatially coupled LDPC code which gives the same threshold and rate as the optimized LDPC code in chapter 3 with a coupling length equal to 4 only.

Lastly, toward designing very good spatially coupled LDPC codes for the CPM, we introduce a two step optimization technique: after finding a good protograph using the method in the previous chapter, we optimize the coupling to obtain very good thresholds. This strategy leads to very competitive codes that operate at only $0.1 - 0.15$dB from the unstructured LDPC codes

thresholds.

The different results of this chapter were published in:

- Paper: "*Protograph-based LDPC Convolutional Codes for Continuous Phase Modulation*", T. Benaddi, C. Poulliat, M.-L. Boucheret, B. Gadat, G. Lesthievent *IEEE International Conference on Communications (ICC), 2015.*
- Paper: "*Design of Unstructured and Protograph-based LDPC Coded Continuous Phase Modulation*", T. Benaddi, C. Poulliat, M.-L. Boucheret, B. Gadat, G. Lesthievent *IEEE International Symposium on Information Theory (ISIT), 2014.*
- Paper: "*Design of Systematic GIRA Codes For CPM*", T. Benaddi, C. Poulliat, M.-L. Boucheret, B. Gadat, G. Lesthievent, *IEEE International Symposium on Turbo Codes and Iterative Information Processing (ISTC), 2014.*

Chapter 4: In this chapter, we focus on some receiver aspects of the CPM and the design on LDPC codes for low complexity receivers. One of the two most used decompositions was introduced by Pierre-André Laurent [Lau86] in 1986. This decomposition makes the synchronisation functions more efficient and helps designing low complexity receivers. The maximum likelihood receivers based on the Viterbi algorithm was introduced by Kaleh in [Kal89]. Unfortunately, no *exact* maximum *a posteriori* probability (MAP) receivers were proposed in the literature: the proposed ones do not take into account the "inter-symbol interference" inherent to Laurent's decomposition and suffers from the non-whiteness of the filtered noise statistics. This approximation becomes even more penalizing for turbo decoding, non-coherent detection, equalization or in multi-carrier applications. In this chapter, after discussing the existing receivers, we derive a new MAP receiver that solves the problem of the "ISI" without introducing any additional processing such as a whitening filter. Futhermore, based on the other CPM decomposition [Rim88], we link both representations to propose an analytic method to derive the new receiver filter bank. By applying the optimization framework in chapter 2, we optimize LDPC codes for low complexity receivers based on the Laurent's decomposition and show

that the performance of the optimized codes remains very good for the low complexity receiver when enough components are taken into account. Finally, we compare the performance of the proposed receiver with the classical one in terms of EXIT chart analysis and bit error rate for the uncoded and the coded CPMs. Finally, the simulated results show that our receiver outperforms the classical one up to 2dB for both uncoded and LDPC-coded CPM schemes.

The different results of this chapter were published in:

- Patent: "*Procédé de génération d'un banc de filtre pour la réception d'un signal modulé par une modulation à phase continue et procédé de réception du dit signal*".
- Paper: *Récepteur Exact pour la Décomposition de Laurent pour les CPM*", T. Benaddi, C. Poulliat, M.-L. Boucheret, B. Gadat, G. Lesthievent, *Colloque GRETSI, 2015.*
- Paper: "*Asymptotic Analysis and Design of LDPC Codes for Laurent-based Optimal and suboptimal CPM Receivers*", T. Benaddi, C. Poulliat, M.-L. Boucheret, B. Gadat, G. Lesthievent, *IEEE Int. Conf. Acoust., Speech, and Signal Proc. (ICASSP), 2014.*

Chapter 5: In this chapter, we apply our optimization code design method to the context which is behind the motivation of this thesis: unmanned aircraft vehicle (UAV) to satellite communications. The channel of this kind of communications is modelled by the air-satellite aeronautical channel [B$^+$63, B$^+$73, SLPF$^+$08, ser09]. Also, we evaluate the performance of the coded CPM when we consider a simple minimum mean square error (MMSE) equalization in the general frequency selective and in the aeronautical channels. The goal in this chapter is to show the feasibility of a *simple* equalization in the aeronautical channel. The proposed schemes are not the ultimate solutions but easy approaches among the equalization techniques. Various simulation results are provided in both the general interference and the aeronautical channel. Results that show that the equalization can be very efficient in such channels for the continuous phase modulations and that the LDPC based proposed scheme is very competitive compared to some proposed schemes such as the one one DVB-S2 [ETS05].

List of publications

International conference papers

1. T. Benaddi, C. Poulliat, M.-L. Boucheret, B. Gadat, G. Lesthievent, « Ensemble Weight Enumerators For Protographs: a Proof of Abu Surra's Conjecture and a Continuous Relaxation for a Faster Enumeration », *IEEE International Symposium on Information Theory (ISIT)*, Hong Kong, China, 2015.

2. T. Benaddi, C. Poulliat, M.-L. Boucheret, B. Gadat, G. Lesthievent, « Protograph-based LDPC Convolutional Codes For Continuous Phase Modulation », *IEEE International Conference on Communications (ICC)*, London, UK, 2015.

3. T. Benaddi, C. Poulliat, M.-L. Boucheret, B. Gadat, G. Lesthievent, « Design of Systematic GIRA Codes for CPM », *IEEE International Symposium on Turbo Codes and Iterative Information Processing (ISTC)*, Bremen, Germany, 2014.

4. T. Benaddi, C. Poulliat, M.-L. Boucheret, B. Gadat, G. Lesthievent, « Design of Unstructured and Protograph-based LDPC Coded Continuous Phase Modulation », *IEEE International Symposium on Information Theory (ISIT),*, Hawaï, USA, 2014.

5. T. Benaddi, C. Poulliat, M.-L. Boucheret, B. Gadat, G. Lesthievent, « Asymptotic Analysis and Design of LDPC Codes for Laurent-based Optimal and Suboptimal CPM Receivers », *IEEE Int. Conf. Acoust., Speech, and Signal Proc. (ICASSP)*, Florence, Italy, 2014.

National conference papers

6. T. Benaddi, C. Poulliat, M.-L. Boucheret, B. Gadat, G. Lesthievent, « Récepteur Exact pour la Décomposition de Laurent pour les CPM », *Colloque GRETSI sur le traitement du Signal*, Lyon, France, 2015.

Patents

7. T. Benaddi, C. Poulliat, M.-L. Boucheret, B. Gadat, G. Lesthievent, « Procédé de Génération d'un Banc de Filtres pour la Réception d'un Signal Modulé par une Modulation à Phase Continue, basé sur une Décomposition de Laurent », brevet déposé avec Thales Alenia Space en 2014.

Chapter 1

Continuous Phase Modulation

Summary

Résumé

Ce chapitre présente une introduction de la CPM, définit ses principaux paramètres et décrit les principales notations. Nous passons en revue les décompositions de la littérature les plus importantes et leurs récepteurs correspondants (la décomposition d'Anderson *et al* [AAS86], la décomposition de Rimoldi[Rim88] et la décomposition de Laurent [AAS86]). Enfin, nous présentons les principaux codes basés sur des graphes creux qui vont être pris en compte dans cette thèse.

1.1 Introducion

Continuous phase modulation (CPM) is a class of coded nonlinear modulations where the phase transitions are insured continuous from one symbol period to the other. The information symbols are filtered by a phase shaping function to form a non-linear constant-envelope signal.

The ancestor of CPM systems was introduced in early 70's under the name of minimum shift keying (MSK) or fast frequency shift keying (FFSK) [DB72, ao61]. For the MSK, each input symbol is convolved with a support-T rectangular waveform (T is the symbol duration) and changes linearly the state of the phase by $\pm 90°$. Later, it was pointed out that the FFSK or the MSK hides actually a trellis structure. In order to improve the euclidean distance properties, this new representation helps to generalize FFSK to continuous phase frequency shift keying (CPFSK) [PDL71, OL74, S$^+$76]. This generalization was made by changing the modulation index of the CPM as we are going to see later. Finally, in 1979, the PhD student Tor Aulin and his supervisor Carl-Erik Sundberg finalized the theoretical work by considering different phase shapings and formalizing the underlying trellis. They introduced the name *continuous phase modulation* in their two seminal papers [ARS81a, ARS81b].

Digital communications that uses CPM have become popular after their invention because of its interesting characteristics. Firstly, they are suitable for communications through non-linear channels where the amplitude is distorted differently during the transmission. Also, since the transmitted signals have a constant envelope, they are very interesting candidates in satellite applications where different non-linearities take place (see chapter 5).

Secondly, unlike the linear modulations (quadrature amplitude modulation (QAM) and phase shift keying (PSK)) where the phase transitions are abrupt, CPM signals benefit from a narrow spectral main lobe and relatively low side lobes. The discontinuity results in the fact that a large part of the power takes place outside of the targeted band due to the presence of high frequencies.

Finally, their coded nature makes this class of modulation suitable for serially concatenated schemes and provides them with an additional robustness against channel noise.

1.2 CPM signal

Let us consider a sequence of N information symbols $\boldsymbol{\alpha} = \{\alpha_i\} \in \{\pm 1, \ldots, \pm(M-1)\}^N$. The transmitted CPM signal is written :

$$s(t) = \sqrt{\frac{2E_s}{T}} \cos\left(2\pi f_0 t + \theta(t, \boldsymbol{\alpha}) + \theta_0\right) = \Re\Big[s_b(t) e^{j2\pi f_0 t}\Big] \tag{1.1}$$

with:

$$\begin{aligned} s_b(t) &= \exp\left(j\theta(t, \boldsymbol{\alpha}) + j\theta_0\right) \\ \theta(t, \boldsymbol{\alpha}) &= 2\pi h \sum_{i=0}^{N-1} \alpha_i q(t - iT) \\ q(t) &= \begin{cases} \int_0^t g(\tau) d\tau, t \leq LT \\ 1/2, t > LT \end{cases} \end{aligned} \tag{1.2}$$

where E_s is the symbol energy, T the symbol period, f_0 the carrier frequency, θ_0 the initial phase, $\theta(t, \boldsymbol{\alpha})$ the information phase, $g(t)$ the pulse response, $h = k/p$ the modulation index (k and p are relatively prime), L the CPM memory, $\Re(.)$ the real part operator and $s_b(t)$ the complex baseband signal.

The various parameters that define a specific CPM scheme can be easily tuned to satisfy different bandwidth and complexity constraints. These parameters are:

The modulation order M

It represents the cardinality of the information symbols alphabet. Usually, it is taken as a power of 2. If large minimum distance is targeted, one should choose high modulation orders.

The frequency pulse width L

It specifies the support length of $g(t)$. It can also be seen as the CPM memory size: *i.e.* the number of past symbols required to determine the signal waveform corresponding to the current information symbol. When $L = 1$, we talk about *total response* CPMs, otherwise, when $L > 1$, we talk about

partial response CPMs. Greater L leads to significantly less out-of-band energy (smaller side lobes), nevertheless, this comes at the cost of a higher encoding and decoding complexity.

The frequency pulse $g(t)$

It defines the phase trajectory shape. The primitive of this function, denoted:

$$q(t) = \int_0^t g(\tau)d\tau$$

is called the *phase response* and must satisfy $q(LT) = 1/2$. The continuity of $q(t)$ is fundamental to keep the phase of the CPM signal continuous. $g(t)$ can have different shapes: rectangular (REC), raised cosine (RC), Gaussian, mixture of rectangular and raised cosine ... The spectral efficiency (SE) is highly dependent on this parameter. Generally, the rectangular waveform has a narrower main lobe (a better SE), however, it has higher side lobes (greater out-of-band power).

The modulation index h

Usually, it is a rational number smaller than 1. If its value changes cyclically during the transmission, the CPM is referred as *multi-h* CPM [PT87]. In this thesis we focus on constant h schemes. This is the case of the majority of the practical CPM schemes. CPM with small h has narrower occupied bandwidth (the occupied bandwidth is defined as the interval that holds 99% of the signal power). Sometimes, an irrational modulation index is assumed [ZGKK12]. However, as we are going to see later, these schemes are to be avoided because they induce high complexity receivers.

For more details on the influence of the different parameters on the minimal distance and the spectral efficiency, the reader is pleased to refer to [AAS86, AS03, CBB+04].

Table 1.1 summarizes some usual CPM schemes according to their frequency pulse, and Table 1.2 shows some of the CPM subclasses. Figure 1.1 depicts the form of some frequency shaping pulses $g(t)$ and the corresponding phase shaping functions $q(t)$.

Notation	Frequency pulse	Support	Parameters
LREC	$g(t) = \begin{cases} \frac{1}{2LT}, \text{ if } 0 \leq t \leq LT \\ 0, \text{otherwise} \end{cases}$	$[0, LT]$	L
LRC	$g(t) = \begin{cases} \frac{1}{2LT}\left[1 - \cos\left(\frac{2\pi t}{LT}\right)\right], \text{ if } 0 \leq t \leq LT \\ 0, \text{otherwise} \end{cases}$	$[0, LT]$	L
TFM	$g(t) = \frac{1}{8}\left[g_0(t-T) + 2g_0(t) + g_0(t+T)\right]$ $g_0(t) \approx \frac{1}{\pi t}\sin\left(\frac{\pi t}{T}\right)\left[1 - \frac{2-(2\pi t/T)cot(\pi t/T)-(\pi t/T)^2}{(t/T)^2}\right]$	infinite	L
LSRC	$g(t) = \frac{1}{LT}\frac{\sin(2\pi t/LT)}{2\pi t/LT}\frac{\cos(2\pi\beta t/LT)}{1-(4\beta t/LT)^2}$	infintie	L $0 \leq \beta \leq 1$
GMSK	$g(t) = \frac{1}{LT}\left[Q\left(2\pi B\frac{t-T/2}{\sqrt{\ln(2)}}\right) - Q\left(2\pi B\frac{t+T/2}{\sqrt{\ln(2)}}\right)\right]$ $Q(t) = \frac{1}{2\pi}\int_t^{+\infty}\exp\left(-\frac{\tau^2}{2}\right)d\tau = \frac{1}{2}\text{erfc}\left(\frac{t}{\sqrt{(2}}\right)$	infinite	L $0 \leq BT \leq 1$

Table 1.1: Examples of phase shaping functions of CPM.

Subclass	CPM parameters
MSK	$M = 2$
	$L = 1$
	$h = \frac{1}{2}$
	$g(t)$ rectagular
GSM GMSK	$M = 2$
	$L = 3$
	$h = \frac{1}{2}$
	$g(t)$ Gaussian
	$BT = 0.3$
CPFSK	$L = 1$
	$h = \frac{1}{M}$
	$g(t)$ rectagular

Table 1.2: Some CPM famillies

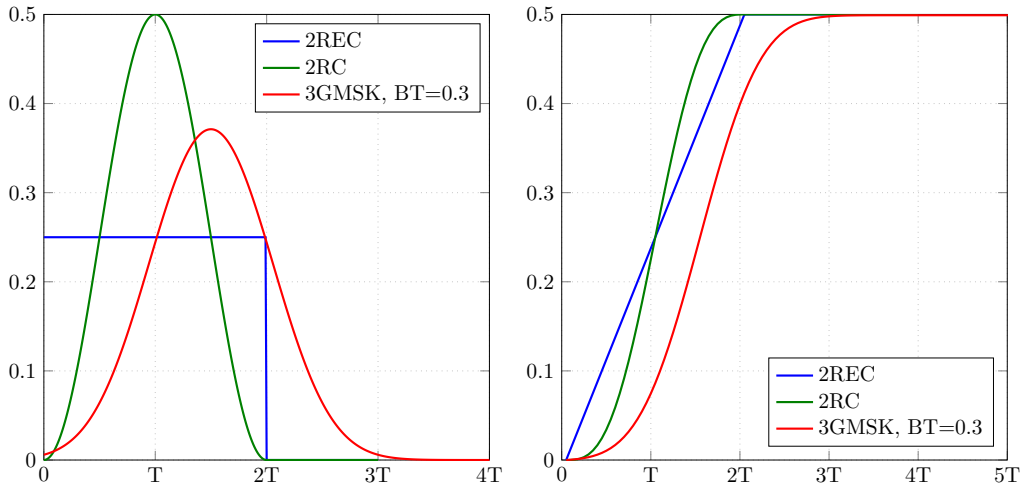

(a) $g(t)$ (b) $q(t)$

Figure 1.1: The frequency shaping pulse $g(t)$ and the phase shaping pulse $q(t)$ of some CPM schemes

Figure 1.2 represents the CPM signal corresponding to an example of a binary sequence. Notice that the signal is continuous and that the transitions are smooth. Observe also that there is no one-to-one correspondence between the bits and the waveforms.

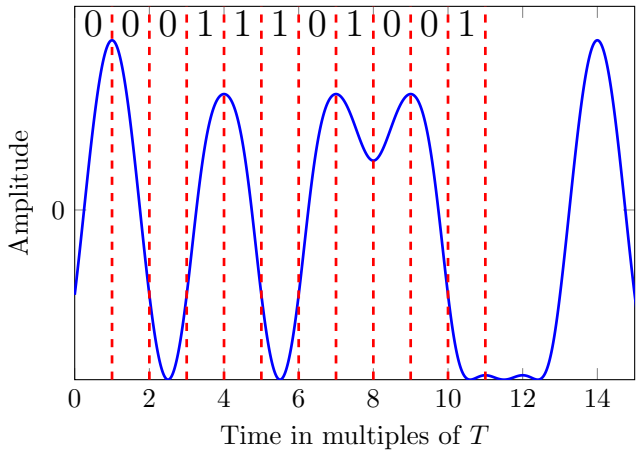

Figure 1.2: An example of a CPM encoding. Considered CPM scheme is ($M = 2$, $L = 3$, $h = 2/3$, RC)

A good way to visualize both the constant envelope property and the phase continuity is to

draw the complex CPM signal in a three dimensional polar plan (amplitude, phase, time). This representation allows to see the amplitude and the phase of the signal as a function of time. The obtained trajectory is a continuous path on the surface of a cylinder whose axis of revolution represents the time (see Figure 1.3).

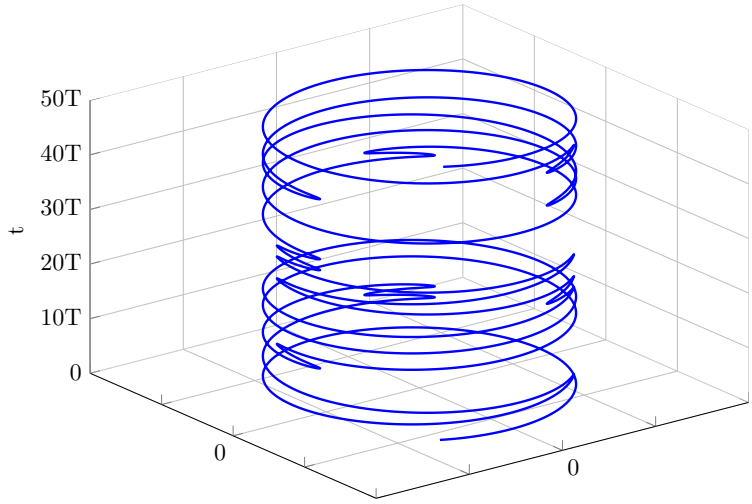

Figure 1.3: CPM signal in a three dimensional polar plan. Considered CPM scheme is ($M = 2$, $L = 3$, $h = 2/3$, RC)

Examples of CPM use cases are met in various contexts:

- Satellite communications such as DVB-RCS2 [BCDB+13]
- Deep space communications [Sim05]
- Bluetooth data transmissions [LTHS03]
- Aeronautical telemetry [Geo00]
- Automatic identification system (AIS) in marine traffic [SDPR+10]
- GSM mobile communications [MPFBH92]
- Tactical communications [CFC10, MIL99]

- Machine to machine communications [DL12]
- Optical communications [Det11]

1.3 Trellis representation

1.3.1 Original trellis representation

Let us consider $n = \lfloor \frac{t}{T} \rfloor$ ($\lfloor . \rfloor$ is the floor operator). $\forall t \in [nT, (n+1)T]$, the phase of the baseband signal in Eq. (1.2) (here $\boldsymbol{\alpha} = \{\alpha_0, \ldots, \alpha_n\}$) can be split into three terms as the following:

$$\begin{aligned}
\theta(t, \boldsymbol{\alpha}) &= 2\pi h \sum_{i=0}^{n} \alpha_i q(t - iT) \\
&= 2\pi h \alpha_n q(t - nT) + 2\pi h \sum_{i=n-L+1}^{n-1} \alpha_i q(t - iT) + 2\pi h \sum_{i=0}^{n-L} \alpha_i q(t - iT) \\
&= \underbrace{2\pi h \alpha_n q(t - nT)}_{A} + \underbrace{2\pi h \sum_{i=n-L+1}^{n-1} \alpha_i q(t - iT)}_{\phi_n(t)} + \underbrace{\pi h \sum_{i=0}^{n-L} \alpha_i}_{\theta_n} \quad \left(q(t) = \frac{1}{2}, \forall t \geq LT \right)
\end{aligned} \tag{1.3}$$

The term A corresponds to the current symbol contribution, the term $\phi_n(t)$ to the contribution of the L last symbols and θ_n to the phase state.

By taking the value of the phase state modulo 2π, one can determine all possible values. We should distinguish between two cases (recall that $h = k/p$ where k and p are relatively prime):

- if the numerator k of h is even, then θ_n takes one of the p values:

$$\theta_n \in \{0, \pi\frac{k}{p}, \pi\frac{2k}{p}, \ldots, \pi\frac{(p-1)k}{p}\}$$

- if the numerator k of h is odd, then θ_n takes one of the $2p$ values:

$$\theta_n \in \{0, \pi\frac{k}{p}, \pi\frac{2k}{p}, \ldots, \pi\frac{(2p-1)k}{p}\}$$

The term $\phi_n(t)$ is completely defined by the $L-1$ last information symbols $\{\alpha_{i-\ell}\}_{1 \leq \ell \leq L+1}$.

Consequently, the encoder state state can be completely characterized by the L-tuple:

$$\sigma_n = [\theta_n, \alpha_{n-L+1}, \ldots, \alpha_{n-1}]$$

and the transmitted signal in the interval $[nT, (n+1)T]$ is completed deduced by Eq. 1.1 and the tuple $[\sigma_n, \alpha_n]$. By recursion, the CPM signal portion corresponding to the symbol α_{n+1} is simply given by:

$$[\sigma_{n+1}, \alpha_{n+1}] \text{ where } \sigma_{n+1} = [(\theta_n + \pi h \alpha_{n-L+1}) \text{ modulo } 2\pi, \alpha_{n-L+1}, \ldots, \alpha_{n-1}, \alpha_n]$$

This description clearly defines a trellis structure where the states are defines by σ_n and the transitions by $[\sigma_n, \alpha_n]$. However, the size of this trellis depends on h: when k is even, we obtain pM^{L-1} states and pM^L transitions, otherwise, we get $2pM^{L-1}$ states and $2pM^L$ transitions.

Remark: When the modulation index h is an irrational number, for example $h = \frac{\sqrt{2}}{3}$ or $h = \frac{\pi}{6}$, it is impossible to exhibit the above mentioned trellis description because the phase has in this case an infinite number of states.

Example

Let us consider the simple MSK scheme ($M = 2$, $L = 1$, $h = 1/2$ and $g(t)$ rectangular). In this case, the total phase state can have 4 different states:

$$\left\{0, \frac{\pi}{2}, \pi, \frac{3\pi}{2}\right\}$$

Since this CPM has memory $L = 1$, the CPM trellis state is simply given by:

$$\sigma_n = \theta_n = \pi h \sum_{i=0}^{n-1} \alpha_i$$

Every input bit α_n can be mapped at most into $2pM^L = 8$ different waveforms. *"at most"* is used here because some of these waveforms, even if defined by different tuples $[\sigma_n, \alpha_n]$, may actually be the same (depending on the CPM parameters L, M and h). Typically, for the MSK, the two transitions $\mathcal{E}_1$ and $\mathcal{E}_2$ defined by:

$$\mathcal{E}_1 = [\sigma_n = 0, \alpha_n = +1] \text{ and } \mathcal{E}_2 = [\sigma_n = \pi, \alpha_n = -1]$$

generate the same waveform (refer to Eq. (1.3)).

Figure 1.4 depicts the 4 possible CPM waveforms during one symbol duration T.

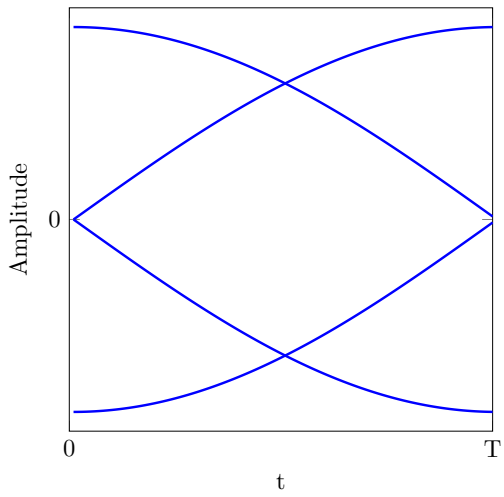

Figure 1.4: Possible MSK signal waveforms.

Figure 1.5a represents the phase tree of the MSK. Performing a modulo-2π operation on the phase tree, it can be reduced to a trellis structure as shown in Fig. 1.5b. This can be interpreted as wrapping Fig. 1.5a arround $\pm 2\pi$. As we can see, this CPM phase trellis is time varying, in that, according to the parity of n, only 2 of the 4 possible states are accessible in each symbol period T.

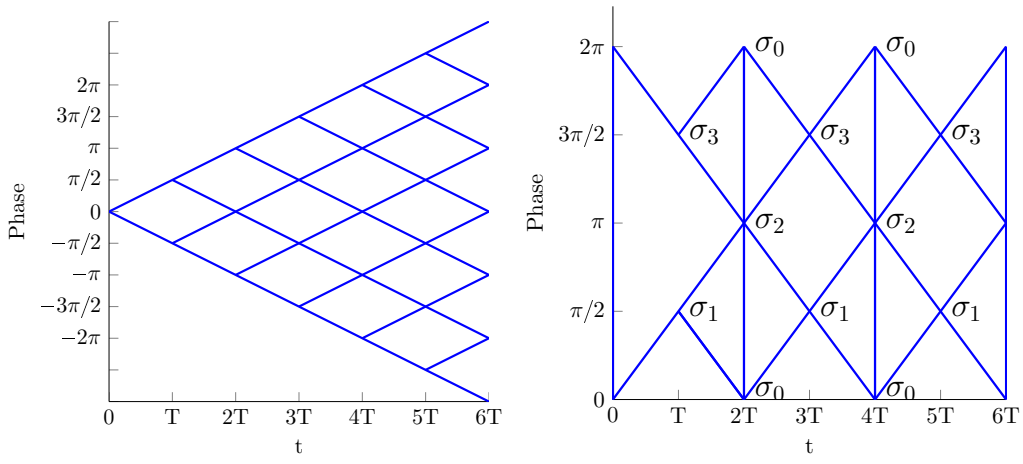

(a) Phase tree of the MSK

(b) Modulo-2π phase tree of the MSK

Figure 1.5: The phase tree and the modulo-2π of the MSK. Trellis states are $\{\sigma_0 = 0,\ \sigma_1 = \frac{\pi}{2},\ \sigma_2 = \pi,\ \sigma_3 = \frac{3\pi}{2}\}$

1.3.2 Rimoldi's decomposition [Rim88]

We have seen that the number of states in the CPM trellis depends on the parity of k the denominator of h: when it is odd, we obtain $2pM^{L-1}$ states, however, when it is even, we get only pM^{L-1} states. Moreover, we showed that the CPM trellis is time variant. In order to simplify this structure, Rimoldi introduced a new trellis representation resulting in a time-invariant trellis which always has pM^{L-1} states independently of the parity of k [Rim88]. The author showed that a CPM signal can be written as a serial concatenation of a continuous phase encoder (CPE), described by a size-pM^{L-1} time-invariant trellis, and a memoryless modulator (MM), represented by a bank of pM^L filters each of length T and denoted here by $s_i(t), i \in \{0, 1, \ldots, pM^L - 1\}$.

To do so, [Rim88] *tilted* the phase by multiplying the CPM signal by:

$$\exp\left(j\frac{\pi h(M-1)t}{T}\right)$$

This leads to a modified phase tree:

$$\psi(t, \boldsymbol{\alpha}) = \theta(t, \boldsymbol{\alpha}) + \frac{\pi h(M-1)t}{T}$$

If the modulation order is even, the symbols α_i are taken in the alphabet $\{\pm 1, \pm 3, \ldots, \pm(M-1)\}$. Otherwise, they are taken in $\{0, \pm 2, \pm 4, \ldots, \pm(M-1)\}$. To avoid this ambiguity, it is more convenient to consider a new symbol:

$$U_i = \frac{\alpha_i + (M-1)}{2}$$

Whatever the parity of M is, we now have $U_i \in \{0, 1, 2, \ldots, (M-1)\}$. Taking this new symbol into consideration, the phase of the tilted signal is given by:

$$\begin{aligned}\psi(\tau + nT, \boldsymbol{U}) =& 2\pi h \sum_{i=0}^{n-L} U_i + 4\pi h \sum_{i=0}^{L-1} U_{n-i} q(\tau + iT) \\ &\underbrace{+ \frac{\pi h(M-1)\tau}{T} - 2\pi h(M-1)\sum_{i=0}^{L-1} q(\tau + iT) + (L-1)(M-1)\pi h,}_{W(\tau)\ :\ \text{it is data independent term}} \qquad 0 \le \tau < T\end{aligned}$$

Taking the modulo-2π value of ψ gives:

$$\bar{\psi}(\tau + nT, \boldsymbol{U}) = [\psi(\tau + nT, \boldsymbol{U})]_{2\pi}$$

$$= \left[2\pi h \sum_{i=0}^{n-L} U_i + 4\pi h \sum_{i=0}^{L-1} U_{n-i} q(\tau + iT) + W(\tau) \right]_{2\pi}$$
$$= \left[2\pi h \left[\sum_{i=0}^{n-L} U_i \right]_p + 4\pi h \sum_{i=0}^{L-1} U_{n-i} q(\tau + iT) + W(\tau) \right]_{2\pi}$$

Hence, the tilted CPM waveform is completely defined by:

$$X_n = \left[U_n, \ldots, U_{n-L+1}, V_n = \left[\sum_{i=0}^{n-L} U_i \right]_p \right] \tag{1.4}$$

V_n can take p values and the tuple $[U_n, \ldots, U_{n-L+1}]$ has M^L different values. Consequently, X_n takes pM^L values.

As depicted in Fig. 1.6, the Rimoldi's continuous phase encoder can then be described by a trellis whose state definition is given by:

$$\sigma_n = [U_{n-1}, \ldots, U_{n-L}, V_n]$$

and the next state, following the current input symbol U_n, is given by the recursion:

$$\sigma_{n+1} = \left[U_n, \ldots, U_{n-L+1}, [U_{n-L+1} + V_n]_p \right]$$

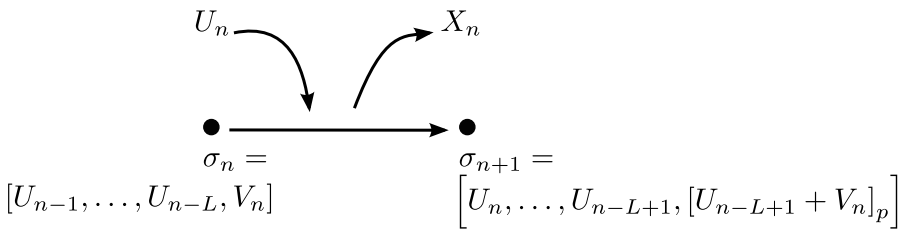

Figure 1.6: CPM transition in the CPE trellis

The CPE maps U_n into X_n which in turn generates the CPM waveform in the interval $[nT, (n+1)T]$. Figure 1.7 illustrates the Rimoldi's decomposition structure.

N.B.: In order to retrieve the real CPM signal, one should go back from the tilted phase to the real phase domain. To do so, we multiply Rimoldi's generated signal as following:

$$s_b(t) = \exp\left(j\bar{\psi}(t, \boldsymbol{U})\right) \exp\left(-j\pi h(M-1)\frac{t}{T}\right)$$

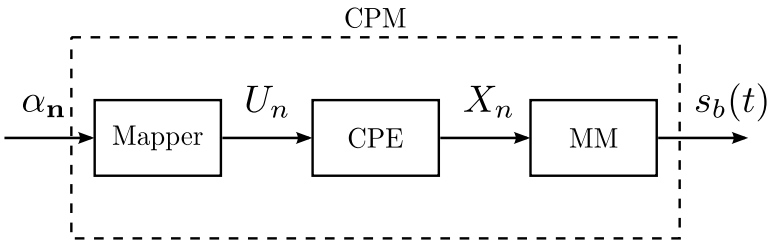

Figure 1.7: Rimoldi's decomposition structure

1.3.2.1 Discussion

The main advantage of the Rimoldi's decomposition is that it separates between the CPE and the MM which allows, especially in concatenated schemes, to study and optimize the coding part (CPE) and the modualtion part (MM) independently.

Also, it gives a concise description of the CPM in comparison to the classical CPM trellis representation [AS03]. The encoding can be easily performed using the recursive architecture depicted in Fig. 1.8.

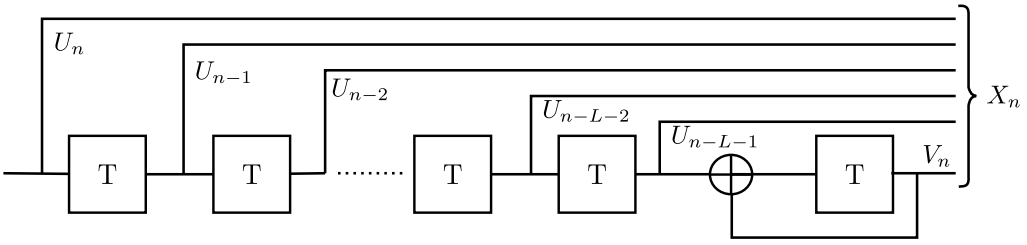

Figure 1.8: CPE

Here, the CPE can be interpreted as a convolutional code over the ring of integers modulo p [Rim88]. Therefore, one can concatenate a convolutional outer code over the same algebra, in this case, no mapper is needed and an extra coding gain is observed [XA06].

We have seen that the size of the memoryless filter corresponds to the cardinality of the set of the values of X_n in Eq. (1.4). At the first sight, one can show that X_n can have pM^L value. However, a more details analysis reports that some waveforms of the memoryless filter bank MM are a linear span of the others, for example, the waveforms corresponding to X_n values that differ only by V_n

are linearly dependent. [AAS86] discussed that the CPM signal dimension is at most M^L (*i.e.* the maximum number of linearly independent waveforms).

[Rim88] pointed out also that the CPE trellis has a recursive structure as depicted in Fig. 1.8. However, when the modulation order M is a power the denominator h (*i.e.* $\exists \ell \in \mathbb{N} : M = p^\ell$), one can use a non-recursive CPE implementation. This case is met with the CPFSK for example, where, by definition, $h = \frac{1}{M}$. The difference between these two implementations is observed in the coded CPM schemes. It is shown in [NAN03] that, in serially concatenated schemes, an iterative gain is observed when the CPM implements the recursive form of the CPE, contrary to the non-recursive form where turbo-iterations are useless. However, both of them lead to the same asymptotic performance.

1.3.3 Laurent's decomposition

1.3.3.1 Derivation

Recall that a binary CPM is given by Eqs. (1.1) and (1.2). Laurent showed that the complex baseband signal $s_b(t)$ can be expressed as the sum of $K = 2^{L-1}$ pulse amplitude-modulated signals as the following:

$$s_b(t) = \sqrt{2E_s/T} \sum_{n=0}^{N-1} \sum_{k=0}^{K-1} a_{k,n} C_k(t - nT) \tag{1.5}$$

$$C_k(t) = s_0(t) \prod_{j=1}^{L-1} s_{j+L\beta_{k,j}}(t), \quad 0 < k \leq K-1$$

$$a_{k,n} = e^{j\pi h A_{k,n}}$$

$$A_{k,n} = \sum_{i=0}^{n} \alpha_i - \sum_{j=1}^{L-1} \alpha_{n-j}\beta_{k,j} \tag{1.6}$$

$$s_j(t) = \frac{sin(\psi(t + jT))}{sin(\pi h)}$$

$$\psi(t) = \begin{cases} 2\pi h q(t), & 0 \leq t \leq LT \\ \pi h - 2\pi h q(t - LT), & LT \leq t \leq 2LT \\ 0, & \text{elsewhere} \end{cases}$$

where $\beta_{k,j}$ refer to the j^{th} bit in the binary representation of the summation index k:

$$k = \sum_{j=1}^{L-1} \beta_{k,j}, \quad k \in \{0, 1, \ldots, K-1\}$$

The components $\{C_k(t)\}_k$ have different duration lengths [Lau86] as reported by Tab. 1.3.

Component	Duration
$C_0(t)$	$(L+1)T$
$C_1(t)$	$(L-1)T$
$C_2(t), C_3(t)$	$(L-2)T$
$C_4(t), C_5(t), C_6(t), C_7(t)$	$(L-3)T$
$\vdots$	
$C_{K/2}(t), \ldots, C_{K-1}(t)$	LT

Table 1.3: Durations of the Laurent's components

Figure 1.9 plots the $\{C_k\}_k$ components of the CPM scheme ($M = 2, L = 3, h = 1/2, \text{REC}$), also called the lengthened MSK. The extension of the Laurent's decomposition to the M-ary case was proposed by Mengali *et al* [MM95].

1.3.3.2 Trellis representation

[Kal89] demonstrates that one can form the signal in Eq. (1.5) from a particular trellis. Actually, at each nT, one can compute all the pseudo-symbols $a_{k,n}$ knowing only the input symbol α_n and the current phase state $\sigma_n^L = [a_{0,n-L}, \alpha_{n-L+1}, \ldots, \alpha_{n-1}]$, according to the following recursion:

$$A_{k,n} = A_{0,n-L} + \alpha_n + \sum_{i=1}^{L-1} \alpha_{n-i}.(1 - \beta_{k,i}) \tag{1.7}$$

Discussion

Figure 1.10 transposes the generated CPM signal according to the classical representation(section 1.3.1) and to the Laurent's decomposition of an arbitrary symbols sequence. We notice that the two signals differ in the interval $[0, LT]$. This is explained by the fact that:

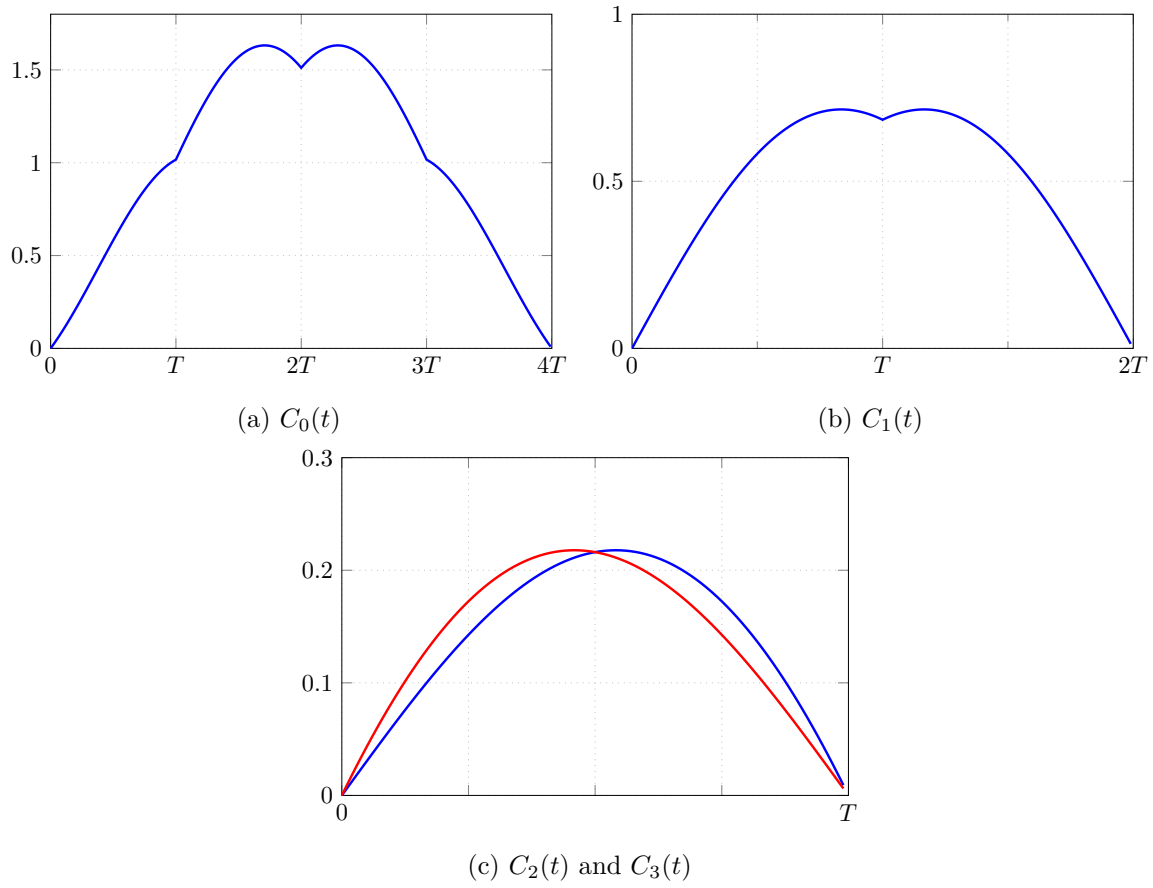

(a) $C_0(t)$ (b) $C_1(t)$

(c) $C_2(t)$ and $C_3(t)$

Figure 1.9: The 4 Laurent's components of the CPM scheme ($M = 2, L = 3, h = 1/2, \text{REC}$)

- the first $(L-1)$ pseudo-symbols $\{a_{k,n}\}_{0 \leq n \leq L-2}$ are not correctly generated because there is not enough information symbols α_i in the memory to correctly compute the recursion Eq. 1.6.

- even if the pseudo-symbols $a_{k,L-1}$ are correctly calculated, the corresponding CPM signal is not correct. Actually, the past erroneous pseudo-symbols continue to affect the CPM signal in the next periods because they modulate the components $\{C_k(t)\}_k$ whose support are greater than T (see Tab. 1.3)

To avoid this discrepancy, one can append initialization bits at the beginning of the information frame.

Thanks to the Laurent's decomposition, low complexity receivers can be easily and efficiently

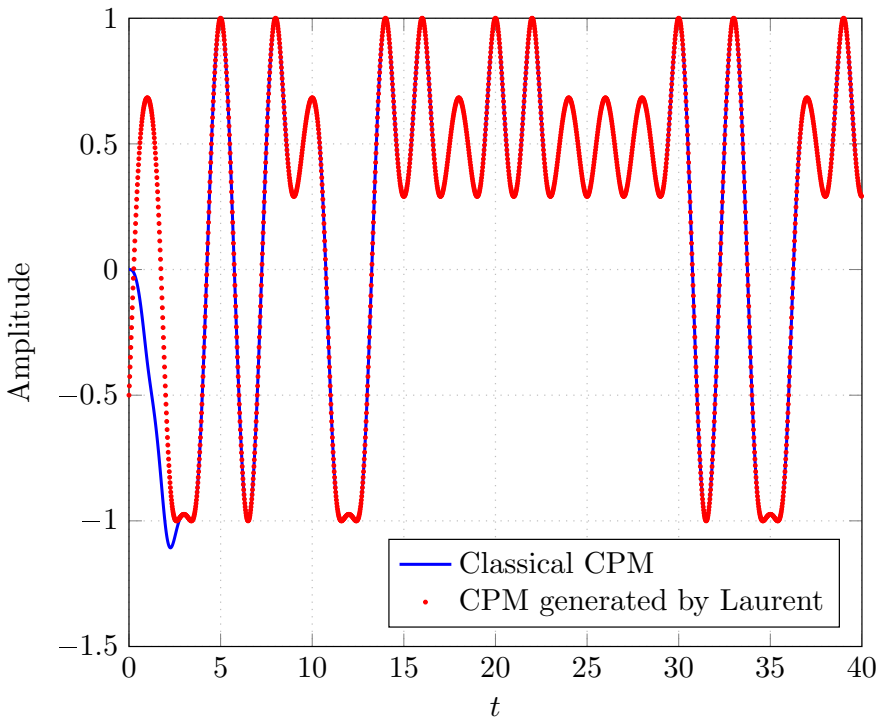

Figure 1.10: CPM signal realization example according to the classical and to the Laurent's decomposition. The considered CPM is the ($M = 2, L = 3, h = 2/3$, RC)

derived by truncating the summation in Eq. (1.5): one can approximate the CPM signal with only the first $K' < K$ components since the first components convey the most significant part of the signal energy [MM95, Lau86]. Table 1.4 illustrates the energy distribution over the Laurent's components for (a) the CPM used in the GSM ($L = 3$, $BT = 0.3$, Gaussian pulse) and (b) the MSK of memory $L = 3$.

CPM	1^{st} component	2^{nd} component	Others
(a)	99.6%	0.37%	2.6 10^{-4}%
(b)	93%	6.25%	0.23%

Table 1.4: Energy distribution in Laurent's components

1.3.4 Other decomposition

Other CPM decompositions exist in the literature. In order to exhibit the cyclostationarity property of CPM signals, Napolitano *et al* [NS01] described an expansion of the binary CPM signal in terms of a sum of PAM signals. This decomposition, unlike [Lau86], handles both integer and non-integer modulation indices. Authors in [PR04] proposed a decomposition that generalizes [MM95] to M-ary Multi-h CPMs with an exponential increase in the total number of the PAM components. Finally, [WG06] derived a different approach of [PR04] that can be universally applied to all variants of the CPM with a reasonable increase in complexity. However, the generated pulses are data dependent.

1.4 Receivers

Because both CPM representations mentioned above (Rimoldi and Laurent decompositions) can be described by a trellis, we are interested in the two trellis-based decoders: the Viterbi algorithm [Vit67] and the bit-wise BCJR (Bahl, Cocke, Jelinek and Raviv) algorithm [BCJR74] for their high performance and their importance in concatenated schemes. The Viterbi algorithm implements the maximum likelihood sequence decoder (MLSD): it returns the most likely sequence that can be inferred from the receiver observations. On the other hand, the BCJR is an algorithm for maximum *a posteriori* probability (MAP) symbol decoding: it maximizes the probability of each symbol given the whole observation sequence.

Consider that the signal $s_b(t, \boldsymbol{\alpha})$ is corrupted by an additive white Gaussian noise (AWGN) $n(t)$ with double-sided power spectral density $N_0/2$:

$$r(t) = s_b(t) + n(t), \quad t > 0 \tag{1.8}$$

Considering any support-T orthonormal basis $\{e_i(t)\}_i$ of the transmitted signal space [PS07], let us denote $\boldsymbol{r} = \{\boldsymbol{r}_i = [r_i(n)]_n\}_i$, the projection of the received signal $r(t)$ on $e_i(t)$ at $t = nT$, $\forall i$, in other words:

$$\begin{aligned} r_i(n) &= \langle r(t), e_i(t - nT) \rangle \\ &= \langle s(t), e_i(t - nT) \rangle + \langle n(t), e_i(t - nT) \rangle \end{aligned}$$

$$= s_i(n) + n_i(n)$$

where

$$\langle f, g \rangle = \int f(t) g^*(t) dt$$

Similarly to $\boldsymbol{r}$, $\boldsymbol{s} = \{\boldsymbol{s}_i\}$ and $\boldsymbol{n} = \{\boldsymbol{n}_i\}$.

1.4.1 MLSD receiver

The ML receiver finds the estimated bits sequence $\hat{\boldsymbol{\alpha}}$:

$$\hat{\boldsymbol{\alpha}} = \arg\max_{\bar{\boldsymbol{\alpha}}} p(\boldsymbol{r}|\bar{\boldsymbol{\alpha}}) \tag{1.9}$$

One can prove that $\{n_i(n)\}_n$ and $\{r_i(n)\}_n$, are uncorrelated, consequently, the probability of the observed data $\boldsymbol{r}$ under the sequence $\bar{\boldsymbol{\alpha}}$ can be expressed as [PS07]:

$$p(\boldsymbol{r}|\bar{\boldsymbol{\alpha}}) \propto \exp\left(\frac{-1}{N_0} \sum_k \sum_i |r_i(k) - \bar{s}_i(k)|^2\right)$$

where $\bar{s}_i(k)$ implicitly depends on $\bar{\boldsymbol{\alpha}}$. Then:

$$\begin{aligned}
p(\boldsymbol{r}|\bar{\boldsymbol{\alpha}}) &\propto \exp\left(\frac{-1}{N_0} \sum_k \sum_i \langle r(t) - \bar{s}(t), e_i(t - kT)\rangle^2\right) \\
&= \exp\left(\frac{-1}{N_0} \sum_k \int_{kT}^{(k+1)T} |r(t) - \bar{s}(t)|^2 dt\right) \quad \text{(Parseval's identity)} \\
&= \exp\left(\frac{-1}{N_0} \int_0^{NT} |r(t) - \bar{s}(t)|^2 dt\right) \\
&= \exp\left(\frac{-1}{N_0} \int_0^{NT} \left[r(t)r^*(t) + \bar{s}(t)\bar{s}^*(t) - 2\Re(r(t)\bar{s}^* i(t))\right] dt\right) \\
&= \underbrace{\exp\left(\frac{-1}{N_0} \int_0^{NT} r(t) r^*(t) dt\right)}_{\text{independent of } \bar{\boldsymbol{\alpha}}} \times \underbrace{\exp\left(\frac{-1}{N_0} \int_0^{+\infty} \bar{s}(t)\bar{s}^*(t) dt\right)}_{\text{constant}} \times \exp\left(\frac{2}{N_0} \int_0^{NT} \Re(r(t)\bar{s}^*(t)) dt\right) \\
&\propto \exp\left(\frac{2}{N_0} \Re\left(\int_0^{NT} r(t)\bar{s}^*(t) dt\right)\right)
\end{aligned} \tag{1.10}$$

1.4.2 MAP receiver

Consider a generic soft input soft output (SISO) component depicted in Fig. 1.11. The considered SISO component has a trellis structure whose transitions at nT are driven by the current state σ_n and the input bit α_n. Figure 1.11 summarizes the input and the output of such module.

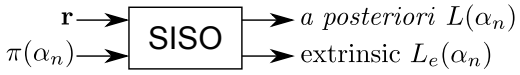

Figure 1.11: SISO component

$\boldsymbol{r} = \{r_k\}_k$ is the channel observation and $\pi(\alpha_n)$ the *a priori* probability of α_n.

The MAP criterion for the information bit α_n is given by:

$$\hat{\alpha}_n = \arg\max_{\alpha_n} p(\alpha_n/\boldsymbol{r}) = \text{sign}\left(L(\alpha_n)\right)$$

where $L(\alpha_n)$ is the *a posteriori* log-likelihood ratio (LLR) relative to the bit α_n and is defined as:

$$L(\alpha_n) = \log\left(\frac{p(\alpha_n = +1|\boldsymbol{r})}{p(\alpha_n = -1|\boldsymbol{r})}\right)$$

Using Bayes rule, we can rewrite the expression above as:

$$\begin{aligned} L(\alpha_n) &= \ln\left(\frac{p(\alpha_n = +1|\boldsymbol{r})}{p(\alpha_n = -1|\boldsymbol{r})}\right) \\ &= \ln\left(\frac{p(\alpha_n = +1, \boldsymbol{r})}{p(\alpha_n = -1, \boldsymbol{r})}\right) \quad \text{(Bayes rule)} \\ &= \ln\left(\frac{\sum_{(s,s')\in\mathcal{S}^+} p(\sigma_{n-1} = s, \sigma_n = s', \boldsymbol{r})}{\sum_{(s,s')\in\mathcal{S}^-} p(\sigma_{n-1} = s, \sigma_n = s', \boldsymbol{r})}\right) \end{aligned}$$

where $\mathcal{S}^+$ and $\mathcal{S}^-$ are the set of state tuples (s, s') such that:

$$\mathcal{S}^+ = \{(s, s')/(\sigma_{n-1} = s) \mapsto \sigma_n = s'|\alpha_n = +1\}$$
$$\mathcal{S}^- = \{(s, s')/(\sigma_{n-1} = s) \mapsto \sigma_n = s'|\alpha_n = -1\}$$

Denoting $\boldsymbol{r}_k^l = [r_i(j)]_{i,k\leq j\leq l}$, $p(\sigma_{n-1} = s, \sigma_n = s', \boldsymbol{r})$ can be factorized as:

$$p(\sigma_{n-1} = s,\sigma_n = s', \boldsymbol{r}) = p(\sigma_{n-1} = s, \sigma_n = s', \boldsymbol{r}_0^{n-1}, \boldsymbol{r}_n, \boldsymbol{r}_{n+1}^N)$$

$$
\begin{aligned}
&= p(\boldsymbol{r}_{n+1}^{N}|\sigma_{n-1}=s,\sigma_n=s',\boldsymbol{r}_0^{n-1},\boldsymbol{r}_n)p(\sigma_{n-1}=s,\sigma_n=s',\boldsymbol{r}_0^{n-1},\boldsymbol{r}_n)\\
&= p(\boldsymbol{r}_{n+1}^{N}|\sigma_{n-1}=s,\sigma_n=s',\boldsymbol{r}_0^{n-1},\boldsymbol{r}_n)p(\sigma_n=s',\boldsymbol{r}_n|\sigma_{n-1}=s,\boldsymbol{r}_0^{n-1})p(\sigma_{n-1}=s,\boldsymbol{r}_0^{n-1})\\
&= p(\boldsymbol{r}_{n+1}^{N}|\sigma_n=s')p(\sigma_n=s',\boldsymbol{r}_n|\sigma_{n-1}=s)p(\sigma_{n-1}=s,\boldsymbol{r}_0^{n-1})\\
&= p(\boldsymbol{r}_{n+1}^{N}|\sigma_n=s')p(\sigma_n=s'|\sigma_{n-1}=s)p(\boldsymbol{r}_n|\sigma_{n-1}=s,\sigma_n=s')p(\sigma_{n-1}=s,\boldsymbol{r}_0^{n-1})\\
&= p(\boldsymbol{r}_{n+1}^{N}|\sigma_n=s')p(\alpha_n)p(\boldsymbol{r}_n|\sigma_{n-1}=s,\sigma_n=s')p(\sigma_{n-1}=s,\boldsymbol{r}_0^{n-1})\\
&= \underbrace{p(\boldsymbol{r}_{n+1}^{N}|\sigma_n=s')}_{\mathcal{B}_n(s')}\underbrace{p(\alpha_n)p(\boldsymbol{r}_n|\sigma_{n-1}=s,\sigma_n=s')}_{\mathcal{G}_n(s',s)}\underbrace{p(\sigma_{n-1}=s,\boldsymbol{r}_0^{n-1})}_{\mathcal{A}_n(s)}
\end{aligned}
$$

$\mathcal{A}_n(s)$ and $\mathcal{B}_n(s')$ define respectively a forward and a backward recursion expressed by:

$$
\begin{aligned}
\mathcal{A}_n(s) &= \textstyle\sum_{s'} \mathcal{G}_n(s',s)\mathcal{A}_{n-1}(s')\\
\mathcal{B}_{n-1}(s) &= \textstyle\sum_{s} \mathcal{G}_n(s',s)\mathcal{B}_n(s')
\end{aligned}
\tag{1.11}
$$

while the transition probability $\mathcal{G}_n(s',s)$ is equal to:

$$
\begin{aligned}
\mathcal{G}_n(s',s) &= p(\sigma_n=s,r_n|s_{n-1}=s')\\
&= p(y_n|s',s)p(s'|s)
\end{aligned}
\tag{1.12}
$$

with

$$
p(s'|s) = \begin{cases} 0, \text{if } \{s' \to s\} \text{ is not valid} \\ \pi(\alpha_n), \text{otherwise} \end{cases}
$$

Let us note by $|\sigma|$ the number of the trellis state and by σ_0 the zero state of the encoder. The starting conditions of $\mathcal{A}_n(s)$ can be taken as:

$$
\mathcal{A}_0(0) = \begin{cases} 1, \text{ if } s=\sigma_0 \\ 0, \text{otherwise} \end{cases}
$$

If termination bits are appended at the end of the information block, then:

$$
\mathcal{B}_N(0) = \begin{cases} 1, \text{ if } s=\sigma_0 \\ 0, \text{otherwise} \end{cases}
$$

otherwise, $\mathcal{B}_N(s') = 1/|\sigma|, \forall s'$.

Remark: Authors in [MA00] showed that one can terminate the CPM encoding using at most T_s symbols independently of the CPM parameters:

$$T_s = \left\lfloor \frac{p-1}{M-1} \right\rfloor + L$$

When the transmitted signal is corrupted with an additive white Gaussian noise of a double-sided power spectral density $N_0/2$, $\mathcal{G}_n(s', s)$ is given by [PS07]:

$$\mathcal{G}_n(s', s) \propto \exp\left(-\frac{\sum_m |r_n^{(m)} - \mathcal{F}^{(m)}(s', s)|^2}{N_0}\right) p(s'|s) \tag{1.13}$$

where $\mathcal{F}^{(m)}(s', s)$ is the observation output relative to the m^{th} bit of the output symbol corresponding to the trellis transition $\{\sigma_{n+1} = s', \sigma_n = s\}$.

1.4.2.1 Log domain MAP

The computation of the forward/backward recursions and the iterative decoding may lead to numerical problems: the absolute values of $\mathcal{A}_n$ or $\mathcal{B}_n$ rapidly grow to infinity, sometimes even if a normalization is taken into account. To prevent these memory issues, we run the BCJR algorithm in the logarithmic domain. The Eq. (1.11) becomes:

$$\tilde{\mathcal{A}}_n(s) = \max_{s'}{}^* \left(\tilde{\mathcal{A}}_n(s) + \tilde{\mathcal{G}}_n(s', s)\right)$$
$$\tilde{\mathcal{B}}_{n-1}(s') = \max_{s}{}^* \left(\tilde{\mathcal{B}}_n(s') + \tilde{\mathcal{G}}_n(s', s)\right)$$

where $\max^*$ is defined by:

$$\max{}^*(x, y) = \max(x, y) + \log\left(1 + e^{-|x-y|}\right)$$

To reduce the complexity, the $\max^*$ operator can be simply replaced by the max operator. This induces an error of at most:

$$\max_{x,y} \log\left(1 + e^{-|x-y|}\right) = \log 2 \simeq 0.6931$$

Since we are dealing with very high values, this correction term can be neglected.

Another complexity reduction technique is to use a look-up table to approximate $\log\left(1+e^{-|x-y|}\right)$ instead of computing the exact values.

1.5 CPM receivers

This section summarizes the two main CPM receivers in the literature. For further details on the derivation of these receivers, especially for Laurent-based receiver, please refer to the chapter 4. Throughout this dissertation, we denote by A^{-1} the decoder corresponding to the component A (for example: $MM\text{-}MM^{-1}$, $CPE\text{-}CPE^{-1}$, $CPM\text{-}CPM^{-1}$, ...).

Let us consider a sequence of N information symbols $\boldsymbol{\alpha} = \{\alpha_i\} \in \{\pm 1, \ldots, \pm(M-1)\}^N$. The transmitted CPM signal is given by Eq. (1.1) as:

$$\begin{aligned} s(t) &= \sqrt{\frac{2E_s}{T}}\cos\left(2\pi f_0 t + \theta(t,\boldsymbol{\alpha}) + \theta_0\right) \\ &= \Re\left[s_b(t)e^{j2\pi f_0 t}\right] \end{aligned} \tag{1.14}$$

Figure 1.12 depicts the considered serially concatenated coded CPM scheme.

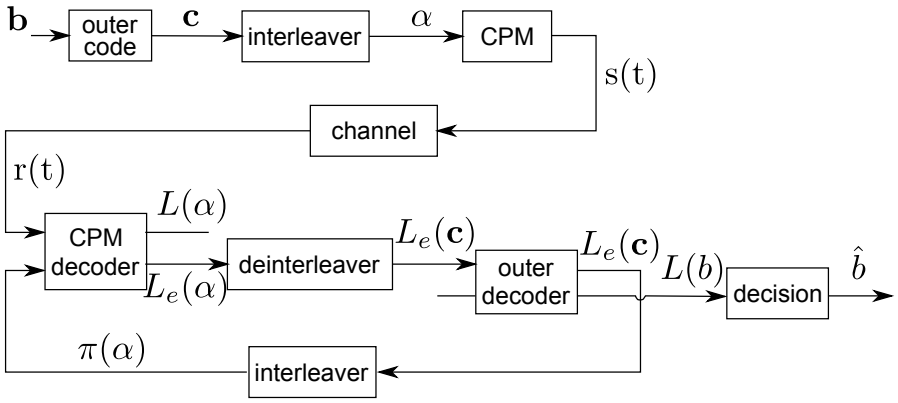

Figure 1.12: Coded interleaved CPM scheme with iterative decoding

In the following, we focus on the SISO CPM module. We suppose that the signal is corrupted by an additive white Gaussian noise (AWGN) $n(t)$ with double-sided power spectral density $N_0/2$.

1.5.1 Rimold-based receiver

The receiver architecture corresponding to the Rimoldi's decomposition is depicted in Fig. 1.13.

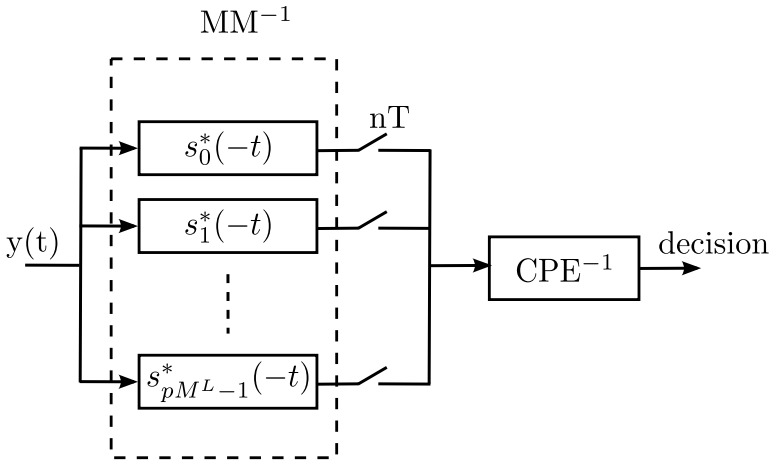

Figure 1.13: Rimoldi's decomposition-based receivers

1.5.1.1 MLSD receiver

Using any orthonormal expansion of the receiver matched filters bank (MM), the branch metric in Eq. (1.10) can be rewritten as:

$$
\begin{aligned}
p(\boldsymbol{r}|\bar{\boldsymbol{\alpha}}) &\propto \exp\left(\frac{2}{N_0}\Re\left(\int_0^{NT} r(t)\bar{s}^*(t)dt\right)\right) \\
\log\left(p(\boldsymbol{r}|\bar{\boldsymbol{\alpha}})\right) &\propto \Re\left(\int_0^{NT} r(t)\bar{s}^*(t)dt\right) \\
&= \Re\left(\sum_k \int_{kT}^{(k+1)T} r(t)\bar{s}^*(t)dt\right) \\
&= \sum_k \Re\left(\int_{kT}^{(k+1)T} r(t)\bar{s}^*(t)dt\right)
\end{aligned}
$$

Consequently, Eq. (1.9) can be directly implemented using the expression above via the Viterbi algorithm [Vit67] performed over the CPE trellis to compute the cross-correlation between the received sequence and the possible waveforms that form the receiver signal space.

1.5.1.2 MAP receiver

The outputs of receiver matched filters bank in Fig. 1.13 are sampled once each nT. We then obtain the correlator output [PS07]:

$$\boldsymbol{r^n} = \left[r_i(n) = \int_{nT}^{(n+1)T} r(t) s_i^*(t) dt \right]_{1 \leq i \leq pM^L}$$

It is shown that $\{\boldsymbol{r^n}\}_n$ is a sufficient statistic to estimate symbols [MA01]. Since the length of the matched filters is equal to T, the samples of the noise filtered by $s_i^*(-t)$, denoted $\{n_i\}_i$, are Gaussian and independent. Using any orthonormal expansion of receiver matched filters bank [MA01], the joint probability density function of $\boldsymbol{r^n}$ in Eq. (1.13) can be reduced as:

$$p(\boldsymbol{r^n}|X_n) \propto \exp\left(\frac{2\Re(r_i(n))}{N_0}\right)$$

1.5.2 Laurent-Kaleh's receiver

1.5.2.1 MLSD receiver

The receiver structure corresponding to the Laurent's decomposition was presented by [Kal89] and is depicted in Fig. 1.14.

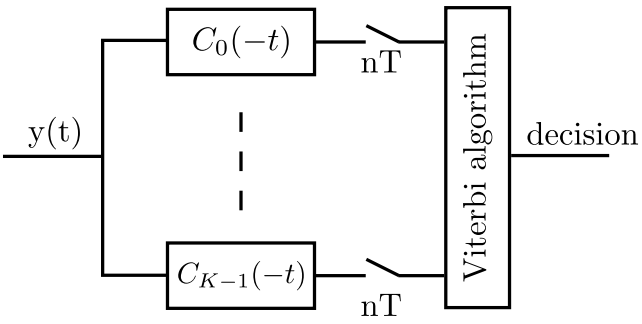

Figure 1.14: Kaleh's Laurent-based receiver

Starting from Eq. (1.10) and by substituting Eq. (1.5), the new metric corresponding to the sequence $\bar{\boldsymbol{\alpha}}$, denoted hereafter $\Gamma(\bar{\boldsymbol{\alpha}})$, is written as:

$$\Gamma(\bar{\boldsymbol{\alpha}}) = \Re\left[\int_0^{NT} r(t) \bar{s}_i^*(t) dt \right]$$

$$
\begin{aligned}
&= \Re\left[\int_0^{NT} r(t) \sum_{n=0}^{N-1}\sum_{k=0}^{K-1} \bar{a}_{k,n}^* C_k^*(t-nT)dt\right] \\
&= \Re\left[\int_0^{NT} \sum_{n=0}^{N-1}\sum_{k=0}^{K-1} \bar{a}_{k,n}^* r(t) C_k^*(t-nT)dt\right] \\
&= \Re\left[\sum_{n=0}^{N-1}\sum_{k=0}^{K-1} \bar{a}_{k,n}^* \int_0^{NT} r(t) C_k^*(t-nT)dt\right] \\
&= \sum_{n=0}^{N-1} \Re\left[\sum_{k=0}^{K-1} \bar{a}_{k,n}^* \int_0^{NT} r(t) C_k^*(t-nT)dt\right] \\
&= \sum_{n=0}^{N-1} \Re\left[\int_0^{NT} r(t) \sum_{k=0}^{K-1} \bar{a}_{k,n}^* C_k^*(t-nT)dt\right]
\end{aligned}
$$

since $\sum_{k=0}^{K-1} \bar{a}_{k,n}^* C_k^*(t-nT)$ has support of maximum the support of $C_0(t)$ which is $(L+1)T$, we can write:

$$
\begin{aligned}
\Gamma(\bar{\boldsymbol{\alpha}}) &= \sum_{n=0}^{N-1} \Re\left[\int_{nT}^{(n+L+1)T} r(t) \sum_{k=0}^{K-1} \bar{a}_{k,n}^* C_k^*(t-nT)dt\right] \\
&= \sum_{n=0}^{N-1} \Re\left[\sum_{k=0}^{K-1} \bar{a}_{k,n}^* \int_0^{(L+1)T} r(t+nT) C_k(t)dt\right]
\end{aligned} \tag{1.15}
$$

More details and interpretations concerning this receiver are given in the chapter 4.

1.5.2.2 MAP receiver

In [MFG97, CB05, CR97], authors derived the Maximum *a posteriroi* (MAP) receivers [BCJR74]. However, in their derivations, they neglect the non-whiteness of the filtered noise by the Laurent's components (the matched filters have a support which is longer than the symbol period) in comparison to the noise of the channel. In order to implement the exact receiver for the MAP detector, one should introduce a whitening filter. This filter becomes even more important when we consider non-coherent detections [LTHS03], equalization [TS05] or multicarrier signals [MH]. To our knowledge no exact bit-wise MAP receiver for Laurent-based receiver exist in the literature. In chapter 4, we discuss the existing decoders and provide a new and exact symbol-wise MAP receiver.

Chapter 2

Design of unstructured LDPC codes

Summary

Résumé

Dans ce chapitre, nous dérivons une méthode générique pour optimiser des codes LDPC non structurés pour la CPM. Notre méthode est basée sur une analyse EXIT Chart et peut être vu comme une généralisation des résultats dans [tBKA04]. Contrairement aux méthodes existantes et en tenant en compte les propriétés de la CPM, nous allons introduire une proportion de noeuds de variables de degré 1 afin d'améliorer le seuil de décodage itératif. Pour assurer un décodage réussi, cette proportion est soumise à une condition de stabilité qui est une généralisation de [RU01] dans le sens où elle prend en compte les degrés 1 et 2 et qu'elle peut être appliquée à tout autre détecteur. Differemment de [RSU01], nous dériverons cette condition de stabilité généralisée à partir d'une analyse EXIT

Chart. Enfin, les résultats de simulation et les divers codes LDPC optimisés sont fournis. Nous allons voir qu'on est en mesure de trouver des codes LDPC qui fonctionne à seulement 0.01dB du seuil de décodage minimal théorique. Dans ce chapitre, nous nous concentrons sur la performance asymptotique et l'évaluation du rendement maximal atteignable, les résultats de cette famille seront utilisés le long de la thèse et comparés avec d'autres codes plus pratiques.

2.1 Introduction

After the advant of turbo-codes [BG96], coded CPM systems have greatly benefited from the concept of iterative decoding. If several papers consider the serial concatenation of CPM with a trellis based code [MA01, GiAND09, NS99, CBB+04], only few references have studied the concatenation with LDPC codes. In most of the cases, the proposed approaches are dedicated to a specific subfamily of CPM modulations and thus lack generality. The first related work is due to [NAN01] where a study of the concatenated LDPC code and the Minimum Shift Keying (MSK) modulation has been performed using density evolution framework. It was shown that the optimal design depends on the implementation of the continuous phase encoder, if implemented as a recursive encoder, there is a design enabling interleaving gain with an iterative detection and decoding scheme, otherwise a non-iterative scheme with an optimal code for the designed binary input AWGN case is sufficient. In [NAN03], the same authors proposed an LDPC code optimized with differential evolution program for the recursive MSK considering a heuristic approach that enables the introduction of some degree-1 variables nodes. Based on the EXIT properties, they were the first to conjecture the possible use of degree-1 nodes, a fact that has a major difference compared to the classical optimization of the LDPC codes over memoryless channels where this class of nodes are prohibited (if we except the particular case of LDGM codes). They did not use a stability constraint on the degree-1 or degree-2 variables node proportions but instead a heuristic approach that allows easily encodable codes: the sum of the fraction of degree-1 and degree-2 variable nodes should not exceed $(1-R)$ where R is the code rate. In [Gan03], the author studied the optimization of M-ary Continuous-Phase Frequency-Shift Keying (CPFSK) schemes from a bit interleaved coded modulation (BICM) approach. Only degree-2 ans higher variable nodes were considered. Finally, [XA05, CVT09, XA07] have considered an irregular-repeat accumulate (IRA) like concatenated scheme. The proposed structure replaces the IRA accumulator part by the CPM encoder. This has been motivated by the fact that the CPM can be seen as a phase accumulator. All the introduced concatenated schemes consider a full interleaving between the CPM and the outer code and the CPM representation was always considered within the Rimoldi's decomposition framework [Rim88].

In this chapter, we will observe that the extrinsic information transfer (EXIT) curves [tB01d, Hag04] of the CPM join the point $(1, 1)$, except perhaps in some very particular and rare cases that are usually avoided. This allows us to introduce a proportion of degree-1 variable nodes which helps to improve the achievable designed code rates as long as a particular stability condition is satisfied. We will provide a proof of this stability condition and to its generalization to any detector. Furthermore, we derive the asymptotic analysis to design unstructured LDPC codes for general CPM schemes. By considering partial interleavers, we will show that the optimization can be efficiently performed solving a simple linear optimization programming. We point out that our optimization framework and its built-in scheduling can be generalized to any other trellis-based coded modulation or linear modulation. In order to alleviate the threshold computation complexity, one often use a mono-dimensional evolution analysis based on the study of the evolution of a scalar parameter.

In this chapter, we will consider the Rimoldi's decomposition for ease of presentations but the proposed method can be applied to any other SISO detector as it will be shown in chapter 4. The chapter is organized as follows: first we give the system description and recall the main notations and properties of the different communication blocks we are considering. Then, we derive our asymptotic approach to design LDPC codes for CPM. Furthermore, in the context of the EXIT chart analysis, we will derive the stability condition for the degree-1 and the degree-2 variables nodes. This necessary condition is to be taken into account when designing the LDPC codes to insure a convergence to a zero error probability [RSU01, RU01]. Finally, we provide some simulation results and the optimized profiles for various CPM schemes.

2.2 LDPC codes

2.2.1 Description

Turbo-codes were invented by Berrou *et al* in 1993 [BG96]. They revolutionize the field or error-correcting codes by proposing coding schemes that operate very near to the Shannon limit [Sha01] over different channels. The novelty was about concatenating two convolutional codes separated by an interleaved and jointly decoded within an iterative procedure. Since their introduction and until

today, several studies have been conducted to analyze and to design high performance schemes.

Trying to explain why turbo-codes behave so well, Mac Kay *et al*[MN96] rediscovered a second major coding schemes called low density parity check (LDPC) codes. They were originally invented by Gallager in 1962 in his PhD thesis [Gal62]. However, they were soon after ignored due to the high complexity of the corresponding decoder for the concurrent hardware maturity.

It was shown later that both LDPC codes and turbo codes are sparse graph-based codes [Wib96], and that the iterative decoding of turbo codes and the belief propagation decoding for LDPC codes are actually connected [MMC98]. [RU01, RSU01] provided remarkable tools to analysis and to design LDPC codes that operate very close to the Shannon limit.

An LDPC code is described by a parity check matrix $\boldsymbol{H}$ such that a valid codeword verifies the property $\boldsymbol{H}\boldsymbol{x}^T = \mathbf{0}$, where:

- $.^T$ is the transpose operator
- $\boldsymbol{H}$ is the parity check matrix of size $M \times N$
- When $\boldsymbol{H}$ is full rank, the rate of the code R equals

$$R = 1 - \frac{M}{N}$$

- The i^{th} parity equation, $\forall i = 1 \dots M$, is given by:

$$\sum_{j:\boldsymbol{H}(i,j)\neq 0} x_j = 0 \text{ modulo } 2$$

The matrix $\boldsymbol{H}$ is binary (*i.e.* the entries are 0's or 1's) and sparse (*i.e.* mostly filled by 0's). The number of 1's in a row (or in a column) is called the degree of that row (respectively of that column). In terms of degrees, the ensemble to which an LDPC code belongs is characterized by the two degree polynomials $\lambda(x)$ and $\rho(x)$ which specify the rows and the columns degree distributions:

$$\lambda(x) = \sum_{i=2}^{d_{v,max}} \lambda_i x^{i-1} \qquad \rho(x) = \sum_{j=2}^{d_{c,max}} x^{j-1}$$

where:

- $\lambda_i = \frac{\text{total number of 1's in } \textbf{all} \text{ degree-}i \text{ columns}}{\text{total number of 1's in } \boldsymbol{H}}$
- $\rho_j = \frac{\text{total number of 1's in } \textbf{all} \text{ degree-}j \text{ rows}}{\text{total number of 1's in } \boldsymbol{H}}$
- $d_{v,max}$ ($d_{c,max}$) maximum degree of rows (respectively columns)

The rate of an LDPC is given by:

$$R \geq 1 - \frac{\int_0^1 \rho(x)dx}{\int_0^1 \lambda(x)dx} = 1 - \frac{\sum_{j=2}^{d_{c,max}} \rho_j/j}{\sum_{i=2}^{d_{v,max}} \lambda_i/i}$$

with equality when $\boldsymbol{H}$ is full rank.

2.2.2 Graphical representation

Tanner [Tan81] introduced a graphic representation of LDPC codes called *Tanner graph*. It is under the form of a bipartite graph with two types of nodes: the columns of $\boldsymbol{H}$ are represented by *variable nodes* (VN) while the rows of $\boldsymbol{H}$ are represented by *check nodes* (CN). An edge connects the VN j to the CN i if the entry $H(i,j) = 1$.

As an example, consider the following parity check matrix:

$$\boldsymbol{H} = \begin{pmatrix} 0 & 1 & 1 & 0 & 1 & 0 & 0 \\ 1 & 0 & 1 & 1 & 0 & 0 & 0 \\ 1 & 1 & 0 & 1 & 1 & 1 & 1 \\ 0 & 0 & 1 & 0 & 1 & 1 & 1 \end{pmatrix} \tag{2.1}$$

The corresponding Tanner graph is depicted in Fig. 2.1. This matrix is full rank, consequently, the rate of the corresponding LDPC code is $R = 3/7$. The profile polynomials are given by:

$$\lambda(x) = \frac{5}{8}x + \frac{3}{8}x^2 \qquad \rho(x) = \frac{3}{8}x^2 + \frac{1}{4}x^3 + \frac{3}{8}x^5$$

and an example of a valid codeword can be $\boldsymbol{x} = [1\ 0\ 0\ 1\ 0\ 1\ 1]^T$.

The Tanner graph not only provides a compact representation, but also helps to describe the decoding algorithm. λ_i (respectively ρ_j) represents the proportion of edges on the Tanner graph that are connected to variable nodes of degree i (respectively to check nodes of degree j).

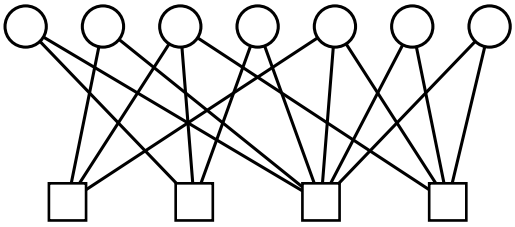

Figure 2.1: The Tanner graph of the parity check matrix in Eq. (2.1). The VNs are represented by circles while the CNs are represented by squares

2.2.3 Decoding

The maximum *a posteriori* (MAP) decoding is very complex for LDPC codes, alternatively, we use the sum-product algorithm (SPA), also referred as the belief propagation algorithm (BP) [Gal62]. Gallager proposed this algorithm as a MAP near-optimal LDPC decoding procedure. The algorithm was independently proposed by J. Pearl *et al* in 1982 [Pea82, KP83, Pea14] who formulated this algorithm for artificial intelligence. SPA applies the Bayes' rule locally and tries to approximate the *a posteriori* probabilities (APP) by iterating over the whole graph. It the graph is cycle-free, then the sum product algorithm is optimal.

Consider the codeword $\boldsymbol{x} = [x_0, \ldots, x_{N-1}]$ transmitted with binary phase shit keying (BPSK) modulation. The corresponding received observation $\boldsymbol{y} = [y_0, \ldots, y_{N-1}]$ over a binary-input additive white Gaussian noised (BI-AWGN) channel is written as:

$$y_j = x_j + n_j, \forall j = 0, \ldots, N-1$$

where $x_j \in \{+1, -1\}$ and $n_j \sim \mathcal{N}(0, \sigma^2)$.

The APP of the bit x_j, given the channel output observation $\boldsymbol{y}$ is given by:

$$P(x_j = 1|\boldsymbol{y})$$

The channel LLR of the bit x_j is computed as:

$$L_{\text{ch}}(x_j) = \log\left(\frac{P(x_j = +1|\boldsymbol{y})}{P(x_j = -1|\boldsymbol{y})}\right) = \frac{2y_j}{\sigma^2}$$

During the decoding process, The extrinsic LLR messages passing between the VN v_j and the check node c_i follows the rules:

$$L_{v_j \to c_i} = L_{\text{ch}}(x_j) + \sum_{\substack{k \\ H(k,j)=1 \\ k \neq i}} L_{c_k \to v_j}$$

$$\tanh\left(\frac{L_{c_i \to v_j}}{2}\right) = \prod_{\substack{k \\ H(k,j)=1 \\ k \neq j}} \tanh\left(\frac{L_{v_k \to c_i}}{2}\right)$$

At the end of the decoding process, the estimated bit $\hat{x}_j$ is decoded according to the sign of the APP:

$$\hat{x}_j = \text{sign}\left(L_{\text{ch}}(x_j) + \sum_{\substack{k \\ H(k,j)=1}} L_{c_k \to v_j}\right)$$

2.3 System Description

We consider a serially concatenated coded scheme where a binary LDPC encoder is concatenated with a CPM modulator as depicted in Fig. 2.2.

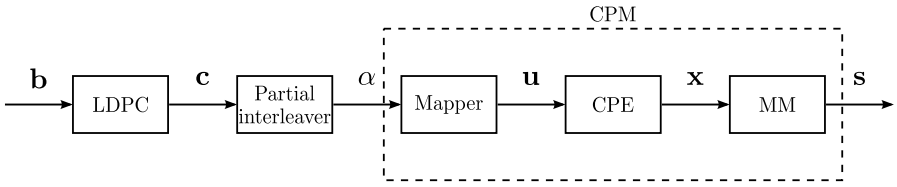

Figure 2.2: Transmitter

At the transmitter, a binary message vector $\boldsymbol{b} \in \mathbb{F}_2^K$, is first encoded using an LDPC code of rate $R = K/N$ to produce a codeword $\boldsymbol{c} \in \mathbb{F}_2^N$. K is the number of information bits, N the codeword length and $\mathbb{F}_2$ the binary Galois field. An LDPC code is usually defined using its corresponding binary sparse parity check matrix H of size $M \times N$ with $M = NK$. $\boldsymbol{c}$ is a binary vector that belongs to the null space of H ($H\boldsymbol{c}^T = 0$ where $.^T$ is the transposition operator). Based on the matrix H, an LDPC code can be represented by its corresponding Tanner graph [Tan81]. This later consists in

two sets of nodes: the variable nodes (circular vertices) associated with the codeword bits (columns of H) and the check nodes (square vertices) associated with the parity check constraints (rows of H). An edge joins a variable node (VN) n to a check node (CN) m if $H(m,n) = 1$. Irregular LDPC codes are usually defined with their edge-perspective degree distribution polynomials:

$$\lambda(x) = \sum_{i=d_{v,min}}^{d_{v,max}} \lambda_i x^{i-1} \qquad \rho(x) = \sum_{j=2}^{d_{c,max}} \rho_j x^{i-1} \tag{2.2}$$

where λ_i (and ρ_j) is the proportion of edges in the Tanner graph connected to VNs of degree i (respectively to CNs of degree j), and $d_{v,max}$ ($d_{c,max}$) is the maximum VN (respectively CN) degree. $d_{v,min}$ is the minimum VN degree, when degree-1 VNs are taken into account, $d_{v,min} = 1$, otherwise $d_{v,min} = 2$. When H is full rank, These two polynomials are related to the design code rate as:

$$R = 1 - \frac{\sum_{j=2}^{d_{c,max}} \rho_j / j}{\sum_{i=d_{v,min}}^{d_{v,max}} \lambda_i / i} \tag{2.3}$$

Each codeword $\boldsymbol{c}$ is then interleaved and mapped into M-ary symbols $\boldsymbol{\alpha} = \{\alpha_i\}_i$ and finally encoded by the CPM modulator as:

$$\begin{aligned} s(t, \boldsymbol{\alpha}) &= \sqrt{\frac{2E_s}{T}} \cos\left(2\pi f_0 t + \theta(t, \boldsymbol{\alpha}) + \theta_0\right) \\ &= \Re[s_b(t, \boldsymbol{\alpha}) e^{j2\pi f_0 t}] \end{aligned} \tag{2.4}$$

with

$$\theta(t, \boldsymbol{\alpha}) = \pi h \sum_{i=0}^{N-1} \alpha_i q(t - iT), \quad q(t) = \begin{cases} \int_0^t g(\tau) d\tau \\ \frac{1}{2}, t \geq L \end{cases}$$

f_0 is the carrier frequency, θ_0 the initial phase shift, $\theta(t, \boldsymbol{\alpha})$ the information carrying phase, $g(t)$ the frequency pulse, $h = k/p$ the modulation index, L the memory and $\Re(.)$ the real part. Practically, the shape of $q(t)$ (rectangular (REC), raised cosine (RC), Gaussian, ...) and L determine the smoothness of the signal transitions. Concerning the interleavers, we consider here partial interleavers rather than a global interleaver: it implies a random interleaving of the LDPC codewords bits using a different interleaving patterns among variable nodes of the same degree. This is in contrast with approaches

that mainly consider full interleaving between the LDPC code and the CPM as classically done for serially concatenated schemes. The rationale behind this choice will be made clearer when presenting the asymptotic analysis.

At the receiver side, the decoder is formed by the soft input soft output (SISO) CPM detector followed by a SISO LDPC decoder separated by the partial interleavers. Without lack of generality, the SISO CPM is based on the Rimoldi's decomposition [Rim88] which splits the CPM modulator into a serial concatenation of the continuous phase encoder (CPE), represented by a trellis, and the memoryless modulator (MM), seen as a filter bank, as depicted in Fig. 2.2. Using the Rimoldi's decomposition, the CPM signal can then be described as:

$$s_b(t, \boldsymbol{\alpha}) = \sqrt{\frac{2E_s}{T}} \cos\left(\psi(t, \boldsymbol{\alpha}) + \psi_0\right) \tag{2.5}$$

where the information symbols $\boldsymbol{\alpha}$ are taken in $\{\pm 1, \ldots, \pm(M-1)\}$ whatever the parity of M is and figure in the Rimoldi's tilted phase as:

$$\psi(\tau + nT, \boldsymbol{\alpha}) = \left[2\pi h \sum_{i=0}^{n-L} U_i + 4\pi h \sum_{i=0}^{L-1} U_{n-i} q(\tau + iT) + W(\tau)\right] \text{ modulo } 2\pi, \quad 0 \leq \tau < T$$

where $U_i = (\alpha_i + (M-1))/2$ and $W(\tau)$ is a data independent term (see [Rim88] and chapter 1).

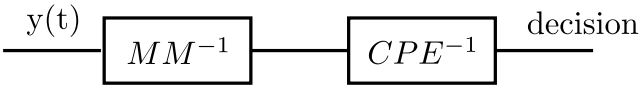

Figure 2.3: Rimoldi's decomposition-based receivers

This decomposition provides a trellis of pM^{L-1} state defined by the tuple $\sigma_n = [U_{n-1}, \ldots, U_{n-L+1}, V_n]$ where U_i is an M-ary modified data digit and $V_n = \sum_{i=0}^{n-L} U_i$ [Rim88].

The transmitted signal $s(t, \boldsymbol{\alpha})$ is corrupted with an additive white Gaussian noise (AWGN), having a double-sided power spectral density $N_0/2$. From Eq. (2.5), the complex baseband representation of the noisy signal becomes:

$$y(t) = \sqrt{\frac{2E_s}{T}} \exp\{j\psi(t, \boldsymbol{\alpha}\} + n(t), \quad t > 0 \tag{2.6}$$

The bloc diagram of the receiver is depicted in Fig. 2.4. The outputs of the receiver matched filters bank $\{s_i^*(t-T)\}_i$ are sampled at the symbol period T to obtain the correlator metric [PS07]:

$$\boldsymbol{y}^n = \left[y_i^n = \int_{nT}^{(n+1)T} y(l) s_i^*(l) dl \right]_{1 \leq i \leq pM^L}$$

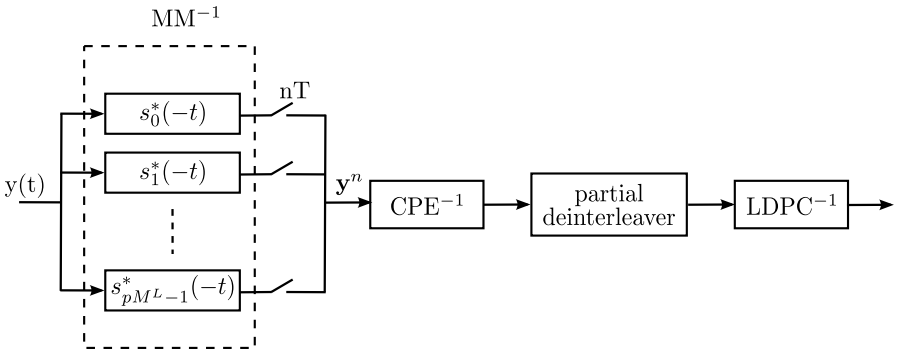

Figure 2.4: Bloc diagram of the receiver

It can be shown that $\{\boldsymbol{y}^n\}_n$ is a sufficient statistics to estimate the symbols [MA01]. Furthermore, considering any orthonormal expansion of the receiver matched filters, the joint probability $p(\boldsymbol{y}^n/X_n)$ can be simplified to [MA01]:

$$p(\boldsymbol{y}^n/X_n) \propto \exp\left(\frac{2}{N_0}\Re(y_i^n)\right)$$

where X_n is the output of the CPE at nT (see chapter 1 for more details). This measure can be used to compute the branch metrics of the CPE trellis, exploiting the BCJR algorithm [BCJR74]. The outer LDPC decoder is implemented with an instance of the belief propagation (BP) algorithm [RU01].

In this chapter, we assume the following scheduling: a global iteration ℓ is composed of one BCJR forward-backward recursion for the CPM detector followed by one BP iteration (one data-pass + one check-pass update) for the LDPC code. Recall that we assume partial interleavers: each one is associated with the VNs of the same degrees. It is implicitly assumed that BCJR recursions are run independently between different trellis section groups delimited by each partial interleaver. This is not the case in practice but this assumption allows us to neglect transition effects when running the decoding. The factor graph corresponding to our receiver is depicted in Fig. 2.5.

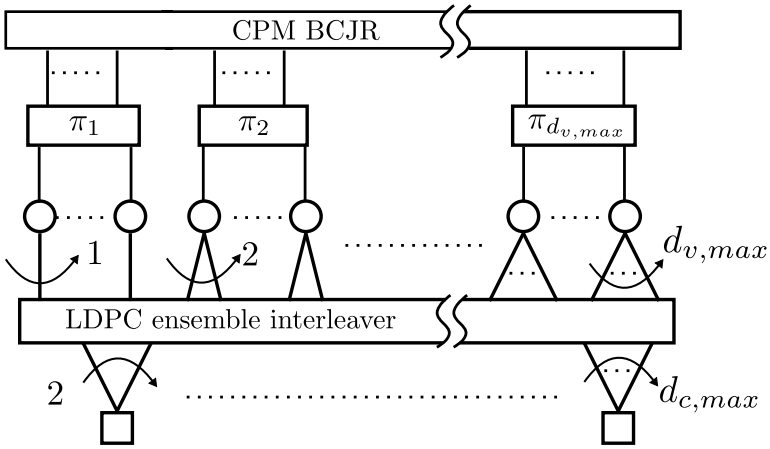

Figure 2.5: LDPC code ensemble for joint detection and decoding

2.4 Asymptotic Analysis of unstructured LDPC codes

One of the most relevant parameters for serially concatenated schemes optimization is the convergence threshold, *i.e.* the lowest channel parameter (here the signal to noise ratio (SNR)) at which the decoding is possible given long codeword size and a large number of iterations [tB01c]. For large block size, one can use density evolution techniques to estimate the threshold of an iterative system by simulation [RU01] [DDP01]. It consists of tracking the probability density function (PDF) of the exchanged log likelihood ratio (LLR) messages through iterations. For general channels and concatenated schemes, this technique can be computationally challenging. In particular, for symmetric channels, we have to resort to a coset based approach [HSMP03, KMM03]. Therefore, we mainly consider an extrinsic information transfer (EXIT) chart analysis. This tool uses the mutual information (MI) between the transmitted bits and the extrinsic LLRs to estimate the convergence threshold, which implicitly resort to a coset approach.

First introduced in [tB01c, tB01d], EXIT chart is a common asymptotic tool that is used to analyse the convergence of iterative systems. It aims to compute the input-output transfer function of a general SISO block (for instance, the SISO block of the CPM is given in Fig. 2.6). At the input, a general SISO block can have LLRs from the channel observations and some *a priori* LLRs. For a given signal to noise ratio (SNR), extrinsic information is computed at the output. Based on these

inputs and outputs, the EXIT transfer function, denoted here by f, computes the mutual information I_e between the sent bits and the extrinsic LLRs *versus* the mutual information I_e between the *a priori* LLRs and the corresponding bits such that: $I_a = f(I_e)$. This mutual information quantities can be directly related to the LLRs distributions. For very large data blocks, these LLRs can be assumed independent and identically distributed random variables [RSU01]. The mutual information between a binary random variable $X \in \{\pm 1\}$ and the corresponding LLRs is given by:

$$I(X, \text{LLR}) = \frac{1}{2} \sum_{x \in \pm 1} \int p(\text{llr}|x) \log_2 \left(\frac{2p(\text{llr}|x)}{p(\text{llr}|x=1) + p(\text{llr}|x=-1)} \right) d\text{llr} \tag{2.7}$$

When using EXIT charts and in order to mitigate the computations, it is also commonly assumed that the random variable corresponding to the exchanged extrinsic LLRs is [Hag04]:

- symmetric, *i.e.* $p(\text{LLR}|X=1) = p(-\text{LLR}|X=-1)$
- consistent, *i.e.* $p(-\text{LLR}|X=1) = \exp(\text{LLR}) p(\text{LLR}|x=1)$

However, this assumption is not always true for general SISO blocks, consequently we have to resort to Eq. (2.7). In this case, the computation of $p(\text{llr}|x)$ is not straightforward and is usually estimated by means of histograms. For the noisy binary input Gaussian channel, *i.e.* when the $X \in \{\pm 1\}$ is corrupted with a Gaussian noise, this leads to a Gaussian distributed LLRs [Hag04], we can evaluate the MI of the LLR messages by only tracking their variance σ^2_{LLR} or their mean $m_{LLR} = \sigma^2_{LLR}/2$. When all these assumptions are gathered, Eq. (2.7) simplifies to:

$$\begin{aligned} I(X, \text{LLR}) &= 1 - \int_{-\infty}^{+\infty} p(\text{llr}|x=1) \log(1 + e^{-\text{llr}}) d\text{llr} \\ &= 1 - \frac{1}{\sqrt{2\pi\sigma^2_{LLR}}} \int_{-\infty}^{+\infty} \exp\left(-\frac{(\text{llr} - \sigma^2_{LLR}/2)^2}{2\sigma^2_{LLR}} \right) \log(1 + e^{-\text{llr}}) d\text{llr} \\ &= 1 - E_{\text{LLR}}(\log_2(1 + e^{-\text{LLR}})), \quad \text{LLR} \sim \mathcal{N}(\frac{\sigma^2_{LLR}}{2}, \sigma^2_{LLR}) \end{aligned} \tag{2.8}$$

A closed form of the mono-dimensional function $I(X, \text{LLR})$ is not easy. Alternatively, [tB01d] gives a polynomial approximation of $I(X, \text{LLR})$ and of its inverse, denoted by $J(\sigma_{LLR})$ and $J^{-1}(\sigma_{LLR})$

respectively:

$$J(\sigma) = \begin{cases} -0.0421061.\sigma^3 + 0.209252.\sigma^2 - 0.00640081.\sigma, & 0 \leq \sigma < 1.6363 \\ 1 - \exp\left(0.00181491.\sigma^3 - 0.142675.\sigma^2 - 0.0822054.\sigma + 0.0549608\right), & \sigma \geq 1.6363 \end{cases}$$

$$J^{-1}(I) = \begin{cases} 1.09542.I^2 + 0.214217.I + 2.33727.\sqrt{I}, & 0 \leq I < 0.3646 \\ -0.706692 \log\left[0.386013(1-I)\right] + 1.75017.I, & I \geq 0.3646 \end{cases}$$

When computing the EXIT charts for ga eneral SISO block,I_e is measured at the output of the block based on Eq. (2.7). To be independent of the other block in a given iterative scheme, the *a priori* information is usually considered as Gaussian following a Gaussian consistent distribution as given in Eq. (2.8) ans such that $\sigma_{LLR}^2 = J^{i1}(I_a)$. For LDPC codes, we will see that the EXIT approach gives an approximation analytic description of the information transfer at both the check nodes and the variable node.

2.4.1 EXIT curve of the detector

Consider the SISO CPM block in Fig. 2.6, where $y(t)$ is the channel observation, LLR_a the *a priori* LLR vector of the bits and LLR_e the extrinsic LLR vector. The extrinsic LLRs are computed using the BCJR algorithm relative to the Rimoldi's decomposition detailed in chapter 1. In the considered LDPC-coded CPM, LLR_a is computed using the Gaussian approximation and corresponds actually to the LLRs values of the coded bits and I_a is measured using Eq. (2.7).

Figure 2.6: SISO CPM

Let $T(.)$ denotes the input-output EXIT transfer characteristic (also referred to as the EXIT curve) of the SISO CPM demodulator implicitly depending on the signal to noise ratio E_s/N_0:

$$I_{cpm,vn}^{\ell} = T(I_{vn,cpm}^{\ell-1}) \tag{2.9}$$

When inserting the this SISO block in an iterative system, we assume that the messages are Gaussian distributed. As discussed, the Gaussian approximation is commonly assumed over the literature: for the CPM, This assumption remains accurate as depicted by the histograms in Fig. 2.7.

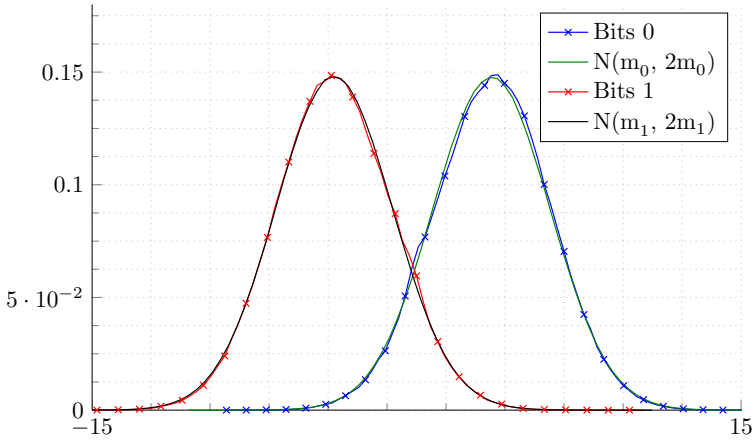

Figure 2.7: Probability density function of the LLRs at the output of the GSM GMSK decoder in comparison to a symmetric Gaussian distribution when the *a priori* mutual information is 0.5. m_0 (and m_1) is the expected value of the LLRs associated with the bits 0 (respectively the bits 1)

The analytic expressions of $T(.)$ are not available, but they can be estimated by Monte Carlo simulations. In practice, $T(.)$ is approximated by a polynomial curve fitting. Figure 2.8 presents the results at different SNRs for various CPMs. For a better representation, the SNR here is characterized by E_d/N_0 where $E_d = E_s - 10\log(\log_2(M))$.

2.4.2 The area theorem and the curve fitting approach

In [AKtB04], authors show that the area under the EXIT curve of an iterative component is related to its rate over the binary erasure channel. It is usually assumed that it is also a good approximation of other channels and that it can be extended to soft detectors [Hag04, LSL06, SB13, BTP+13]. Based on the commonly observed generalization of the area theorem, we can extend this property to serial concatenation with CPM to characterize a lower bound of the maximum achievable rates for the inner code given an E_s/N_0. In our framework, this lower bound is given by the area under the

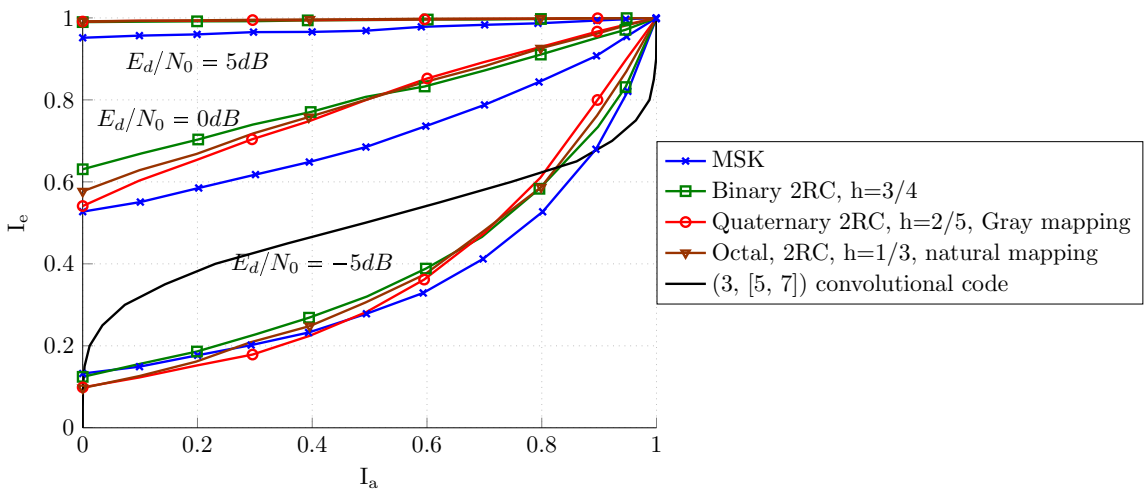

Figure 2.8: EXIT curves for various CPM systems. For reference the rate-1/2 $[5, 7]$ convolutional code is also illustrated. The considered SNRs are $E_d/N_0 = -5, 0$ and 5dB

EXIT curve of the CPM:

$$R \leq R^* = \int_0^1 T(\mu) d\mu \tag{2.10}$$

Graphically (see Fig. 2.8), as long as the EXIT curve of the inner code (which is independent of the channel parameter) is below the CPM EXIT curve, the decoder performance is improved with iterations. Since we are conducting an asymptotic analysis, we say that the decoding was successful if the error probability vanishes with a large enough number of iterations. Consequently, finding the decoding threshold can be graphically interpreted as finding the lowest SNR such that the former EXIT curve lies below the latter everywhere in $[0, 1]$.

Our goal in this case will be to design LDPC codes whose rates R_{opt} are as close as possible to R^* and that have thresholds $(E_s/N_0)_{opt}$ as close as possible to $(E_s/N_0)^*$. By varying the SNR and computing the corresponding maximal achievable rate in Eq. (2.10), we can define the curve in Fig. 2.9. The blue area corresponds to the achievable code rates region. The blue line can be seen as a lower bound of the Shannon limit for CPMs, since computing capacities and rates with the Gaussian approximation gives generally optimistic results. For a particular rate, the goal of our optimization will be to find an LDPC code whose threshold is as close as possible to the blue curve for a targeted

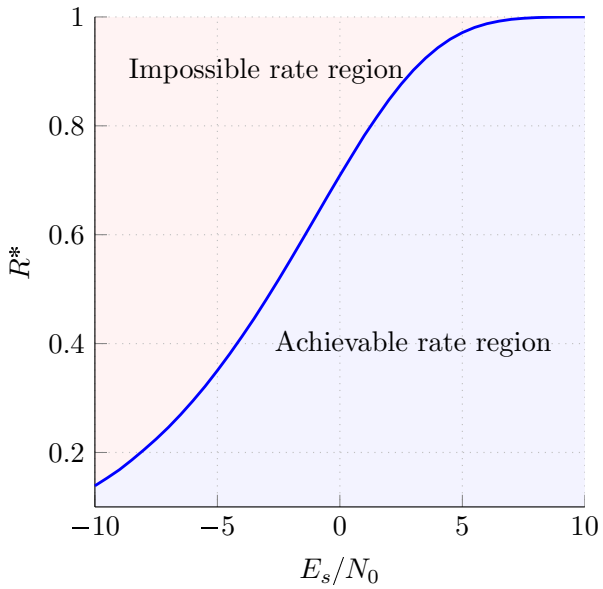

Figure 2.9: Maximum achievable rates for the GMSK: $(M = 2, L = 3, h = 1/2, BT = 0.3, \text{Gaussian})$ as a function of the SNR (E_s/N_0)

design rate R^*.

Example

Consider the CPM scheme defined by $(M = 2, L = 3, h = 1/2, BT = 0.3, \text{Gaussian})$. Figure 2.10 depicts the corresponding EXIT chart at $E_s/N_0 = -2.75$dB. For this CPM scheme, we can conjecture from this graph that there exist an outer code of maximum rate $R^* = 1/2$ that allow successful decoding at $(E_s/N_0)^* = -2.75$dB. Figure 2.11 summarizes the maximum achievable rates as a function of E_s/N_0 for some CPM schemes.

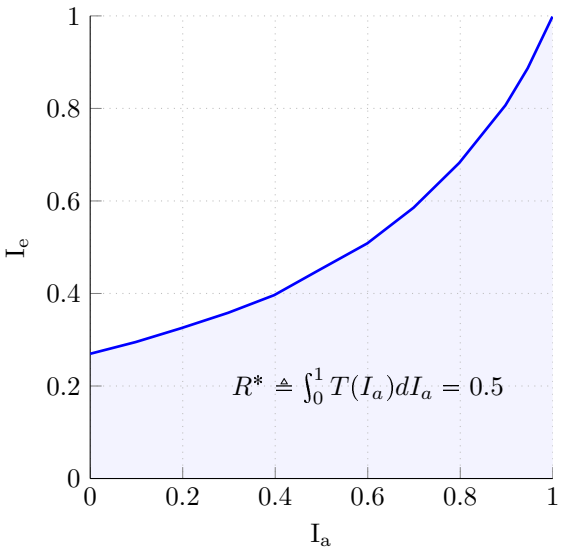

Figure 2.10: EXIT chart of the GMSK: $(M = 2, L = 3, h = 1/2, BT = 0.3, \text{Gaussian})$ at $E_s/N_0 = -2.75$dB

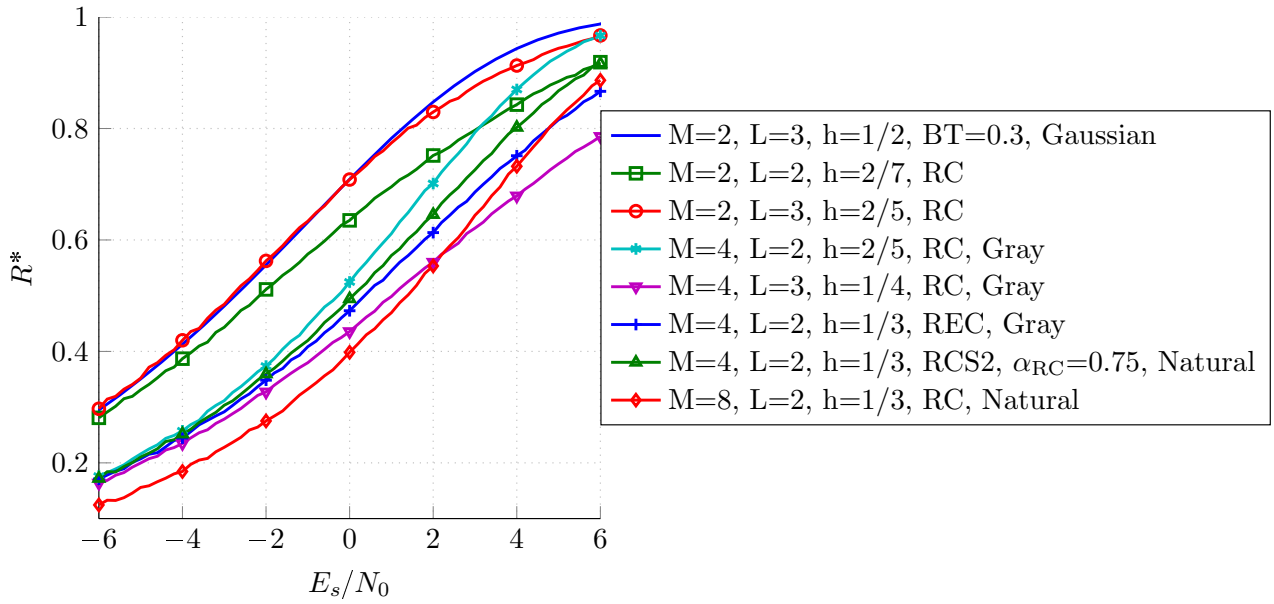

Figure 2.11: Maximum achievable rates different CPM schemes. The RCS2 CPM scheme is defined in [BCDB+13].

2.4.3 A combined EXIT approach for CPM and LDPC code

2.4.3.1 Model

If we consider a global interleaver between the CPM and the LDPC code, the LDPC component EXIT function is clearly a two dimensional function: the LLRs sent from the VNs to the CPMs iteration depends on the received LLR message from the CN and on received LLR message from the SISO CPM. Under these conditions, the convergence analysis of the system requires the study of multidimensional EXIT functions which is not simple. Moreover, this analysis provides equations which are not linear in $\{\lambda_i\}_i$. For these reasons, we consider instead partial interleavers and the integration of the detector in the variable node. This approach can be seen as a generalization of [tB01c]. Fig. 2.12 depicts the Tanner graph corresponding to receiver and introduces the main notations of the MI that are going to be used in this section.

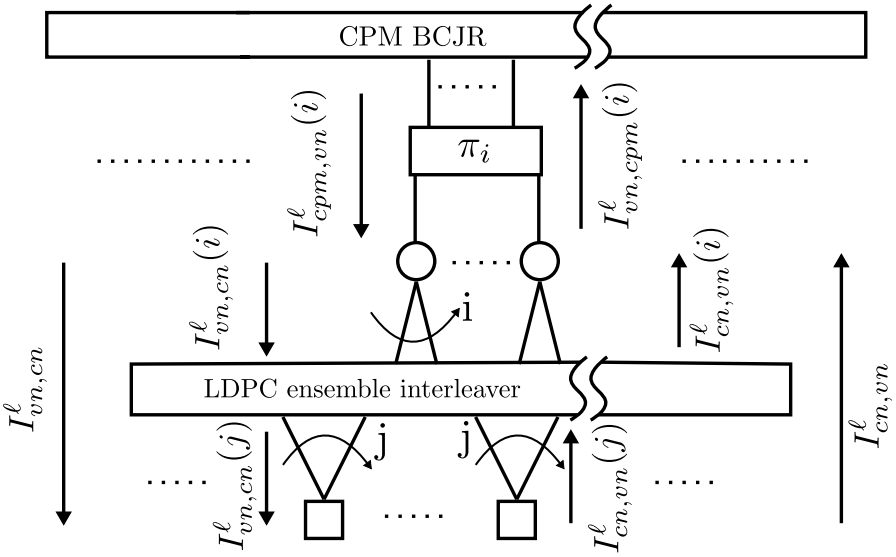

Figure 2.12: LDPC code ensemble for joint detection and decoding with partial interleavers

2.4.3.2 Combined EXIT curve of the variable nodes and the detector

A variable node of degree i has i incoming messages, $\{LLR^i_{vn,in}(j)\}_{j\in\{1,2\ldots,i\}}$, from the check nodes and one message from the CPM detector as depicted in Fig. 2.13.

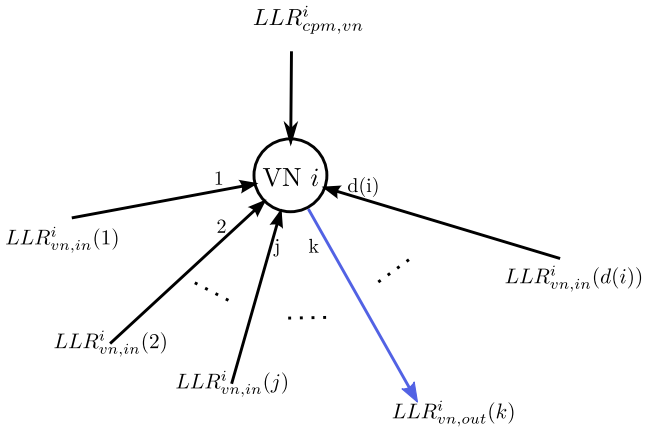

Figure 2.13: Variable node update

The extrinsic message $LLR^i_{vn,out}(k)$ computed at this variable node under the sum product algorithm [MN96] on the k^{th} edge ($\forall k \in \{1, 2\ldots, i\}$), is given by:

$$LLR^i_{vn,out}(k) = LLR^i_{cpm,vn} + \sum_{\substack{j=1 \\ j\neq k}}^{i} LLR^i_{vn,in}(j)$$

where $LLR^i_{cpm,vn}$ is the extrinsic LLR value at the output of the detector relative to the bit corresponding to a degree-i variable node.

Under the Gaussian approximation, the average combined EXIT function $I^{\ell}_{vn,cn}$ of the VN and the SISO CPM module for a variable node of degree i at the ℓ^{th} iteration is then given by [CFJRU01]:

$$I^{\ell}_{vn,cn} = \sum_{i=1}^{d_{v,max}} \lambda_i I^{\ell}_{vn,cn}(i) \tag{2.11}$$

with:

$$I^{\ell}_{vn,cn}(i) = J\left(\sqrt{(i-1)\left[J^{-1}\left(I^{\ell-1}_{cn,vn}\right)\right]^2 + \left[J^{-1}\left(I^{\ell}_{cpm,vn}(i)\right)\right]^2}\right) \tag{2.12}$$

$$I^{\ell}_{cpm,vn}(i) = T\left(I^{\ell-1}_{vn,cpm}(i)\right) \tag{2.13}$$

$$I^{\ell}_{vn,cpm}(i) = J\left(\sqrt{i}J^{-1}\left(I^{\ell-1}_{cn,vn}\right)\right) \tag{2.14}$$

where:

- $I^{\ell}_{vn,cn}(i)$ is the average MI associated with LLR messages passed from a VN of degree i to CNs
- $I^{\ell-1}_{cn,vn}$ is the average MI associated with LLR messages passed from CNs to VNs
- $I^{\ell}_{cpm,vn}(i)$ is the MI for degree-i VN associated with LLR messages passed from the CPM decoder to the LDPC decoder. Recall that without the partial interleavers, we are not allowed to write Eq. (2.13)

Figure 2.14 plots different VN trajectories as a function of the degree. The dashed line corresponds to an arbitrary VN profile chosen here for illustration purposes only. Notice that the VNs EXITs do not start from the origin $(0, 0)$. High degree VNs clearly converge more quickly in comparison to lower degree VNs. However, as stated in [RU08], since the introduction of degree-2 edges improves the performance, it is natural to conjecture that introducing lower degree edges can bring further benefits. For structured protograph based LDPC codes [Tho03], it was shown that codes with some degree-1 VNs (also called precoding VNs) can have excellent thresholds and very low error floors [LC07, DDJA09]. In unstructured LDPC codes, and in the classical setting where the detector EXIT curve do not converge to $(1, 1)$ [tBKA04], it is not possible to introduce degree-1 variable nodes because they will not converge.

The degree-1 VN EXIT corresponds actually to the EXIT transfer function of the SISO CPM decoder because we have no *a priori* information from adjacent CNs: replace i by 1 in Eq. (2.12) and get $I^{\ell}_{vn,cn}(1) = T\left(I^{\ell-1}_{cn,vn}\right)$. Because the CPM EXITs join the point $(1, 1)$ (see Fig. 2.8), the MI $I^{\ell}_{vn,cn}(i)$ (and thus the mixture $I^{\ell}_{vn,cn}$) will also converge to $(1, 1)$ even if we allow some degree-1 VNs (unlike in [tBKA04]).

Taking into account the partial interleavers, the VNs to the SISO CPM update for a degree-i VN can be written as:

$$I^{\ell}_{vn,cpm}(i) = J\left(\sqrt{i}J^{-1}\left(I^{\ell-1}_{cn,vn}\right)\right) \tag{2.15}$$

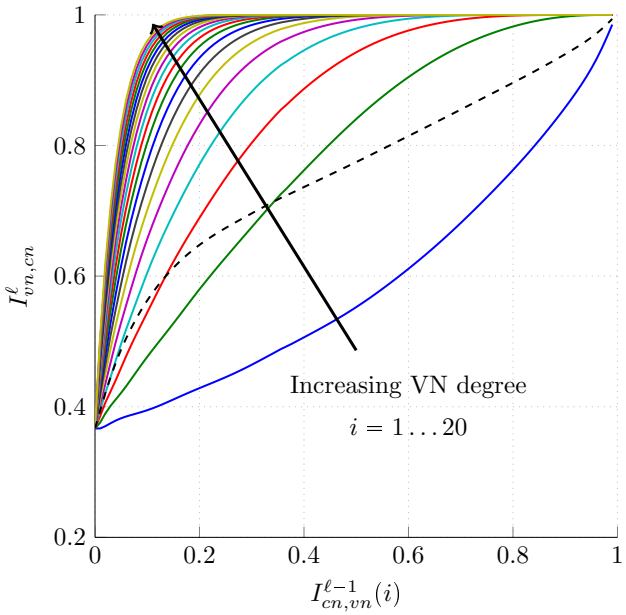

Figure 2.14: Combined VN+CPM trajectories as a function of the degree. The detector is ($M = 2, L = 3, BT = 0.3, h = 1/2$) and the SNR is $Es/N_0 = -1.5$. For the dashed line, the considered profile is ($\lambda_1 = 0.42, \lambda_2 = 0.23105, \lambda_3 = 0.00938, \lambda_4 = 0.00104, \lambda_{10} = 0.33853$)

Note: If we were not using the partial interleavers but a total interleaver, we will not be allowed to write Eq. (2.15), but instead an averaging has to be made with respect to the node-perspective variable nodes proportions:

$$I^{\ell}_{vn,cpm} = \sum_{i=1}^{d_{v,max}} \tilde{\lambda}_i J\left(\sqrt{i} J^{-1}\left(I^{\ell}_{cn,vn}\right)\right) \tag{2.16}$$

where $\tilde{\lambda}_i$ is the proportion of variable nodes of degree i,. This quantity is related to λ_i by the non linear relation:

$$\tilde{\lambda}_i = \frac{\lambda_i / i}{\sum_k \lambda_k / k}$$

Furthermore, we would not have been allowed neither to write Eq. (2.13) because the CPM SISO module will not have access to $I^{\ell-1}_{vn,cpm}(i)$ but instead to an averaged MI corresponding to the LLR messages sent from the VNs to the CPM SISO module. In this case, Eq. (2.13) becomes:

$$I^{\ell}_{cpm,vn} = T(I^{\ell-1}_{vn,cpm}) \tag{2.17}$$

It is clear that combining Eqs. (2.17) and (2.16) will lead to a nonlinear equation in $\{\lambda_i\}_i$.

2.4.3.3 EXIT chart of check nodes

A check node of degree j has j incoming messages $\{LLR^j_{cn,in}(i)\}_{i\in\{1,2,\ldots,j\}}$ from the variables nodes as depicted in Fig. 2.15.

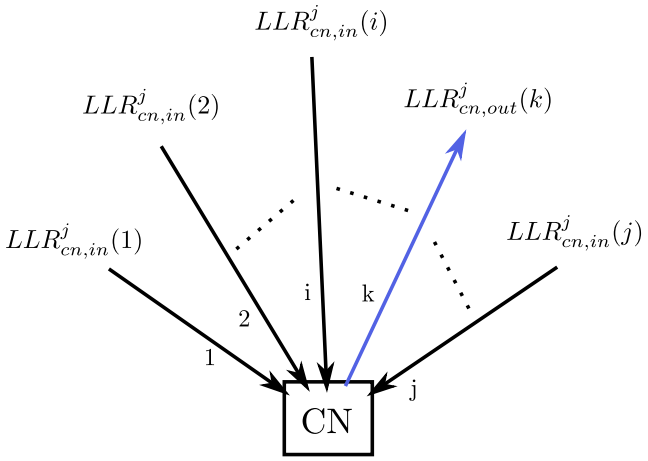

Figure 2.15: Check node update

The extrinsic message $LLR^j_{cn,out}(k)$ computed at this check node on the k^{th} edge ($\forall k \in \{1,2,\ldots,j\}$ is given by the following product [Gal62]:

$$\tanh\left(\frac{LLR^j_{cn,out}(k)}{2}\right) = \prod_{\substack{i=1\\ i\neq k}}^{j} \tanh\left(\frac{LLR^j_{cn,in}(i)}{2}\right)$$

where tanh(.) is the hyperbolic tangent function.

For the binary erasure channel, a closed form of the EXIT curve can be derived for CNs [AKtB04]. However, for other channels, one can use the duality property approximation or the reciprocal channel approximation [Chu00, AKtB04] (which is exact in the case of the binary erasure channel). It states that the EXIT function I_{cn} of a CN given an *a priori* knowledge I_a and the EXIT curve of an arbitrary VN of the same degree are related as:

$$I_{cn}(I_a) = 1 - I_{vn}(1 - I_a)$$

Consequently, for a CN with degree j, the MI $I_{cn,vn}^{\ell-1}$ associated with the extrinsic LLR messages passed from the CNs to VNs and the relative coded bits at the iteration $\ell-1$ is given, under the reciprocal channel approximation, as:

$$I_{cn,vn}^{\ell-1} = \sum_{j=2}^{d_{c,max}} \rho_j I_{cn,vn}^{\ell-1}(j) \tag{2.18}$$

$$I_{cn,vn}^{\ell-1}(j) = 1 - J\left(\sqrt{j-1}J^{-1}(1-I_{vn,cn}^{\ell-1})\right) \tag{2.19}$$

Figure 2.16 plots the 'inverted' EXIT curve of a CN as a function of its *a priori* MI. Observe that the EXIT curve of a degree-2 CN is nothing but the first bisector of the plan: replace j by 2 in Eq. (2.19) and get $I_{cn,vn}^{\ell-1}(j) = I_{vn,cn}^{\ell-1}$.

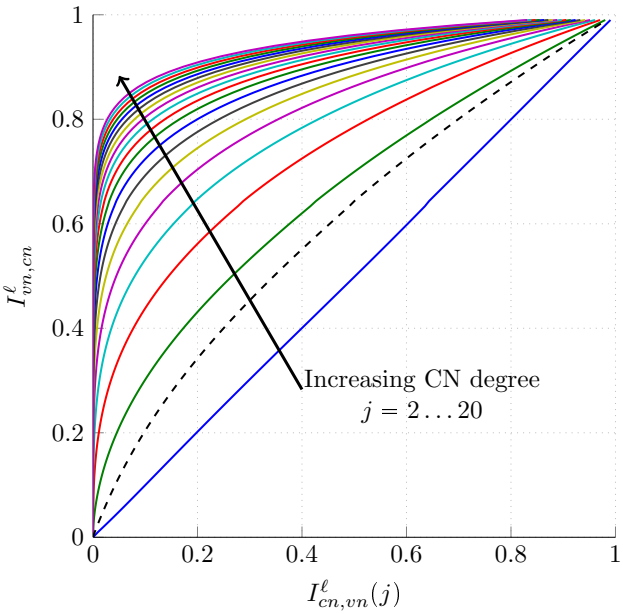

Figure 2.16: CN EXIT trajectories. The dashed line corresponds to the profile ($\rho_2 = 0.34, \rho_3 = 0.66$

2.4.4 Combined EXIT recursion and formulation of the optimization problem

Combining Eqs. (2.11) and (2.18) will finally give the recursion Ψ:

$$I_{vn,cn}^{\ell} = \Psi\left(\lambda(.), \rho(.), T(.), I_{vn,cn}^{\ell-1}\right) \tag{2.20}$$

Thanks to the partial interleavers and the considered scheduling, the obtained recursion is a linear function with respect to the parameters $\{\lambda_i\}_i$; for a given $\rho(x)$ and a given signal to noise ratio. With concentrated check node profiles [CFJRU01], *i.e.* of the form: $\rho(x) = (1-\rho)x^{j-1} + \rho x^j$, the rate maximization design is equivalent to the maximizing linear problem:

$$\arg\max_{\lambda(x)} \sum_i \frac{\lambda_i}{i} \tag{2.21}$$

subject to:

$$\text{[C0] Mixture} : \sum_i \lambda_i = 1 \tag{2.22}$$

$$\text{[C1] Convergence} : \Psi\left(\lambda(x), \rho(x), T(.), y\right) > y \tag{2.23}$$

This system is efficiently solved by classical linear programming using discretization of the convergence constraint for $y \in [0, 1]$. This problem statement will be latter completed by adding a constraint on the degree-1 VN proportion. To summarize, our code design strategy can be outlined in Algorithm 2.1.

Algorithm 2.1 Code design strategy

```
Fix an SNR value Es/N0
Fix the maximum and the minimum VNs and CNs degree
Initialize the designed code rate R_opt = 0
Compute the CPM EXIT curve T(.) at Es/N0
Generate a set C of concentrated CN degree profiles [CFJRU01]
for each ρ(x) in C do
    Solve the linear problem in Eq. (2.21) and obtain λ(x)
    Compute the new designed code rate R
    if R > R_opt then
        R_opt = R
        λ_opt(x) = λ(x) and ρ_opt(x) = ρ(x)
    end if
end for
```

2.4.4.1 Example

Let us suppose that we want to design a code for the $(M = 2, L = 3, h = 2/3,$ Raised cosine pulse) CPM at $E_s/N_0 = -3.375$dB. In this example, we take $d_{v,min} = 2$. Solving Eq. (2.21) gives:

$$(\lambda_2 = 0.654, \lambda_{20} = 0.346) \quad \text{and} \quad (\rho_4 = 0.4, \rho_5 = 0.6) \tag{2.24}$$

Fig. 2.17 depicts the CNs and the combined VNs+CPM EXIT curves of the optimized code. Note that all the area between the two EXIT curves (the shadowed area) translates into a rate loss.

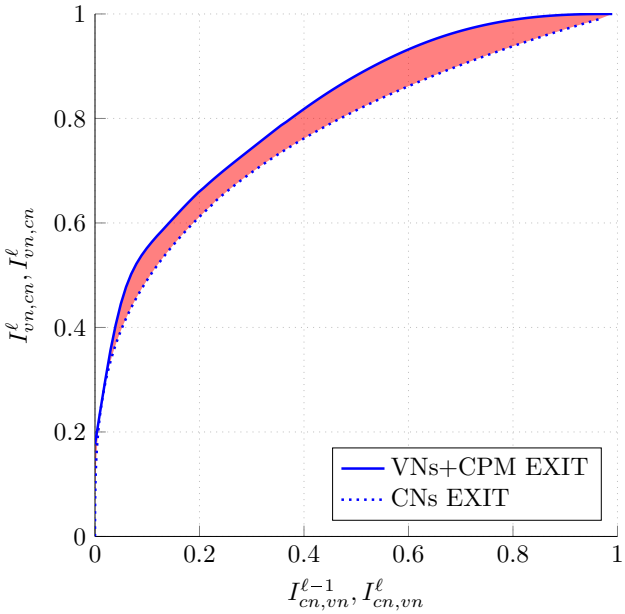

Figure 2.17: The CNs and the combined VNs+CPM EXIT curves of the optimized code in Eq. (2.24)

This area can be minimized by introduce some degree-1 VNs. This is suggested by the fact that the degree-1 VN EXIT curve is very low (see Fig. 2.15). Figure 2.18 plots the CNs and the combined VN+CPM EXIT curves of the following optimized code:

$$(\lambda_1 = 0.191, \lambda_2 = 0.493, \lambda_6 = 0.0154, \lambda_7 = 0.0676, \lambda_{20} = 0.233) \quad \text{and} \quad (\rho_4 = 0.7, \rho_5 = 0.3) \tag{2.25}$$

It is clear that, thanks to the introduction of the degree-1 variable nodes, we have much less rate loss.

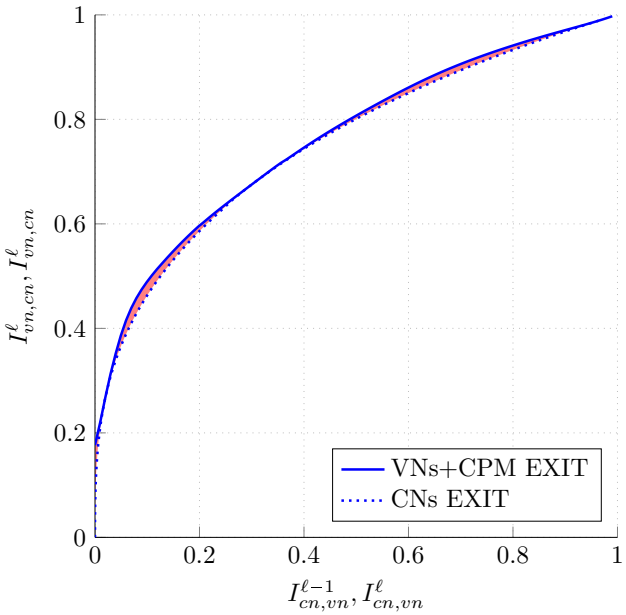

Figure 2.18: The CNs and the combined VNs+CPM EXIT curves of the optimized code in Eq. (2.25)

2.4.5 Stability condition

Authors in [RSU01] states that the density evolution iterations converge to a fixed point. In [RU01, Theorem 5], they corroborate the importance of the study of the stability of this convergence in the analysis of the density evolution algorithm behavior around this fixed point. More specifically, the analysis of the stability condition allows to define a necessary condition on the code parameters in order to insure the convergence to a zero error probability. Let us denote:

$$S = \int f_0(x) e^{-x^2/2} dx \qquad \lambda'(x) = \sum_{i=2}^{d_{v,max}} (i-1)\lambda_i x^{i-2} \qquad \rho'(x) = \sum_{j=2}^{d_{c,max}} (j-1)\rho_j x^{j-2}$$

where $f_0(x)$ is the density of the initial LLR messages, and $\lambda'(x)$ (respectively $\rho'(x)$) is the first derivative of the polynomial profile $\lambda(x)$ (respectively $\rho(x)$). Authors show that if the LDPC code profile verifies:

$$\lambda'(0)\rho'(1) < \frac{1}{S}$$

then, the error probability will vanish to zero, otherwise, it can be lower bounded by a value greater than zero. For the binary input AWGN channel, the equation above simplifies to [RSU01, Example 12]:

$$\lambda'(0)\rho'(1) < e^{\frac{1}{2\sigma^2}}$$

where σ^2 is the variance of the channel noise. In this channel, σ^2 si related to the channel output LLRs variance σ^2_{LLR} by:

$$\sigma^2_{LLR} = \frac{4}{\sigma^2}$$

The stability condition then becomes:

$$\lambda'(0)\rho'(1) < e^{\frac{\sigma^2_{LLR}}{8}}$$

Since this stability condition involves $\lambda'(0) = \lambda_2$, it gives an upper bound on the proportion λ_2. Degree-1 variable nodes were not considered in the study, because they were prohibited in the study of unstructured LDPC codes over binary memoryless channels.

In the context of EXIT chart analysis and under the Gaussian approximation, it is also possible to derive this stability condition. As for the density evolution, this constraint controls the behavior of the evolution of the mutual information when the error probability is near to zero (or equivalently, when the average VN mutual information $I^{\ell}_{vn,cn}$ is near to one).

It the case of the AWGN channel with variance σ^2, where the EXIT curve of the detector does not reach the point $(1,1)$ (*i.e.* $T(1) < 1$) and where degree-1 VNs are not considered, the stability condition for the EXIT chart analysis is conjectured in the literature [LSL06, SB13] as:

$$\lambda'(0)\rho'(1) < \exp\left(\frac{J^{-1}\left(T(1)\right)^2}{8}\right)$$

In the following, we provide a proof of the following generalized stability condition for any detector and for $d_{v,min} \geq 1$:

Theorem 1. *Under EXIT evolution, the stability condition can be written as:*

$$\lambda_1 T'_\sigma(1) + \lambda_2 \delta(T(1)) < \frac{1}{\sum_j \rho_j (j-1)} \tag{2.26}$$

where:

$$\delta(x) = \begin{cases} 0, \textit{ if } x = 1 \\ \exp\left(-\frac{\left[J^{-1}(x)\right]^2}{8}\right), \textit{otherwise} \end{cases}$$

Sketch of proof(The detailed proof is provided in Annex B)

For ease of notations, $\Psi\left(\lambda(.), \rho(.), T(.), x\right)$ in Eq. (2.20) is simply denoted by $\Psi\left(x\right)$, and the standard deviation-based function $J(.)$ is replaced by the mean-based function $\tilde{J}(.)$ defined as:

$$\tilde{J}(x) = J(\sqrt{2x})$$

By abuse of notation in this section only, $\tilde{J}(.)$ is simply denoted $J(.)$.

Recall that the EXIT chart recursion is given by Eq. (2.20) as:

$$x^\ell = \Psi\left(x^{\ell-1}\right) = \sum_{i=1}^{d_{v,max}} \lambda_i J\left[(i-1)\, J^{-1} \circ f\left(x^{\ell-1}\right) + J^{-1} \circ T_\sigma \circ J\left(iJ^{-1} \circ f\left(x^{\ell-1}\right)\right)\right]$$

where $\circ$ denotes the standard composition operator of two functions.

Deriving Ψ gives:

$$\begin{aligned} \frac{d\Psi}{dx}(x) = {} & \lambda_1 T'(J(\mu(x))) \sum_j \rho_j (j-1) \frac{J'\left((j-1)J^{-1}(1-x)\right)}{J'(J^{-1}(1-x))} \\ & + \sum_{i\geq 2} (i-1)\lambda_i \frac{J'\left[(i-1)\,\mu(x) + \eta(i\mu(x))\right]}{J'\left(\mu(x)\right)} \times \sum_j \rho_j (j-1) \frac{J'\left((j-1)J^{-1}(1-x)\right)}{J'(J^{-1}(1-x))} \\ & + \sum_{i\geq 2} i\lambda_i T'(J(i\mu(x))) \times \frac{J'(i\mu(x))}{J'(\eta(i\mu(x)))} \times \frac{J'\left[(i-1)\,\mu(x) + \eta(i\mu(x))\right]}{J'\left(\mu(x)\right)} \\ & \times \sum_j \rho_j (j-1) \frac{J'\left((j-1)J^{-1}(1-x)\right)}{J'(J^{-1}(1-x))} \end{aligned}$$

where:

$$\mu = J^{-1} \circ f \qquad \text{and} \qquad \eta = J^{-1} \circ T \circ J$$

The Taylor expansion of $J(.)$ can be obtained from the asymptotic expansion given in [RU08] as:

- For small x:

$$J(x) = \frac{x}{4} - \frac{x^2}{16} + \frac{x^3}{48} + O(x^4)$$

- For large x:

$$J(x) = 1 - \frac{\sqrt{\pi}}{\ln(2)} e^{-\frac{x}{4}} \left(x^{\frac{-1}{2}} - \frac{8+\pi^2}{4} x^{\frac{-3}{2}} + O(x^{\frac{-5}{2}}) \right)$$

By deriving this Taylor expansion, using the Sandwich theorem [Wei05] and considering the following results:

$$J(0) = 0 \quad , \quad J^{-1}(0) = 0$$

$$\lim_{x \to +\infty} J(x) = 1, \quad \lim_{x \to 1^-} J^{-1}(x) = +\infty$$

$$\lim_{x \to 1^-} \mu(x) = \lim_{x \to 1^-} J^{-1}\left(1 - \sum_{j=2}^{d_{c,max}} \rho_j J\left((j-1) J^{-1}(1-x)\right)\right) = +\infty$$

one can compute the limits of the different terms in $\frac{d\Psi}{dx}(x)$ when x tends to 1.

$x = 1$ is an attractive point of the recursion function $\Psi(.)$ if $\frac{d\Psi}{dx}(1) < 1$. Expanding this inequality concludes the proof.

□

In the context of the CPM, this stability constraint simplifies to:

$$\text{[C2] Stability} : \lambda_1 < \frac{1}{T'(1) \sum_j \rho_j (j-1)} \tag{2.27}$$

One can see that in our context, variable nodes of degree-2 are not constrained anymore.

2.4.5.1 Example

Taking the same context of the example in the Section 2.4.4.1, Fig. 2.19 depicts the CNs and the combined VNs+CPM EXIT curves of the optimized code adding the stability condition Eq. (2.27). It is to be compared with Fig. 2.17. The profile of the optimized code is:

$$(\lambda_1 = 0.1793, \lambda_2 = 0.5395, \lambda_7 = 0.1168, \lambda_{20} = 0.1644) \tag{2.28}$$

$(\rho_4 = 0.85, \rho_5 = 0.15)$

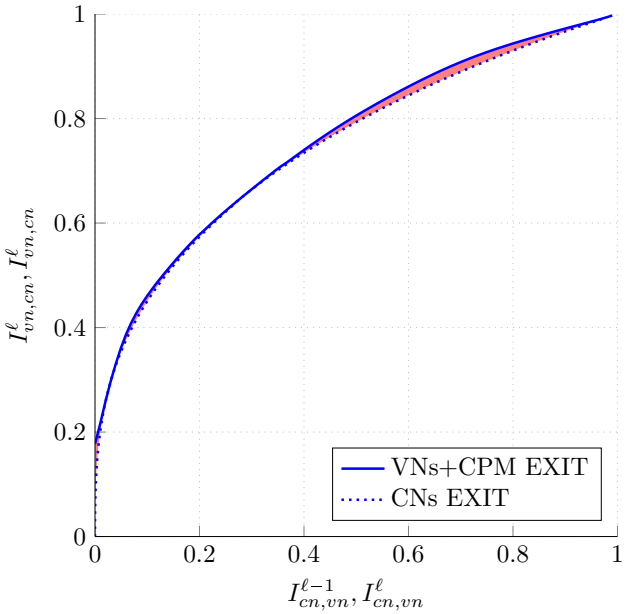

Figure 2.19: The CNs and the combined VNs+CPM EXIT curves of the optimized code in Eq. (2.28)

Besides the constraints $[C_0], [C_1]$ and $[C_2]$ in Eqs. (2.22), (2.23) and(2.27), our design frame work allows to add different constraints for elaborate structure and efficient encoding, for instance:

- Sometimes, especially for high rates, the optimization provides a designed code with a high fraction of degree-2 variable nodes in order to achieve better thresholds. In such cases, one should avoid having cycles containing only degree-2 VNs because it induces high error floors. A practical workaround is to use the irregular repeat accumulate (IRA) code's double diagonal structure to prevents such cycles [YRL04]. The corresponding constraint can be written as:

$$\lambda_2 \leq 2 \sum \frac{\rho_j}{j}$$

- When the sum of the degree-1 and degree-2 VNs equals $(1 - R)$, a construction that allows easily encodable codes is possible as proposed in [NAN03]. To this end, we can append the

constraint:

$$\lambda_1 + \frac{1}{2}\lambda_2 < \sum \frac{\rho_j}{j}$$

2.4.6 Simulation results

Figure 2.20 plots the optimized rate R_{opt} *versus* the maximum achievable rate R^* at different SNRs for the considered binary, quaternary and octal CPM schemes. When the degree-1 VN are allowed, the stability condition was taken into account. We observe that by allowing degree-1 VNs and when $d_{v,\max} = 50$, we almost achieve the maximum achievable rate for the three CPM schemes. By considering degree-1 and taking $d_{v,\max} = 4$ only, we do better than all schemes with $d_{v,\min} = 2$. Tables 2.1, 2.2 and 2.3 summarize some optimized LDPC codes for different CPM schemes at different code rates.

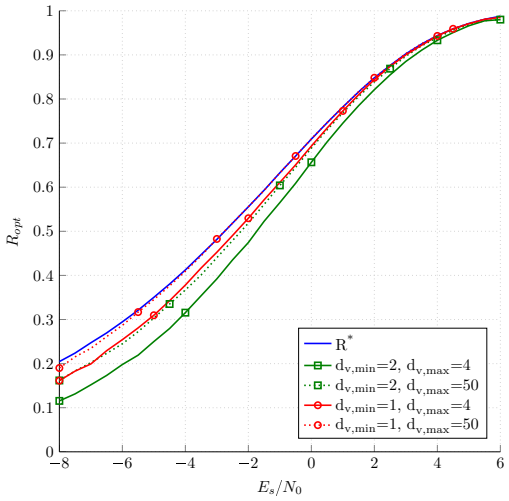

(a) CPM ($M = 2, h = 1/2, L = 3$, Gaussian pulse)

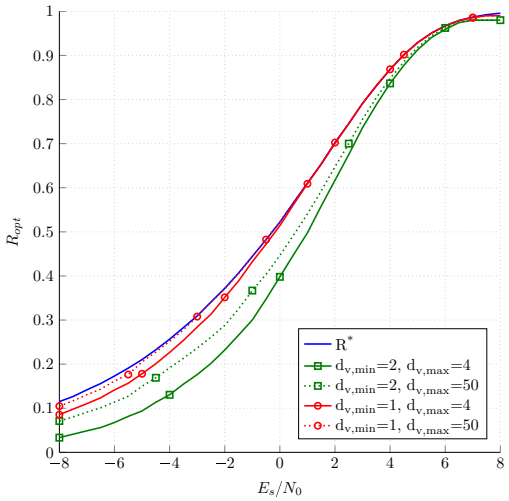

(b) CPM ($M = 4, h = 1/3, L = 1$, Rectangular pulse, natural mapping)

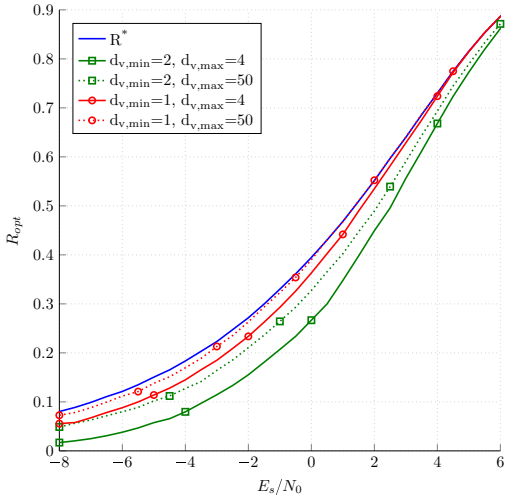

(c) CPM ($M = 8, h = 1/3, L = 2$, RC pulse, natural mapping)

Figure 2.20: R_{opt} *versus* R^* for different CPM schemes as function of E_s/N_0

R_{opt}	1/3				1/2				3/4			
$d_{v,max}$	4		50		4		50		4		50	
$d_{v,min}$	1	2	1	2	1	2	1	2	1	2	1	2
	(1)	(2)	(1)	(2)	(1)	(2)	(1)	(2)	(1)	(2)	(1)	(2)
λ_1	0.1172		0.057523		0.1609		0.073945		0.1534		0.068721	
λ_2	0.7989	0.9756	0.51868	0.59651	0.6239	0.9634	0.41648	0.54986	0.5971	0.9002	0.33863	0.49598
λ_4	0.0839	0.0244			0.2152	0.0366			0.2495	0.0998		
λ_7			0.064677				0.061984					
λ_8			0.1949				0.18719				0.18871	
λ_9				0.14249								
λ_{10}				0.085041								
λ_{11}							0.020966	0.26716				
λ_{12}												0.082474
λ_{13}												0.19822
λ_{50}			0.164122	0.17597			0.23944	0.18192			0.40395	0.22333
ρ_2	0.15											
ρ_3	0.85	0.95			0.15							
ρ_4		0.05	0.7	0.35	0.85	0.9						
ρ_5			0.3	0.65		0.1						
ρ_6							0.75	0.35				
ρ_7							0.25	0.65	0.1			
ρ_8									0.8	0.5		
ρ_9										0.5		
ρ_{14}											0.05	0.4
ρ_{15}											0.95	0.6
$(E_s/N_0)_{opt}$	-4.42	-3.73	-5	-4.5	-2.29	-1.72	-2.72	-2.23	0.83	1.08	0.55	0.75
$(E_s/N_0)^*$	-5.33				-2.78				0.55			

Table 2.1: Different optimized LDPC codes for the GMSK: ($h = 1/2, L = 3$, $BT = 0.3$, Gaussian pulse) and their corresponding thresholds.

R_{opt}	1/3				1/2				3/4			
$d_{v,max}$	4		50		4		50		4		50	
$d_{v,min}$	1	2	1	2	1	2	1	2	1	2	1	2
	(1)	(2)	(1)	(2)	(1)	(2)	(1)	(2)	(1)	(2)	(1)	(2)
λ_1	0.196		0.099964		0.2098		0.10663		0.3021		0.26752	
λ_2	0.7174	0.99	0.48514	0.62102	0.7028	0.997	0.45782	0.58927	0.4180	0.9898	0.46926	0.54111
λ_4	0.0866	0.01			0.0874	0.003			0.28	0.0102		
λ_6			0.067866									
λ_7			0.15975								0.26322	
λ_8							0.20968					
λ_9							0.03807					
λ_{10}				0.098234								
λ_{11}				0.11141								
λ_{12}								0.054822				
λ_{13}								0.1144				
λ_{17}												0.14931
λ_{18}												0.055436
λ_{22}			0.048									
λ_{50}			0.13929	0.16933			0.1878	0.24151				0.25415
ρ_2	0.3											
ρ_3	0.7	1	0.05		0.5							
ρ_4			0.95	0.45	0.5	0.95						
ρ_5				0.55		0.05	0.55					
ρ_6							0.45	0.65	0.1			
ρ_7								0.35	0.9		0.55	
ρ_8										0.85	0.45	
ρ_9										0.15		
ρ_{13}												0.1
ρ_{14}												0.9
$(E_s/N_0)_{opt}$	-1.8	-0.69	-2.31	-1.49	0.44	1.2	0.09	0.63	3.2	3.73	3.12	3.45
$(E_s/N_0)^*$	-2.49				-0.04				3.12			

Table 2.2: Different optimized LDPC codes for the CPM ($M = 4, h = 1/3, L = 1$, Rectangular pulse, natural mapping) and their corresponding thresholds.

R_{opt}	1/3				1/2				3/4			
$d_{v,max}$	4		50		4		50		4		50	
$d_{v,min}$	1	2	1	2	1	2	1	2	1	2	1	2
λ_1	0.2026		0.099188		0.2592		0.13612		0.333		0.25716	
λ_2	0.7633	0.9833	0.50878	0.67108	0.6854	0.9868	0.46893	0.60909	0.5173	0.9966	0.47969	0.56155
λ_4	0.0341	0.0167			0.0554	0.0132			0.1497	0.0034		
λ_7			0.15798									
λ_8			0.058629				0.11355					
λ_9							0.11957				0.19527	
λ_{10}											0.06788	
λ_{11}				0.12558								
λ_{12}				0.01786								
λ_{15}								0.10265				
λ_{20}			0.024615									
λ_{23}												0.12617
λ_{24}												0.043737
λ_{50}			0.15081	0.18548			0.16183	0.28826				
ρ_2	0.35											
ρ_3	0.65	0.95	0.1		0.7							
ρ_4		0.05	0.9	0.7	0.3	0.95	0.05					
ρ_5				0.3		0.05	0.95					
ρ_6								0.65	0.6			
ρ_7								0.35	0.4	0.05	0.35	
ρ_8										0.95	0.65	
ρ_{13}												0.35
ρ_{14}												0.65
$(E_s/N_0)_{opt}$	-0.23	0.9	-0.75	0.078	1.71	2.53	1.38	2.12	4.31	4.74	4.21	4.56
$(E_s/N_0)^*$	-0.99				1.36				4.21			

Table 2.3: Different optimized LDPC codes for the CPM ($M = 8, h = 1/3, L = 2$, RC pulse, natural mapping) and their corresponding thresholds.

Figure 2.21 depicts the 3MSK and the 3GMSK bit error rate (BER) and frame error rate (FER) results. The optimized LDPC codes have rate 1/2. Simulations were performed using 16000 information bits and a maximum of 250 turbo iterations. Table 2.4 summarizes the optimized degree distribution profiles of the LDPC codes. As expected, the simulated thresholds agree with the theoretical ones and no error floors are observed before 10^{-3}.

	MSK	3MSK	3GMSK
$(E_s/N_0)^*$	-2.5	-2.4	-2.5
$(E_s/N_0)_{opt}$	-2.4	-2.3	-2.5
λ_1	0.1294	0.1475	0.1273
λ_2	0.5148	0.545	0.5201
λ_5	0.0679	0.0223	0.0577
λ_{10}	0.2879	0.2852	0.2949
ρ_4	0.25	0.5	0.3
ρ_5	0.75	0.5	0.7

Table 2.4: Optimized LDPC codes for design rate $R = 0.5$

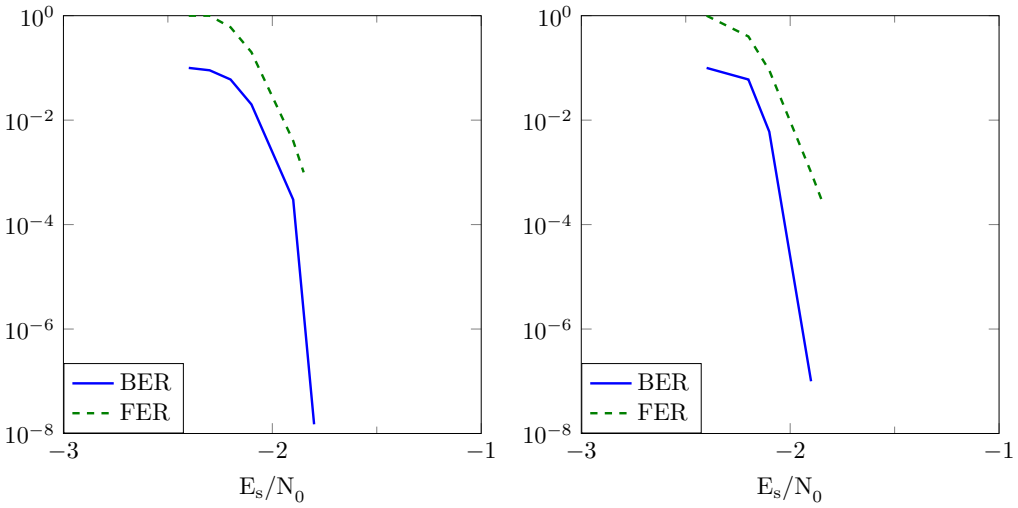

(a) 3MSK (b) 3GMSK

Figure 2.21: BER and FER for optimized concatenated LDPC code with 3MSK and 3GMSK

Authors in [GiAND09] proposed to design serially concatenated CPM with an extended Bose-Chaudhuri-Hocquenghem (eBCH) code [BRC60, BE97]. They conducted both threshold and error floor optimization to achieve low error floors and good thresholds. Here, we compare our results with their obtained thresholds.

The channel capacity was estimated using the lower bound given by symmetric information rate (SIR) method for CPM in [KC04]: the SIR is defined as the mutual information rate between the channel input and the channel output for independent and identically distributed inputs with an uniform distribution. Their optimization approach is different from the one conducted in this chapter: they fix an outer code and a spectral efficiency, and try to optimize the CPM and the outer code rate with respect to spectral efficiency and to have low thresholds. On the contrary, in our approach, after choosing a targeted CPM scheme and fix the LDPC code rate, we design the best LDPC profile with the lowest threshold.

In [GiAND09], two CPM schemes with spectral efficiency of 0.9bits/s/Hz were optimized for the concatenation with a $(64, 51, 6)$ eBCH. The Table 2.5 compares the provided results in [GiAND09] and our optimization results for the two schemes:

(1) $M = 4, L = 2, h = 2/5$, Raised cosine pulse and Gray mapping concatenated with an eBCH outer code rate of 0.8

(2) $M = 4, L = 3, h = 2/7$, Raised cosine pulse and Gray mapping concatenated with an eBCH outer code rate of 0.5

The two methods of bounding the capacity gives relatively close results. A fact that corroborates our conjectured generalization of the area theorem for CPM. Our optimized LDPC code for the CPM in (2) is only at 0.08dB far from $(E_s/N_0)^*$. However, authors in [GiAND09] observed that the CPM in (1) improves significantly the threshold in comparison to (2). For this scheme, our optimized LDPC codes allows to operate at 0.65dB from the obtained threshold in [GiAND09].

The threshold gain of our optimized LDPC codes should come at the cost of higher error floors, however, by taking relatively large codewords, for example 16000 information bits, errors floors can be made lower (below 10^{-4}) in terms of FER as observed in Fig. 2.21.

	(1)	(2)
our $(E_s/N_0)^*$	3.1	0.62
$(E_s/N_0)^*$ of [GiAND09]	2.97	0.55
our $(E_s/N_0)_{opt}$	3.1	0.7
$(E_s/N_0)_{opt}$ of [GiAND09]	3.75	2.91
λ_1	0.3764	0.2505
λ_2	0.4012	0.432
λ_5		0.1711
λ_6	0.0179	
λ_7	0.2045	
λ_{20}		0.1464
ρ_2		0.1
ρ_3		0.9
ρ_7	0.75	
ρ_8	0.25	

Table 2.5: Optimized LDPC codes for the CPM schemes (1) and (2)

2.5 Conclusion

In this chapter, we proposed a framework to design unstructured LDPC codes for the CPM. The proposed method can be applied to any detector. Using the properties of the CPM, we showed that on can improve the convergence threshold by introducing a controlled proportion of degree-1 VNs subject to a particular stability condition. We also provide a proof of this stability condition in the general case in the context of EXIT chart analysis. We focused on the asymptotic performance and the evaluation of the maximum achievable rates of unstructured LDPC codes. The results of this class will be used along the thesis to compare with other more practical codes that benefit from better encoding and implementation advantages.

Chapter 3

Design of LDPC codes with structure

Summary

Résumé

Dans ce chapitre, nous menons une analyse asymptotique pour concevoir des codes LDPC plus pratiques pour le CPM. Tout d'abord, nous étudions les codes IRA en raison de leur performance et de leur encodage facile. Comparés aux codes LDPC non structurés, ils ont de bons seuils et sont facilement encodable grâce à leur partie structurée. Par ailleurs, nous généralisons cette famille aux codes Generalized IRA (GIRA). Contrairement à la méthode de design proposée dans [XA05] pour les codes LDGM et afin de s'affranchir de l'optimisation des noeuds de dopage, nous proposons d'étudier les codes GIRA systématiques. Cette considération implique un ordonnancement de décodage particulier.

Deuxièmement, nous étudions la performance des codes LDPC basés sur des protographes [Tho03]. Cette classe bénéficie d'une représentation compacte, d'une analyse des performances plus simple et d'une implémentation facilement parallélisable. Nous allons montré qu'on peut optimiser des codes LDPC-protographe qui opèrent à 0.5dB seulement des LDPC non-structurés. Les résultats de simulation et la comparaison avec les protographes optimisés du canal Gaussian, ARJA et AR3A [LC07, DDJ06], sont fournis. Les protographes conçus ont été optimisés pour minimiser le seuil de décodage. Par conséquent, ils ne disposent pas nécessairement de bonnes propriétés de distances minimales en raison de l'introduction d'une grande proportion de noeuds de variables de degré 1 et 2. Toutefois, étant donné le contexte de nos applications, avec des trames de données longues, notre méthode donne de très bons résultats à 10^{-3} en terme de taux d'erreur paquet.

Finalement, afin d'obtenir des protographes avec de bonnes performances à la fois dans la région *waterfall* et la région du plancher d'erreur, nous étudions les codes LDPC spatialement couplés basés sur des protographes [MLCJ14] parce qu'il a été démontré que cette famille de code atteint universellement de bons seuils sur une large variété de canaux. En plus de tous les avantages des codes LDPC basés sur des protographes, ces codes présentent un *gain de convolution* qui améliore les performances de la famille précédente. Nous allons montrer que par couplage de protographes simples tel que le $(3, 6)$ régulier, nous atteignons déjà des seuils satisfaisants et par construction, une bonne distance minimale. En outre, pour remédier à la perte de rendement inhérente à la terminaison des codes LDPC spatialement couplés, nous introduisons une nouvelle terminaison qui préserve le rendement du protographe sous-jacent indépendamment de la longueur de couplage, tout en présentant un gain de convolution. C'est la première fois à notre connaissance qu'on envisage la possibilité d'utiliser un seul *effet de vague* pour les LDPC spatialement couplés. Cette nouvelle terminaison nous permet de concevoir un couplage du $(3, 6)$ qui donne le même seuil et le même rendement que le code LDPC optimisé au chapitre 3 avec une longueur de couplage égale à 4 seulement.

Enfin, afin de concevoir de très bons codes LDPC spatialement couplés en terme de seuil de décodage pour le CPM, nous introduisons une technique d'optimisation en deux étapes: après avoir trouvé un bon protographe, nous optimisons le couplage afin d'obtenir de très bons seuils. Cette stratégie conduit à des codes très compétitifs qui fonctionnent à des seuils de seulement $0.1 - 0.15$ dB des codes LDPC non structurés.

3.1 Introduction

We have seen in the chapter 2 a general framework to design unstructured LDPC codes. In this chapter, we focus on the families of LDPC codes that have more structure, either partial structure such as as irregular repeat accumulate codes or protograph-based LDPC codes. Many studies have been conducted trying to jointly optimize iterative schemes with different CPM configurations and convolutional outer codes [MA01, NS99, BFC09]. Later on, several structured sparse graph based codes families emerged such as irregular repeat accumuluate (IRA) codes [Jin01]. The main advantage of IRA codes is their low encoding and decoding complexity (linear in code length) while showing similar performance close to low density parity check (LDPC) codes. Only few papers studied the convergence behaviour and the asymptotic design of these codes for general CPM schemes without relying on properties of some particular CPM families. [XA05, CVT09, XA07] have considered a non systematic IRA-like coded CPM. The proposed structure replaces the IRA accumulator with a CPM modulator. This was motivated by the fact that CPM acts as a phase accumulator.

The main contribution of this chapter is that we first propose an asymptotic analysis for the design of serially concatenated turbo schemes that works for both systematic generalized irregular repeat accumulate (GIRA) and low density generator matrix (LDGM) codes concatenated with a continuous phase modulation (CPM). The proposed design is based on an EXIT chart method. By considering a particular scheduling, inserting partial interleavers between GIRA accumulator and CPM and allowing degree-1 variable nodes, we show that one can achieve very good thresholds for this subensemble. In GIRA codes, the accumulator $1/(1+D)$ is replaced by a generalized accumulator with a polynomial transfer function $1/G(D)$. Not only this class offers more flexibility, but also embraces all previously discussed codes by choosing the right accumulator function. Furthermore, we point out that for systematic GIRA codes, the optimization is not as straightforward as the non systematic case [XA05, StBLL12] but requires a well-thought scheduling. Also, since all bits are transmitted, we do not have to consider, at the difference of [tBK03, XA05], a careful design of doping check nodes [tB01b]. As mentioned in chapter 2, we can remark that the extrinsic information transfer function (EXIT) [AKtB04] of CPM detectors, at the difference of the MIMO detector in [tBK03], joins the point $(1,1)$. Consequently, we can introduce a controlled proportion of degree-1 variable nodes in order to improve the performance in terms of itarative decoding threshold.

The second contribution is an asymptotic analysis and design of protograph-based LDPC codes for CPMs. This code family has been studied extensively in the recent years. First introduced in [Tho03],

protograph codes show very good thresholds and low encoder/decoder complexity implementation. These codes are described by a small Tanner graph that is used as a layout to construct the final LDPC code by following a copy-and-permute procedure: after duplication the protograph N times, the end points of the replicas of each edge are permuted so that all the protograph copies are interconnected with respect to the local constraints. Unlike unstructured LDPC codes, parallel edges are allowed in the protograph (but not in the generated code) as well as degree-1 variable nodes. This idea not only provides a concise way to define the code, but also implies that the performance of the protograph-based LDPC code can be predicted from its underlying protograph. Many protograph-based LDPC codes have been proposed [RL09] (accumulate repeat accumulate codes, quasi-cyclique codes, ...). In the context of CPM, no study has been made to evaluate the performance and to design protograph-based LDPC codes. We show that optimized protographs for the additive white Gaussian noise (AWGN) channel [LC07] do not exhibit necessarily good performance when concatenated with the CPM and propose some protographs with very good performance.

Finally, we study the protograph-based LDPC convolutional codes (LDPC-C) [MLCJ14]. They are obtained by spatial coupling protograph codes. This coupling is an efficient technique that leads to susbtentially better theresholds even with relatively simple protographs under belief propagation decoding. Since their introduction, numerous papers were written on the reasons why they perform so good in comparison to classical LDPC codes (see [KRU11, MLC11, KRU12] and references therein for more details). To our knowledge, no work has been done to design and analyse the performance of LDPC-C codes concatenated with CPM. In [SB13], the authors compared the performance of some LDPC-C codes over the Gaussian channel, proposed a $3/4 - rate$ universally good (with any mapping/MIMO detector) LDPC-C code candidate and illustrated it with the $16 - QAM$ receiver with different mappings. [NYPN11] showed that LDPC-C codes achieve the symmetric achievable rate for intersymbol-interference channels. For bit-interleaved coded modulations, [HAB+13] studied the performance of the LDPC-C codes and the mapping optimization where each bit channel is modelled by an independent binary erasure channel. We will see that, due to the inner structure of CPM, good codes for the Gaussian channel do not exhibit necessarily good performance with CPM. We investigate the performance of the concatenated scheme formed by the serial concatenation of a LDPC-C code and a general CPM modulation scheme. We focus on finding LDPC-C codes that are good for a particular CPM modulator. We also see that coupling optimized protographs for the CPM improves their threshold. Finally, we will show that we can adapt an unusual LDPC-C termination without rate loss but still having a very good threshold.

3.2 Generalized Irregular Repeat Accumulate codes

3.2.1 System Description

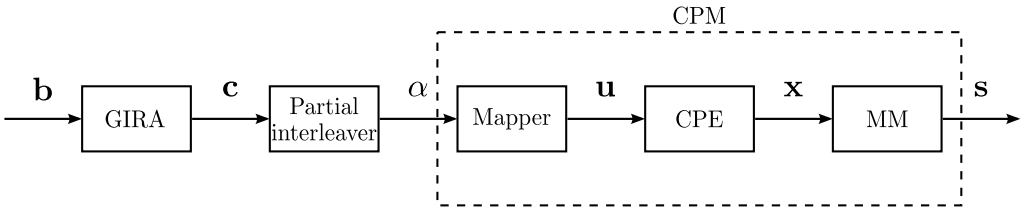

Figure 3.1: Transmitter

A systematic GIRA code serially concatenated with a CPM modulator is depicted in Fig. 3.1 and in the Tanner graph in Fig. 3.3. The GIRA encoder can be seen as a serial concatenation of repetition codes with a convolutional code named accumulator. In non systematic GIRA codes, the information bits are not transmitted. At the beginning of the coding process, each bit of a binary message $u \in \{0,1\}^K$ is irregularly repeated with a factor corresponding to the degree of its associated variable node. After interleaving by a random interleaver π_{GIRA}, the repeated bits are first combined (using the so-called combiner [JW05]) and then are fed to the "generalized" accumulator (a classical rate-1 recursive convolutional code), with polynomial transfer function $1/G(D)$. Figure 3.2 depicts the systematic GIRA codes seen as serially concatenated scheme.

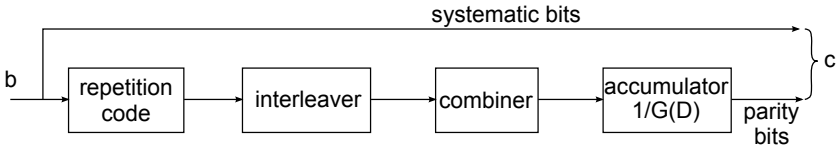

Figure 3.2: A systematic GIRA encoder seen as a serial concatenation

The parity check matrix of a systematic GIRA code is of the form:

$$H = [H_u \; H_p]$$

where H_u refers to the connections between the systematic bits variable nodes and the check nodes while the squared matrix H_p describes the connections between the check nodes and the parity bit variable nodes.

GIRA codes generalize IRA codes in that the accumulator $1/1+D$ is replaced by any convolutional

code with transfer function $1/G(D)$ where:

$$G(D) = 1 + \sum_{i=1}^{i=r} g_i D^i \quad \text{where} \quad g_i \in \{0,1\}$$

. The number of '1's diagonals in H_p corresponds to the number of non-null coefficient of $G(D)$. To name only a few, when:

- $G(D) = 1$, we obtain a LDGM code
- $G(D) = 1 + D$ we have an IRA code

As for irregular LDPC codes, the sub-matrix H_u of GIRA codes ensemble can be represented with its edge-perspective degree distribution polynomials [1]:

$$\lambda(x) = \sum_{i=1}^{d_{v,max}} \lambda_i x^{i-1} \quad , \quad \rho(x) = \sum_{j=1}^{d_{c,max}} \rho_j x^{j-1}$$

where λ_i (resp. ρ_j) is the proportion of edges in the Tanner graph connected to variable nodes (VN) of degree i (resp. to check nodes (CN) of degree j) and $d_{v,max}$ (reps. $d_{c,max}$) is the maximum VN (resp. CN) degree.

Observe that the check node edge degree starts with $j = 1$, this is due to the fact that these polynomial profiles concern only the systematic part H_u and hence do not reflect the total connectivity (the connections in both H_u and H_p).

When the GIRA code is systematic and check-regular, the design code rate is given by:

$$R = \frac{d_{c,max} \sum \lambda_i / i}{1 + d_{c,max} \sum \lambda_i / i} \tag{3.1}$$

Unlike [XA05], authors considered an non systematic IRA, consequently, more caution should be taken when optimizing the code: the check nodes in H_u of degrees higher than 1 cannot decode at the first iterations, consequently, a controlled proportion of degree-1 check nodes should be added: this is called *doping* [tBK03].

Each code word $\boldsymbol{c}$ is then interleaved, mapped into M-ary symbols $\boldsymbol{\alpha} = \{\alpha_i\}_i$ and finally encoded by the CPM as:

$$s(t, \boldsymbol{\alpha}) = \sqrt{\frac{2E_s}{T}} cos\left(2\pi f_0 t + \theta(t, \boldsymbol{\alpha}) + \theta_0\right) \tag{3.2}$$

[1] note that this representation slightly differs from the classical LDPC case in the previous chapter

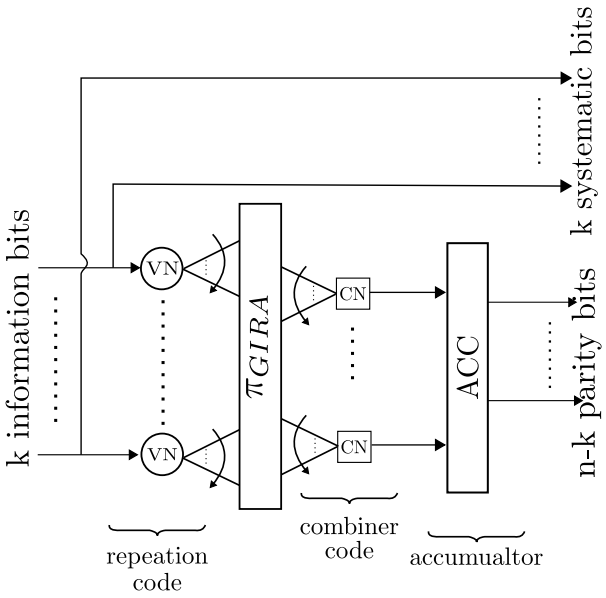

Figure 3.3: Systematic GIRA encoder

$$\theta(t,\boldsymbol{\alpha}) = \pi h \sum_{i=0}^{N-1} \alpha_i q(t-iT) \tag{3.3}$$

$$q(t) = \begin{cases} \int_0^t g(\tau)d\tau \\ 1/2,\ t > L \end{cases}$$

Recall that f_0 is the carrier frequency, θ_0 the initial phase shift, $\theta(t,\boldsymbol{\alpha})$ the information carrying phase, $g(t)$ the frequency pulse, $h = k/p$ the modulation index, L the memory and $\Re$ the real part.

At the receiver side, a soft-input soft-output (SISO) CPM decoder is used, based on the Rimoldi's decomposition [Rim88] (without any loss of generality). The transmitted signal $s(t,\boldsymbol{\alpha})$ is corrupted with an additive white Gaussian noise (AWGN) having a double-sided power spectral density $N_0/2$. As seen in chapter 2, let us denote:

$$\boldsymbol{y^n} = \left[y_i^n = \int_{nT}^{(n+1)T} y(l)s_i^*(l)dl \right]_{1\le i\le pM^L}$$

where $\{s_i(t)\}_i$ form the Rimoldi's memomryless modulator. $\{\boldsymbol{y^n}\}_n$ is a sufficient statistic to estimate the information symbols [MA01].

For the outer decoder, we can use either LDPC-like decoding exploiting the belief-propagation (BP) algorithm [RU01] on the Tanner graph associated to GIRA code (see Fig. 3.4) or a turbo-like

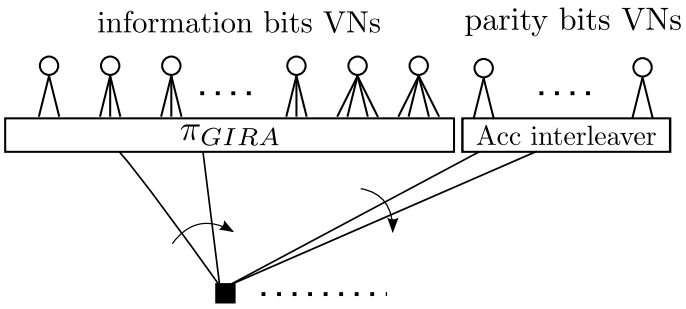

Figure 3.4: GIRA Tanner graph

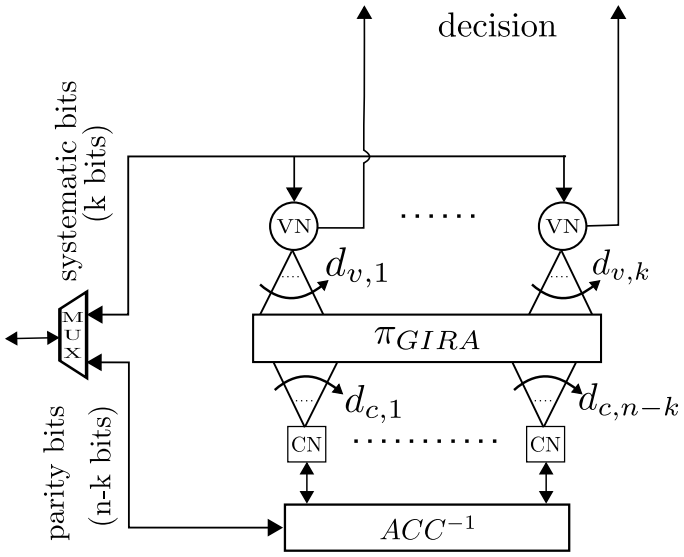

Figure 3.5: Systematic GIRA soft decoder

decoding interpreting the GIRA code as the serial concatenation of an LDGM and an accumulator [StBLL12, JW05] (see Fig. 3.2). These two methods are equivalent when the GIRA parity check matrix H is cycle free. Fig. 3.5 depicts the GIRA soft decoder architecture.

3.2.2 Code design

As seen earlier in chapter 2, the density evolution algorithms to study the asymptotic convergence behavior of concatenated system can be cumbersome, instead, EXIT charts [tB01c] are exploited. Partially inspired from [XA05], our optimization method returns the best degree profiles using EXIT curve-fitting. In our case, since we have an accumulator and a systematic encoder, we need to define a

particular scheduling to obtain linear equations with respect to $\{\lambda_i\}$: the CPM decoder communicates its extrinsic log likelihood ratios (LLR values) to all variable nodes. Systematic variable nodes perform a data-pass operation to the check nodes that, in their turn, forward their LLR messages to the accumulator. At this stage, we consider a subsystem formed by serially concatenated convolutional codes: the accumulator and the CPE. After a certain number of turbo-iterations, which will be characterized later, the accumulator propagates its extrinsic information all the way back to the systematic variable nodes. This defines one global iteration ℓ.

In our analysis, we will consider tail-bited GIRA codes. When tail-biting is used for the accumulator, H_p is given by:

$$H_p = \begin{pmatrix} 1 & & & & & g_r & \cdots & g_1 \\ g_1 & 1 & & & & & \ddots & \vdots \\ \vdots & g_1 & \ddots & & & & & g_r \\ g_r & \vdots & \ddots & \ddots & & & & \\ & g_r & \ddots & \ddots & \ddots & & & \\ & & \ddots & \ddots & \ddots & \ddots & & \\ & & & \ddots & \ddots & \ddots & \ddots & \\ & & & & g_r & g_{r-1} & \cdots & 1 \end{pmatrix}$$

where each column has the same weight and depends only on $G(D)$. It allows neglecting the "edge" effects when considering the non regular graph associated with the non tail-biting version.

When choosing the accumulator, one should avoid girth-4 H_p matrices, for instance, taking $G(D) = 1 + D + D^2$ is not allowed. Furthermore, we will consider systematic GIRA codes so that there is no need to consider introducing doping check nodes as it is done in [tB01b][XA05].

Designing a GIRA code consists in finding out the variable nodes profile $\lambda(x)$ and the check nodes profile $\rho(x)$ that maximize the design rate for a given signal to noise ratio (SNR) E_s/N_0 with respect to the convergence of the decoder. Fig. 3.6 introduces the main notations of different mutual information associated with LLR messages and the corresponding involved bits:

- $I^{\ell}_{vn,cn}(i)$ is the average MI associated with LLR messages passed from a VN of degree i to CNs
- $I^{\ell}_{vn,cn}$ is the average MI associated with LLR messages passed from a VNs to CNs
- $I^{\ell}_{cn,vn}(j)$ is the average MI associated with LLR messages passed from a CN of degree j to VNs

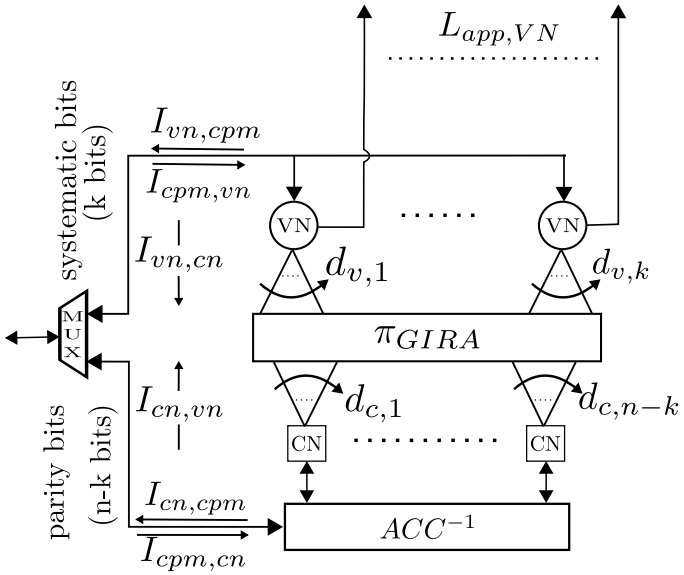

Figure 3.6: Systematic GIRA soft decoder

- $I^{\ell}_{cn,vn}$ is the average MI associated with LLR messages passed from CNs to VNs
- $I^{\ell}_{cpm,vn}(i)$ is the MI for degree-i VN associated with LLR messages passed from the CPM decoder to the LDPC decoder.

Remember that the set of edges connecting check nodes to parity variable nodes in Fig. 3.4 is not included neither in $\lambda(x)$ nor in $\rho(x)$. These connections, directly linked to the type of the accumulator, are taken into account in the EXIT transfer function as it is going to be explained later on. Besides, following the same argument in the chapter 2, partial interleavers one per each VN degree are considered between CPM and the systematic part of IRA.

3.2.2.1 CPM transfer function

Assume $I_{.,cpm}$ and $I_{cpm,.}$ denote respectively the *a priori* and extrinsic mutual information of the CPM soft decoder. Analytical study of the input-output EXIT transfer function of SISO CPM module is not straightforward. Alternatively, we compute the CPM transfer chart $T(., E_s/N_0)$ using Monte Carlo simulation and polynomial approximation. Thus, we have:

$$I_{cpm,.} = T(I_{.,cpm}, E_s/N_0) \tag{3.4}$$

As we will consider a curve fitting approach and based on the commonly observed generalization of the results of [AKtB04] for the binary erasure channel, an upper bound on the achievable rate for the outer code given an SNR E_s/N_0 can be approximately using the area under the CPM detector EXIT curve (see chapter 2), *i.e.*:

$$R \leq R^* = \int_0^1 T(I_{vn,cpm}, E_s/N_0) dI_{vn-cpm}$$

Unlike the MIMO receiver in [tBK03], CPM detector EXIT curves join the point $(1,1)$: it allows us to introduce degree-1 VNs. Here also, it is implicitly assumed that BCJR recursions are run independently between different trellis section groups delimited by each partial interleaver. This is not the case in practice but this assumption allows us to neglect transition effects when running the decoding. Marker-free line in Fig. 3.8 presents EXIT chart of GSM GMSK with $L = 3$, $h = 1/2$ and $BT = 0.3$ at $E_s/N_0 = 0$dB.

3.2.2.2 IRA EXIT transfer functions

a. EXIT Transfer Function of VNs and CNs

Let $I^{\ell}_{vn,cn}$ denotes the averaged mixture of extrinsic MI output passed from the variable nodes to check nodes at the ℓ^{th} iteration. This mixture is equal to:

$$I^{\ell}_{vn,cn} = \sum_{i=1}^{d_{v,max}} \lambda_i I^{\ell}_{vn,cn}(i) \tag{3.5}$$

where $I^{\ell}_{vn-cn}(i)$ is the average mutual information associated with LLRs passed from a VN of degree i to CNs and is given by:

$$I^{\ell}_{vn,cn}(i) = J\left(\sqrt{(i-1)[J^{-1}(I^{\ell-1}_{cn,vn}(i))]^2 + [J^{-1}(I^{\ell}_{cpm,vn}(i))]^2}\right) \tag{3.6}$$

Likewise, VN to CPM update function is given by:

$$I^{\ell-1}_{vn,cpm}(i) = J(\sqrt{i} J^{-1}(I^{\ell-1}_{cn,vn})) \tag{3.7}$$

Since the VN profile is not regular, assuming Eq. (3.7) is equivalent to considering partial interleavers per VN degree between the CPM and the systematic part of GIRA.

On the other hand, the information passed from CN of degree j to the parity bits nodes and to the systematic variable nodes are respectively:

$$I^{\ell-1}_{cn,acc}(j) = 1 - J(\sqrt{j} J^{-1}(1 - I^{\ell-1}_{vn,cn})) \tag{3.8}$$

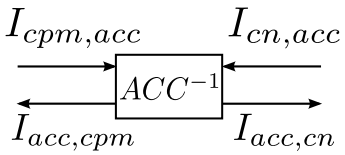

Figure 3.7: Accumulator soft decoder

$$I_{cn,vn}^{\ell-1}(j) = 1 - \quad J\left(\sqrt{(j-1)J^{-1}(1-I_{vn,cn}^{\ell-1}) + J^{-1}(1-I_{acc,cn}^{\ell-1})}\right) \tag{3.9}$$

Without loss of generality, we can suppose check-regular GIRA code with uniform check degree $d_{c,max}$.

b. EXIT Transfer Function of the Accumulator

Figure 3.7 summarizes the accumulator SISO decoder. [tBK03] approximates the mutual information $I_{acc,cn}^{\ell}$ between the LLR messages sent from the accumulator to the CNs and the corresponding bits, by the equation:

$$I_{acc,cn}^{\ell} = \left[\frac{1-q}{1-qI_{cn,acc}^{\ell}}\right]^2 \quad \text{with} \quad q = 1 - \overline{I^{\ell}}_{cpm,acc}$$

where $\overline{I^{\ell}}_{cpm,acc}$ corresponds to the MI value at the convergence between the CPM seen as inner code and the accumulator seen as outer code. However, this expression was inspired from the binary erasure channel and holds correct only for $G(D) = 1 + D$ and $d_{c,max} = 1$ [Jin01].

In the general case, this expression is not accurate anymore. Instead, we shall precompute the different EXIT charts of the accumulator ($I_{acc,cn}^{\ell}$ and $I_{acc,cpm}^{\ell}$) using Monte Carlo simulations:

$$I_{acc,cn}^{\ell} = T_{acc,cn}(\overline{I^{\ell}}_{cpm,acc}, I_{cn,acc}^{\ell}) \tag{3.10}$$

$$I_{acc,cpm}^{\ell} = T_{acc,cpm}(I_{acc,cn}^{\ell}, I_{cpm,acc}^{\ell}) \tag{3.11}$$

The former is the MI over uncoded bits whereas the latter is the MI over encoded bits.

Figures 3.8a and 3.8b illustrate the location of the convergence (intersection points) of the concatenated subsystem CPM+ACC. The unmarked curves correspond to the EXIT chart of the CPM (here a GMSK). The marked curves represent the EXIT transfer functions of different accumulators as function of different *a priori* values. Figure 3.9 shows how $\overline{I^{\ell}}_{cpm,acc}$ (the intersection point) varies as a function of the *a priori* mutual information $I_{cn,acc}$.

$\overline{I^{\ell}}_{cpm,acc}$ for a particular SNR can be easily provided by a polynomial approximation of the curves depicted in Fig. 3.9. Even if GIRA codes present a small degradation of the decoding threshold in comparison to IRA codes [JW08], observe that the MI curve in Fig. 3.9 of the former is better than the latter. Finally, we point out that for the special case of a LDGM code, there is no accumulator, i.e. $G(D) = 1$, therefore, $I^{\ell}_{acc,cn}$ and $I^{\ell}_{acc,cpm}$ are equal to $I^{\ell}_{cpm,acc}$ and $I^{\ell}_{cn,acc}$ respectively.

From Eqs. (3.7),(3.8),(3.9),(3.10) and (3.11) we can compute the transfer function of joint CN and ACC+CPM. When combined with Eqs. (3.5), (3.4) and (3.6), this leads to a linear programming problem that maximizes the design rate R in Eq. (3.1) under the convergence constraints:

$$\text{[C1] Convergence} : \Phi(\lambda(x), I^{(l)}_{vn,cn}, \frac{E_s}{N_0}) = I^{(l+1)}_{vn,cn} > I^{(l)}_{vn,cn}, \forall I^{(l)}_{vn,cn} \in [0,1]$$

$$\text{[C1] mixture constraint} : \sum_i \lambda_i = 1$$

By convention, $I^{(0)}_{vn,cpm}(i) = 0, \forall i = 1, ..., d_{v,max}$ and $I^{(0)}_{cn,vn} = 0$.

Concerning the stability condition of the degree-1 variable nodes, we use the same one as in the chapter 2, since IRA codes can be seen as a sub-ensemble of unstructured LDPC codes. Note that more caution should be taken when adding the constraint relative to the stability condition since it requires the polynomial profile of the whole IRA code not only of H_u. This can be easily achieved by considering the new regular variable nodes in H_p.

3.2.3 Simulation Results

In this section, we present some simulation results obtained from our optimization for four different GIRA codes: LDGM, IRA, $G_1(D) = 1 + D + D^3$ and $G_2(D) = 1 + D + D^4$. Figure 3.10 depicts obtained thresholds and it compares them to the maximum achievable rate R^* for GSM GMSK. We observe that we operate very close to R^*. These results can be improved by allowing higher $d_{v,max}$ (here $d_{v,max} = 10$). Table 3.1 presents some optimized profiles and their corresponding asymptotic thresholds.

Note that the profile coefficients λ_i and $d_{c,max}$ refer to H_u only and do not include the proportions in H_p. If one needs to obtain the total LDPC-like profiles, one can apply the transformation:

$$\lambda(x) = \sum_{i=1}^{d_{v,max}} \lambda_i \frac{d_{c,max}}{d_{c,max} + a} x^{i-1} + \frac{d_{c,max}}{a + d_{c,max}} x^{a-1}$$

$$\rho_{d_{c,max}+a} = 1$$

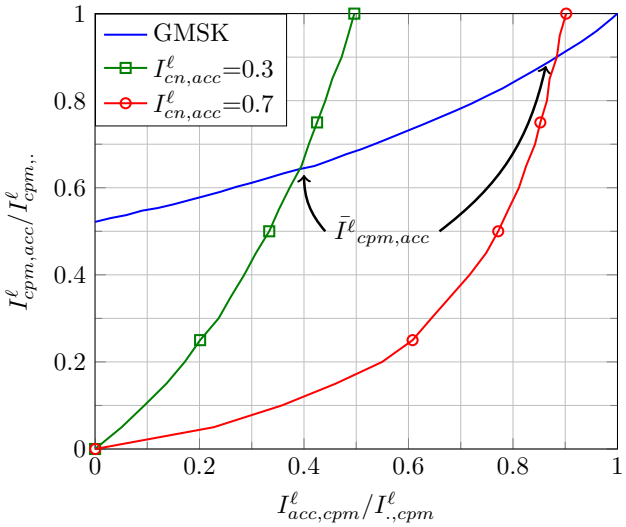

(a) IRA

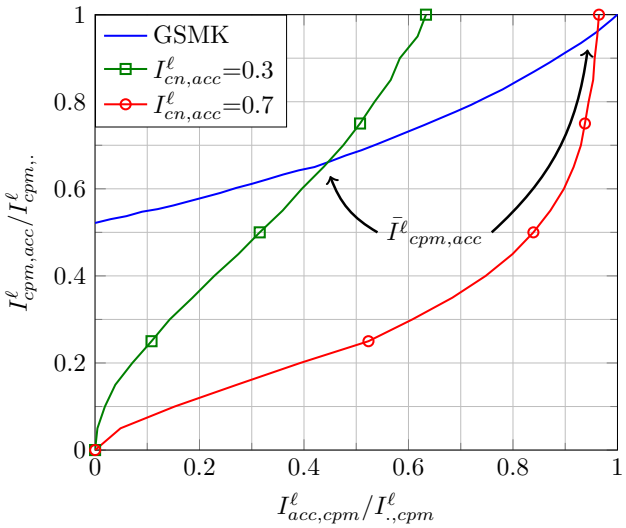

(b) GIRA with $G(D) = 1 + D + D^4$

Figure 3.8: $I^{\ell}_{acc,cpm}$ as a function of $I^{\ell}_{cpm,acc}$ with different *a priori* $I^{\ell}_{cn,acc}$ at $E_s/N_0 = 0$dB.

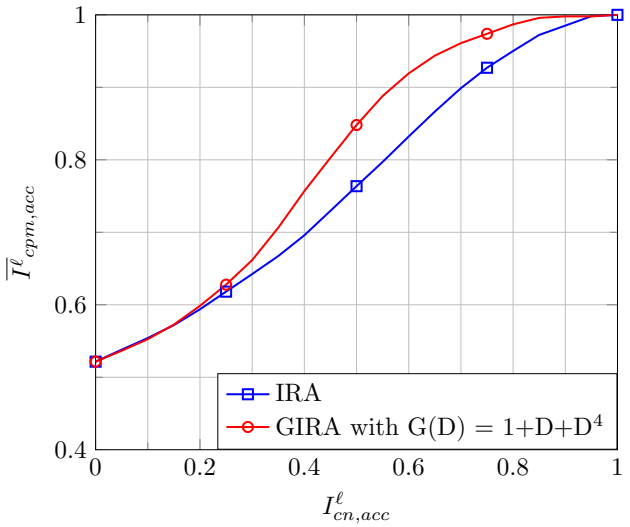

Figure 3.9: Accumulator and GMSK convergence point (intersection) at $E_s/N_0 = 0$dB as function of $I_{cn,acc}$

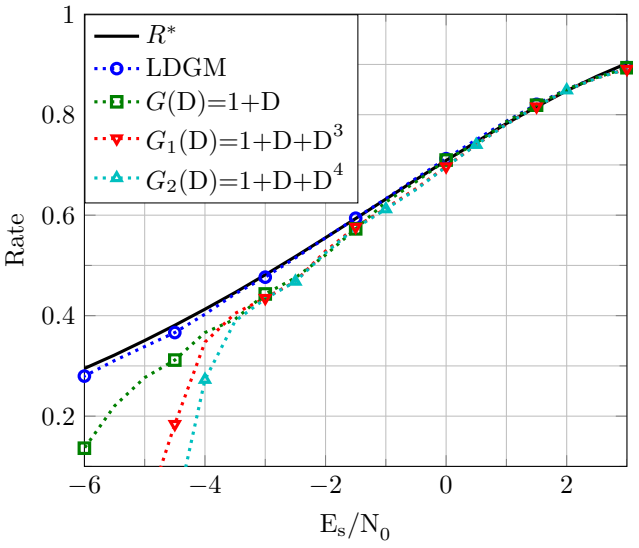

Figure 3.10: Achievable and optimized rates when VNs degrees are constrained to be ≥ 1

where a corresponds to the column weight of H_p.

For comparison, taking the case of the memory-1 Minimum Shift Keying (MSK) CPM, the threshold for the designed nonsystematic rate-1/2 LDGM in [XA05] is $E_s/N_0 = -2.61$dB, while

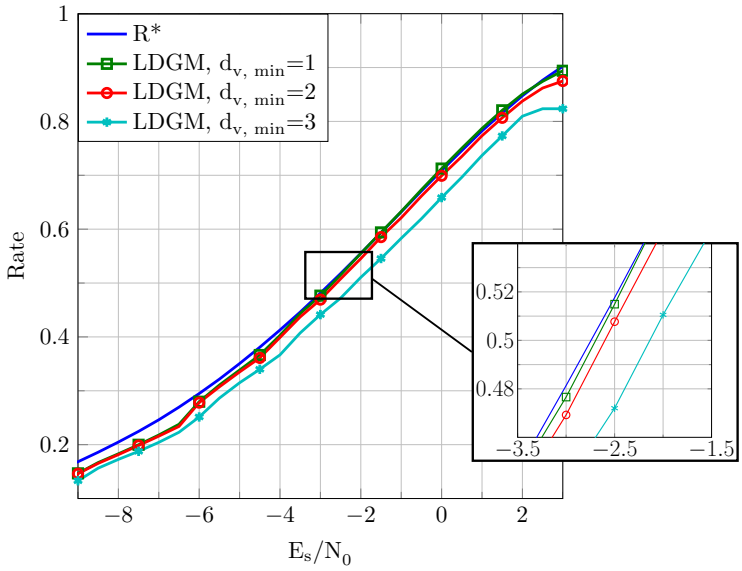

(a) LDGM

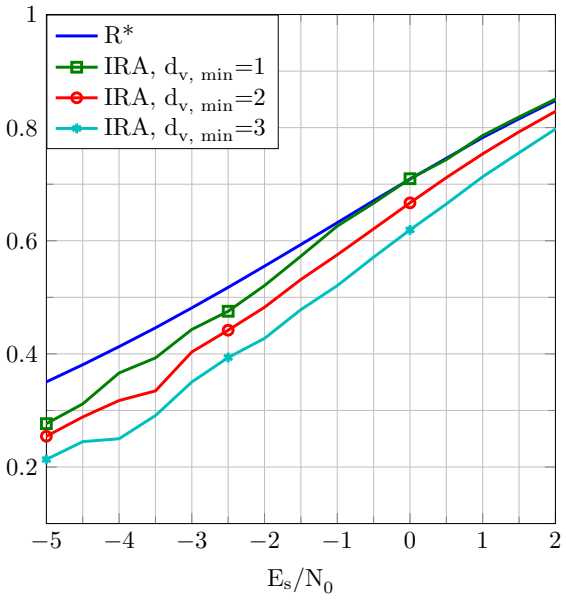

(b) IRA

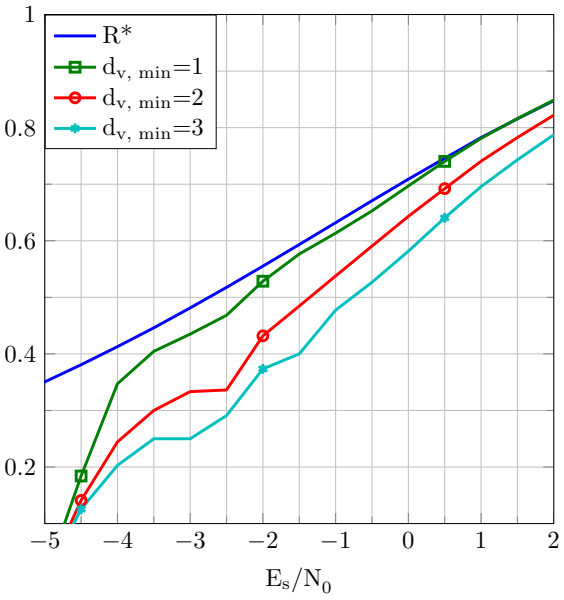

(c) $G(D) = 1 + D + D^4$

Figure 3.11: Maximum achievable and optimized rates for some GIRA codes with GMSK

our optimization gives a systematic rate-1/2 LDGM code with threshold -2.7dB (values are to be compared with the MSK theoretical threshold $(E_s/N_0)^* = -2.8$dB).

GMSK: Threshold -2.73dB			
LDGM		IRA	
Threshold -2.7dB		Threshold -2.22dB	
$\lambda_1 = 0.051$	$d_{c,max} = 3$	$\lambda_1 = 0.185$	$d_{c,max} = 2$
$\lambda_2 = 0.357$		$\lambda_2 = 0.551$	
$\lambda_5 = 0.023$		$\lambda_8 = 0.086$	
$\lambda_6 = 0.568$		$\lambda_9 = 0.176$	
G(D)=$1 + D + D^3$		G(D)=$1 + D + D^4$	
Threshold -2.22dB		Threshold -2.22dB	
$\lambda_1 = 0.411$	$d_{c,max} = 2$	$\lambda_1 = 0.424$	$d_{c,max} = 2$
$\lambda_7 = 0.103$		$\lambda_2 = 0.04$	
$\lambda_8 = 0.485$		$\lambda_{10} = 0.536$	
Unstructured LDPC			
Threshold -2.7dB			
$\lambda_1 = 0.1125$	$\rho_3 = 0.2$		
$\lambda_2 = 0.5294$	$\rho_4 = 0.8$		
$\lambda_5 = 0.0086$			
$\lambda_{10} = 0.3495$			

Table 3.1: Optimized GIRA codes for design rate $R \simeq 0.5$. For LDPC code, we obtain $\lambda_1 = 0.1125, \lambda_2 = 0.5294, \lambda_5 = 0.0086, \lambda_{10} = 0.3495, \rho_3 = 0.2, \rho_4 = 0.8$ with a threshold of -2.7dB

Figure 3.11 illustrates how the designed rates depend on the minimum degree of VNs $d_{v,min}$. While introducing degree-1 VNs leads to a slight improvement in the case of LDGM, in the case of IRA, GIRA $G_1(D)$ and GIRA $G_2(D)$, it outperforms clearly $d_{v,min} = 2$ schemes by a gain of 0.4 dB, 0.9 dB and 0.92 dB respectively at rate of 1/2. Finally, Fig. 3.12 plots bit error rate (BER) as function of E_s/N_0 for different optimized GIRA profiles in Tab. 3.1. We used 16000 information bits with 200 CPM-GIRA turbo iterations. The liftng of H is done randomly. As expected, the IRA code presents a small gain in the threshold region in comparison to the GIRA code corresponding to the generator polynomial $G_2(D)$. For the LDGM code only, we constrain $d_{v,min} \geq 2$ (This constraint has only a minor impact on the theoretical threshold, as depicted in Fig. 3.11a). The used profile, always

for the H_u part, is given by $\lambda_2 = 0.367, \lambda_{10} = 0.633, d_{c,max} = 4$. No floors have been observed in the simulations in Fig. 3.12. Recall that the EXIT curves of the CPM reach the point $(1, 1)$ and that the introduced proportion of degree-1 variable nodes was subject to the stability condition developed in chapter 2.

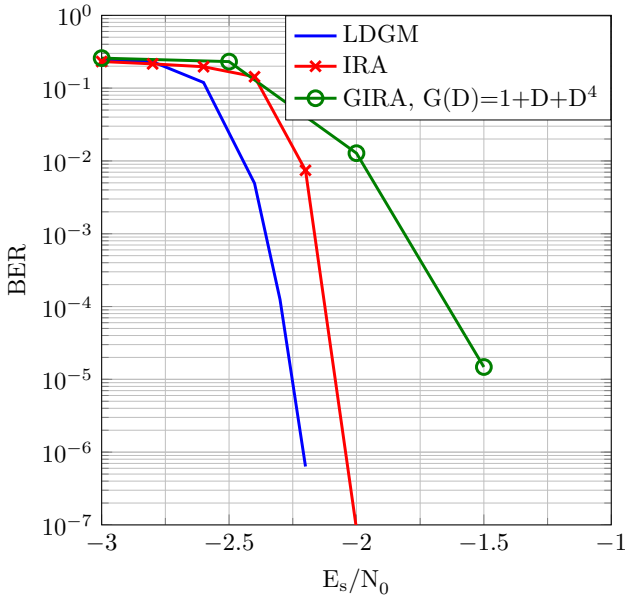

Figure 3.12: Obtained BER of GIRA codes with GMSK

3.3 Protograph-based LDPC codes

In this section, we propose a method to design protograph-based LDPC coded CPMs. This class benefits from a compact representation (copy-and-permute generation), an easy performance analysis (same performance as the underlying small protograph) and an efficient implementation (the decoding can be easily parallalized). The presented design approach can be directly extended to any CPM class, or generally to any trellis coded modulation. As it well be seen, the optimized protographs for the AWGN channel [LC07, DJDT05] do not exhibit necessarily good performance when concatenated with the CPM.

3.3.1 System description and notations

Consider a protograph based LDPC codes [Tho03]. A Protograph is a small Tanner graph described by a base matrix H where the element $H(q,r)$ is the number of edges between the VN r and the CN q. The corresponding LDPC code can be obtained by the so-called "Copy-and-permutation" operation. It consists of making a certain number of copies of the protograph and connecting them by permuting between the endpoints of the edge copies. Figure 3.13 depicts the protograph (left) and the protograph LDPC code (right) associated with the following base matrix:

$$H = \begin{pmatrix} 2 & 1 & 1 \\ 1 & 1 & 1 \end{pmatrix} \tag{3.12}$$

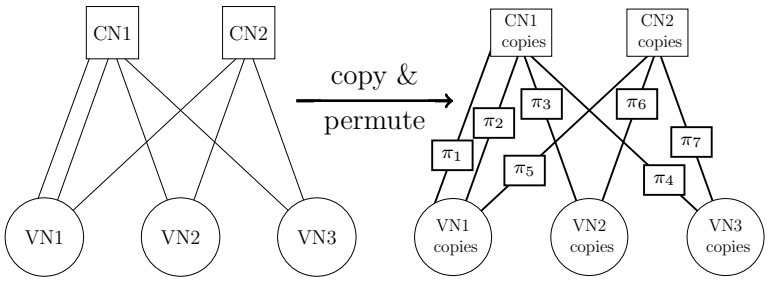

Figure 3.13: The 'factorized' protograph code generated by "copy-and-permute" operations. Each interleaver $\pi_i|_{1\leq i\leq 7}$ permutes the bundle of replicas of each edge.

The receiver factor graph of the CPM+protograph base LDPC code is depicted in Fig. 3.14.

Unlike LDPC codes, parallel edges are allowed. For this class of codes, EXIT charts cannot predict accurately the threshold. Instead, we use the protograph or multidimensional EXIT chart

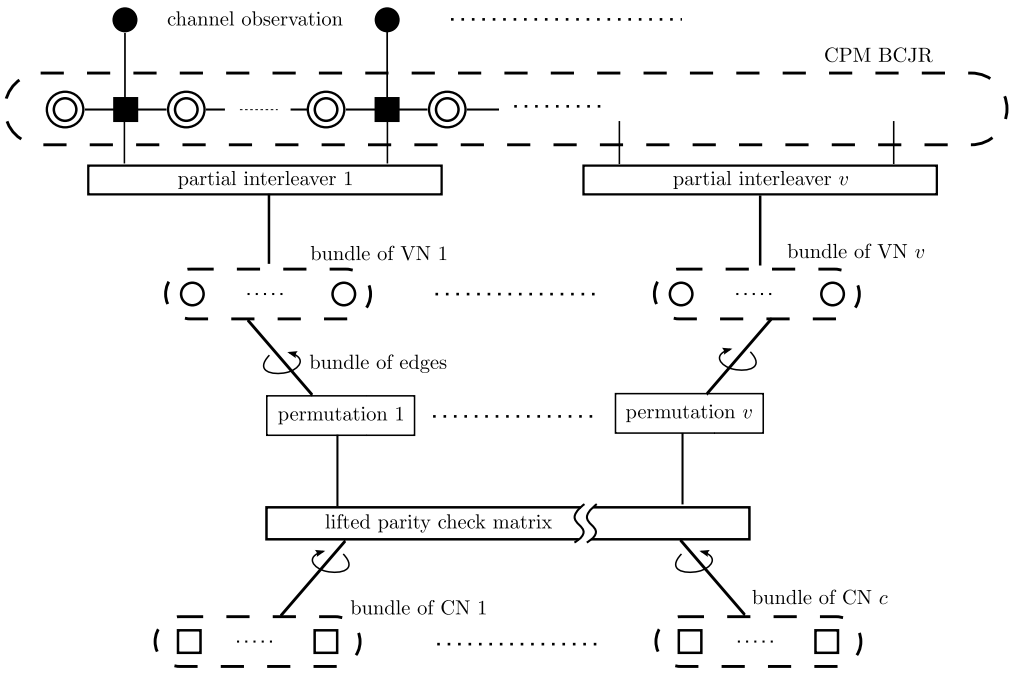

Figure 3.14: Factor graph of the receiver.

approach (denoted PEXIT) developed in [LC07]. This extension of the usual EXIT charts turns to be necessary to evaluate the asymptotic threshold of protographs because of their heigh structure: unlike unstructured LDPC codes, the averaging of the mutual information among the same degree VNs to CNs is not justified here because they do not "see" a mixture of all CNs extrinsic MI, but instead, each VN (in the lifted graph) always "sees" a mixture of the same CNs types depending on the graph connectivity described by H. Moreover, this new approach allows to take into account some critical node and edge types such as parallel edges, degree-1 VNs and punctured VNs. The factor graph of the protograph+CPM receiver is depicted in Fig. 3.15. For ease of notations, we use hereafter the following notations relative the the ℓ^{th} itaration:

- $I_{E,v}^{\ell}(q,r)$: the extrinsic MI between the code bits associated with the VN r and the LLRs sent from this VN to the CN q.
- $I_{E,c}^{\ell}(q,r)$: the extrinsic MI corresponding to the CN q and the LLRs sent from this CN to the VN r.
- $I_{APP}^{\ell}(r)$: *a posteriori* MI of a the VN r

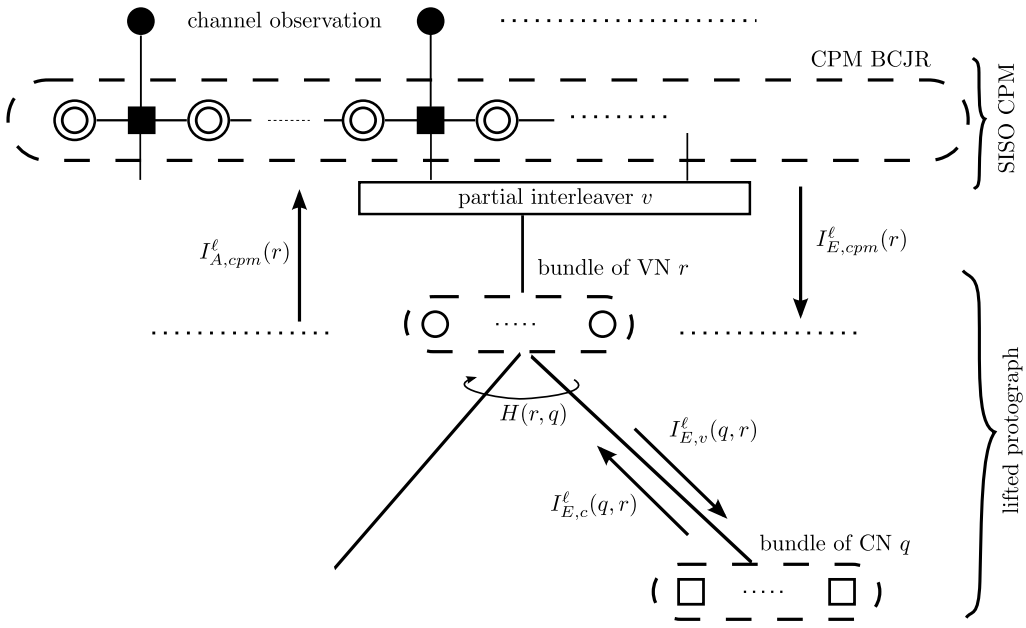

Figure 3.15: Factor graph of the CPM and protograph based LDPC code receiver.

- $I^{\ell}_{A,cpm}(r)$ and $I_{E,cpm}(r)$: *a priori* and extrinsic MI at the input (resp. output) BCJR demodulator relative to the VN r.

From the VN r (resp. the CN q) perspective, $I^{\ell}_{E,c}(q,r)$ (resp. $I^{\ell}_{E,v}(q,r)$) is nothing but the *a priori* knowledge got from the CN q (resp. the VN r).

Once the different PEXIT equations have been obtained, we track the evolution of the MI for a given SNR. The threshold is always defined as the lowest value of E_s/N_0, that insures the probability of block error at the VN r fades to zeros (or equivalently $I_{APP}(r)$ converges to 1 $\forall r$). This is slightly different from the unstructured case where only the bit error rate is tracked.

3.3.2 PEXIT analysis of concatenated protographs with CPM

In the following, we study the the PEXIT chart analysis of our concatenated scheme and we propose our optimization procedure. First we derive all EXIT evolution equations according to the PEXIT analysis and track the evolution of the MI during iterations. A decoding is said successful if the *a posteriori* MI (or error probability) of each VN converges to 1 (respectively to 0).

Optimizing a protograph-based LDPC code for a CPM scheme consists in finding the best protomatrix H in terms of iterative decoding threshold, given a fixed protograph size and code rate. In

other words, given the EXIT chart evolution equations, one tries to solve a non-linear integer programming problem where the unknown variables are the entries of H. This leads to very prohibitive computations and is infeasible for relatively large protographs. To alleviate this computational complexity, we will use some heuristics inspired from the unstructured LDPC code optimized profiles (see chapter 2), in order to design the general structure of the base matrix and thus reduce the dimensionality of the search space. Once a good protograph is obtained, the lifting is done carefully with respect to random circulant permutations coupled with the PEG algorithm [HEA01] and the ACE metric [JK05].

Following the analysis in chapter 2, we will also use partial interleavers between the VNs of the lifted LDPC code and the CPM. These partial interleavers are not meant to linearise the optimization equations as for the unstructured LDPC codes, but rather respect the averaging of decoding behaviour of variable nodes of the same type implicitly induced by the PEXIT analysis. Consequently, we have one partial interleaver per bundle of VN (instead of per VN degree) as depicted in Fig. 3.15.

The proposed approach is in spirit equivalent to [Liv06] and [NND12] and can be seen as their generalization:

- The first difference is that we consider here a turbo iterative decoding with any detector.

- At the difference of [NND12], we are interested here in finding the best protograph given a fixed rate and not the best trade-off between threshold and rate-compatibility. Furthermore, in our case, the definition of the search space is guided by the results of the unstructured LDPC codes optimization : *i.e.* we try to design protograph-based LDPC codes that belong to the unstructured LDPC family described by the optimized profiles.

3.3.2.1 EXIT Transfer curve of the CPM demodulator

As in section 3.2.2, the EXIT transfer characteristic of CPM detector seen by the VN r is formally given by:

$$I^{\ell}_{E,cpm}(r) = T(I^{\ell-1}_{A,cpm}(r), E_s/N_0) \tag{3.13}$$

3.3.2.2 EXIT Transfer Function of the Protograph

If $H(q,r) \neq 0$, the VN to CN update equation $\forall (q,r) \in \{1,...,M\} \times \{1,...,N\}$, is given by:

$$I_{E,v}^{\ell}(q,r) = J\left(\sqrt{\sum_{s\neq q} H(s,r)\left[J^{-1}(I_{E,c}^{\ell-1}(s,r)\right]^2 + (H(q,r)-1)\left[J^{-1}(I_{E,c}^{\ell-1}(q,r)\right]^2 + \left[J^{-1}(I_{E,cpm}^{\ell}(r)\right]^2}\right) \tag{3.14}$$

Otherwise, $I_{E,v}^{\ell}(q,r) = 0$.

Always using the reciprocal channel approximation, CN to VN update is given by:

$$I_{E,c}^{\ell}(q,r) = 1 - J\left(\sqrt{\sum_{s\neq r} H(q,s)\left[J^{-1}(1-I_{A,c}^{\ell}(q,s)\right]^2 + (H(q,r)-1)\left[J^{-1}(1-I_{A,c}^{\ell}(q,r)\right]^2}\right) \tag{3.15}$$

If $H(q,r) = 0$, then $I_{E,c}^{\ell}(q,r) = 0$.

Seen as an *a priori* of the SISO CPM component, the MI sent from a VN r to the CPM demodulator is:

$$I_{A,cpm}^{\ell}(r) = J\left(\sqrt{\sum_{s} H(s,r)\left[J^{-1}(I_{A,v}^{\ell}(s,r))\right]^2}\right) \tag{3.16}$$

Combining Eqs. (3.13),(3.14),(3.15) and (3.16). At the end of each iteration, the a posteriori MI can be evaluated for $r = 1...N$ by:

$$I_{APP}^{\ell}(r) = J\left(\sqrt{\sum_{s} H(s,r)\left[J^{-1}(I_{A,v}^{\ell}(s,r))\right]^2 + \left[J^{-1}(I_{E,cpm}^{\ell}(r))\right]^2}\right) \tag{3.17}$$

Consequently, one can compute the threshold of a particular protograph by conducting a simple binary search algorithm.

Note that Eq. (3.16) is different from [VNND12] where the computation of the MI corresponding to the LLR message sent from the VNs to the CPM is averaged over all VNs, which actually induces a global interleaver between the CPM and the LDPC code. In our case, and in order to write Eq. (3.16), we suppose partial interleaver per protograph VN r, $\forall r$, and not per VN degree as in the previous section.

3.3.2.3 Optimization

It was shown in [VNND11, VNND12] that the optimized protographs for the AWGN channel (ARJA codes [DJDT05]) do not necessarily perform well in partial response and inter-symbol interference

channels. Consequently, new protograph-based LDPC codes should be designed for these contexts independently.

Authors in [RSU01] mentioned that including a controlled proportion of degree-2 VNs improves the decoding threshold of based LDPC codes. In order to preserve the minimum distance when adding degree-2 VNs, Divsalar *et al* proposed a check splitting procedure [DDJA09]. In [ADY07], authors show that a careful insertion of degree-1 nodes can improve the iterative decoding threshold of protograph-based LDPC codes. In the context of protographs, this construction is referred as *precoding*: it consists of placing a CN between a degree-1 VN and a higher-degree VNs, which is then optionally punctured [DDJA09]. Besides that, the introduction of degree-1 variable nodes in our context is corroborated by the fact that the EXIT curves of CPM schemes always join the point $(1, 1)$ (see chapter 2 for further details).

In this section, we optimize protographs for CPM with threshold in mind. We are not interested by the minimun distance for the moment (ARJA family do not perform well with CPM as we are going to see later). We are rather interested in proposing protograph structures that help controlling to code design, that can be easily encodable (quasi-cyclic LDPC codes) and highly parallelizable. Guided by the obtained profiles in our unstructured LDPC code optimization (chapter 2), the protographs search set can be described by a relatively small base matrix that follows a certain pattern and contain small proportion of degree-1, some degree-2 and high-degree VNs. Assuming this, combined with some simple heuristics drawn from our inspection process, we observed that good protographs can be found with good encoding properties if we consider, for example, base matrices of the form:

$$H = \begin{pmatrix} x_{1,1} & x_{1,2} & x_{1,3} & x_{1,4} & 1 & 1 & 0 & 0 \\ x_{2,1} & x_{2,2} & x_{2,3} & x_{2,4} & 0 & 1 & 1 & 0 \\ x_{3,1} & x_{3,2} & x_{3,3} & x_{3,4} & 0 & 0 & 1 & 1 \\ x_{4,1} & x_{4,2} & x_{4,3} & x_{4,4} & 0 & 0 & 0 & 1 \end{pmatrix} \tag{3.18}$$

where the entries $x_{i,j}$ is a natural number $\forall (i, j) \in \{1, 2, 3, 4\}^2$. For small protographs like Eq. 3.18, we can enumerate all possible protographs within the search space and choose the one with the lower threshold. We can also add some heuristics based on the observed optimized unstructured profiles leading to protographs of the form:

$$H = \begin{pmatrix} x_{1,1} & x_{1,2} & 0 & 0 & 1 & 1 & 0 & 0 \\ x_{2,1} & x_{2,2} & 0 & 1 & 0 & 1 & 1 & 0 \\ x_{3,1} & x_{3,2} & 1 & 0 & 0 & 0 & 1 & 1 \\ x_{4,1} & x_{4,2} & 0 & 0 & 0 & 0 & 0 & 1 \end{pmatrix}$$

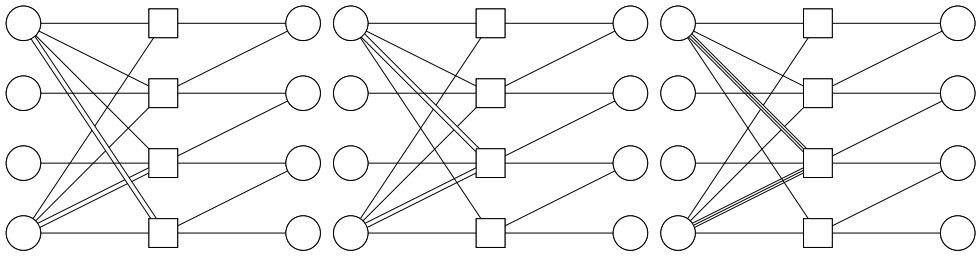

(a) Binary GSMK (b) Quateranary 2RC (c) Octal 2REC

Figure 3.16: Obtained protographs for different CPM systems.

	AR3A	AR4JA	protograph threshold	unstructured LDPC threshold	$(E_s/N_0)^*$
binary GMSK	-0.45	-0.20	-2.11	-2.7	-2.76
quaternary 2RC	3.36	3.68	1.36	0.7	0.62
Ocatl 3RC	7.29	7.92	3.79	2.256	2.25

Table 3.2: Optimized asymptotic thresholds E_s/N_0 for protograph and unstructured LDPC codes with design $R = 1/2$

However, for larger protograph, we perform a differential evolution optimization [SS05, SP97].

3.3.3 Simulation Results

This section gives simulation results for the binary GMSK, the quaternary 2RC (M=4, gray mapping, L=2, h=1/4, raised cosine) and the octal 2REC (M=8, gray mapping, L=2, h=1/4, rectangular). The targeted protograph rate is $R = 1/2$. Simulations were performed using a maximum of 250 turbo iterations. In order to limit the size of the protograph ensemble, $x_{q,r}$ in Eq. (3.18) are limited to $\{1, 2, 3\}$, $\forall(q, r) \in \{1, ..., 4\}^2$. Table 3.2 summarizes the achieved thresholds of the protographs depicted in Fig. 3.16. Thresholds of rate-1/2 AR3A and AR4JA from [LC07] are shown for comparison. We can observe that it is possible to operate close to the theoretical CPM threshold $(E_s/N_0)^*$, with an average gain which is $1.5-4$ dB better than the AWGN protographs and only a small degradation in comparison to the designed unstructured LDPC codes.

Figure 3.17 shows the bit error rate (BER), the frame error rate (FER) and the predicted error probability (PEP) (respectively marked dotted curves, marked dashed curves and marked solid

curves). The Asymptotic PEP is evaluated as the following [Liv06]: after the ℓ^{th} iteration, the expected bit error probability associated with a VN r is related to the a posteriori MI $I_{APP}(r)$ in Eq. (3.17) as:

$$P_b(r) = \frac{1}{2} erfc\left(\frac{J^{-1}(I_{APP}(r))}{2\sqrt{2}}\right) \tag{3.19}$$

For protograph-based LDPC codes of size 5000 and 4000 information bits, the simulated threshold matches the theoretical ones. The poor performance of the ARJA and AR4JA corroborates the observations in [VNND12, VNND11]. For the small size code (1500 information bits), we notice the apparition of an error floor at FER=10^{-3} (BER=2.10^{-6}). Closer investigations showed that only few bits are incorrect. In order to lower this error floor while maintaining a good threshold, one can simply consider a Bose-Chaudhuri-Hocquenghem (BCH) code [Hoc59, BRC60] as proposed in [GiAND09] for serially concatenated schemes of the CPM with convolutional codes. On the other hand, to improve the decoding threshold, one can consider the optimization of bigger protograph than the one described by Eq. (3.18). Further investigations are required to characterize the weight enumerator properties of such codes.

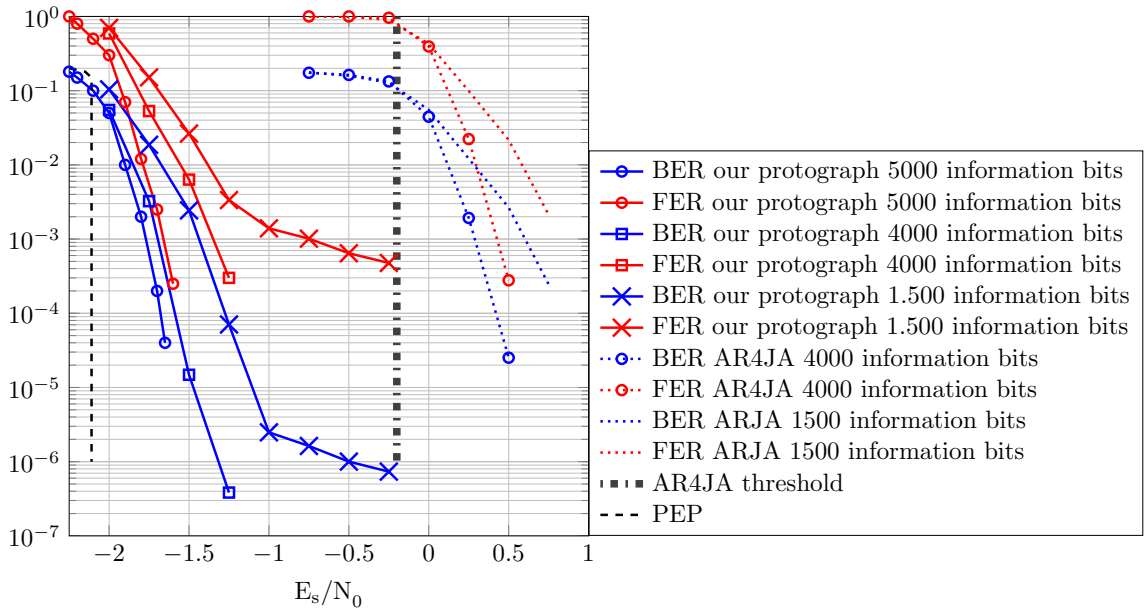

Figure 3.17: BER and FER of optimized protographs for GMSK.

3.4 Spatially coupled LDPC codes

3.4.1 System Description

We now consider a concatenated scheme composed of a binary LDPC convolutional code serially concatenated with a CPM modulator.

A binary LDPC convolutional (LDPC-C) code can be described as the ensemble of codewords $\boldsymbol{c}_{[\mathbf{0},\infty]} = \{c_0, c_1, ..., c_t, ...\}$, $c_t \in GF(2)$, that satisfy the equation $\boldsymbol{c}_{[\mathbf{0},\infty]}\boldsymbol{B}^T_{[0,\infty]} = \mathbf{0}$. Given a protograph base matrixe $\boldsymbol{B}$, the spatial coupling can then be obtained as the following [MLCJ14]: the graph is replicated an infinite number of times, then each VNs bundle is connected to its pairing CNs bundle through a permutation of the corresponding edges bundle only in the forward direction, *i.e.* from the protograph at time t to the protographs at time $t' > t$. These connections are described by the components base matrices $\{\boldsymbol{B}_i\}_i$ which must satisfy:

$$\sum_{i=0}^{m_s} \boldsymbol{B}_i = \boldsymbol{B}$$

Then, $\boldsymbol{B}^T_{[0,\infty]}$ has the form:

$$\boldsymbol{B}^T_{[0,\infty]} = \begin{bmatrix} \boldsymbol{B}^T_0(0) & \cdots & \boldsymbol{B}^T_{m_s}(m_s) & & & \\ & \ddots & & \ddots & & \\ & & \boldsymbol{B}^T_0(t) & \cdots & \boldsymbol{B}^T_{m_s}(t+m_s) & \\ & & & \ddots & & \ddots \end{bmatrix}$$

$\boldsymbol{B}^T_{[0,\infty]}$ is called the syndrome former of the code, $\{\boldsymbol{B}_i(t)\}_i$ the component matrices, m_s the syndrome former memory and $v_s = (m_s + 1)$ the constraint length. A more detailed definition can be found in [JFZ99].

$\boldsymbol{B}_{[0,\infty]}$ can be seen as a *protograph* (V, C, E) where the set of variable nodes V (of cardinality v) is connected to the set of check nodes C (of cardinality c) through edges E. In this class of LDPC-C codes, the design rate of the base matrix can be written as $R = 1 - c/v$. Figure 3.18 illustrates an example of a spatially coupled $(3, 6)$-regular LDPC code with respect to $\boldsymbol{B_0} = \boldsymbol{B_1} = \boldsymbol{B_2} = [1 \quad 1]$.

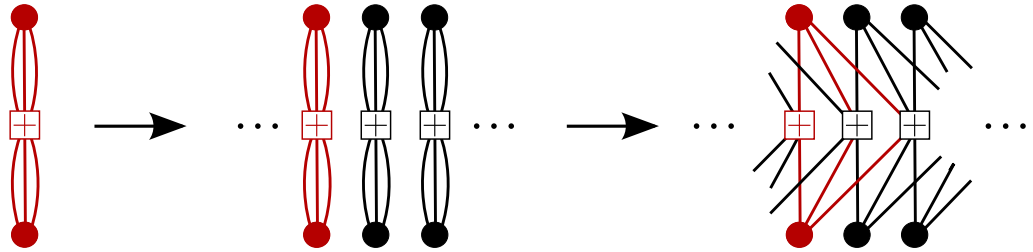

Figure 3.18: (3, 6) regular LDPC convolutional code with $m_s = 2$: firstly, the protograph is replicated, then it is spatially coupled with respect to $\boldsymbol{B_0} = \boldsymbol{B_1} = \boldsymbol{B_2} = [1 \quad 1]$

The corresponding syndrome former code is given by:

$$\boldsymbol{B}_{[0,\infty]} = \begin{bmatrix} 1 & 1 & 0 & 0 & 0 & 0 & 0 & 0 & \\ 1 & 1 & 1 & 1 & 0 & 0 & 0 & 0 & \\ 1 & 1 & 1 & 1 & 1 & 1 & 0 & 0 & \\ 0 & 0 & 1 & 1 & 1 & 1 & 1 & 1 & \cdots \\ 0 & 0 & 0 & 0 & 1 & 1 & 1 & 1 & \\ 0 & 0 & 0 & 0 & 0 & 0 & 1 & 1 & \\ & & & & \vdots & & & & \ddots \end{bmatrix}$$

In this chapter, we will consider mainly terminated time invariant LDPC convolutional codes [MLC11]. They can be described by mean of convolutional protograph with the base matrix $\boldsymbol{B}_{[0,L-1]}$ of size $(L + m_s)c \times Lv$. In this case, L is called the termination factor or the coupling length.

$$\boldsymbol{B}^T_{[0,L-1]} = \begin{bmatrix} \boldsymbol{B}^T_0 & \cdots & \boldsymbol{B}^T_{m_s} & & \\ & \ddots & & \ddots & \\ & & \boldsymbol{B}^T_0 & \cdots & \boldsymbol{B}^T_{m_s} \end{bmatrix} \tag{3.20}$$

The design rate of terminated LDPC-C codes without puncturing becomes:

$$R_L = 1 - \frac{(L + m_s)}{L}(1 - R) = R - \frac{m_s}{L}(1 - R) \tag{3.21}$$

One should observe that the termination as shown in Eq. (3.20) results in a rate loss by a penalty of $\frac{m_s}{L}(1 - R)$ as depicted by Eq. (3.21). Note that, as L increases, R_L increases and approaches the design rate R, and the singularity in the code profile introduced by the firsts and lasts check nodes (less connected) becomes minor. At the decoder side, we consider BP decoding algorithm [RU01].

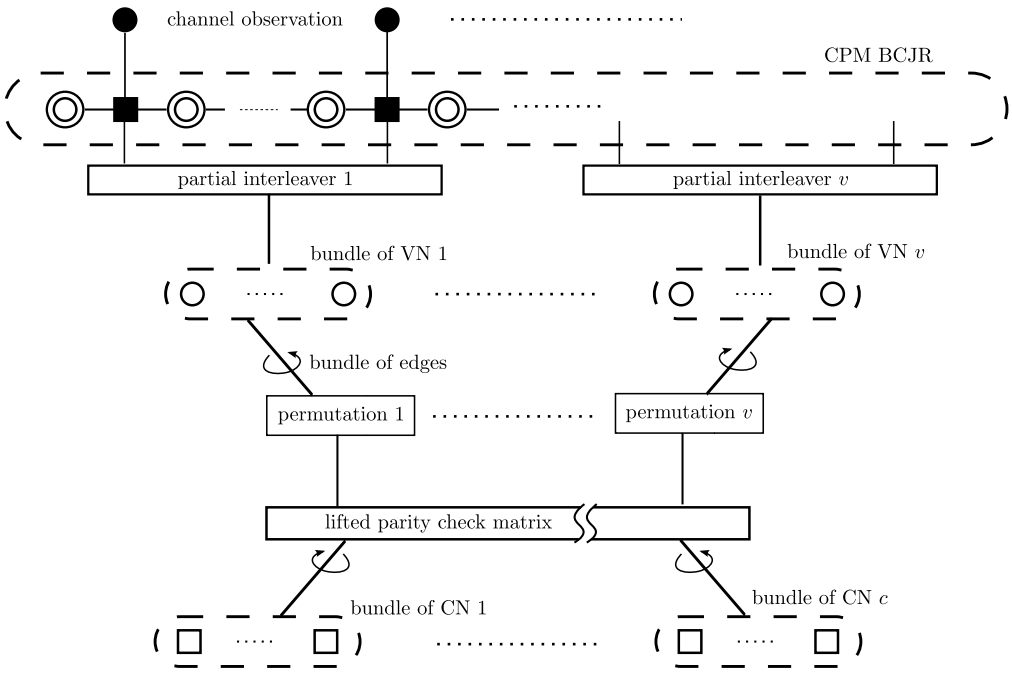

Figure 3.19: Factor graph of the receiver.

Each codeword $\boldsymbol{c}_{[\boldsymbol{0},\boldsymbol{L-1}]}$ is interleaved, mapped into M-ary symbols $\boldsymbol{\alpha} = \{\alpha_i\}_i$, where $\alpha_i \in \{\pm 1, ..., \pm(M-1)\}$, and encoded by the CPM modulator. The copy-and-permute operation (called also lifting) of the convolutional protograph is done by replacing each node with a bundle of node of the same type and replacing each edge with the bundle of a permutation of edges of the same type. The receiver factor graph is depicted in Fig. 3.19.

3.4.2 Asymptotic Convergence analysis

We consider the notations depicted in the receiver factor graph 3.20. As for protographs, let us consider hereafter the following notations relative to the ℓ^{th} iteration:

- $I_v^\ell(q,r)$: extrinsic mutual information (eMI) between the code bits associated with VN r and the LLRs sent from this VN to the CN q.
- $I_c^\ell(q,r)$: eMI associated with messages sent from CN q to VN r.
- $I_{app}^\ell(r)$: *a posteriori* MI associated with the VN r.
- $I_{a,CPM}^\ell(r)$: *a priori* MI associated with messages sent from the VN r to the CPM soft decoder.

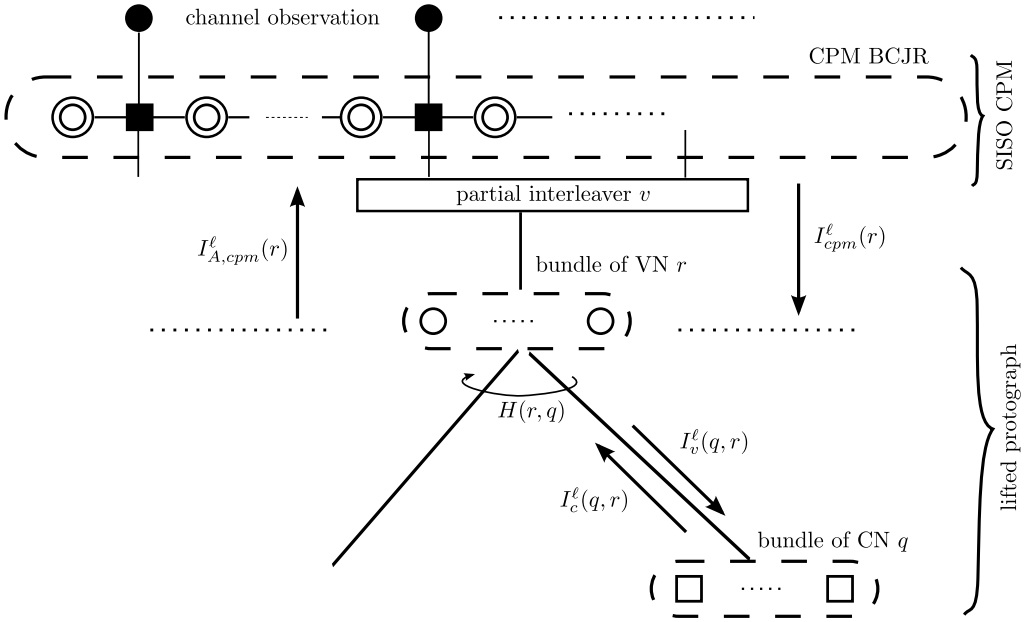

Figure 3.20: Factor graph of the CPM and protograph based LDPC code receiver.

- $I^{\ell}_{CPM}(r)$: eMI associated with messages sent from CPM soft decoder to the VN r.
- $T(.,E_s/N_0)$: input-output EXIT transfer function of the CPM detector implicitly depending the noise variance σ^2_{noise}. Analytic expression is not straightforward, but it can be evaluated with Monte Carlo simulations.

Let us consider a mother protograph $\boldsymbol{B}$, of size $c \times v$, which generates the terminated LDPC-C code $\boldsymbol{B_{[0,L-1]}}$ of size $Lv \times (L+m_s)c$, noted hereafter $\boldsymbol{B_L}$ for ease of notations. The CPM update equations at iteration ℓ seen by the variable node r are given by:

$$I^{\ell}_{CPM}(r) = T(I^{\ell-1}_{a,CPM}(r), E_s/N_0) \tag{3.22}$$

$$I^{\ell}_{a,CPM}(r) = J\left(\sqrt{\sum_s B_L(s,r)\left[J^{-1}(I^{\ell-1}_{v}(s,r))\right]^2}\right) \tag{3.23}$$

When $B_L(q,r) \neq 0$, the VN r to CN q update equation is formally given by:

$$I^{\ell}_{v}(q,r) = J\left(\sqrt{\sum_s B_L(s,r)\left[J^{-1}(I^{\ell-1}_{c}(s,r))\right]^2 - \left[J^{-1}(I^{\ell-1}_{c}(q,r))\right]^2 + \left[J^{-1}(I^{\ell}_{CPM}(r))\right]^2}\right) \tag{3.24}$$

otherwise, $I_v^\ell(q,r) = 0$. Similarly, using reciprocal channel approximation, CN q to VN r update is given by:

$$I_c^\ell(q,r) = 1 - J\left(\sqrt{\sum_s B_L(q,s)\left[J^{-1}(1-I_v^\ell(q,s))\right]^2 - \left[J^{-1}(1-I_v^\ell(q,r))\right]^2}\right) \tag{3.25}$$

otherwise, $I_c^\ell(q,r) = 0$.

Considering partial interleavers [BPB+14b], at the end of each iteration, the *a posteriori* MI evaluated at the VN r is:

$$I_{app}^\ell(r) = J\left(\sqrt{\sum_s B_L(s,r)\left[J^{-1}(I_c^{\ell-1}(s,r))\right]^2 + \left[J^{-1}(I_{CPM}^\ell(r))\right]^2}\right) \tag{3.26}$$

Combining Eqs. (3.26),(3.25),(3.24),(3.22) and (3.23), we can track the evolution of I_{app}^ℓ for each VN through iterations. The threshold is defined as the smallest E_b/N_0 such that for all r, $I_{app}^\ell(r) = 1$ after a certain number of iterations ℓ. This analysis is similar to the analysis of protograph based codes in section 3.3.

3.4.3 Code design

We are interested here by finite length block codes, *i.e.* the LDPC-C codes with finite L. We now try to design efficient LDPC convolutional codes for the CPM detector. We conduct a two step optimization technique: after finding a good protograph using the method in the section 3.3, we optimize the coupling to obtain very good thresholds.

3.4.3.1 Classical methods for protograph construction

As for convolutional codes, there are two main methods to terminate LDPC-C codes:

Termination (T): in each input bits sequence, some bits (not necessarily zeros) is appended at the end to enforce the encoder to terminate to the all-zero state. Without puncturing, these bits results in a rate loss as showed by the Eq. (3.21). When the LDPC-C code in interpreted from its base matrix B_L, T termination is equivalent to truncating all VNs of $\boldsymbol{B}_{[0,\infty]}$ after the L^{th} copy as in Fig. 3.18, and keeps only the CNs that are connected up to the L^{th} stage of VNs. Figure 3.21 shows an example of the corresponding Tanner graph.

Tail-bitting (TB): In order to avoid the rate loss, a tail-biting method has been introduced [MLC13]. The idea behind tail-bitting is using the last bits of a data block to initialize the encoder

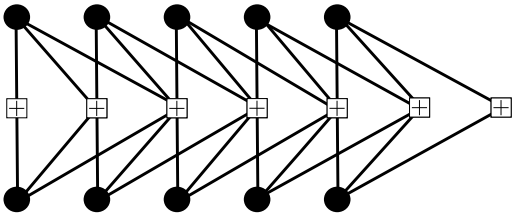

Figure 3.21: (3, 6) regular LDPC convolutional code with $m_s = 2$, $L = 5$ and $\boldsymbol{B_0} = \boldsymbol{B_1} = \boldsymbol{B_2} = [1 \quad 1]$ with normal termination T

(cyclic encoding property). Consequently, at the end of encoding the data block, the encoder is forced to end in the same initialized state. The corresponding parity check matrix $\boldsymbol{B}_L^{tb}$ can be found in [LMFC10]. Because the most right-hand and left-hand CNs are no more 'irregular', there is no coupling gain with this familly and the threshold will remain the same as for the underlying protograph $\boldsymbol{B}$. However, since the CNs and VNs profiles remain unchanged in comparison to the mother protograph, TB LDPC-C codes are used generally to obtain some bounds (free distance, trapping set, ...) of the T termination LDPC-C codes [MLC13]. Figure 3.22 shows an example of the corresponding Tanner graph.

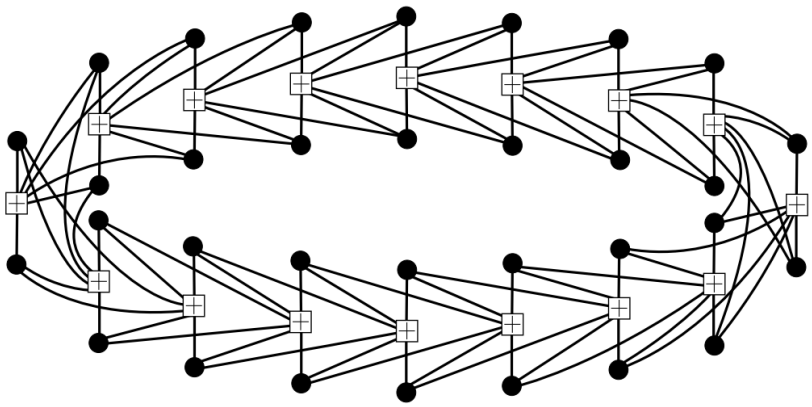

Figure 3.22: (3, 6) regular LDPC convolutional code with $m_s = 2$, $L = 16$ and $\boldsymbol{B_0} = \boldsymbol{B_1} = \boldsymbol{B_2} = [1 \quad 1]$ with normal termination TB (the figure was taken from [MLCJ14])

As already pointed out, the iterative decoding threshold improvement gained with LDPC-C codes in comparison to the unstructured LDPC codes is due the *wave effect* induced by the boundaries check

nodes (less connected check nodes). This phenomenon is depicted in Fig. 3.23a: the less connected check nodes generated more reliable LLRs, which, as iterations go along, gradually propagates from both sides to the internal nodes. For the middle VNs, as far as the wave effect did not affect them yet, they behave roughly the same way as their counterparts VNs in $\boldsymbol{B}$. If E_b/N_0 is larger than the threshold of $\boldsymbol{B}_L$ (which is lower than the threshold of $\boldsymbol{B}$), the decoding wave is strong enough to make them converge as depicted in Fig. 3.23b. As mentioned before, the advantage of TB termination is to insure the same rate as $\boldsymbol{B}$. However, since the edges CNs are no more irregular, properties of $\boldsymbol{B}$ are conserved (same rate and threshold) as depicted in Fig. 3.23c.

3.4.3.2 A new method: direct truncation

In this section, we introduce a new protograph based LDPC-C code termination that we believe is interesting for some concatenated schemes. Similarly to convolutional codes [MW86], one can suggest to consider a direct truncation (DT) for the LDPC-C code. It is constructed like tailbitting LDPC-C, but instead of adding $m_s c$ CNs at the right-hand end to satisfy L^{th} set of VNs connections, we remove all unconnected edges. The main advantage is that the rate R does not depend on L, the threshold is now fixed and independent of L. Consequently, taking small L is satisfactory. Figure 3.24 shows an example of the corresponding Tanner graph.

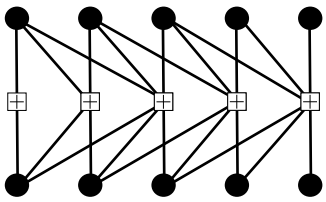

Figure 3.24: (3, 6) regular LDPC convolutional code with $m_s = 2$, $L = 5$ and $\boldsymbol{B_0} = \boldsymbol{B_1} = \boldsymbol{B_2} = [1 \quad 1]$ with normal termination DT

The parity check matrix is written as:

$$\boldsymbol{B}_L^{DT} = \begin{bmatrix} \boldsymbol{B}_0 & & & \\ \vdots & \boldsymbol{B}_0 & & \\ \boldsymbol{B}_{m_s} & \vdots & \ddots & \\ & \boldsymbol{B}_{m_s} & \dots & \boldsymbol{B}_0 \end{bmatrix} \tag{3.27}$$

It is obvious that the left-hand nodes configuration did not change, compared to B_L, which

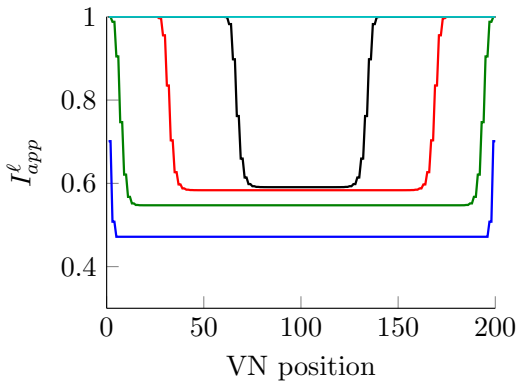

(a) T, R=0.49, E_b/N_0=3.1dB, iterations {1, 5, 20, 60, 63}

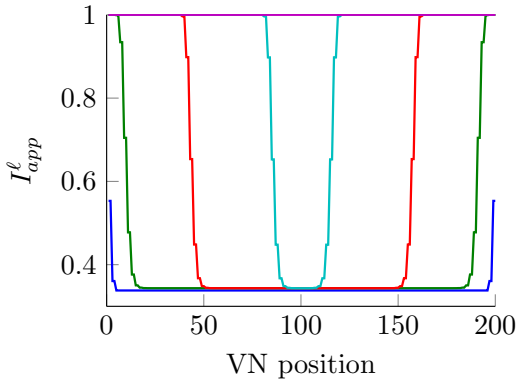

(b) T, R=0.49, E_b/N_0=1.1dB, iterations {1, 20, 100, 200, 235}

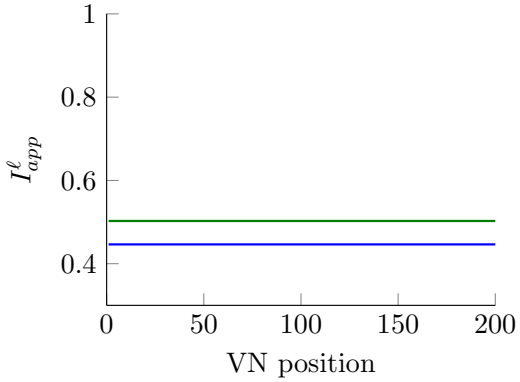

(c) TB, R=0.5, E_b/N_0=2.1dB, iterations {1, 1000}

Figure 3.23: Evolution of I^{ℓ}_{app} per variable nodes of the LDPC-C depicted in Fig. 3.18 concatenated with GMSK, $L = 100$. threshold of B is 2.22dB

means that the convolutional gain induced by these nodes is preserved. On the contrary, among the most right-hand nodes, a small proportion of poorly connected VNs is introduced while the previous low connected CNs disappears. The drawback of these VNs is that they will converge slowly in comparison to their counterparts in $\boldsymbol{B}_L$: in other words, the corresponding bits have less error protection in comparison to other bits. However, an advantage of this termination is that since we do not terminate the code anymore, the encoding operation is new simplified. In order to design good direct truncated spatially coupled protographs, different optimization trials leads to the following conclusions:

- The syndrome former memory m_s should not be very large, it should not exceed 3, otherwise, the degrees of the most-right VNs of $\boldsymbol{B}_L^{DT}$ in Eq. (3.27) will too low.
- The first component matrix $\boldsymbol{B}_0$ should contain more edges than the others, otherwise, the threshold of the most-right protograph corresponding to $\boldsymbol{B}_0$ is going to be very high (very low VN degrees).
- The convolution gain corresponding of the most-left part of $\boldsymbol{B}_L^{DT}$ must be strong enough to make the most-right VNs converge. To this end, the most-left CNs of $\boldsymbol{B}_L^{DT}$ should not be highly connected. A trade-off is to be made between this criterion and the previous rule
- All-zero columns in $\boldsymbol{B}_0$ are to be avoided. All-zero rows are allowed.
- The CNs of the protograph corresponding to $\boldsymbol{B}_0$ should be as much as possible connected to high degree VNs of the previous sections
- Two degree-1 variable nodes should not be connected to the same CN especially in the protograph corresponding to $\boldsymbol{B}_0$

Besides that, one would say that having at least one $degree - 1$ VNs among the last v VNs may affect the convergence. Actually, by choosing a good coupling component matrices, not only the proportion of these tedious VNs vanishes with increasing L, but also their effect is surprisingly alleviated by both the coupling gain and the fact that, unlike other modulations, usual CPM schemes have EXIT curves that converge to the point $(1, 1)$ [BPB+14a].

For small protogaphs $\boldsymbol{B}$ and small syndrome former memory m_s, the optimization of the coupling can be done by performing an exhaustive search. For larger search space, a genetic algorithm, guided with the aforementioned guidelines, can be applied [GH88].

3.4.4 Simulation results

As an example, we consider the following codes:

- $C^{(1)}$: $(3, 6)$ – *regular* protograph
- $C^{(2)}$: optimized protograph in Fig. 3.16a
- $C^{(1)}_{1,T}$: coupling of $C^{(1)}$ with m_s=1
  $\boldsymbol{B_0^{(1)}} = [1\ 2]$ and $\boldsymbol{B_1^{(1)}} = [2\ 1]$
- $C^{(1)}_{1,DT}$: direct truncation of $C^{(1)}_{1,T}$
- $C^{(1)}_{2,T}$: coupling of $C^{(1)}$ with m_s=2
  $\boldsymbol{B_0^{(2)}} = \boldsymbol{B_1^{(2)}} = \boldsymbol{B_2^{(2)}} = [1\ 1]$
- $C^{(1)}_{2,DT}$: direct truncation of $C^{(1)}_{2,T}$
- $C^{(2)}_{1,T}$: coupling of $C^{(2)}$ with m_s=1 and:

$$\boldsymbol{B_0} = \begin{bmatrix} 1 & 1 & 0 & 0 & 1 & 1 & 0 & 0 \\ 0 & 1 & 0 & 0 & 0 & 0 & 1 & 0 \\ 1 & 1 & 1 & 0 & 0 & 0 & 0 & 1 \\ 0 & 0 & 0 & 0 & 0 & 0 & 0 & 0 \end{bmatrix}, \quad \boldsymbol{B_1} = \begin{bmatrix} 0 & 0 & 0 & 0 & 0 & 0 & 0 & 0 \\ 1 & 1 & 0 & 1 & 0 & 1 & 0 & 0 \\ 1 & 0 & 0 & 0 & 0 & 0 & 1 & 0 \\ 1 & 1 & 0 & 0 & 0 & 0 & 0 & 1 \end{bmatrix}$$

- $C^{(2)}_{2,T}$: coupling of $C^{(2)}$ with m_s=2 and:

$$\boldsymbol{B_0} = \begin{bmatrix} 0 & 1 & 0 & 0 & 0 & 1 & 0 & 0 \\ 0 & 1 & 0 & 0 & 0 & 0 & 0 & 0 \\ 0 & 0 & 1 & 0 & 0 & 0 & 0 & 0 \\ 1 & 0 & 0 & 0 & 0 & 0 & 0 & 0 \end{bmatrix}, \quad \boldsymbol{B_1} = \begin{bmatrix} 1 & 0 & 0 & 0 & 0 & 0 & 0 & 0 \\ 1 & 1 & 0 & 0 & 0 & 1 & 0 & 0 \\ 0 & 0 & 0 & 0 & 0 & 0 & 1 & 0 \\ 0 & 0 & 0 & 0 & 0 & 0 & 0 & 1 \end{bmatrix}$$

$$\boldsymbol{B_2} = \begin{bmatrix} 0 & 0 & 0 & 0 & 1 & 0 & 0 & 0 \\ 0 & 0 & 0 & 1 & 0 & 0 & 1 & 0 \\ 2 & 1 & 0 & 0 & 0 & 0 & 0 & 1 \\ 0 & 1 & 0 & 0 & 0 & 0 & 0 & 0 \end{bmatrix}$$

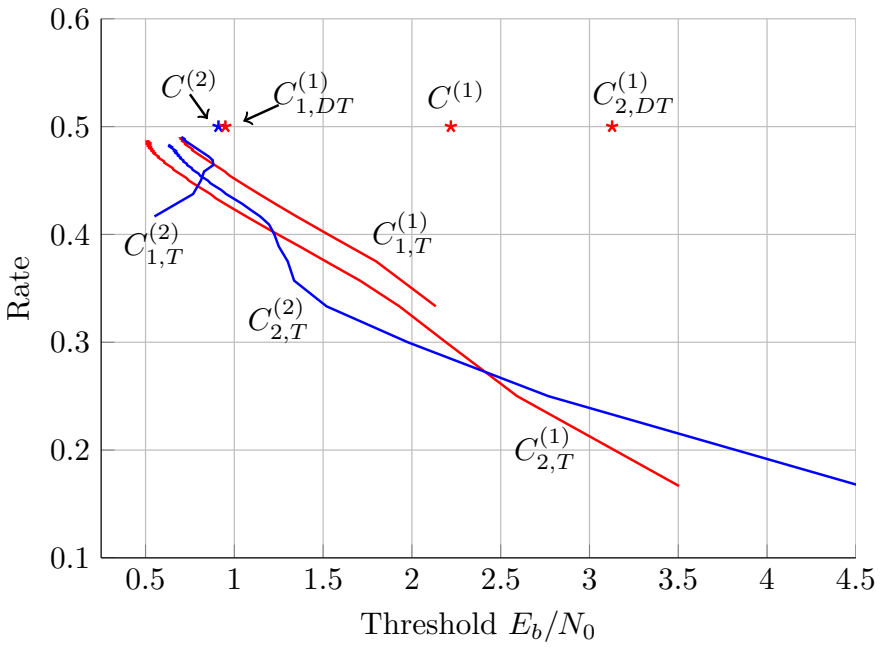

Figure 3.25: Thresholds comparison for different codes when GMSK

Figure 3.25 depicts the decoding thresholds for the above codes with GMSK modulation as a function of L. We observe that with increasing L, the design rate R_L for $C^{(1)}_{1,T}$, $C^{(1)}_{2,T}$, $C^{(2)}_{1,T}$ and $C^{(2)}_{2,T}$ converges to R. Notice that the coupling has significantly improved the thresholds of $C^{(1)}$ and $C^{(2)}$. Concerning our termination method, the spatial coupling of the $(3,6)-regular$ code with respect to $\{B^{(2)}_i\}$, *i.e.* $C^{(1)}_{2,DT}$, drastically decreases the threshold. On the contrary, the direct truncation of the spatial coupling following $\{B^{(1)}_i\}$, *i.e.* $C^{(1)}_{1,DT}$, the DT method allows us to obtain directly a code with rate R. These advantages come with a very small degradation of the threshold. If one want to design convolutional protograph that behave very good with both T and DT terminations, $C^{(1)}_{1,DT}$ is a very good candidate.

The VNs convergence for $C^{(1)}_{1,DT}$ and $C^{(1)}_{2,DT}$ are visualized in Fig. 3.26 at $E_s/N_0 = 1.5$dB. Seen for the first time, notice that the wave effect travels only from the left side to the right side, because of the less connected CNs present at the first rows. Recall that the $C^{(1)}$ threshold is only $E_b/N_0 = 2.2$dB (> 1.5dB), consequently, the middle VNs, which behave as the VNs of $C^{(1)}$, do not converge through iterations and wait for the wave gain. For $C^{(1)}_{1,DT}$ (resp. $C^{(1)}_{2,DT}$), on the most right hand VNs, we recognize, as expected, a small degradation because of the less connected VNs (corresponding to the

last columns of the parity check matrix) whose connections are fully determined only by $\boldsymbol{B}_{\mathbf{0}}^{(1)}$ (resp. $\boldsymbol{B}_{\mathbf{0}}^{(2)}$), $\forall L$. At the contrary of $C_{1,DT}^{(1)}$, the wave effect in $C_{2,DT}^{(1)}$ is not strong enough to make the last two $degree-1$ deficient VNs converge. A the other hand, even if the coupling of $C^{(1)}$ (through $\{\boldsymbol{B}_{\boldsymbol{i}}^{(1)}\}$) leads to a slightly worse performance than the coupling of $C^{(2)}$ (through $\{\boldsymbol{B}_{\boldsymbol{i}}^{(2)}\}$) for the classical termination (T) (0.2dB), it is best suited to our no-rateloss termination (DT) $C^{(3)}$ (which shows a degradation of the threshold of only 0.25dB).

For the protographs designed for the GMSK, the two proposed couplings, $C_{1,T}^{(2)}$ and $C_{2,T}^{(2)}$, show a gain of 0.2dB and 0.3dB respectively over $C^{(2)}$ (if we neglect the small rate loss at high values of L). Because $C^{(2)}$ is optimized for the GMSK, it already presents a good threshold and the spatially coupling operation did not show a large gain as when coupling spatially $C^{(1)}$. Furthermore, at high rates and at equal syndrome former memory m_s, the proposed LDPC-C codes corresponding to both $C^{(1)}$ and $C^{(2)}$ offer approximately the same performance, however, $C_{1,T}^{(2)}$ shows the best trade-off between the rate penalty (at most, when L is small, the gap to 1/2 is only of 0.18) and the threshold (varies between 0.55dB and 0.68dB) for the whole range of values of L. Small values of L, *i.e.* that lead to convolutional protographs with small size, are particularly interesting for finite length design. From this perspective, the performance of the proposed codes is depicted in Fig. 3.27: threshold is plotted as a function of the total number of VNs for different rate families. When we impose relatively strict constraints on the rate loss, the code which exhibits the best trade-off between threshold and protograph size, when the rateloss is of about 0.007, is $C_{2,T}^{(1)}$. On the other hand, when we tolerate a rateloss of 0.083, it is clear that $C_{1,T}^{(2)}$ outperforms all other proposed codes.

For quaternary CPM, Tab. 3.3 summarizes some results. For ease of presentation, we compare the codes with coupling factor $L = 50$ when concatenated with the CPM modulator Q_{CPM} (quaternary, Gray mapping, $L_{CPM} = 2$, Raised cosine pulse and $h = 1/4$). Concerning the optimized protograph codes, $C^{(2)}$ still have a very good performance [BPB+14b]. The performance one can achieve when optimizing rate-1/2 unstructured LDPC codes for this CPM is 0.7dB [BPB+14b], here we almost achieved this limit with $C_{1,T}^{(2)}$. As for the binary case, similar observations can be made, however, the direct truncation $C_{1,DT}^{(1)}$ clearly leads here to better performance in comparison to the classical termination $C_{1,T}^{(1)}$, since both have the same threshold (1.13dB) while the former has a a bigger rate.

Figure 3.28 gives some simulation results for $C^{(2)}$ and $C_{1,T}^{(2)}$ when concatenated with the GMSK. Simulations were performed using 250 turbo iterations and a lifting factor of 1000. For the spatially coupled code, we take $L = 50$.

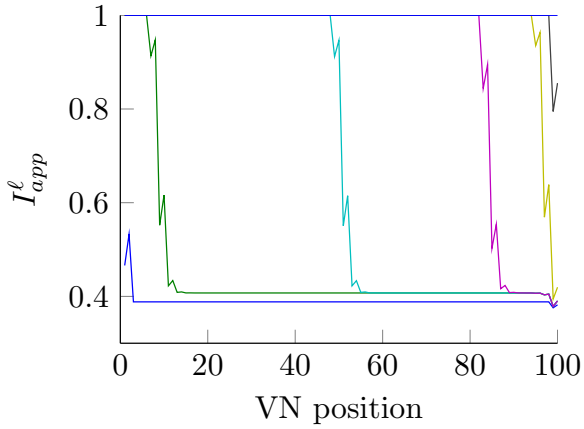

(a) $C^{(1)}_{1,DT}$, iterations {1, 20, 120, 200, 230, 240, 250}. Convergence of all VNs after 250 iterations

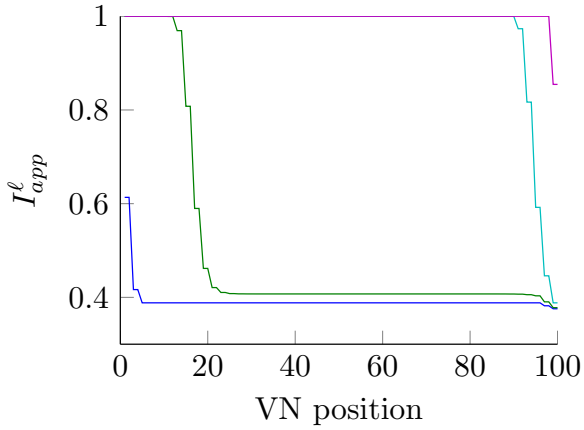

(b) $C^{(1)}_{2,DT}$, iterations {1, 20, 120, 200, 1000}. Curves of the 200^{th} and the 1000^{th} iterations are overlaid

Figure 3.26: Evolution of I^{ℓ}_{app} per VNs of $C^{(1)}_{1,DT}$ and $C^{(1)}_{2,DT}$, with $L = 50$, concatenated with GMSK at 1.5dB

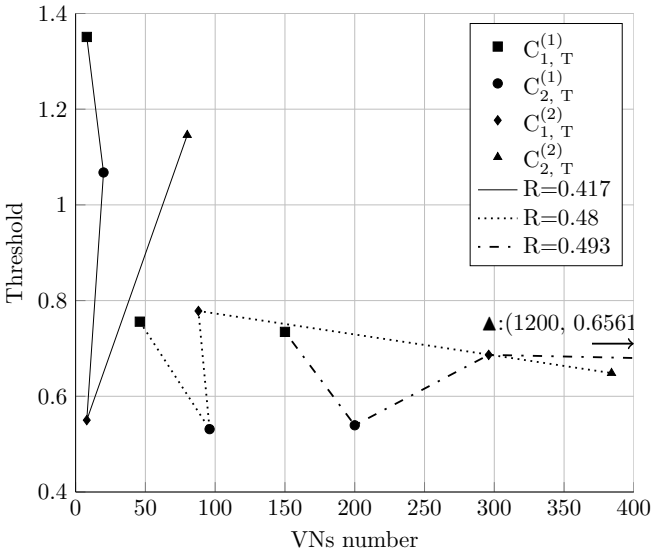

Figure 3.27: Comparison of the threshold as a function of the number of VNs for different rates

	$C^{(1)}$	$C^{(2)}$	$C^{(1)}_{1,T}$	$C^{(1)}_{1,DT}$	$C^{(1)}_{2,T}$	$C^{(1)}_{2,DT}$	$C^{(2)}_{1,T}$	$C^{(2)}_{2,T}$
Threshold	2.84	1.38	1.13	1.13	0.82	3.15	0.97	0.93
Rate	0.5	0.5	0.495	0.5	0.49	0.5	0.49	0.48

Table 3.3: Comparison of the performance of some codes when concatenated with Q_{CPM}

3.5 Conclusion

We introduced a general framework for the asymptotic analysis and design of systematic GIRA codes serial concatenated with CPM. Among all families, it appears from the obtained results that IRA and LDGM codes present the best trade-off threshold performance. Future works will investigate the finite length performance.

Then, we introduced a method to design protograph-based LDPC codes for CPM systems. The discussed method can support any CPM scheme as well as any trellis-based detector. We provided some optimized protograph codes that can achieve good performances. In was shown that classical protographs designed for the AWGN cannot be good candidates for serial concatenations with the CPM. Careful design enable the use of efficient protographsbut at the price of a relatively high error floor.

To overcame this problem, spatially coupled LDPC codes were explored since this family can

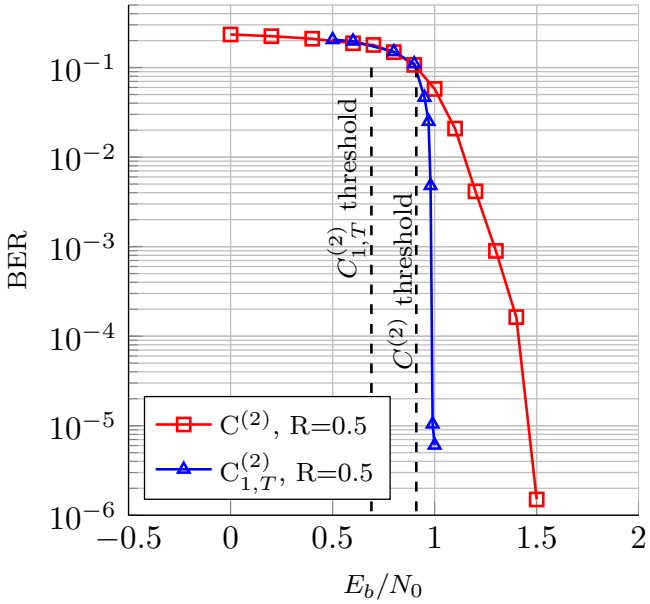

Figure 3.28: Bit error rate for GMSK with different codes

achieve universally good performance over a wide class of channels. We investigated the performance and the convergence behaviour of the $(3, 6)$ spatially coupled LDPC code when concatenated with the CPM. Moreover, we showed that coupling thz optimized protographs improves their threshold and helps designing very good small protographs.

Finally, we described an unusual termination without rate loss that still has a good threshold. Nonetheless, the gain of our termination should come with a degradation of the growth rate. Further research can be done to improve the minimum distance but we point out that, in the framework of spatially coupled LDPC codes, this is the first time to our knowledge that the possibility of using only one wave effect is investigated. Besides the rate, another advantage of this termination is that it leads to easy encodable codes in comparison to the classical one.

Chapter 4

A fresh look on Laurent-based receiver derivation

Summary

Résumé

Dans ce chapitre, nous nous concentrons sur certains aspects des récepteurs CPM et le design de codes LDPC pour les récepteurs CPM à faible complexité. Une des deux décompositions les plus utilisées a été introduite par Pierre-André Laurent [Lau86] en 1986. Cette décomposition rend les techniques de synchronisation plus efficace et permet la conception de récepteurs à faible complexité. Le récepteur maximum de vraisemblance basés sur l'algorithme de Viterbi a été introduit par Kaleh dans [Kal89]. Malheureusement, aucun récepteur maximum *a posteriori* (MAP) *exacte* n'a été proposé dans la littérature: les récepteurs proposés ne prennent pas en compte "l'interférence inter-symbole" inhérente à la décomposition de Laurent et souffrent de la non-blancheur des statistiques de bruit après filtrage. Cette approximation est d'autant plus pénalisante pour le décodage itératif, la détection non-cohérente, l'égalisation ou les applications multi-porteuses. Dans ce chapitre, après avoir discuté les récepteurs existants, nous dérivons un nouveau récepteur MAP qui résout le problème de l'ISI sans introduire des traitements supplémentaires, de type filtres de blanchiment. D'autre part, sur la base de l'autre décomposition CPM [Rim88], nous explicitons le lien entre les deux représentations et nous proposons une méthode analytique pour calculer le nouveau banc de filtre de réception. En appliquant la méthode d'optimisation du chapitre 2, nous optimisons des codes LDPC pour les récepteurs à faible complexité basé sur la décomposition de Laurent et montrons que les codes optimisés restent très efficaces pour le récepteur à faible complexité pour peu qu'on considère suffisamment de composantes. Enfin, nous comparons la performance du récepteur MAP proposé avec le récepteur classique en termes d'EXIT Chart et de taux d'erreur pour la CPM non codée et codée.

4.1 Introduction

After the invention of turbo codes [BG96], coded CPM benefited greatly from iterative decoding. Actually, it was shown in [Rim88] that a CPM signal can be decomposed into the serial concatenation of a continuous phase encoder (CPE) with a memoryless modulator (MM), this allows to consider trellis based receivers that can be efficiently used for turbo detection schemes [MA01, GiAND09]. Independently, [Lau86] derived another decomposition of the binary CPM rewriting a particular signal as the sum of some amplitude modulated signals. The major advantage of this representation is that almost all of the signal energy is concentrated within the first few components only, even for high levels of modulations. This allows us to implement low complexity receivers. The extension of the Laurent's decomposition in the M-ary case is described in [MM95]. In this chapter, we give more emphasize on the binary case.

In [Kal89, MFG97, CB05, CR97], the authors developed the underlying trellis of the Laurent's decomposition and derived the Maximum Likelihood (ML) and the Maximum *a posteriroi* (MAP) receivers [BCJR74]. However, in their derivations, they neglect the non-whiteness of the filtered noise by the Laurent's components (the matched filters have a support which is longer than the symbol period) in comparison to the noise of the channel. In order to implement the exact receiver for the MAP detector, one should introduce a whitening filter. This filter becomes even more important when we consider non-coherent detections [LTHS03], equalization [TS05] or multicarrier signals [MH]. In this chapter, we first revisit the derivation of the ML receiver and propose a new derivation which is more intuitive, and useful especially in order to express the exact MAP receiver without introducing any whitening filter but simply by considering a new filter bank. We will also show a method to calculate the new filter bank and the relationship between this representation and the Rimoldi's decomposition.

4.2 Continuous phase modulator

Let us consider a sequence of N information symbols $\boldsymbol{\alpha} = \{\alpha_i\} \in \{\pm 1, \ldots, \pm(M-1)\}^N$. The transmitted CPM signal is written :

$$s(t) = \sqrt{\frac{2E_s}{T}} \cos\left(2\pi f_0 t + \theta(t, \boldsymbol{\alpha})\right)$$

$$= \Re\left[\underbrace{e^{j\theta(t,\boldsymbol{\alpha})}}_{s_b(t)} e^{j2\pi f_0 t}\right] \tag{4.1}$$

where:

$$\theta(t,\boldsymbol{\alpha}) = \pi h \sum_{i=0}^{N-1} \alpha_i q(t-iT)$$

$$q(t) = \begin{cases} \int_0^t g(\tau)d\tau, t \leq L \\ 1/2, t > L \end{cases}$$

where E_s is the symbol energy, T the symbol period, f_0 the carrier frequency, θ_0 the initial phase, $\theta(t,\boldsymbol{\alpha})$ the information phase, $g(t)$ the pulse response and $h = k/p$ the modulation index where $(k \wedge p = 1)$, L the CPM memory and $\Re(.)$ the real part operator. When $L = 1$ (and $L \geq 2$), we say that the CPM signal is of full response (respectively partial response). In the following we will review the Rimoldi's and Laurent's decompositions and introduce the main notations, please refer to the chapter 1 for more details.

4.2.1 Rimoldi's receiver

Let us consider $U_i = (\alpha_i + (M-1))/2 \in \{0, 1, \dots M-1\}$. The CPE trellis is defined by the state vector $\sigma_n^R = \left[U_{n-1}, \dots U_{n-L+1}, V_n = \left[\sum_{i=0}^{n-L} U_i\right] \mod p\right]$. The CPM signal $s_b(t,\boldsymbol{\alpha})$ is sent over a memoryless additive white Gaussian noise channel (AWGN) with double-sided power spectral density $N_0/2$. The complex envelope of the received signal can be expressed as:

$$y(t) = \sqrt{\frac{2E_s}{T}} \exp\left(j\psi(t,\boldsymbol{\alpha})\right) + n(t), \quad t > 0 \tag{4.2}$$

where $\psi(t,\boldsymbol{\alpha})$ is the *tilted* phase of the signal [Rim88]. The MM filters output $\{s_i(t)\}$ are sampled once each nT, which allows to compute the projection of the received signal Eq. (4.2) over the receiver signal space. Using any orthonormal basis, this is proportional to [MA01]:

$$\boldsymbol{y}^n = [y_i(n)]_{1 \leq i \leq pM^L} = \left[\int_{nT}^{(n+1)T} r(l) s_i^*(l) dl\right]_{1 \leq i \leq pM^L}$$

By considering any orthonormal basis of this signal space [MA01], the probability $p(\boldsymbol{y}^n / X_n)$ is proportional to $\exp\{2\Re(y_i^n)/N_0\}$. We will use this quantity as a branch metric for the CPE trellis when performing the BCJR algorithm. The receiver architecture is depicted in Fig. 4.1.

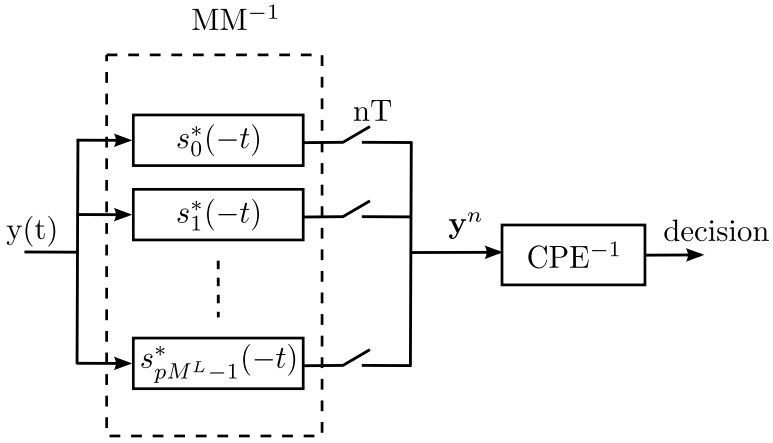

Figure 4.1: Rimoldi's decomposition-based receivers

4.2.2 Laurent-based receiver

The Laurent's representation [Lau86] allows us to rewrite the complex envelope in Eq. (4.1) as the sum of $K = 2^{L-1}$ amplitude modulated signals with the pseudo-symbols $a_{k,n} = \exp(j\pi h A_{k,n})$ such that:

$$s_b(t) = \sqrt{2E_s/T} \sum_{n=0}^{N-1} \sum_{k=0}^{K-1} a_{k,n} C_k(t - nT) \tag{4.3}$$

$$C_k(t) = s_0(t) \prod_{j=1}^{L-1} s_{j+L\beta_{k,j}}(t), \quad 0 < k \leq K-1$$

$$a_{k,n} = e^{j\pi h A_{k,n}}$$

$$A_{k,n} = \sum_{i=0}^{n} \alpha_i - \sum_{j=1}^{L-1} \alpha_{n-j}\beta_{k,j} \tag{4.4}$$

$$s_j(t) = \frac{sin(\psi(t + jT))}{sin(\pi h)}$$

$$\psi(t) = \begin{cases} 2\pi h q(t), & 0 \leq t \leq LT \\ \pi h - 2\pi h q(t - LT), & LT \leq t \leq 2LT \\ 0, & \text{elsewhere} \end{cases}$$

where $\beta_{k,j}$ refer to the j^{th} bit in the binary representation of the index k. The components $\{C_k(t\}_k$ have different duration lengths as following [Lau86]:

Component	Duration
$C_0(t)$	$(L+1)T$
$C_1(t)$	$(L-1)T$
$C_2(t), C_3(t)$	$(L-2)T$
$C_4(t), C_5(t), C_6(t), C_7(t)$	$(L-3)T$
$\vdots$	
$C_{K/2}(t), \ldots, C_{K-1}(t)$	LT

Table 4.1: Durations of the Laurent's components

Let us define L_k as the length of $C_k(t)$ in terms of the symbol periods T (*i.e.* $C_k(t) = 0, \forall t > L_k T$).

4.3 Maximum Likelihood receiver for Laurent's decomposition

Here we will revisit the ML decoder for the Laurent's decomposition discussed in the chapter 1.

4.3.1 Notations and preliminaries

Consider the received signal:

$$r(t) = s(t) + n(t)$$

where $n(t)$ is a double a memoryless additive white Gaussian noise with double-sided power spectral density $N_0/2$.

Let us denote by $.^*$ and $\Re(.)$ the conjugate and the real part operators respectively. Be $\mathcal{E} = \{e_i(t)\}_{i,0\leq t\leq T}$ any orthonormal basis of the receiver signal space and $\langle ., . \rangle$ the inner product between two functions f and g of this space as:

$$\langle f, g \rangle = \int f(t) g^*(t) dt$$

Since the memory of the CPM L is finite, the dimension of the receiver signal space, denoted $|\mathcal{E}|$, is also finite.

Let us consider an arbitrary signal $x(t)$. Consider the following notations:

$$x(t)|_{a\leq t\leq b} = \begin{cases} x(t) \text{ if } a \leq t \leq b \\ 0 \text{ otherwise} \end{cases}$$

$$x_i(n) = \langle x(t), e_i^*(t - nT)\rangle = \int_{nT}^{(n+1)T} x(t)e_i^*(t - nT)dt \tag{4.5}$$
$$\boldsymbol{x_i} = (x_i(n))_n$$
$$\boldsymbol{x} = (\boldsymbol{x_i})_i$$

For ease of notations, when a function, a vector or a scalar x depends of the binary sequence $\bar{\boldsymbol{\alpha}} = (\bar{\alpha}_1, \ldots, \bar{\alpha}_{N-1}\} \in \{\pm 1\}^N$, it is denoted as $\bar{x}$.

The projection of the received signal $r(t)$ on $e_i(t)$ at $t = nT$, $\forall i$, gives:

$$\begin{aligned} r_i(n) &= \langle r(t), e_i(t - nT)\rangle \\ &= \langle s(t), e_i(t - nT)\rangle + \langle n(t), e_i(t - nT)\rangle \\ &= s_i(n) + n_i(n) \end{aligned}$$

The ML receiver finds the estimated bits $\hat{\boldsymbol{\alpha}}$ such that the distance between the corresponding statistic $\bar{\boldsymbol{s}}$ and the received signal statistic $\boldsymbol{r}$ is minimized; *i.e.*:

$$\hat{\boldsymbol{\alpha}} = \arg\max_{\bar{\boldsymbol{\alpha}}} p(\boldsymbol{r}|\bar{\boldsymbol{\alpha}})$$

One can proof that $\{n_i(n)\}_n$ and $\{r_i(n)\}_n$, are uncorrelated, consequently, the probability of the observed data $\boldsymbol{r}$ under the sequence $\bar{\boldsymbol{\alpha}}$ can be expressed as:

$$p(\boldsymbol{r}|\bar{\boldsymbol{\alpha}}) \propto \exp\left(\frac{-1}{N_0}\sum_k\sum_i |r_i(k) - \bar{s}_i(k)|^2\right)$$

where $\bar{s}_i(k)$ depends implicitly on $\bar{\boldsymbol{\alpha}}$. Then, as seen on the chapter 1:

$$\begin{aligned} p(\boldsymbol{r}|\bar{\boldsymbol{\alpha}}) &= \exp\left(\frac{-1}{N_0}\sum_k\sum_i \langle r(t) - \bar{s}(t), e_i(t - kT)\rangle^2\right) \\ &= \underbrace{\exp\left(\frac{-1}{N_0}\int_0^{NT} r(t)r^*(t)dt\right)}_{\text{common to all paths}} \times \underbrace{\exp\left(\frac{-1}{N_0}\int_0^{+\infty} \bar{s}(t)\bar{s}^*(t)dt\right)}_{\text{constant}} \times \exp\left(\frac{2}{N_0}\int_0^{NT} \Re(r(t)\bar{s}^*(t))dt\right) \\ &\propto \exp\left(\frac{2}{N_0}\Re\left(\int_0^{NT} r(t)\bar{s}^*(t)dt\right)\right) \end{aligned} \tag{4.6}$$

4.3.2 Kaleh's ML receiver

[Kal89] showed that one can form the signal in Eq. (4.3) from a particular trellis. Actually, at each nT, one can compute all the pseudo-symbols $a_{k,n}$ knowing only the input symbol α_n and the current

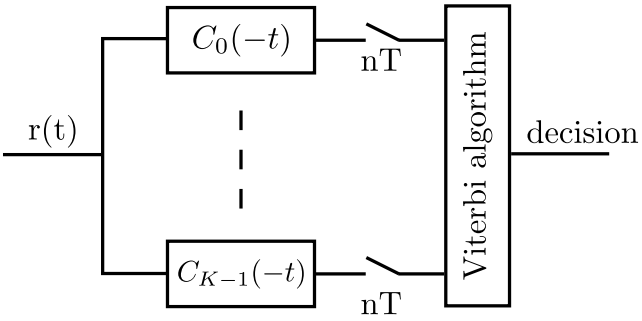

Figure 4.2: Kaleh's ML receiver

phase state $\sigma_n^L = [a_{0,n-L}, \alpha_{n-L+1}, \ldots, \alpha_{n-1}]$, according to the following recursion:

$$A_{k,n} = A_{0,n-L} + \alpha_n + \sum_{i=1}^{L-1} \alpha_{n-i}.(1 - \beta_{k,i}) \tag{4.7}$$

Starting from Eq. (4.6) and by substituting Eq. (4.3), the new metric corresponding to the sequence (or the path) $\bar{\boldsymbol{\alpha}}$, denoted hereafter $\Gamma(\bar{\boldsymbol{\alpha}})$, is written as seen on the chapter 1:

$$\begin{aligned}
\Gamma(\bar{\boldsymbol{\alpha}}) &= \Re\left[\int_0^{NT} r(t)\bar{s}_i^*(t)dt\right] \\
&= \sum_{n=0}^{N-1} \Re\left[\int_0^{NT} r(t) \sum_{k=0}^{K-1} \bar{a}_{k,n}^* C_k^*(t - nT)dt\right] \\
&= \sum_{n=0}^{N-1} \Re\left[\sum_{k=0}^{K-1} \bar{a}_{k,n}^* \int_0^{(L+1)T} r(t + nT)C_k(t)dt\right]
\end{aligned} \tag{4.8}$$

This can be implemented efficiently by means of the Viterbi algorithm [Vit67]. In each trellis section n, we sample the output of the matched filters $\{C_k(-t)\}$ at nT, compute the transition symbols $\{\bar{a}_{k,n}\}_k$ according to Eq. (4.4) and evaluate $\Re\Big(\sum_{k=0}^{K-1} \bar{a}_{k,n}^* \int_0^{(L+1)T} r(t + nT)C_k(t)dt\Big)$. The corresponding receiver structure is given by Fig. 4.2.

Interpretation: By permuting the sum and the integral in Eq. (4.8) we can write:

$$\begin{aligned}
\Gamma(\bar{\boldsymbol{\alpha}}) &= \sum_{n=0}^{N-1} \Re\left[\sum_{k=0}^{K-1} \bar{a}_{k,n}^* \int_0^{(L+1)T} r(t + nT)C_k(t)dt\right] \\
&= \sum_{n=0}^{N-1} \Re\left[\int_0^{(L+1)T} r(t + nT) \sum_{k=0}^{K-1} \bar{a}_{k,n}^* C_k(t)dt\right] \\
&= \sum_{n=0}^{N-1} \Re\left[\int_0^{(L+1)T} r(t + nT) \left(\sum_{k=0}^{K-1} \bar{a}_{k,n} C_k(t)\right)^* dt\right]
\end{aligned} \tag{4.9}$$

Consequently, it might seem that at each section n, the current metric is about computing the correlation between the waveform $\sum_{k=0}^{K-1} \bar{a}_{k,n} C_k(t)|_{0\leq t\leq (L+1)T}$ and the received noisy signal $r(t)|_{nT\leq t\leq (n+L+1)T}$. At the first sight, in the section n, one can wonder why we are not taking into account the contribution of the previous pseudo-symbols $\{\bar{a}_{k,m}\}_{m<n}$ since the first $K/2$ Laurent's components $\{C_k(t)\}_k$ have support greater than T. Actually, this "symbol interference" was already computed but in the metrics of the L previous sections. Hence, since this is the ML decoder, and the decision is made over the whole sequence, Eq. (4.8) turns out to be optimal. This can be illustrated as following:

$$\begin{aligned}
\Gamma(\bar{\boldsymbol{\alpha}}) &= \sum_{n=0}^{N-1} \Re\left[\int_0^{(L+1)T} r(t+nT)\left(\sum_{k=0}^{K-1} \bar{a}_{k,n} C_k(t)\right)^* dt\right] \\
&= \sum_{n=0}^{N-1} \Re\left[\int_0^{T} r(t+nT)\left(\sum_{k=0}^{K-1} \bar{a}_{k,n} C_k(t)\right)^* dt + \int_T^{(L+1)T} r(t+nT)\left(\sum_{k=0}^{K-1} \bar{a}_{k,n} C_k(t)\right)^* dt\right] \\
&= \sum_{n=0}^{N-1} \Re\left[\int_0^{T} r(t+nT)\left(\sum_{k=0}^{K-1} \bar{a}_{k,n} C_k(t)\right)^* dt + \sum_{i=1}^{i=L} \int_{iT}^{(i+1)T} r(t+nT)\left(\underbrace{\sum_{k=0}^{K-1} \bar{a}_{k,n} C_k(t)}_{A(t)|_{iT\leq t\leq (i+1)T}}\right)^* dt\right]
\end{aligned}$$

$A(t)|_{iT\leq t\leq (i+1)T}$ represents the symbol interference terms that occur at the sections $\{n+i\}_{i=1\ldots L}$ due to the pseudo-symbols $\{a_{k,n}\}_{0\leq k\leq K-1}$ of the section n. This interference is taken into account *a priori* in the section n but, from a theoretic point of view, it is formally considered at the sections $\{n+i\}_{i=1\ldots L}$ through the summation of the ML estimator $\sum_{n=0}^{N-1}$. In the context of a sequence decision-based estimator, this receiver is exact, however, this metric is no long valid for symbol-based decision receiver as we are going to expose later.

4.3.3 A new derivation for an ML receiver

Starting from Eq. (4.6) and by splitting the integral, we get:

$$\begin{aligned}
\Gamma(\bar{\boldsymbol{\alpha}}) &= \Re\left[\int_0^{NT} r(t)\bar{s}_i^*(t)dt\right] \\
&= \Re\left[\sum_{n=0}^{N-1}\int_{nT}^{(n+1)T} r(t)\bar{s}_i^*(t)dt\right] \\
&= \sum_{n=0}^{N-1} \Re\left[\int_{nT}^{(n+1)T} r(t)\bar{s}_i^*(t)dt\right]
\end{aligned}$$

$$= \sum_{n=0}^{N-1} \Re\left[\int_{nT}^{(n+1)T} r(t) \left(\sum_{\ell=0}^{N-1}\sum_{k=0}^{K-1} \bar{a}^*_{k,\ell} C^*_k(t-\ell T)\right) dt\right]$$
$$= \sum_{n=0}^{N-1} \Re\left[\int_{nT}^{(n+1)T} r(t) \left(\sum_{k=0}^{K-1} \bar{a}^*_{k,n} C_k(t-nT) + \sum_{\ell=1}^{N-1}\sum_{k=0}^{K-1} \bar{a}^*_{k,n-\ell} C_k(t-(n-\ell)T)\right) dt\right]$$

In the second summation, since $\ell > 1$, only the components of support greater than T are non null, *i.e.* the first $K/2$ components only (see Table 4.1). Which gives:

$$\begin{aligned}
\Gamma(\bar{\boldsymbol{\alpha}}) &= \sum_{n=0}^{N-1} \Re\left[\int_{nT}^{(n+1)T} r(t) \left(\sum_{k=0}^{K-1} \bar{a}_{k,n} C_k(t-nT) + \sum_{\ell=1}^{N-1}\sum_{k=0}^{K/2-1} \bar{a}_{k,n-\ell} C_k(t-(n-\ell)T)\right)^* dt\right] \\
&= \sum_{n=0}^{N-1} \Re\left[\int_{nT}^{(n+1)T} r(t) \left(\sum_{k=0}^{K-1} \bar{a}_{k,n} C_k(t-nT) + \sum_{k=0}^{K/2-1}\sum_{\ell=1}^{N-1} \bar{a}_{k,n-\ell} C_k(t-(n-\ell)T)\right)^* dt\right] \\
&= \sum_{n=0}^{N-1} \Re\left[\int_{nT}^{(n+1)T} r(t) \left(\underbrace{\sum_{k=0}^{K-1} \bar{a}_{k,n} C_k(t-nT)}_{B(t)|_{nT\le t\le (n+1)T}} + \underbrace{\sum_{k=0}^{K/2-1}\sum_{\ell=1}^{L_k-1} \bar{a}_{k,n-\ell} C_k(t-(n-\ell)T)}_{C(t)|_{nT\le t\le (n+1)T}}\right)^* dt\right] \qquad (4.10)
\end{aligned}$$

The term $B(t)|_{nT\le t\le (n+1)T}$ represents the part of the signal $\bar{s}(t)|_{nT\le t\le (n+1)T}$ that is generated by the symbols corresponding to the current transition, *i.e.* $\{a_{k,n}\}_{0\le k\le K-1}$, whereas the quantity $C(t)|_{nT\le t\le (n+1)T}$ represents the part of that signal which is generated by the memory symbols $\{a_{k,n-\ell}\}_{\substack{0\le k\le K/2-1\\ 1\le \ell\le L_k}}$. Let us define:

$$\bar{\Phi}(t-nT)|_{0\le t\le T} = B(t)|_{nT\le t\le (n+1)T} + C(t)|_{nT\le t\le (n+1)T} \qquad (4.11)$$

Then we can rewrite:

$$\begin{aligned}
\Gamma(\bar{\boldsymbol{\alpha}}) &= \sum_{n=0}^{N-1} \Re\left[\int_{nT}^{(n+1)T} r(t)\bar{\Phi}^*(t-nT)dt\right] \\
&= \sum_{n=0}^{N-1} \Re\left[\int_{nT}^{(n+1)T} \left(\sum_{k=0}^{|\mathcal{E}|-1} r_k(n) e_k(t-nT)\right)\left(\sum_{q=0}^{|\mathcal{E}|-1} \bar{\Phi}_q(0) e_q(t-nT)\right)^* dt\right] \qquad \text{(see Eq. (4.5))} \\
&= \sum_{n=0}^{N-1} \Re\left[\sum_k r_k(n) \sum_q \bar{\Phi}^*_q(0) \int_{nT}^{(n+1)T} e_k(t-nT) e^*_q(t-nT) dt\right]
\end{aligned}$$

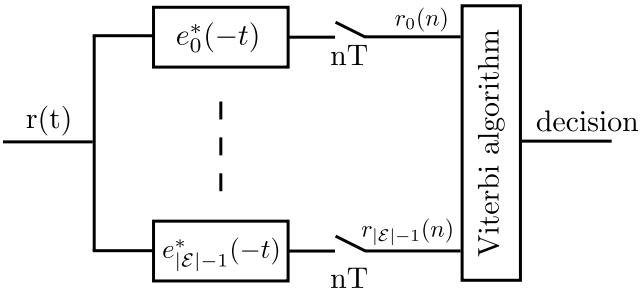

Figure 4.3: A new ML receiver architecture. The family $\{e_i(t)\}_i$ can be any orthonormal basis of the receiver signal space.

$$= \sum_{n=0}^{N-1} \Re\left[\sum_k r_k(n)\bar{\Phi}_k^*(0)\right] \qquad (\{e_i(t)\}_i \text{ is an orthonormal basis}) \tag{4.12}$$

Once we determine $\{\bar{\Phi}_k^*(0)\}_k$, the new ML receiver can be implemented efficiently by means of the Viterbi algorithm working on the same trellis previously defined but with the branch metric in Eq. (4.12). The corresponding receiver architecture is plotted in Fig. 4.3.

Computation of $\{\Phi_k^*(0)\}_k$:

In this section, we will see how we can form the statistic $\{\Phi_k^*(0)\}_k$ from the current state $\sigma_n^L = [a_{0,n-L}, \alpha_{n-L+1}, \ldots, \alpha_{n-1}]$ and the input symbol α_n.

The expression of $B(t)|_{nT\le t\le(n+1)T}$ takes into account only the contribution of the current pseudo-symbols $\{A_{k,n}\}_k$. These can be deduced from the current state σ_n^L and the input symbol α_n according to:

$$\begin{aligned}
A_{k,n} &= \sum_{j=0}^{n} \alpha_j - \sum_{j=1}^{L-1} \alpha_{n-j}\beta_{k,j} \qquad \text{(see Eq. (4.4))} \\
&= \sum_{j=0}^{n-L} \alpha_j + \sum_{j=n-L+1}^{n-1} \alpha_j + \alpha_n - \sum_{j=1}^{L-1} \alpha_{n-j}\beta_{k,j} \\
&= A_{0,n-L} + \sum_{j=1}^{L-1} \alpha_{n-j} + \alpha_n - \sum_{j=1}^{L-1} \alpha_{n-j}\beta_{k,j} \\
&= A_{0,n-L} + \alpha_n + \sum_{j=1}^{L-1} \alpha_{n-j}(1-\beta_{k,j}) \\
&= A_{0,n-L} + \alpha_n + \sum_{j=1}^{L-1} \alpha_{n-j}\beta_{K-1-k,j}
\end{aligned} \tag{4.13}$$

the last step comes from the observation that the inverse of the j^{th} bit in the binary expression of k, where $k \in [0, \dots, K-1 = 2^{L-1}-1]$, is equal to the j^{th} bit in the binary expression of $K-1-k$. This can be proved as following:

$$\begin{aligned} k &= \sum_{j=1}^{L-1} 2^{i-1}\beta_{k,j} \\ &= -\sum_{j=1}^{L-1} 2^{i-1}(1-\beta_{k,j}) + \sum_{j=1}^{L-1} 2^{i-1} \\ &= -\sum_{j=1}^{L-1} 2^{i-1}(1-\beta_{k,j}) + K - 1 \\ K-1-k &= \sum_{j=1}^{L-1} 2^{i-1} \underbrace{(1-\beta_{k,j})}_{\triangleq \beta_{K-1-k,j}} \end{aligned}$$

On the other hand, the term $C(t)|_{nT \le t \le (n+1)T}$ represents the contribution of the past pseudo-symbols $\{A_{k,m-\ell}\}_{\substack{0 \le k \le K/2-1 \\ 1 \le \ell \le L_k}}$. As with Eq. (4.4), we can retrieve the past pseudo-symbols only from the current state σ_n^L. Let us define:

$$\boldsymbol{\alpha}_{n-L+1}^{n} = [\alpha_n, \alpha_{n-1}, \dots, \alpha_{n-L+1}]$$

$$\boldsymbol{\beta}_{K-1-k} = \begin{pmatrix} \beta_{K-1-k,1} \\ \beta_{K-1-k,2} \\ \vdots \\ \beta_{K-1-k,L-1} \end{pmatrix}_{[(L-1)\times 1]}$$

$$\boldsymbol{J} = \begin{pmatrix} 0 & \dots & \dots & \dots & 0 \\ 1 & \ddots & & & \vdots \\ 0 & \ddots & \ddots & & \vdots \\ \vdots & \ddots & \ddots & \ddots & \vdots \\ 0 & \dots & 0 & 1 & 0 \end{pmatrix}_{[L\times L]}$$

Therefore, inspired from Eq. (4.13), the past pseudo-symbols $A_{k,n-\ell}$ can be simply calculated with the following recursion:

$$A_{k,n-\ell} = A_{0,n-L} + \boldsymbol{\alpha}_{n-L+1}^{n} \boldsymbol{J}^{\ell} \begin{bmatrix} 1 \\ \boldsymbol{\beta}_{K-1-k} \end{bmatrix}, \quad 1 \le \ell \le L$$

Considering that J^0 is the identity matrix, this expression can be merged with Eq. (4.13) to form our new recursion formula:

$$A_{k,n-\ell} = A_{0,n-L} + \boldsymbol{\alpha}_{n-L+1}^{n} \boldsymbol{J}^{\ell} \begin{bmatrix} 1 \\ \boldsymbol{\beta}_{K-1-k} \end{bmatrix}, \quad 0 \leq k \leq K-1, 0 \leq \ell \leq L_k - 1 \tag{4.14}$$

Example: for $L = 4$ (in this case $K = 8$), we have:

$$\boldsymbol{\alpha}_{n-3}^{n} = \begin{pmatrix} \alpha_n \\ \alpha_{n-1} \\ \alpha_{n-2} \\ \alpha_{n-3} \end{pmatrix}^T$$

$$\boldsymbol{B}_{8-1-1} = \boldsymbol{B}_6 = \begin{pmatrix} 0 \\ 1 \\ 1 \end{pmatrix}$$

$$\boldsymbol{J} = \begin{pmatrix} 0 & 0 & 0 & 0 \\ 1 & 0 & 0 & 0 \\ 0 & 1 & 0 & 0 \\ 0 & 0 & 1 & 0 \end{pmatrix}$$

N.B.: For $\ell \geq L_k$, we cannot compute the corresponding $A_{k,n-\ell}$ since we do not have access to $\{\alpha_{n-m}\}|_{m \geq L}$ in the state definition σ_n^L. However, we do not need this pseudo-symbol since it does not generate any interference at nT (its component has only length L_k).

Finally, the statistic $\{\Phi_k^*(0)\}_k$ corresponding to the transition (σ_n^L, α_n) is nothing but:

$$\Phi_k(0) = \left\langle \underbrace{\sum_{k'=0}^{K-1} a_{k',n} C_{k'}(t)}_{B(t)} + \underbrace{\sum_{k'=0}^{K/2-1} \sum_{\ell=1}^{L_k-1} a_{k',n-\ell} C_{k'}(t+\ell T)}_{C(t)}, e_k(t) \right\rangle, \quad 0 \leq k \leq |\mathcal{E}| - 1 \tag{4.15}$$

This whole computations do not involve additional complexity when performing the Viterbi algorithm since, when implementing a particular CPM receiver, the transition 'labels' $\{\Phi_k^*(0)\}_k$ are computed only once and are hard coded in the trellis structure.

This new derivation of the ML receiver is equivalent to the previous one in Section 4.3.2, with the difference that the branch metric computed at the instant nT corresponds now only to the observed signal at time nT (including the interference of the past symbols). The main advantage is that we can derive easily the symbol-based decision receivers without introducing a whitening filter as we are going to see later.

4.3.4 Relation with Rimoldi's memoryless modulator

The expression in Eq. (4.10) can be interpreted as evaluating the correlation between the portion of the signal $r(t)|_{[nT,(n+1)T]}$ and the length-T function $\bar{\Phi}(t-nT)|_{[nT,(n+1)T]}$, the generated waveform corresponding to the considered transition $(\sigma_n^L, \bar{\alpha}_n)$. This is equivalent to filtering the received signal by the filter bank formed by the matched filters of all $\bar{\Phi}(t)$ and sampling the output each nT. Generally, In order to derive an analytical expression of the filter bank $\{\Phi(t)\}$, one can use the Rimoldi's decomposition. In fact, starting from a CPE state σ_n^R and the input symbol U_n, the output symbol X_n is mapped into the pulse $\Omega(t)$ of the memoryless modulator as [Rim88]:

$$
\begin{aligned}
&X_n = [U_n, \sigma_n^R] = [U_n, U_{n-1} \ldots, U_{n-L+1}, V_n] \\
&\Omega(t) = \exp\left(j\psi(\tau, X_n)\right) \\
&\psi(\tau, X_n) = \left[2\pi h V_n + 4\pi h \sum_{k=0}^{L-1} U_{n-k} q(\tau + kT) + W(\tau)\right] \\
&W(\tau) = \pi h(M-1)\tau/T - 2\pi h(M-1) \sum_{i=0}^{L-1} q(\tau + iT) + (L-1)(M-1)\pi h
\end{aligned}
$$

Recall that the Rimoldi's representation is given in term of the *tilted* phase. We can recover the CPM signal with the non-shifted phase by simply multiplying $\{\Omega(t)\}$ in any trellis section, say the section at nT, by:

$$
\exp(j2\pi(f_1 - f_0)t) \text{ where } f_1 = f_0 - \frac{(M-1)h}{2T}
$$

i.e.:

$$
\begin{aligned}
\exp(j2\pi(f_1 - f_0)t) &= \exp\left(-j\pi\frac{(M-1)h}{T}t\right) \\
&= \exp\left(-j\pi\frac{(M-1)h}{T}\tau\right)\exp\left(-j\pi(M-1)hn\right) \quad (t = \tau + nT) \qquad (4.16)
\end{aligned}
$$

In the following instant, *i.e.* $n+1$:

• if k (the numerator of h) is even, (and then p is odd since k and p are relatively prime), the right exponential factor in Eq. (4.16) becomes:

$$
\begin{aligned}
\exp\left(-j\pi h(M-1)(n+1)\right) &= \exp\left(-j\pi h(M-1)n\right)\exp\left(-j\pi h(M-1)\right) \\
&= \exp\left(-j\pi h(M-1)n\right)\exp\left(-j\pi h(M-1) + j\pi hp\right) \quad (\text{since } \pi hp \equiv 0[2\pi]) \\
&= \exp\left(-j\pi h(M-1)n\right)\exp\left(j\pi(p-M+1)h\right) \qquad (4.17)
\end{aligned}
$$

It is clear that $p - M + 1$ is even (difference of two odd numbers), *i.e.*:

$$\exists \beta \in \mathbb{N} / p - M + 1 = 2\beta$$

consequently, when we multiply Eq. (4.17) by $\Omega(t)$, we obtain in the argument (for ease of notation, we did not mention the term $\pi h(M-1)n$):

$$\begin{aligned}\psi(\tau, X_n) + \pi(p - M + 1)h &= 2\pi h V_n + 4\pi h \sum_{k=0}^{L-1} U_{n-k} q(\tau + kT) + W(\tau) + 2\pi h\beta \\ &= 2\pi h(V_n + \beta) + 4\pi h \sum_{k=0}^{L-1} U_{n-k} q(\tau + kT) + W(\tau) \\ &= \bar{\psi}(\tau, X'_n) \quad (\text{where } X'_n = [U_n, \ldots, U_{n-L+1}, V_n + \beta])\end{aligned}$$

Note that $\psi(\tau, X'_n)$ has already been computed at the section nT.

As a result, we can find the filters of the filter bank $\{\Phi(t)\}$ by operating according to one section $n, \forall n \geq 0$ only. Figure 4.4 depicts the different filters obtained for a CPM with $L = 2$, rectangular pulse and $h = 2/3$ at any section nT. Observe that our Laurent's receiver filter bank holds less filter than the Rimoldi's one.

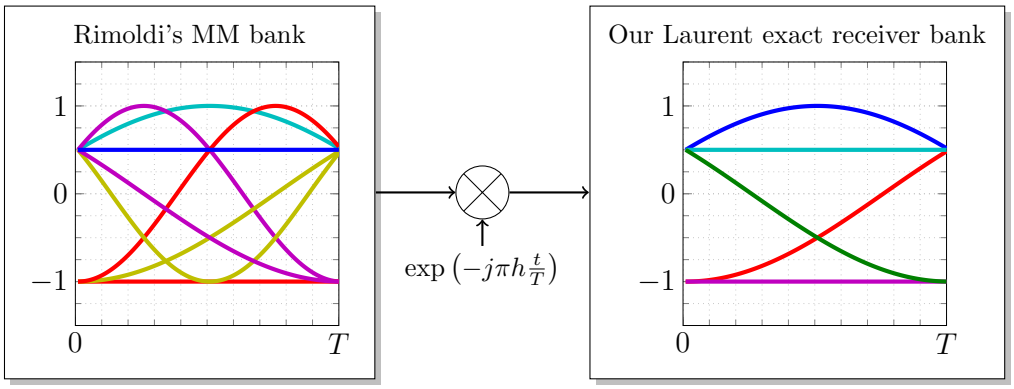

Figure 4.4: Rimoldi's MM and our Laurent's exact filter bank for the CPM with $M = 2$, $L = 2$, rectangular pulse and $h = 2/3$

- In contrast, if k is odd, we get:

$$\begin{aligned}\exp(-j\pi h(M-1)(n+1)) &= \exp(-j\pi h(M-1)n)\exp(-j\pi h(M-1)) \\ &= \exp(-j\pi h(M-1)n)\exp(-j\pi h(M-1) + j2\pi hp) \qquad (2\pi hp = 0[2\pi])\end{aligned}$$

$$= \exp\left(-j\pi h(M-1)n\right)\exp\left(j\pi 2(p-M+1)h\right)\exp\left(j\pi h(M-1)\right)$$

Now $2(p-M+1)$ is even. Following the same steps as for the previous case, one can easily show that the filter bank at $n+1$ is new and can be computed by multiplying the filters in the previous filter bank, *i.e.* at nT, by $\exp\left(j\pi h(M-1)\right)$.

In general, and in the same manner, we show that the filter bank at $n+\ell, \forall \ell \in \mathbb{N}$ is exactly the same as the one at $n+(\ell \text{ modulo } 2)$. As a result, to find all the receiver filters, we begin by computing all the $\{\Phi(t)\}$ corresponding to the section $n, \forall n \geq 0$, then, we multiply the obtained filter bank by $\exp\left(j\pi h\right)$, which is equivalent to recomputing all the $\{\Phi(t)\}$ at the section $(n+1)T$. Figure 4.5 depicts the different filters obtained for the CPM with $L=2$, rectangular pulse and $h=3/4$ in two consecutive trellis sections. Observe that our Laurent's receiver filter bank contains less filter than the Rimoldi's one (12 and 16 respectively).

To summarize, the filter bank $\{\Phi(t)\}$ of our Laurent-based receiver is obtained from Rimoldi's MM filter bank by, $\forall t \in [0,T]$:

$$\{\Phi(t)\} = \begin{cases} \left\{\Omega(t)\exp\left(-j\pi\frac{(M-1)h}{T}t\right)\right\}, \text{if } k \text{ in } h \text{ is even} \\ \underbrace{\left\{\Omega(t)\exp\left(-j\pi\frac{(M-1)h}{T}t\right)\right\}}_{\text{filter bank at even instants}} \cup \underbrace{\left\{\Omega(t)\exp\left(-j\pi\frac{(M-1)h}{T}t\right)\exp\left(j\pi h(M-1)\right)\right\}}_{\text{filter bank at odd instants}}, \text{otherwise} \end{cases} \tag{4.18}$$

4.4 Maximum *a posteriori* symbol receiver

4.4.1 Discussions

In the context of the CPM, only few works have been conducted to derive a MAP symbol detector. [MFG97] proposed a method to perform MAP symbol detection on Kaleh's trellis by the mean of asymmetrical backward/forward recursions. Only slight degradation in performance is observed when using only the proposed forward recursion.

However, the proposed algorithm is not exact since it uses some approximations for the proposed recursions and neglects the noise correlation at the output of the receiver filter bank $\{C_k(t)\}_k$ as suggested by the transition metric [MFG97, Eq. (47)]. This is due to the fact that some of these filters have support greater than T. Figure 4.6 shows the power spectrum densities of the white noise $n(t)$ filtered by the components $\{C_k\}$ and sampled each nT.

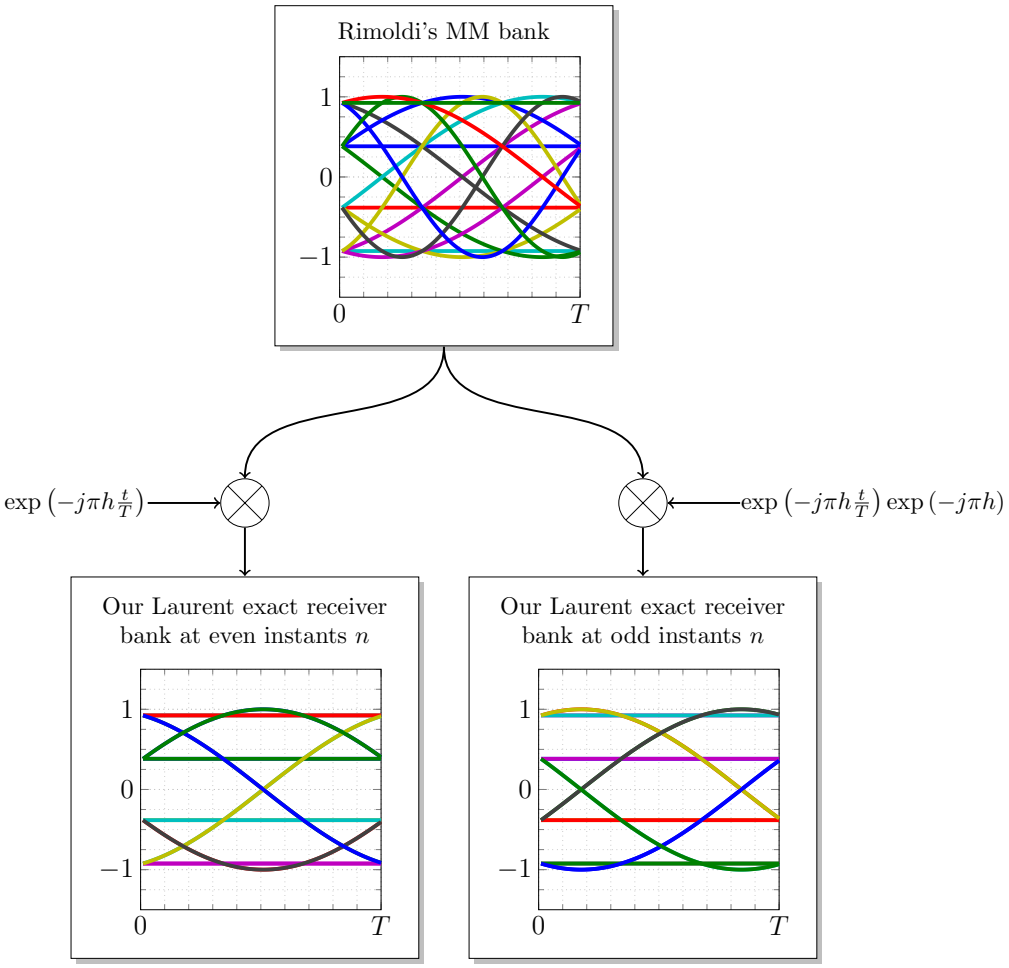

Figure 4.5: Rimoldi's MM and our Laurent's exact filter bank for the CPM with $M = 2$, $L = 2$, rectangular pulse and $h = 3/4$

In [CB05], authors proposed a MAP symbol derivation based on the Ungerboeck model [Ung82] for a CPM receiver. It is shown that the joint *a posteriori* probabilities (APP) can be obtained by using a factor graph (FG) and a sum product algorithm (SPA) framework [KFL01]. This method can be summarized as the following:
Consider an arbitrarily multivariate function $\mathcal{I}(i_1, \ldots, i_n)$ that can be factorized as a product of other multivariate functions $\mathcal{J}_j$ as following:

$$\mathcal{I}(i_1, \ldots, i_n) = \prod_j \mathcal{J}_j(i_{Q_j}), \quad i_{Q_j} \subset \{i_1, \ldots, i_n\}$$

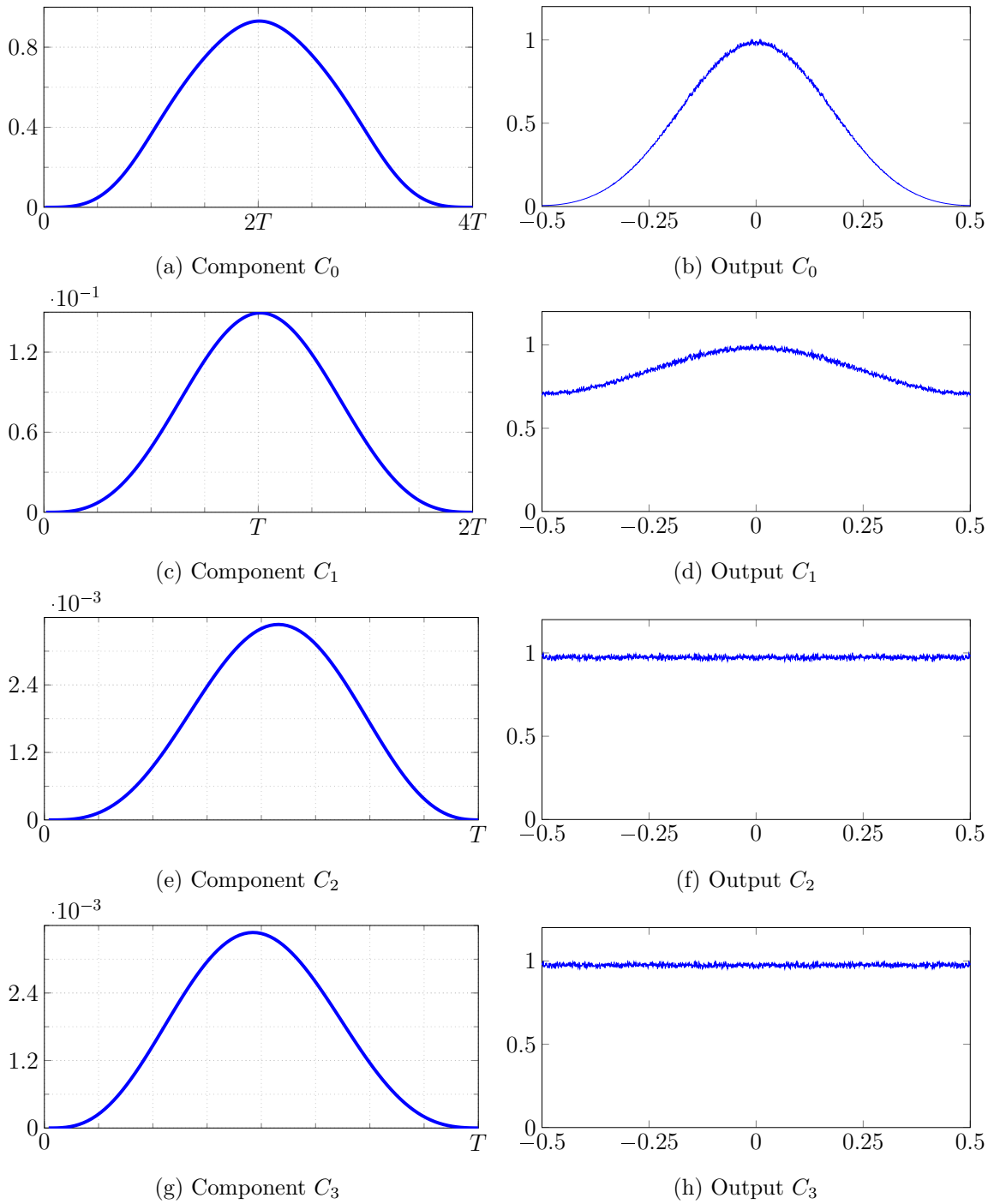

(a) Component C_0 (b) Output C_0

(c) Component C_1 (d) Output C_1

(e) Component C_2 (f) Output C_2

(g) Component C_3 (h) Output C_3

Figure 4.6: Normalized power spectrum densities of a white noise samples filtered by Laurent's Components of a binary $(L = 3, h = 2/3, RC)$ CPM

This factorization can be modeled by a factor graph where each variable i_k (and each function $\mathcal{J}_j$) is represented by a variable node (respectively by a factor node). An edge exists between the variable node i_k and the factor node $\mathcal{J}_j$ if $i_k \in i_{Q_j}$. By performing the SPA algorithm on the described factor graph, one can approximate the marginal of the global function $\tilde{\mathcal{I}}(i_k)$ with respect to all other variables $i_j, j = 1, \dots n$, as following [WS01]:

$$\tilde{\mathcal{I}}(i_k) = \sum_{i_j, j \neq k} \mathcal{I}(i_1, \dots, i_n)$$

The final result will depend on how many SPA update iterations are performed and in which scheduling they are performed. However, if the graph is finite and has no cycles, then it can be shown that there exists scheduling that computes the exact value $\tilde{\mathcal{I}}(i_k)$ [WS01].

In [CB05], it is stated that although the proposed receiver has a forward/backward structure, it is different from the BCJR [BCJR74] algorithm (in the context of the Forney model, *i.e.* using a whitening filter), because the local functions are not necessarily probability mass functions and the algorithm cannot be derived using probabilistic arguments. However, it is mentioned that the performance of the two algorithms should be the same. In the context of the optimal CPM receiver, neither the branch metric nor the scheduling are explicitly given. In the case of the reduced complexity detection, the given branch metric [CB05, Eq. (21)] uses the fact that the first Laurent's components concentrate most of the signal power (see section Section 4.5). Besides that, authors made an implicit approximation in order to derive the metric in [CB05, Eq. (20)]. It seems that they reused the same branch metric of the ML sequence receiver in [CR97]. In the scope of sequence detector, we have shown in Section 4.3 that this criterion is exact. However, if we want to implement this strategy for the symbol-based MAP detector, $p(\alpha_n|\boldsymbol{r})$ is different from [CR97, Eq. (19)] since the inter-symbol interference (ISI) is not taken into account and the noise samples $\{n_i(n)\}_n, \forall i \in [\![0, K/2]\!]$ are correlated.

Inspired from our ML receiver, we will expose in the following a new and exact MAP symbol detector based on the BCJR algorithm by changing simply the receiver filter bank and without introducing any whitening filter.

4.4.2 Exact MAP receiver derivation

4.4.2.1 Notations and preliminaries

In this section, for ease of notation, σ_n^L is simply denoted σ_n. Define the log-likelihood ratio (LLR) of the symbol bit $\alpha_n = \pm 1$ as:

$$\begin{aligned} LLR(\alpha_n) &= \ln\left(\frac{p(\alpha_n = +1|\boldsymbol{r})}{p(\alpha_n = -1|\boldsymbol{r})}\right) \\ &= \ln\left(\frac{\sum_{(s,s')\in\mathcal{S}^+} p(\sigma_{n-1} = s, \sigma_n = s', \boldsymbol{r})}{\sum_{(s,s')\in\mathcal{S}^-} p(\sigma_{n-1} = s, \sigma_n = s', \boldsymbol{r})}\right) \end{aligned}$$

where $\mathcal{S}^+$ and $\mathcal{S}^-$ are the set of state tuples (s, s') such that:

$$\begin{aligned} \mathcal{S}^+ &= \{(s,s')\diagup(\sigma_{n-1} = s) \mapsto \sigma_n = s'|\alpha_n = +1\} \\ \mathcal{S}^- &= \{(s,s')\diagup(\sigma_{n-1} = s) \mapsto \sigma_n = s'|\alpha_n = -1\} \end{aligned}$$

Denoting $\boldsymbol{r}_k^l = [r_i(j)]_{i,k\leq j\leq l}$, $p(\sigma_{n-1} = s, \sigma_n = s', \boldsymbol{r})$ can be factorized as:

$$\begin{aligned} p(\sigma_{n-1} = s, \sigma_n = s', \boldsymbol{r}) &= p(\sigma_{n-1} = s, \sigma_n = s', \boldsymbol{r}_0^{n-1}, \boldsymbol{r}_n, \boldsymbol{r}_{n+1}^N) \\ &= \underbrace{p(\boldsymbol{r}_{n+1}^N|\sigma_n = s')}_{\mathcal{B}_n}\underbrace{p(\alpha_n)p(\boldsymbol{r}_n|\sigma_{n-1} = s, \sigma_n = s')}_{\mathcal{G}_n}\underbrace{p(\sigma_{n-1} = s, \boldsymbol{r}_0^{n-1})}_{\mathcal{A}_n} \end{aligned}$$

Please refer to the chapter 1 for more details.

4.4.2.2 Exact MAP-symbol detector

It is known that $\mathcal{A}_n$ and $\mathcal{B}_n$ can be computed by means of a forward and a backward recursions [BCJR74] using $\mathcal{G}_n$. $p(\alpha_n)$ is the *a priori* probability of the bit α_n. Using the introduced orthonormal basis, the transition metric is given by:

$$\begin{aligned} p(\boldsymbol{r}_n|\sigma_{n-1} = s, \sigma_n = s') &\propto \exp\left(\frac{-1}{N_0}\sum_i |r_i(n) - \Phi_i(0)|^2\right) \\ &\propto \exp\left(\frac{2}{N_0}\Re\left(\sum_i r_i(n)\Phi_i(0)^*\right)\right) \end{aligned} \tag{4.19}$$

$\{\Phi_i(0)\}_i$ is here the signal statistic relative to the transition $(\sigma_{n-1} = s, \sigma_n = s')$ that takes into account the current pseudo-symbols $\{a_{k,n}\}_k$ and the ISI symbols $\{a_{k,n-\ell}\}_\ell$ and that is shown to be a sufficient statistic for $[nT, (n+1)T]$ interval. The corresponding duration-T time waveforms $\Phi(t)$ are given by Eqs. (4.11) and (4.18) as defined in Eq. (4.15)

CPM	1^{st} component	2^{nd} component	Others
(a)	99.6%	0.37%	2.6 10^{-4}%
(b)	93%	6.25%	0.23%

Table 4.2: Energy distribution in Laurent's components

4.5 Complexity reduction

Thanks to the Laurent's decomposition, low complexity receivers can be easily and efficiently derived by truncating the second summation in Eq. (4.3), which approximates the CPM signal with only $K' < K$ components. Usually taking $K = M - 1$ is a very good approximation since the first components convey the most significant part of the signal energy [MM95]. Table 4.2 illustrates the energy distribution over the Laurent's components for (a) the CPM used in the GSM ($L = 3$, $BT = 0.3$, Gaussian pulse) and (b) the MSK of memory $L = 3$(rectangular pulse).

Kaleh's state vector is define as $\sigma_n^L = [a_{0,n-L}, \alpha_{n-L+1}, \ldots, \alpha_{n-1}]$. If we truncate the CPM representation to the first component $C_0(t)$ only, we still need the whole information in σ_n^L to compute $a_{0,n}$ (see Eq. (4.7)). However, redefining the state vector as $\sigma_n^{L'} = [a_{0,n-1}, \alpha_{n-L+1}, \ldots, \alpha_{n-1}]$ and using Eq. (4.4) to compute $a_{0,n}$, allows us to reduce the number of the trellis states from $p2^{L-1}$ to p states only. Similar result can be drawn for M-ary CPM signals. The recursion Eq. 4.14 becomes:

$$
\begin{aligned}
A_{k,n-\ell} &= A_{0,n-L} + \boldsymbol{\alpha}_{n-L+1}^n \boldsymbol{J}^\ell \begin{bmatrix} 1 \\ \boldsymbol{\beta}_{K-1-k} \end{bmatrix}, \quad 0 \le k \le K-1, 0 \le \ell \le L_k - 1 \\
&= A_{0,n-1} - \sum_{j=1}^{L-1} \alpha_{n-j} + \boldsymbol{\alpha}_{n-L+1}^n \boldsymbol{J}^\ell \begin{bmatrix} 1 \\ \boldsymbol{\beta}_{K-1-k} \end{bmatrix} \\
&= A_{0,n-1} - \boldsymbol{\alpha}_{n-L+1}^n \begin{bmatrix} 0 \\ 1 \\ \vdots \\ 1 \end{bmatrix} + \boldsymbol{\alpha}_{n-L+1}^n \boldsymbol{J}^\ell \begin{bmatrix} 1 \\ \boldsymbol{\beta}_{K-1-k} \end{bmatrix} \\
&= A_{0,n-1} + \boldsymbol{\alpha}_{n-L+1}^n \left(\boldsymbol{J}^\ell \begin{bmatrix} 1 \\ \boldsymbol{\beta}_{K-1-k} \end{bmatrix} - \begin{bmatrix} 0 \\ 1 \\ \vdots \\ 1 \end{bmatrix} \right)
\end{aligned}
$$

Scheme	$\sigma_n^{L'}$	#states	Current symbols	ISI symbols
(1)	$[a_{0,n-1}]$	p	$a_{0,n}$	$a_{0,n-1}$
(2)	$[a_{0,n-1}, \alpha_{n-1}]$	$2p$	$a_{0,n}$, $a_{1,n}$	$a_{0,n-1}$, $a_{0,n-2}$
(3)	$[a_{0,n-1}, \alpha_{n-1}, \alpha_{n-2}]$	$4p$	$a_{0,n}$, $a_{1,n}$, $a_{2,n}$, $a_{3,n}$	$a_{0,n-1}$, $a_{0,n-2}$, $a_{0,n-3}$ $a_{1,n-1}$
	$\vdots$			
(L)	$[a_{0,n-1}, \alpha_{n-1}, \ldots, \alpha_{n-L+1}]$	$2^{L-1}p$	all $\{a_{k,n}\}_{0\leq k\leq K-1}$	all $\{a_{k,n-\ell}\}_{\substack{0\leq k\leq K/2-1 \\ 1\leq \ell\leq L_k-1}}$

Table 4.3: State vector and different availlable pseudo-symbols of our Laurent's receiver when different trellis reduction factors are considered

$$= A_{0,n-1} + \boldsymbol{\alpha}_{n-L+1}^{n} \left(\boldsymbol{J}^{\ell} \begin{bmatrix} 1 \\ \boldsymbol{\beta}_{K-1-k} \end{bmatrix} - \begin{bmatrix} 0 \\ \boldsymbol{\beta}_{K} \end{bmatrix} \right) \tag{4.20}$$

In our receiver model, approximating the signal with only $C_0(t)$ leads to filtering the signal with $C_0(t)|_{0\leq t\leq T}$ modulated by $a_{0,n}$ (the term $B(t)$ in Eq. (4.10)) and $C_0(t+T)|_{0\leq t\leq T}$ modulated by $a_{0,n-1}$ (the ISI term $C(t)$ in Eq. (4.10)). If we want to take into account additional components and ISI terms, we should extend our state vector by one or more symbols $\{\alpha_{n-\ell}\}_{\ell}$. Table 4.3 summarizes the trade-off between the trellis reduction factor and the accuracy of the recomputed current and ISI terms.

The current and the ISI pseudo-symbols that are accessible from a reduce state trellis depends on the number of the symbols on the trellis state definition, the component index k and the past trellis section ℓ. They can be characterized by the second term in Eq. 4.20: the pseudo-symbol $A_{k,n-\ell}$ is recoverable from the transition $(\sigma_n^{L'}, \alpha_n)$ if the indices of the non-zero elements in the column vector:

$$\boldsymbol{J}^{\ell} \begin{bmatrix} 1 \\ \boldsymbol{\beta}_{K-1-k} \end{bmatrix} - \begin{bmatrix} 0 \\ \boldsymbol{\beta}_{K} \end{bmatrix} \tag{4.21}$$

correspond to entries in $\boldsymbol{\alpha}_{n-L+1}^{n}$ that belong to the set $\{\sigma_n^{L'}, \alpha_n\}$. Or alternatively, the pseudo-symbol $A_{k,n-\ell}$ is recoverable if the information bit α_{n-g+1} belongs to $\{\sigma_n^{L'}, \alpha_n\}$ where g is the greatest index of the non-zero elements in Eq. (4.21).

4.6 Asymptotic analysis for iterative and non-iterative receivers: impact of the new MAP receiver

4.6.1 General behavior

To have insights on the performance improvement of the proposed new receiver, one can conduct an asymptotic analysis using the Extrinsic information transfer (EXIT) chart analysis [Hag04]. Based on this analysis, one can approximate the maximum achievable rate R^* for an outer serially concatenated code by the area under the EXIT curves [Hag04] associated with the iterative MAP decoder performed on the two CPM receivers (the classical and the one introduced in this paper). In this section, I_a and I_e denote respectively the *a priori* and extrinsic mutual information of the soft CPM decoder.

4.6.2 Scheme 1: GMSK pulse, $h = 1/3, L = 3, BT = 0.3$

Figure 4.7a depicts the maximum achievable rate R^* of both receivers for the this CPM scheme for an iterative detector. Figure 4.7b shows the curve corresponding to R^* in a non-iterative decoder: *i.e.* the ordinate of the point corresponding to the *a priori* mutual information equal to zero of the corresponding EXIT function. In the iterative decoding scheme, the receiver introduced in this paper allows a noticeable gain over the classical one. For instance, for a rate-1/2 outer code, we observe a gain of almost 1.74 dB, and this is reached by changing only the receiver filter bank.

Concerning the uncoded CPM, Fig. 4.8 depicts the performance comparison between the two receivers. One can see that the performance is almost the same in both receivers except in low SNRs. We observe that for a BER of 10^{-1}, a gain of 1dB is observed explaining that an itrative receiver can benifit from the new receiver.

4.6.3 Scheme 2: Rectangular pulse, $h = 3/4, L = 3$

We know that the Rimoldi's receiver introduced in Section 4.2.1 and its decoder [MA01] are exact and optimal by construction. As a result, even if the Laurent's and Rimoldi's receivers are different, a good criterion to evaluate the performance of the two Laurent's receivers is to compare they performance to the Rimoldi's one.

Unlike the previous CPM, a great improvement is made in this uncoded CPM scheme as suggested by the different curve values at $I_a = 0$ in Fig. 4.9; same conclusion can be made for the coded iterative scheme as showed by the big difference between the curves of the two Laurent's receivers at higher I_a.

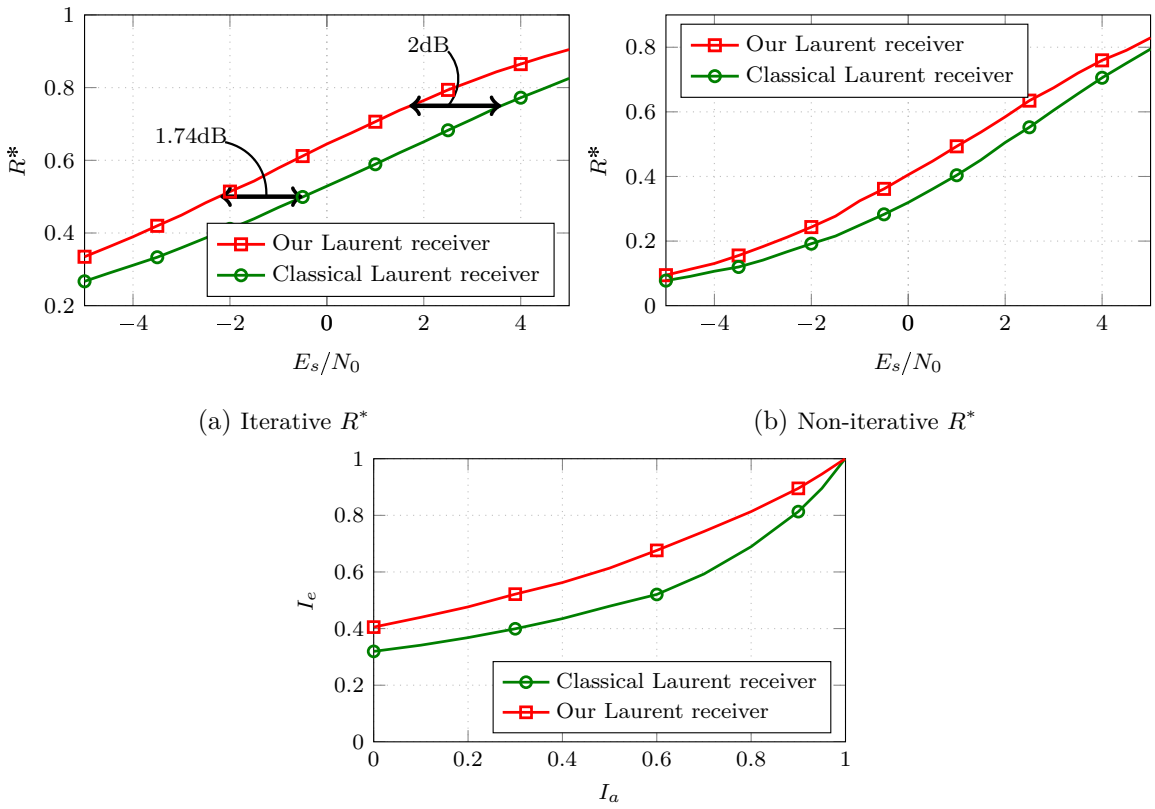

(a) Iterative R^*

(b) Non-iterative R^*

(c) EXIT chart at $E_b/N_0 = 0$dB

Figure 4.7: An EXIT curve and comparison of R^* of the coded GMSK $h = 1/3, L = 3, BT = 0.3$

In comparison to the Rimoldi's receiver, which is optimal, we observe that the new Laurent-based receiver has the same performance in terms of the EXIT chart curves. Finally, Fig. 4.10 depicts the performance comparison between the three receivers: one can see that the performance of our Laurent's receiver is the same as the Rimoldi's one, and that both of them outperform the classical Laurent's receiver. This can be explained by the EXIT charts of the detectors as depicted in Fig. 4.9: for the non concatenated scheme, we are interested only by the points corresponding to a null *a priori* mutual information. The difference between the two curves is noticeable at low signal to noise ratios (SNR). However, because the bit error rate of the two decoders is quite high, it is hard to distinguish between the bit error rate (BER) curves of the two detectors. For middle SNRs, the different between the EXIT curves is noticeable, which leads to quite big gap in terms if the BER. And finally, for high SNRs, since the points at the origin of both detector EXIT curves get very close

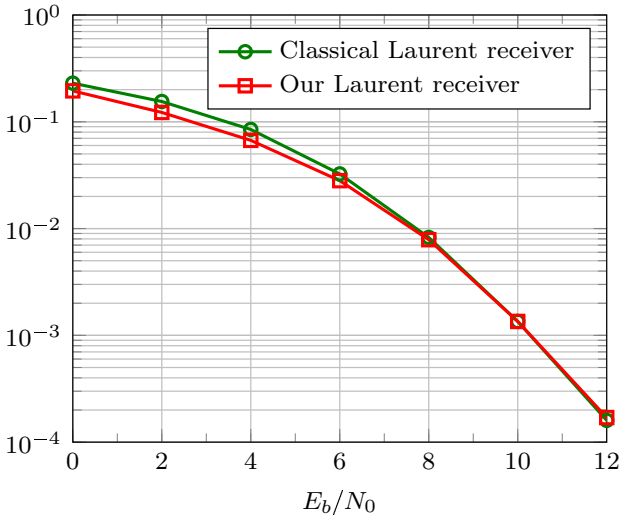

Figure 4.8: Comparison of the BER performance of the two receivers for uncoded GMSK with $h = 1/3, L = 3$ and $BT = 0.3$

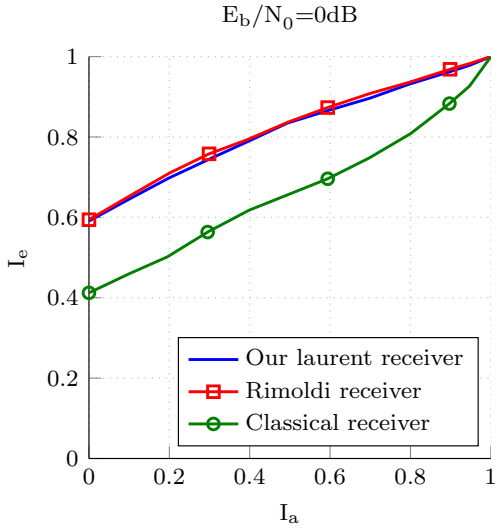

Figure 4.9: Comparison of the EXIT chart curves of the Rimoldi's, classical Laurent's and the new Laurent's receivers. The considered CPM scheme is: $(M = 2, h = 3/4, L = 3,$ rectangular pulse)

(actually they both converge to the point $(0, 1)$), the difference between the two detectors in terms of BER becomes very small.

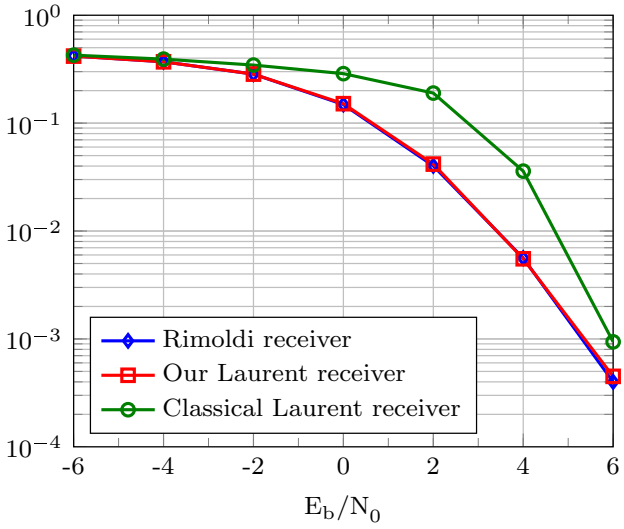

Figure 4.10: Comparison of the BER performance of the two receivers for uncoded CPM with $h = 3/4, L = 3$ and a rectangular pulse

4.6.4 Code design

We can optimize Low Density Parity Check (LDPC) codes for the two receivers. For this design, we consider the receiver factor graph depicted in Fig. 4.11. $\{\pi_i\}_i$ are partial interleavers and d_v (or d_c) the variable node (respectively check node) maximum degree (please refer to the chapter 2 for more details).

Using the same method introduced in the chapter 2, Table 4.4 summarizes the degree profiles of the optimized LDPC codes and their corresponding asymptotic threshold. λ_i (and ρ_j) is the fraction of edges connected to a degree-i bit node (respectively degree-j constraint node).

4.6.5 Simulation results

This section provides simulation results for coded CPM schemes. Table 4.4 summarizes the optimized rate-1/2 and rate-1/3 LDPC codes. The considered LDPC codes have 12000 and 6000 information bits respectively. A maximum number of 200 turbo iterations is considered. Figures 4.12 and 4.13 depict the Bit Error Rate (BER) for the considered schemes. As expected, our receiver outperforms the classical one.

	$R = 1/3$		$R = 1/2$		$R = 3/4$	
	classical	ours	classical	ours	classical	ours
$R^* = R$ at $E_s/N_0 =$	-3.49	-5	-0.5	-2.24	3.6	1.7
Optimized threshold at	-3.3	-4.93	-0.47	-1.87	3.6	1.7
λ_1	0.087	0.05	0.11	0.12	0.03	0.16
λ_2	0.55	0.46	0.48	0.59	0.4	0.37
λ_4	-	-	0.12	-	-	-
λ_6	0.133	-	-	-	-	0.13
λ_7	0.12	-	-	-	0.15	0.06
λ_8	-	0.18	-	-	-	-
λ_9	-	0.06	-	0.009	-	-
λ_{10}	-	-	0.29	0.28	-	-
λ_{20}	-	-	-	-	0.42	0.28
λ_{39}	-	0.12	-	-	-	-
λ_{40}	0.11	0.13	-	-	-	-
ρ_2	0.24	-	-	-	-	-
ρ_3	0.76	0.29	-	-	-	-
ρ_4	-	0.71	0.2	0.4	-	-
ρ_5	-	-	0.8	0.6	-	-
ρ_9	-	-	-	-	-	0.81
ρ_{10}	-	-	-	-	-	0.19
ρ_{13}	-	-	-	-	0.77	-
ρ_{14}	-	-	-	-	0.23	-

Table 4.4: Different optimized degree profiles for the GMSK with $h = 1/3, L = 3$ and $BT = 0.3$ and the corresponding thresholds for the classical and the proposed receivers

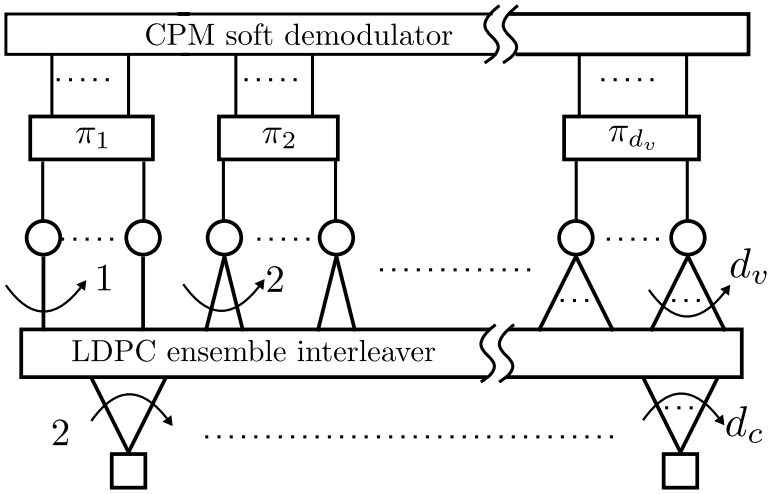

Figure 4.11: Receiver structure for the unstructured LDPC codes

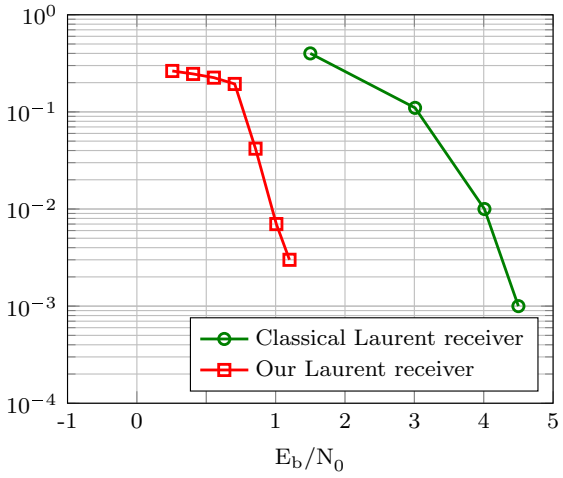

Figure 4.12: BER of the two receivers with a rate-1/2 optimized LDPC code

4.7 Code design and complexity reduction

As seen in the section 4.5, low complexity receivers can be easily designed, with a negligible performance degradation, using only the most significant components, remaining ones can be neglected or treated as interference. Surprisingly, no works have been conducted to study the joint optimization of an LDPC code concatenated with such optimal or low complexity CPM detector. In this section, we will show that performance of the optimized LDPC codes for full complexity receivers remain

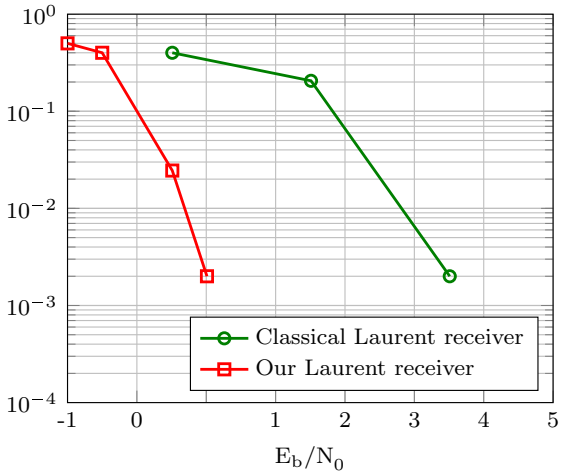

Figure 4.13: BER of the two receivers with a rate-1/3 optimized LDPC code

optimal for low complexity receivers as long as a proper set of the Laurent's components is selected.

For the code design, we apply to same method and notations introduced in chapter 2. Fig 4.14 depicts the EXIT curves and the achievable rates R^* of the 3GMSK ($M = 2, L = 3, BT = 0.3, h = 1/2$, Gaussian pulse) and the 3MSK ($M = 2, L = 3, h = 1/2$, rectangular pulse) CPMs at different SNRs.

For the 3MSK, since $C_1(t)$ is not negligible compared to $C_0(t)$ (see Fig 4.14a), considering only the first order approximate modifies considerably the EXIT charts, as depicted in Fig. 4.14e, and thus produces a rate loss, for example when $R^* = 1/2$, the loss is of almost 0.5dB as depicted in Fig. 4.14c. In this case, a second order approximate is necessary. Whereas for the 3GMSK, the first component $C_0(t)$ holds enough energy to remain a good approximation of the optimal detector EXIT as illustrated in Fig. 4.14f. The idea behind considering enough pulses according to the EXIT curves is that, as long as they have the same EXIT curves, the same optimized LDPC code can be used with either optimal or reduced complexity CPM receiver.

4.7.1 Simulation results

This section gives simulation results of some optimized rate-1/2 LDPC codes for the 3GMSK and the 3MSK. Simulations were performed using 16000 information bits and 250 turbo iterations. Table 4.5 summarizes the optimized degree distribution profiles of the LDPC codes.

Figure 4.15 depicts the 3MSK and the 3GMSK bit error rate (BER) and frame error rate (FER)

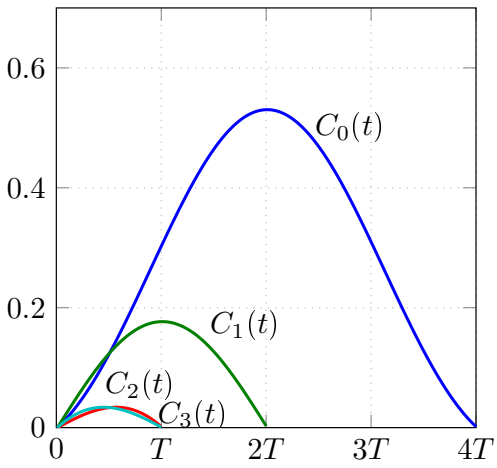

(a) 3MSK components

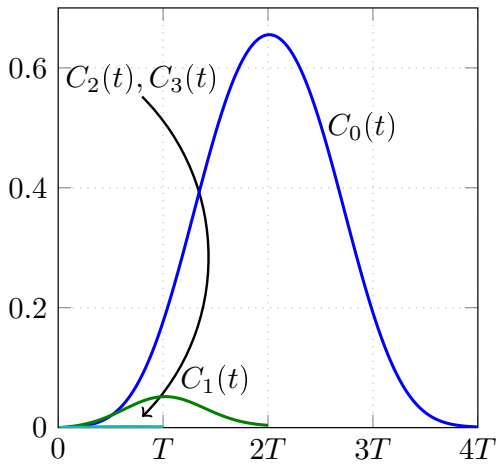

(b) 3GMSK components

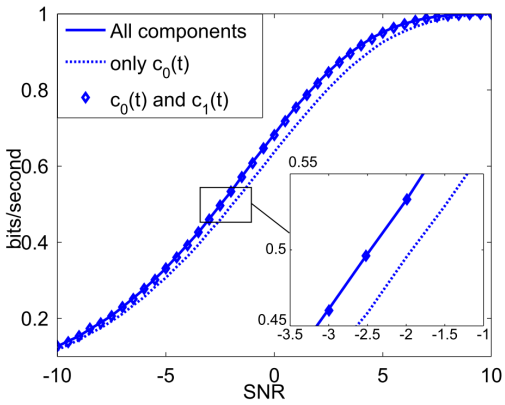

(c) 3MSK achievable rate R^*

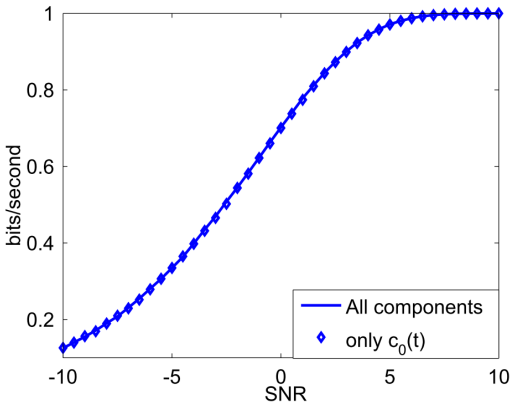

(d) 3GMSK achievable rate R^*

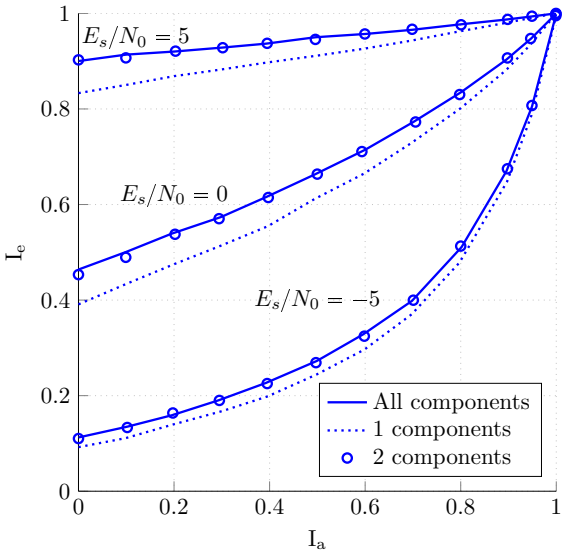

(e) 3MSK EXIT charts

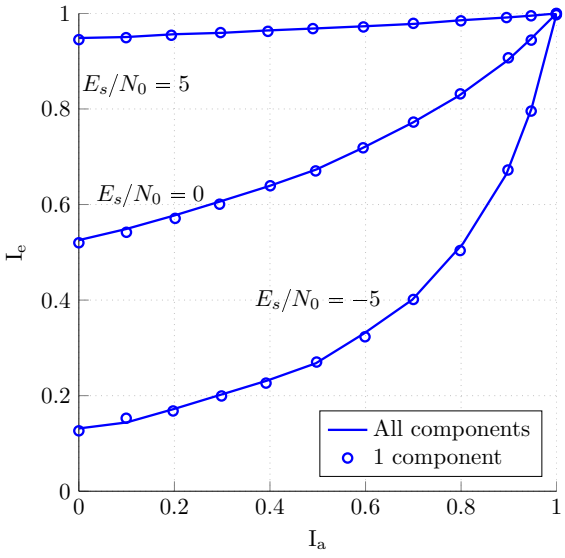

(f) 3GMSK EXIT charts

Figure 4.14: Laurent's components, R^* and EXIT curves for 3GMSK and 3MSK

	MSK	3MSK	3GMSK
$(E_s/N_0)^*$	-2.5	-2.4	-2.5
$(E_s/N_0)_{opt}$	-2.4	-2.3	-2.5
λ_1	0.1294	0.1475	0.1273
λ_2	0.5148	0.545	0.5201
λ_5	0.0679	0.0223	0.0577
λ_{10}	0.2879	0.2852	0.2949
ρ_4	0.25	0.5	0.3
ρ_5	0.75	0.5	0.7

Table 4.5: Optimized LDPC codes for design rate $R = 0.5$

results. As expected, the simulated thresholds agree with the theoretical ones. By considering enough components, it is clear that the optimal-receiver optimized LDPC codes provide very satisfactory results when used with the low complexity receivers.

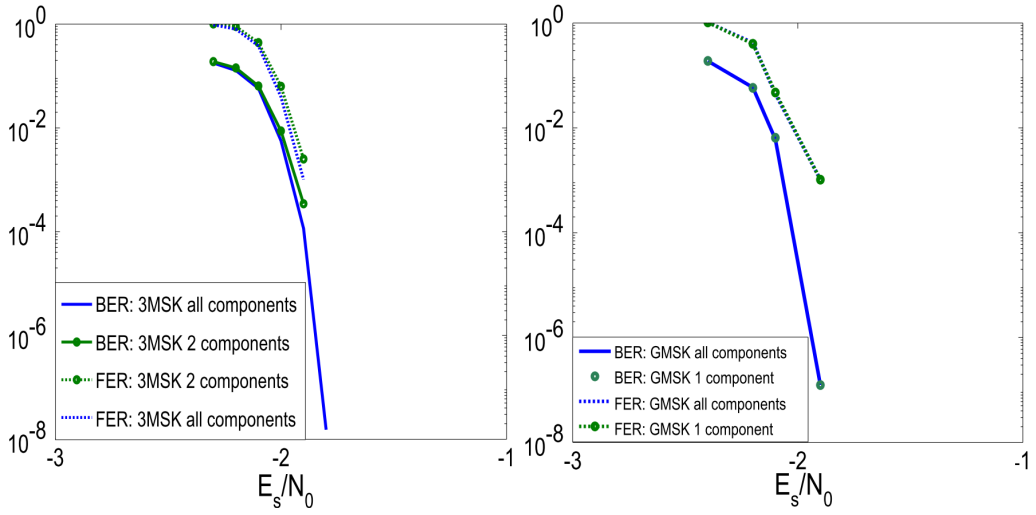

(a) 3MSK (b) 3GMSK

Figure 4.15: BER and FER for optimized concatenated LDPC code with 3MSK and 3GMSK

4.8 Conclusion

In this chapter, we designed an optimal and exact receiver based on the Laurent's decomposition. This receiver allows to take into account the inter-component interference, and to design receiver filters whose support is equal to the symbol period. Besides that, we derived two methods to compute the proposed filter bank. The first one is based on the Laurent's decomposition itself, and the second is computed from the Rimoldi's decomposition. The simulated results shows that our receiver outperforms the classical one by changing only the filter bank and avoiding the theoretical need for noise whitening as considered in the classical receiver. Finally we proposed a method to design LDPC codes for full complexity Laurent's new receiver that remain optimal for the low complexity one.

Chapter 5

Application to the aeronautical channel

Summary

Résumé

Dans ce chapitre, nous appliquons notre méthode de design dans le contexte qui est derrière la motivation de cette thèse: communication pour les drones sur des liens satellites. Ce type de communication est modélisé par le canal satellite aéronautique [B$^+$63, B$^+$73, SLPF$^+$08, ser09]. En outre, nous évaluons la performance des CPM codées lorsque nous considérons une égalisation par minimisation de l'erreur quadratique moyenne (MMSE) dans le cas d'un canal séléctif en fréquence générique. Le but

de ce chapitre est de montrer la faisabilité d'une *simple* égalisation dans le cadre du canal aéronautique. Les schémas proposés ne sont pas la solution ultime, mais une approche directe parmis les techniques d'égalisation. Divers résultats de simulation sont fournis. Des résultats qui montrent que l'égalisation peut être très efficace dans ces canaux pour la CPM et que les schémas concaténés LDPC proposés sont très compétitifs par rapport à certains systèmes proposés, comme celui du DVB-S2 [ETS05].

In this chapter, we compare the performance of our coded-CPM design with the DVB-RCS2 standard [BCDB+13] in both the AWGN and the aeronautical channel. Moreover, we evaluate the performance of the coded CPM when we consider a simple frequency domain minimum mean square error (FDE MMSE) equalization for both the general frequency selective and the aeronautical channels.

5.1 Main CPM notations

Consider a sequence of N information symbols $\boldsymbol{\alpha} = \{\pm 1, \pm 3, \ldots, \pm(M-1)\}^N$. Recall that the transmitted CPM signal can be written as:

$$\begin{aligned} s(t, \boldsymbol{\alpha}) &= \sqrt{\frac{2E_s}{T}} \cos\left(2\pi f_0 t + \theta(t, \boldsymbol{\alpha}) + \theta_0\right) \\ &= \Re[s_b(t, \boldsymbol{\alpha}) e^{j2\pi f_0 t}] \end{aligned} \tag{5.1}$$

with

$$\theta(t, \boldsymbol{\alpha}) = \pi h \sum_{i=0}^{N-1} \alpha_i q(t - iT), \quad q(t) = \begin{cases} \int_0^t g(\tau) d\tau \\ \frac{1}{2}, t \geq L \end{cases}$$

f_0 is the carrier frequency, θ_0 the initial phase shift, $\theta(t, \boldsymbol{\alpha})$ the information carrying phase, $g(t)$ the frequency pulse, $h = k/p$ the modulation index, L the memory and $\Re(.)$ the real part. $s_b(t, \boldsymbol{\alpha})$ is the complex envelope of the CPM signal and is given by:

$$s_b(t, \boldsymbol{\alpha}) = \sqrt{\frac{2E_s}{T}} e^{j(\theta(t, \boldsymbol{\alpha}) + \theta_0)}$$

We clearly see here that the signal is a non-linear function of the transmitted symbols. Without loss of generality, we consider $\theta_0 = 0$.

5.2 Performance comparison in the Aeronautical channel

5.2.1 The aeronautical channel model

As depicted by Fig. 5.1, the aeronautical channel is characterized by the direct path or the line of sight (LOS) which is often present. Depending on the location and the geometry of the environment,

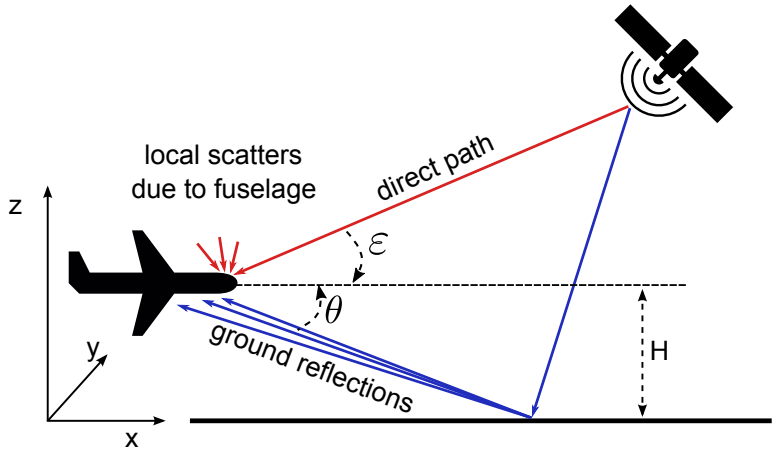

Figure 5.1: Aeronautical channel

multiple attenuated ground reflections reach the UAV antenna. Moreover, local reflections may also take place depending on the fuselage and the wings surface.

The aeronautical channel modelling started with the papers of Bello *et al* [B+63, B+73]. Later on, the German Aerospace Center (DLR) consolidated the established theoretical models by series of measurement campaigns [NHP+87, HNP+86]. Finally, the measurements organized in [SLPF+08] completed the channel modelling by characterizing the local scatters occurring on the aircraft fuselage and wings surface. The final obtained model was finally adopted by the ITU recommendations [ser09].

In this thesis, we assume that the frame duration is smaller than the channel coherence time. In this case, the different channel parameters are considered constant during the whole frame transmission, but still random form one frame to the other. The statistical aeronautical channel considered in this thesis is characterized by a two-taps model:

- The first component is composed of the LOS path. This latter is divided into two different paths: the direct LOS (DLOS) path and the local scatters (SC).
- The second component is composed of the delayed and the attenuated ground reflections (GR)
- Without loss of generality, in order to insure that the direct LOS signal has power equal to 1, we normalize all the paths by the attenuation factor of the DLOS path.
- The local scatters and the ground reflections are modulated by two different complex colored Gaussian processes, h_{SC} and h_{GR} respectively. The absolute value of these Gaussians gives a Rayleigh amplitude fading.

The diagram in Fig. 5.2 summarizes the different parameters of our considered aeronautical channel model (refer to Fig. 5.1 for the main physical quantities):

- The power of the total LOS path (DLOS+SC) is attenuated by a factor α_{LOS}
- The power of the DLOS and the SC signals are attenuated by k_1 and k_2 respectively according to the power ratio k_{LOS} as the following:

$$\begin{cases} k_{LOS} = \frac{k_1}{k_2} \\ k_1 + k_2 = 1 \end{cases}$$

- The ground reflections corresponds to the sent signal delayed by τ_{GR} and attenuated by α_{GR} according to the power ration $\frac{C}{M}$ as following:

$$\begin{cases} \frac{C}{M} = \frac{\alpha_{LOS}}{\alpha_{GR}} \\ \alpha_{LOS} + \alpha_{GR} = 1 \\ \tau_{GR} = \frac{2H \sin \varepsilon}{c} \end{cases}$$

- The local scatters and the ground reflections are modulated by two different complex colored Gaussian processes, h_{SC} and h_{GR} respectively. h_{SC} and h_{GR} are generated following:

$$h_{SC} = \exp\left(-\frac{8\pi^2\alpha^2}{\lambda^2}\left[(v_x \sin\varepsilon + v_z \cos\varepsilon)^2 + (v_y \sin\varepsilon)^2\right] t^2\right)$$
$$h_{GR} = \exp\left(-\frac{8\pi^2\alpha^2}{\lambda^2}\left[(v_x \sin\theta + v_z \cos\theta)^2 + (v_y \sin\theta)^2\right] t^2\right)$$

- Doppler shifts are applied to the LOS path, f_{LOS}, and ground reflections, f_{GR}, such as:

$$f_{LOS} = \frac{v_x \cos(\varepsilon) + v_z \sin(\varepsilon)}{\lambda}$$
$$f_{GR} = \frac{v_x \cos(\theta) + v_z \sin(\theta)}{\lambda}$$

$v = (v_x, v_y, v_z)$ is the speed vector of the aircraft in the Cartesian plan, λ the wavelength, c the speed of light and α the standard deviation of the ground reflection surface.

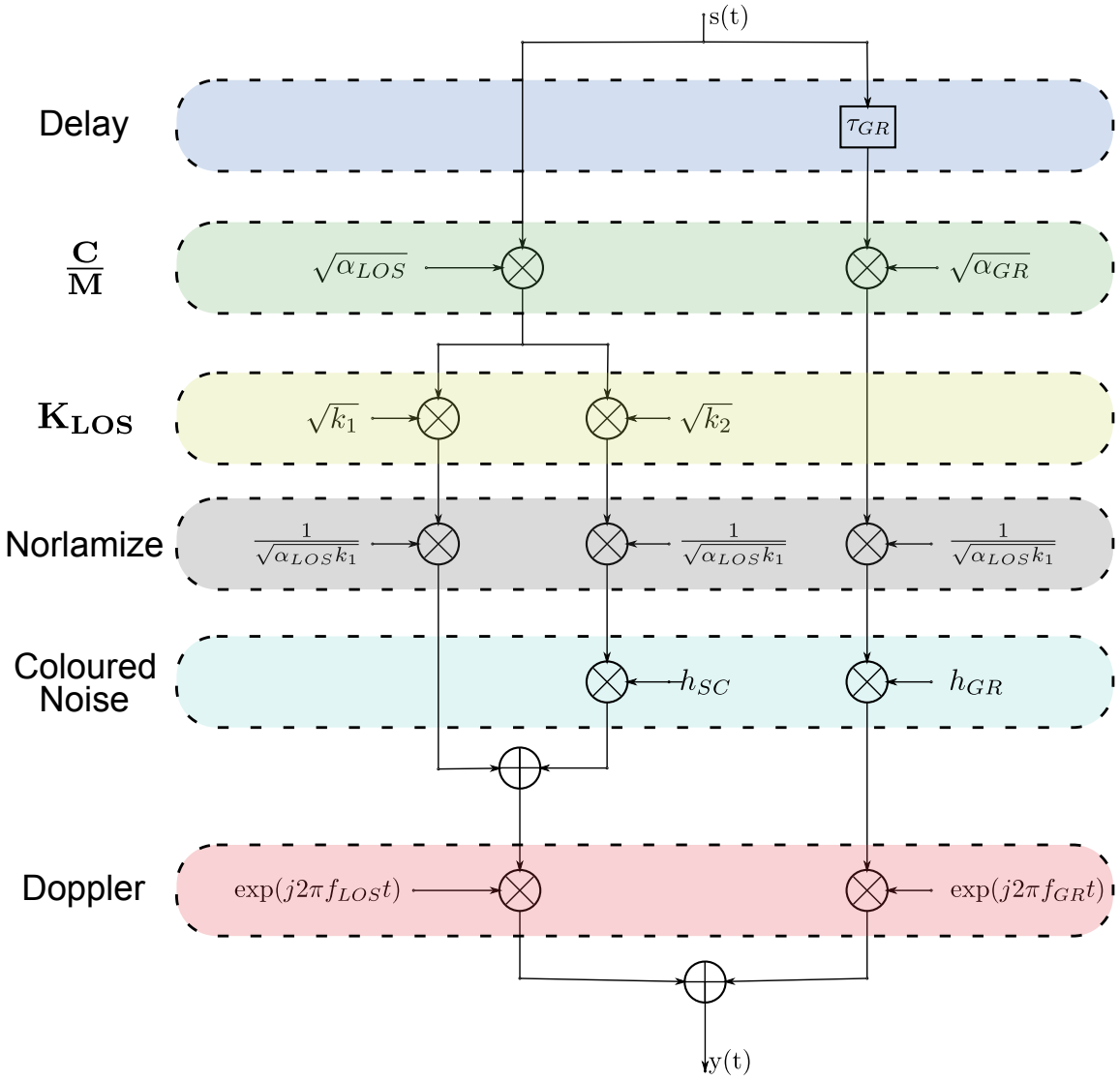

Figure 5.2: Considered aeronautical channel

5.2.2 Performance of linear modulations and the CPM

For a transmitted frame during a stationary period, the equivalent complex baseband channel impulse response can be written as:

$$h_c(t) = h_1\delta(t) + h_2\delta(t - \tau_{GR}) \tag{5.2}$$

where h_1 and h_2 depends on the previous channel parameters: C/M, K_{LOS}, f_{LOS}, f_{GR}, ...

5.2.2.1 Linear modulation

The base-band emitted signal in a linear modulation can be expressed as the following:

$$s(t) = \sum_k a_k h_e(t - kT)$$

where a_k are the information symbols, T the symbol period and $h_e(t)$ real shaping filter.

The filter $h_e(t)$ is chosen such as, after filtering with the receiver matched filter $h_r(t) = h_e(-t)$, the Nyquist criterion is verified for the global filter $g(t) = h_r * h_e(t)$. The continuous model of the received signal in a frequency selective channel with impulse response h_c (see Eq. (5.2)) is given as:

$$y(t) = \sum_k a_k h(t - kT) + b(t)$$

where:

$$h(t) = h_c * g(t) = h_1 g(t) + h_2 g(t - \tau_{GR})$$

and $b(t)$ is a white Gaussian noise with double-sided power spectral density $N_0/2$. The sampled model is then obtained as the following:

$$y[n] = \sum_k a[k]h[n - k] + b[n] \tag{5.3}$$

where $h[n] = h[nT]$ ($b[n]$) is the equivalent discrete channel impulse response (of the noise respectively). Equation (5.3) is the classical model for the discrete frequency selective channel [PS07].

In the case of linear modulations (with or without memory), the linearity induced by the continuous channel allows to consider a simple interference linear model at the receiver. Consequently, at the decoder, classical equalization techniques can be applied to deal with the interference.

5.2.2.2 CPM in frequency selective channels

For the CPM, we obtain the noised signal at the receiver side as:

$$\begin{aligned} y(t) &= h_c * s_b(t) + b(t) \\ &= h_1 s_b(t) + h_2 s_b(t - \tau_{GR}) + b(t) \\ &= h_1 \sqrt{\frac{2E_s}{T}} \exp\left(j\theta(t, \boldsymbol{\alpha})\right) + h_2 \sqrt{\frac{2E_s}{T}} \exp\left(j\theta(t - \tau_{GR}, \boldsymbol{\alpha})\right) + b(t) \end{aligned}$$

Observe that we do not have the linear transformation as with the linear modulations, hence, the equivalent discrete channel cannot be easily derived as in the previous case. The non-linearity between the channel terms (h_1 and h_2) and the information symbols $\boldsymbol{\alpha}$ does not make the equalization operation as straightforward as with the linear modulations.

At the receiver side, the SISO CPM decoder is based on the Rimoldi's decomposition [Rim88]. When the transmitted signal $s_b(t, \boldsymbol{\alpha})$ is corrupted with an AWGN channel having a double-sided power spectral density $N_0/2$, we can consider the metric:

$$\boldsymbol{y^n} = \left[y_i^n = \int_{nT}^{(n+1)T} y(l) s_i^*(l) dl \right]_{1 \leq i \leq pM^L} \tag{5.4}$$

where $\{s_i(t)\}_i$ are the set of filters that form the Rimoldi's memomryless modulator. $\{\boldsymbol{y^n}\}_n$ is a sufficient statistic to estimate the information symbols [MA01] using the BCJR algorith on the Rimoldi's CPE.

In the context of the aeronautical channel, if no equalization is considered at the receiver, we apply the branch metric given by Eq. (5.4) to the signal:

$$\begin{aligned} y'(t) &= \frac{1}{h_1} y(t) \\ &= s_b(t) + \underbrace{\frac{h_2}{h_1} s_b(t - \tau_{GR}) + \frac{1}{h_1} b(t)}_{b'(t)} \end{aligned}$$

While processing the BCJR algorithm [MA00], one should take into account that the new noise $b'(t)$ has a different power which can be easily computed as a function of the transmitted signal power, h_1, h_2 and N_0. We obtain then a modified Gaussian-like receiver that can be easily integrated in the Gaussian model. However, its performance will be limited by the residual interference $h_2/h_1 s_b(t - \tau_{GR})$ in $b'(t)$. The consequence of this inter-symbol interference (ISI) is the apparition of an error floor.

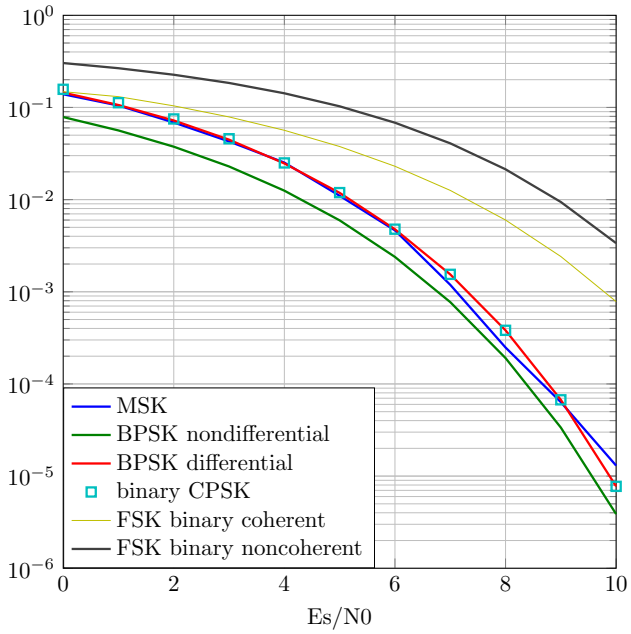

Figure 5.3: Comparison of linear modulations and MSK in the AWGN channel

5.2.3 Simulation results

We give here some comparison results between the CPM and the linear modulations in the case of the AWGN and the aeronautical channel. For this purpose, we consider the simple binary phase shift keying (BPSK) modulation, the differential BPSK (DPBSK), the binary frequency shift keying (FSK), the binary continuous phase shift keying (CPFSK) and the MSK (these modulation schemes are introduced in chapter 1). Over the AWGN channel, the MSK and the DBPSK exhibit similar performance as depicted in Fig. 5.3

The goal of this part is to validate the implementation of the aeronautical channel. Therefore, we consider different aeronautical channel with various C/M and K_{LOS} values. The results of the modified Gaussian-like receiver are shown in Fig. 5.4.

Observe that when the channel interference power increases, both of the MSK and DBPSK show an error floor due to the interference terms in $b'(t)$. Secondly, we notice that in the aeronautical channel, the MSK is more sensitive to the ISI than the DPBSK. Finally, in the aeronautical channel configuration that almost gives an AWGN channel, the MSK and the DBPSK performance are similar and we retrieve the results in Fig. 5.3.

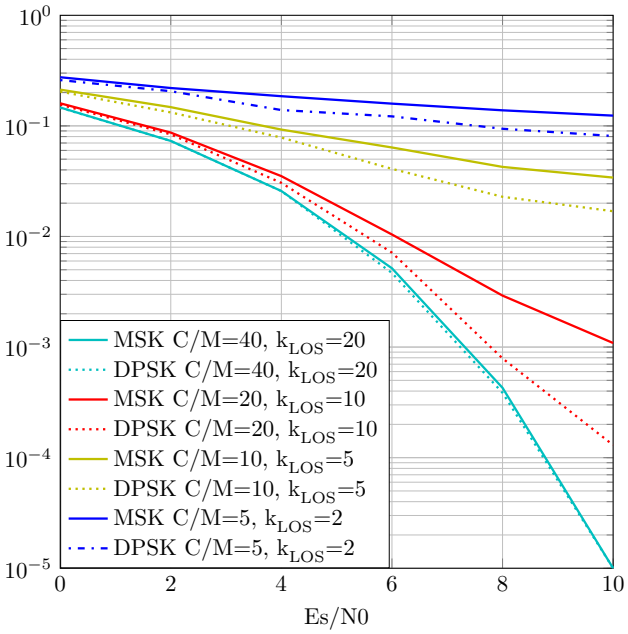

Figure 5.4: Comparison of linear modulations and MSK in the aeronautical channel

5.3 DVB-RCS2 analysis and code design

5.3.1 DVB-RCS waveform

In DVB-RCS2, some specific schemes target the coded CPM[V1.13]. The adopted waveform is a mixture of the REC and the RC type (please refer to the chapter 1). This mixture is parametrized by a mixing factor $0 \leq \alpha_{RC} \leq 1$, such that the phase shaping function is given by:

$$g(t) = \alpha_{RC} g_{RC}(t) + (1 - \alpha_{RC})\, g_{REC}(t)$$

where:

$$g_{RC}(t) = \begin{cases} \frac{1}{4T}\left[1 - \cos\left(\frac{\pi t}{T}\right)\right], \text{ if } 0 \leq t \leq 2T \\ 0, \text{otherwise} \end{cases}$$

$$g_{REC}(t) = \begin{cases} \frac{1}{4T}, \text{ if } 0 \leq t \leq 2T \\ 0, \text{otherwise} \end{cases}$$

An example of the RCS2 phase response function taken from the DVB-RCS2 standard is given in Fig. 5.5.

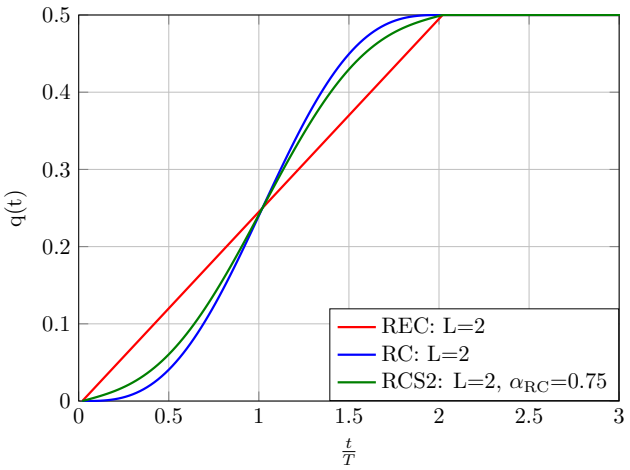

Figure 5.5: Phase response function of the DVB-RCS waveform with $\alpha_{RC} = 0.75$

In the DVB-RCS2, the modulation index $h = k/p$ is taken as $1 \leq k \leq p \leq 7$. Since a quaternary modulation ($M = 4$) was chosen, different mappings are possible when forming the symbols. The Gray mapping is in general considered, except from the case when $h = 1/3$ where, instead, the natural mapping is preferred. This is mainly due to the fact that the natural mapping for these parameters has better performance than the Gray one: this can be seen when drawing the EXIT curves where the natural mapping, at the contrary of the Gray one, reaches the the point $(1, 1)$. In DVB-RCS2, termination symbols might be appended to the information symbols in order to terminate the CPE trellis (As discussed in the chapter 1).

5.3.2 DVB-RCS2 concatenated scheme

The DVB-RCS2 concatenated scheme is depicted in Fig. 5.6. Two rate-1/2 convolutional codes are considered:

- The first one has constraint length=3 and an octal representation $[5, 7]$
- The second one has constraint length=4 and an octal representation $[15, 17]$

By considering puncturing, different rates can be generated from this two mother codes [V1.13, Table 7-14].

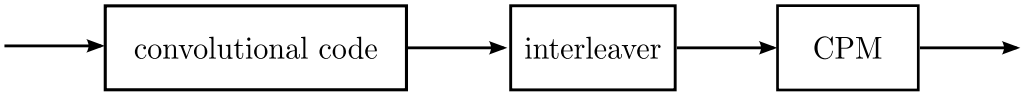

Figure 5.6: Concatenated scheme of the DVB-RCS2 [V1.13]

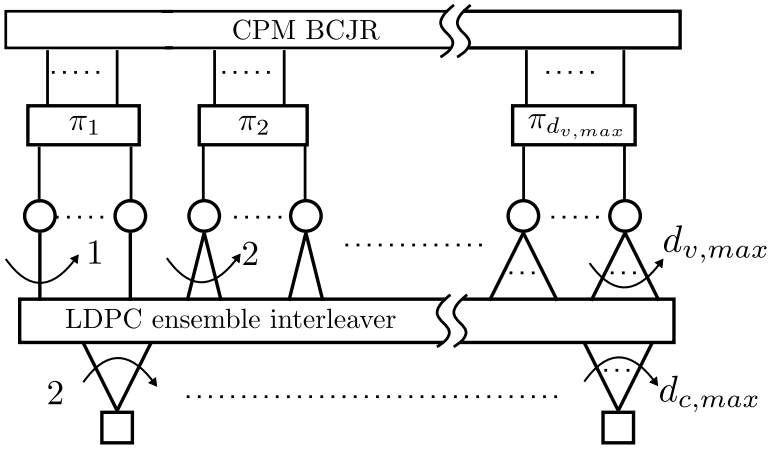

Figure 5.7: Our LDPC-coded DVB-RCS2 concatenated scheme

5.3.3 LDPC coded-RCS2 schemes

As an application of our work, we consider the same scheme as in Fig. 5.6, but with an LDPC code as an outer code, or more specifically, a protograph-based LDPC code. We apply the optimization method introduced in chapter 3. Figure 5.7 represents the Tanner graph of our LDPC-coded DVB-RCS2 concatenated scheme. Note that the interleaver in Fig. 5.6 is replaced by a set of partial interleavers. The choice of an LDPC outer code has also been motivated by some possible compliance with the future terrestrial standards such as the one proposed for STANAG 4660.

The optimization method proposed in the chapter 3 allows to optimize the code parameters (the connectivity of the graph associated with the code) as a function of the EXIT chart of the chosen waveform. This optimization is based on the asymptotic analysis of the iterative decoding threshold.

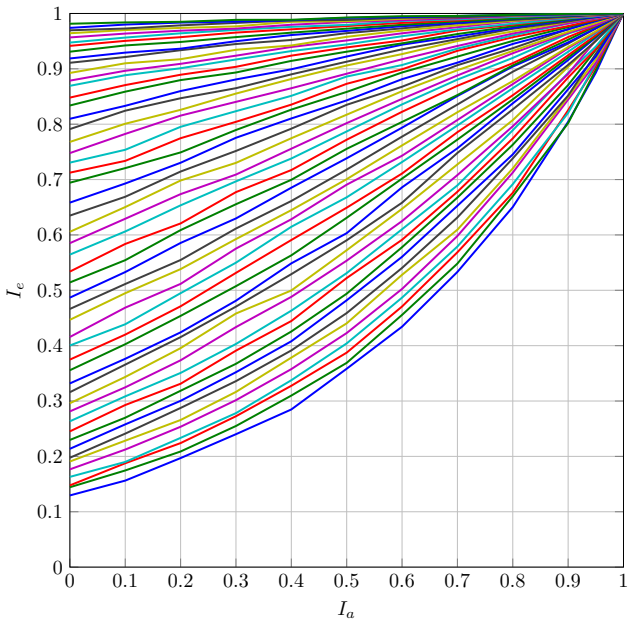

Figure 5.8: EXIT chart of for the CPM ($M = 4, L = 2, h = 1/3, \alpha_{RC} = 0.75$, natural mapping) at different signal to noise ratios: $E_s/N_0 = -1 \ldots 9$ dB with steps of 0.2dB

5.4 Performance comparison of coding schemes

5.4.1 CPM parameters

As an example and without loss of generality, we consider the quaternary CPM with parameters $h = 1/3, \alpha_{RC} = 0.75$ and natural mapping. The value of α_{RC} is an example of the considered shaping parameter in the DVB-RCS2 described in [BCDB+13]. Figure 5.8 depicts the EXIT chart of the Rimoldi-based MAP symbol (BCJR) decoder of the considered CPM schemes. The area under the curve allows to have an approximation of the maximum achievable rate of the LDPC outer code (see chapter 2 for more details).

5.4.2 Asymptotic analysis of the DVB-RCS2 convolutional code

We consider the serial concatenation of the $[5, 7]$ convolutional code (CC) with the CPM. We can interpret the convergence threshold of the system as the lowest SNR such as the EXIT characteristics of the two SISO components (the convolutional code and the CPM) do not intersect [tB01a]. Figure 5.9 plots the two codes EXIT curves at $E_s/N_0 = 1.37$dB. As seen earlier in this thesis, the area

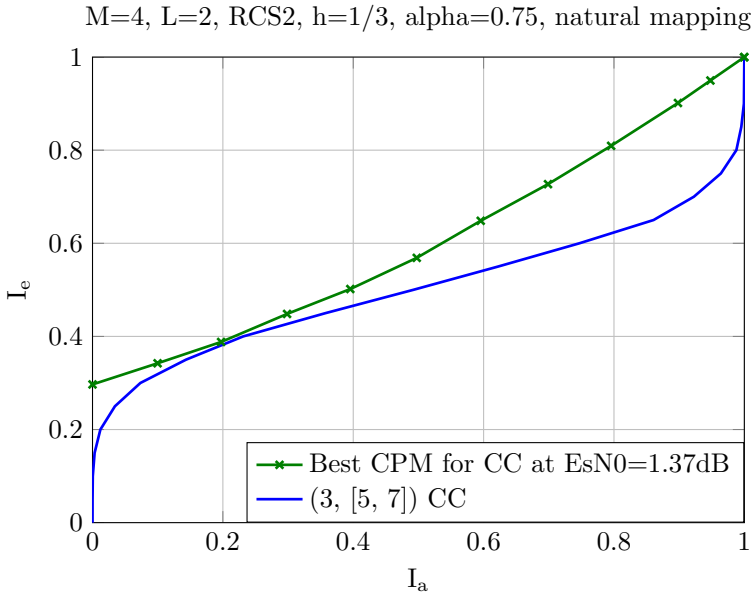

Figure 5.9: EXIT analysis of the the considered CPM concatenated and the (3, [5,7]) convolutional code.

between the two curves corresponds to a spectral efficiency loss of the concatenated scheme. Same analysis can be done for the $[15, 17]$ convolutional code.

5.4.3 Asymptotic analysis of the LDPC coded DVB-RCS2

Different types of LDPC code optimizations have been introduced in this thesis. When we consider unstructured LDPC codes with a maximum variable node degree $d_{v,max} = 10$, the method described in chapter 2 gives an LDPC code that operates at $E_s/N_0 = 0.33$dB, *i.e.* at 0.21dB from the capacity $(E_s/N_0)^*$. The obtained variable nodes and check nodes profiles are:

$$\lambda(x) = 0.177 + 0.576x + 0.247x^9 \qquad \rho(x) = 0.9x^2 + 0.1x^3$$

If we restrict to $d_{v,max} = 7$, we obtain:

$$\lambda(x) = 0.2006 + 0.6116x + 0.1878x^6 \qquad \rho(x) = 0.2x^2 + 0.8x^3$$

The obtained threshold is $E_s/N_0 = 0.45$dB (0.33dB from the capacity and 0.93dB better than the considered convolutional code).

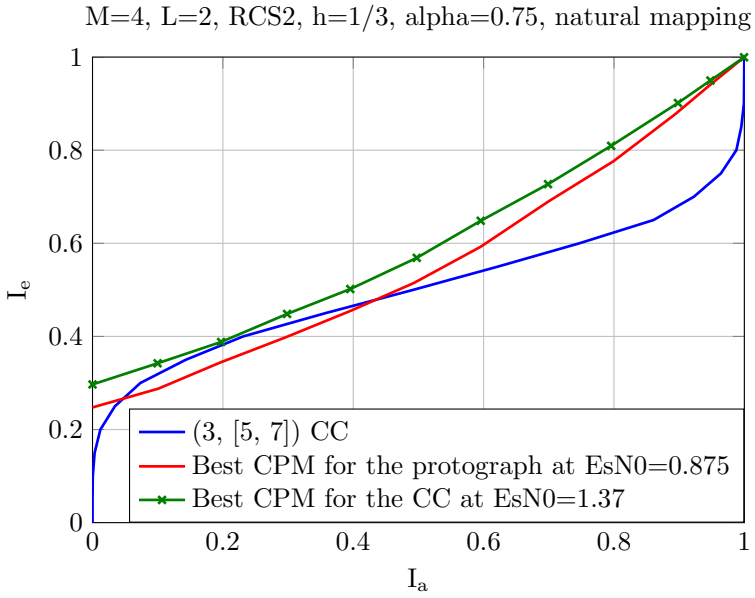

Figure 5.10: Comparison of the convergence threshold of the DVB-RCS2 CPM coded with an optimized LDPC code and with convolutional code

However, for encoding complexity and decoding implementation reasons, we prefer to find solutions within the protograph-based LDPC codes family. The exhaustive search in the chapter 3 gives the following optimized protograph for the considered CPM:

$$H = \begin{pmatrix} 2 & 2 & 0 & 0 & 1 & 1 & 0 & 0 \\ 1 & 3 & 0 & 1 & 0 & 1 & 1 & 0 \\ 1 & 0 & 1 & 0 & 0 & 0 & 1 & 1 \\ 0 & 2 & 0 & 0 & 0 & 0 & 0 & 1 \end{pmatrix}$$

The decoding threshold of this code is $E_s/N_0 = 0.875$dB, *i.e.* at 0.75dB from the capacity and 0.5dB better than the considered convolutional code. For comparison, the CPM EXIT curve at the decoding threshold of the LDPC code is depicted in Fig. 5.10. As a reference, the EXIT curve of the convolutional code is also inserted. It is clear that the convolution code cannot operate at $E_s/N_0 = 0.875$dB (the EXIT curves of the CPM and the convolutional code SISO modules intersect). We finally compare the performance of the two schemes at a information frame size of $N = 2048$ bits. The obtained results in Fig. 5.11 shows the same predicted performance in the asymptotic analysis.

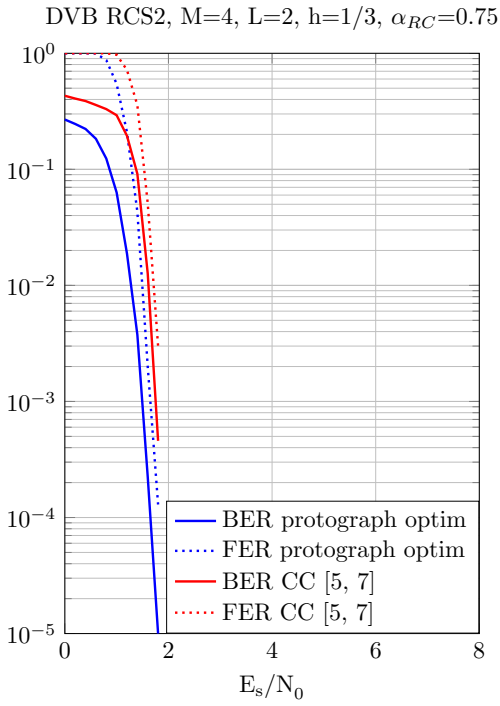

Figure 5.11: Comparison of the bit error rate performance of the convolutional and the LDPC code for size 2048

5.5 Equalization methods for CPM

The goal in this section is to show the feasibility of a *simple* equalization in the aeronautical channel. The proposed schemes are not the ultimate solutions but easy approaches within the equalization techniques. The goal is to show that the equalization can be very effective in the case of the aeronautical channel.

5.5.1 State of the art

The early studies on the CPM equalization over frequency selective channels have considered time-domain equalization. Firstly, the optimal receiver was defined on the joint trellis of the CPM and the memory channel, *i.e.* on the Cartesian product of the two trellises. As a consequence, the number of the waveforms in the filter bank increases because we have to consider all possible period-T waveforms of the receiver signal space. This increase is exponential in terms of the modulation

order, the channel memory and the number of paths [YS97]. Few initiatives tried to perform the equalization using non-linear receivers combined with ML receivers [CS94]. However, theses solutions are limited to low modulation orders.

After the emergence of frequency-domain solutions with techniques like the orthogonal frequency division multiplexing (OFDM), some solutions were proposed for CPM signals [TS05, PV06]. These techniques are based on the insertion of a cyclic prefix (CP) and induce block transmissions. As we are going to see later, this insertion is slightly complex in comparison to the linear modulations because we have to insure the continuity of the phase for within each block and between consecutive blocks. In most of the cases, the equalization is performed independently of the detection: the goal is to cancel the interference induce by the channel in the received signals before being processed by the detector. These equalized signals constitute a sufficient statistics for either the Rimoldi-based or the Laurent-based receiver. In [TS05], a first receiver architecture was proposed derived for both decompositions. The presented solution was not derived with soft decoding in mind. We will implement this architecture to prove its feasibility in our context. It is composed of an orthogonal filter bank adapted to the CPM decomposition followed by another filter bank based on the FFT/IFFT operations and a frequency-domain equalization stage. In the case of the Laurent decomposition, one should consider whitening filters, which increases the complexity of the receiver. Still, we can counterbalance this complexity by considering low complexity CPM receivers.

5.5.2 Making of the CPM signals circular

5.5.2.1 Cyclic prefix

In order to make the CPM signal circular, we divide the information block into two sub-blocks $\boldsymbol{a}$ and $\boldsymbol{b}$. We suppose that the CPE is initialized before coding the information block. After being encoded, each sub-block should initialize the CPM by appending a termination sequence ($\tilde{\boldsymbol{a}}$ and $\tilde{\boldsymbol{b}}$ respectively). As a result, after copying the cyclic prefix $\boldsymbol{b} + \tilde{\boldsymbol{b}}$, the CPM phase is kept continuous between both blocks and sub-blocks. Note that, at the contrary of linear modulations, the CP is inserted before the modulation. Figure 5.12 resumes the CP insertion technique.

5.5.2.2 Unique word

With this approach, first, we terminate the information bits with a termination sequence to initialize the CPE. Then, we append a known sequence referred as *unique word* (UW). This technique helps

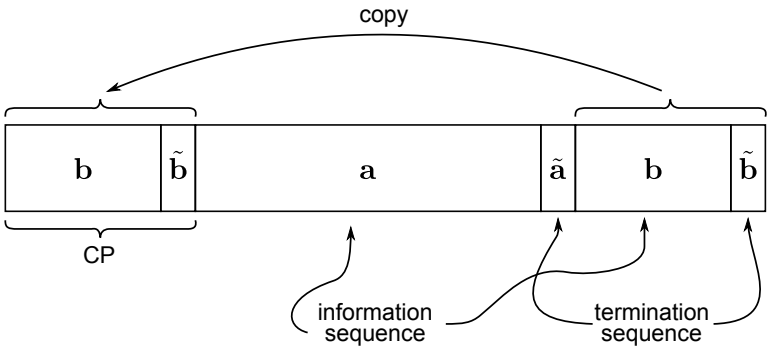

Figure 5.12: CP for CPM [Par10]

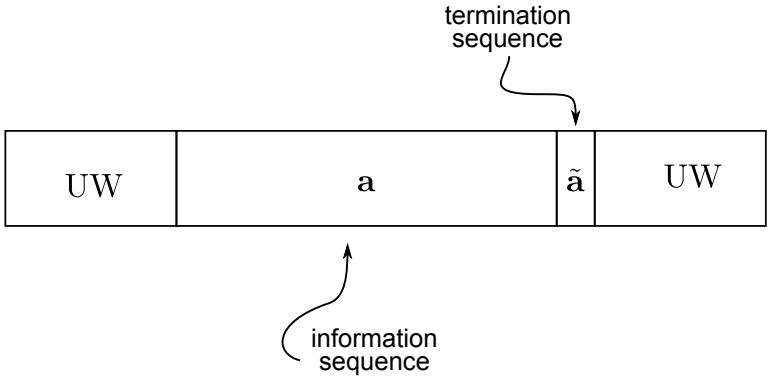

Figure 5.13: UW for CPM [Par10]

to estimate the channel. In order to easily insure the continuity of the phase between consecutive blocks, the CPE should be in its zero state after encoding the UW. Otherwise, more caution should be taken in the sense that the following block should be encoded starting from the last CPE state. Figure 5.13 resumes the UW technique.

5.5.3 Frequency domain equalization

5.5.3.1 Stüber's method [TS05]

Consider a sequence of N information symbols $\boldsymbol{\alpha} = \{\alpha_i\}_i \in \{\pm 1, \ldots, \pm(M-1)\}^N$. We consider the CPM notations described in Eq. (5.1). In this section, we are interested in the Rimoldi's decomposition. The receiver signal space is generated by pM^L pulses. Starting from the definition of the CPE trellis, we notice that, in fact, at most M^L only different pulses are linearly independent (as

discussed in chapter 1). Let us denote $J \leq M^L$ the dimension of the receiver signal space. Using the Gram-Schmidt orthonormalisation, we can define an orthonormal function basis $\{f_p(t)\}_p$ [TS05]. In the following, we denote by $s_{n,p}$ the projection of the CPM signal portion $s_n(t) = s_b(\tau+nT), \tau \in [0, T[$ on $f_p(t)$, *i.e.*:

$$s_{n,p} = \langle s_n(t), f_p(t) \rangle = \int_{nT}^{(n+1)T} s_b(t) f_p^*(t - nT) dt$$

In a frequency selective channel, the received signal is given by:

$$y(t) = \sum_{l=0}^{M_D-1} h_l s_b(t - lT) + w(t)$$

where M_D is the maximum channel delay, h_l the attenuation induced by the l^{th} tap and $w(t)$ a white noise. In this model, we consider different paths whose corresponding delays are multiple of the symbol period T [TS05]. In practice, we approximate the actual tap's delay to the nearest multiple of the symbol period. This is a weakness of the this simple model.

The projection of the received signal $y(t)$ at nT on $f_p(t), \forall p \in \{0, 1, \ldots, J-1\}$ gives:

$$y_{n,p} = \sum_{l=0}^{M_D-1} h_l s_{n-l,p}, w_{n,p} \tag{5.5}$$

where:

$$w_{n,p} = \int_{nT}^{(n+1)T} w(t) f_p^*(t - nT) dt$$

Equation (5.5) can be rewritten under the form of a discrete circular convolution $\circledast$ of the signal and the channel impulse response:

$$\boldsymbol{y}_n = \boldsymbol{h}_n \circledast \boldsymbol{s}_n + \boldsymbol{w}_n$$

where $\boldsymbol{y}_n$, $\boldsymbol{s}_n$ and $\boldsymbol{w}_n$ are vectors of size J containing the elements $r_{n,p}$, $s_{n,p}$ and $w_{n,p}$ respectively ($p \in \{0, 1, \ldots, J-1\}$).

We assume that the signal phase of the information block starts at 0 (initialization of the CPE). In this example and without loss of generality, we will use the cyclic prefix technique. In order to equalize the received signal in the frequency domain, we append a cyclic prefix of size G symbols. Moreover, in order to insure the phase continuity, we insert termination sequences at different places of the frame as depicted in Fig. 5.14.

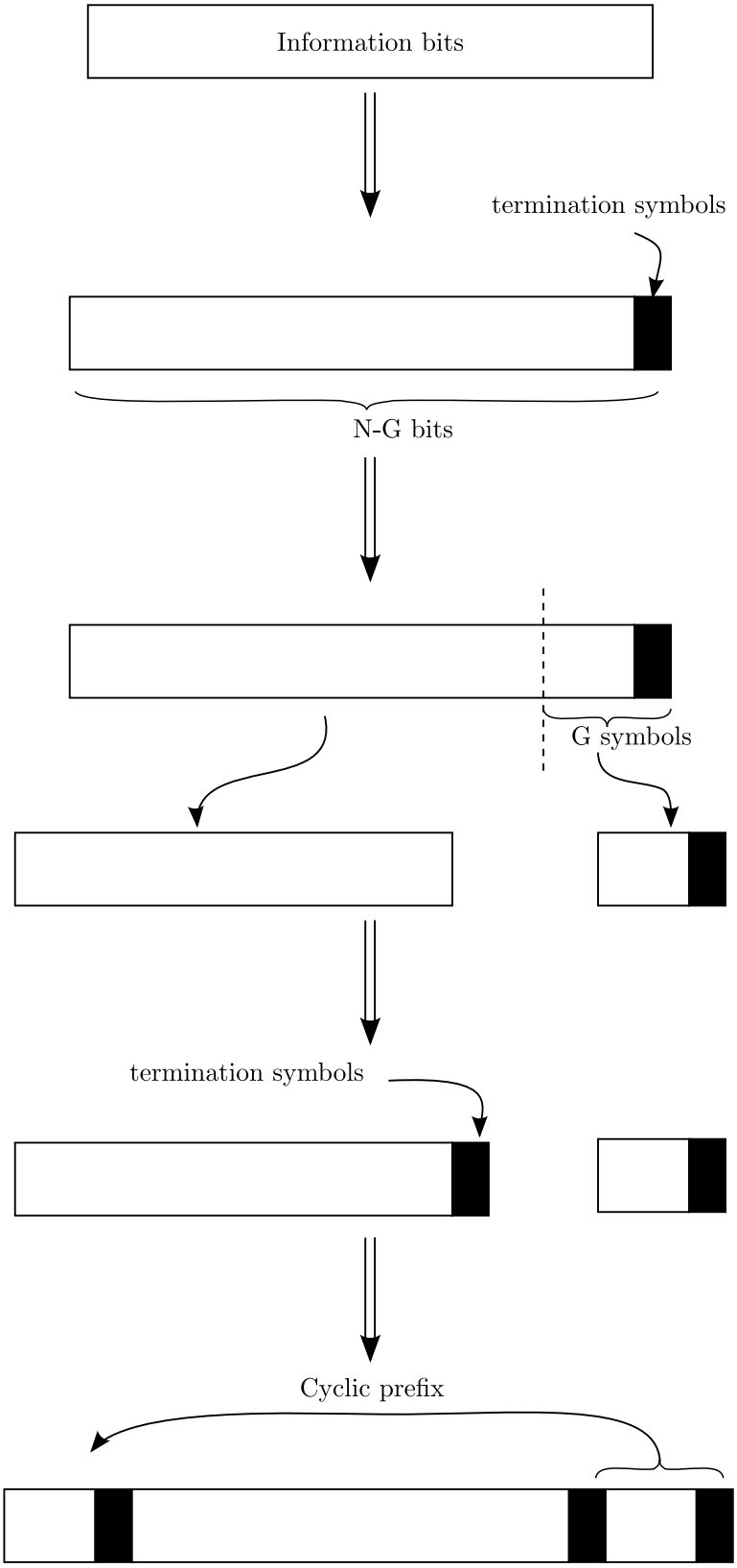

Figure 5.14: CP for the CPM with the size of the different parts

Now, applying the discrete Fourier transform, we obtain in the p^{th} branch corresponding to the outputs of the filter $f_p(t)$:

$$Y_{k,p} = H_k S_{k,p} + W_{k,p}$$

Afterwards, in each branch, we obtain a simple frequency-domain equalization. The frequency response of the MMSE (minimum mean square error) equalizer $\tilde{H}_k$ is given by:

$$\tilde{H}_k = \frac{H_k^*}{|H_k|^2 + \left[\frac{E_s}{N_0}\right]^{-1}}$$

The equalized frequency-domain signal $Y_{k,p}$ is then:

$$\tilde{Y}_{k,p} = \tilde{H}_k Y_{k,p}$$

Finally, we go back to the time domain by an inverse discrete Fourier transform. We obtain then an equalized version of the received signal and a sufficient statistic at the input of the CPM decoder. Figure 5.15 describes the considered receiver.

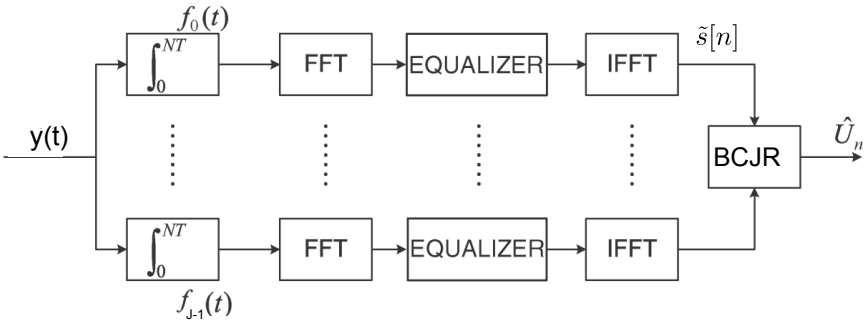

Figure 5.15: Stüber receiver structure

Remark: similar results can be obtained when using UW instead of CP.

The initial Stüber's scheme does not point out that the MMSE estimator is biased, and this bias should be taken into account especially for operation in the low SNR region. This can be proven as: the received signal after the IFFT is given by (the subscript p is omitted for simplification), follows:

$$\begin{aligned}\tilde{s}[n] &= \underbrace{\tilde{h} \circledast s[n]}_{\text{signal}+ISI} + \underbrace{\tilde{h} \circledast b[n]}_{\text{filtered noise}} \\ &= \underbrace{\tilde{s}_u[n]}_{\text{signal of interest}} + \underbrace{\tilde{s}_{ISI}[n]}_{\text{ISI signal}} + \tilde{b}[n]\end{aligned}$$

where:

$$\tilde{s}_u[n] = \tilde{h}[0]s[n]$$

By taking into account this bias in the receiver, we can, by considering a Gaussian channel approximation, use the classical AWGN detector (see chapter 1). The new noise variance $\sigma^2_{\tilde{b}}$ of $\tilde{b}[n]$ is given by:

$$\sigma^2_{\tilde{b}} = \left(\frac{\sigma^2_{\tilde{b}}}{N}\right)^2 \sum_{k=0}^{N-1} |\tilde{H}_k|^2$$

5.5.3.2 Simulation results

Figure 5.16 shows the implementation of the Stüber solution with the CP and with the UW over an arbitrarily aeronautical channel for the uncoded DVB-RCS2 CPM scheme.

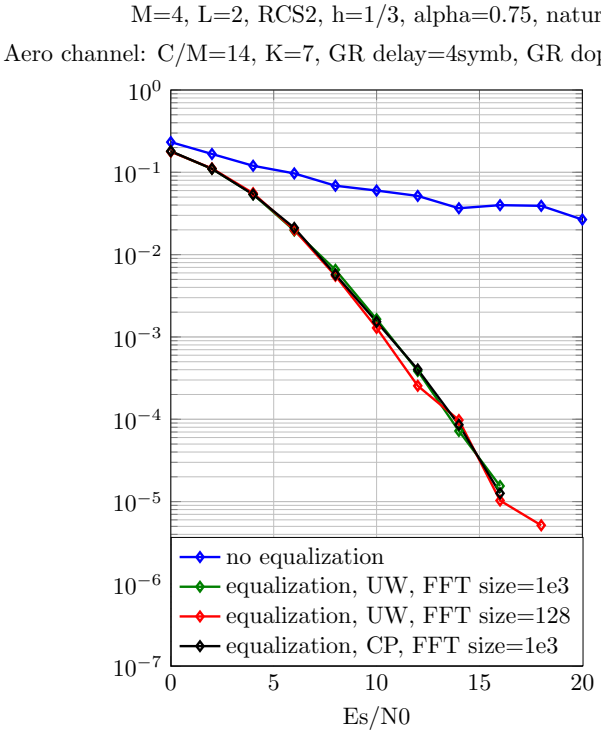

Figure 5.16: BER and FER of the uncoded DVB-RCS2 CPM scheme in the aeronautical channel. The frames have k=1000 bits

Figure 5.17 depicts the performance of the equalization for the coded DVB-RCS2 scheme ([5, 7] convolutional code + CPM) over a frequency selective channel. The considered channel in defined as:

- Taps delay profile (in terms of symbol period delays): [0 1 2 8 12 25]
- Taps power profile: [0.189 0.379 0.255 0.09 0.055 0.032]

As we can see, the equalization plays a very important role.

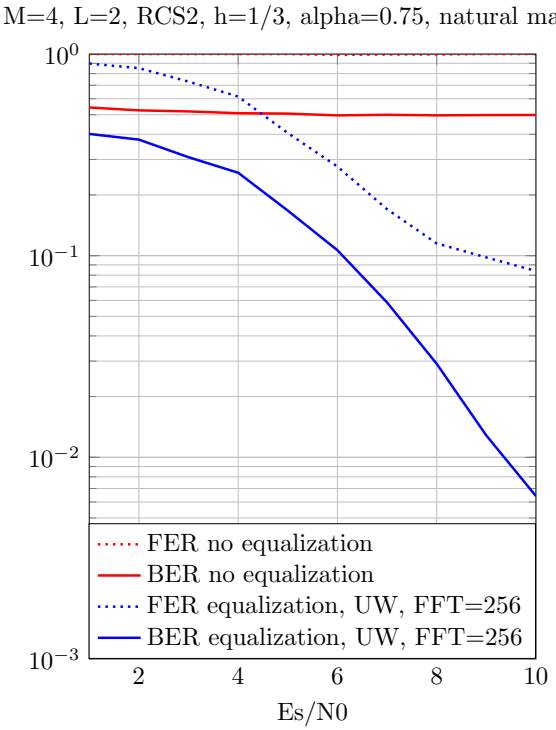

Figure 5.17: BER and FER of the coded DVB-RCS2 CPM scheme with CC in the frequency selective channel. The frames have k=2048 bits

Figures 5.18 and 5.19 depicts the performance of the equalized coded DVB-RCS2 scheme with a convolutional code and with an LDPC code respectively over the aeronautical channel. We see that in both of the cases, the equalization is essential. In the AWGN channel, for the same code length, the LDPC performs better than the convolutional code by 0.5dB at BER=10^{-3}. Our LDPC code is also more robust in the aeronautical channel: at BER=2.10^{-3} for example, our optimized LDPC code is 0.4dB better that the considered convolutional code.

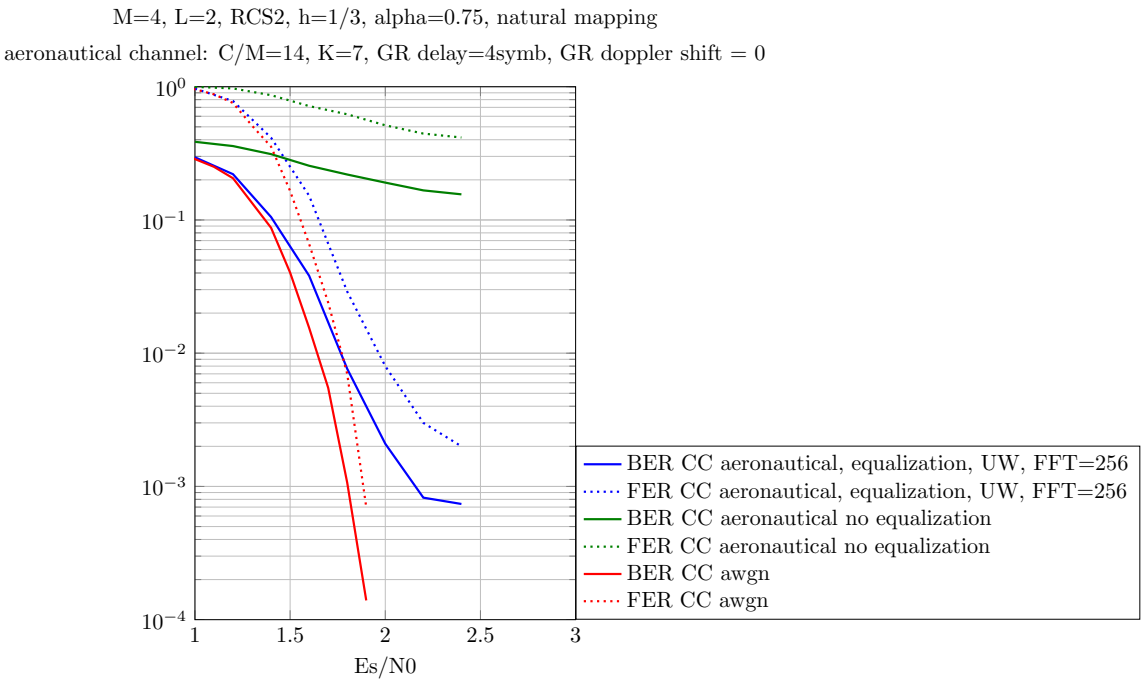

Figure 5.18: BER and FER of the coded DVB-RCS2 CPM scheme with CC in the aeronautical and AWGN channel. The frames have k=2048 bits

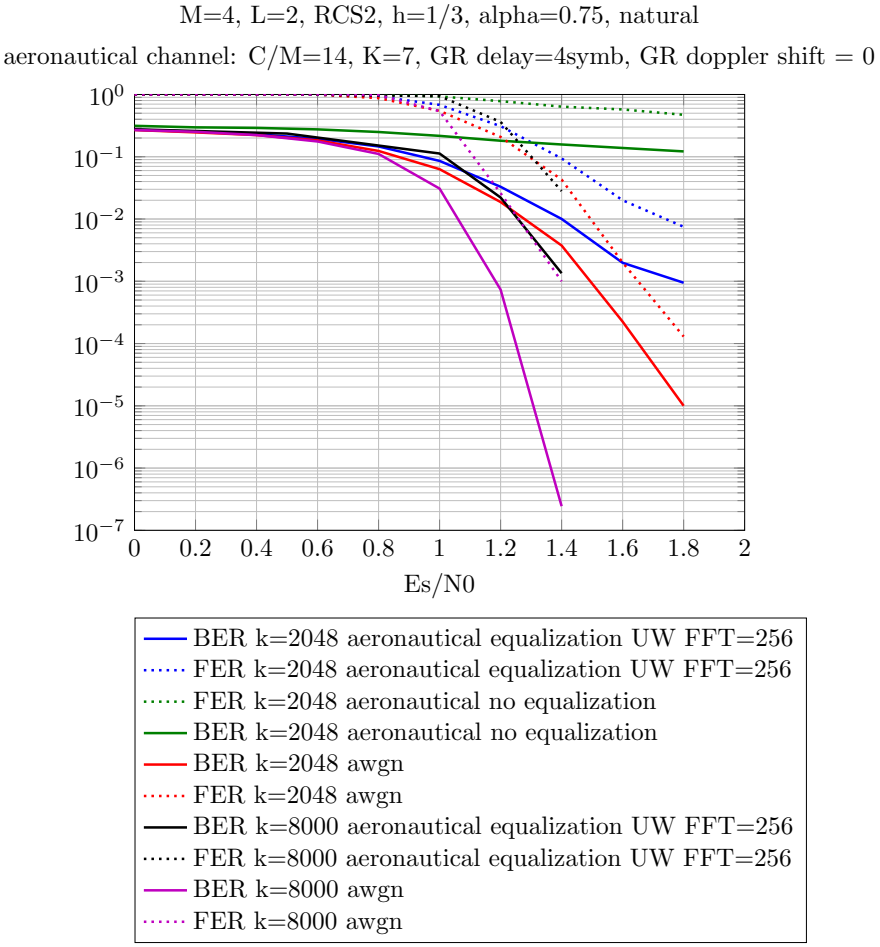

Figure 5.19: BER and FER of the coded DVB-RCS2 CPM scheme with our LDPC code in the aeronautical and AWGN channel. The frames have k=2048 bits

Conclusions et perspectives

Conclusions

Dans cette thèse, nous nous sommes intéressés aux défis liés à la demande croissante des allocations de fréquences pour les applications de drones civils. En effet, grâce à leurs très bonnes propriétés, les modulations à phase continues ont été prescrites par l'UIT et les recommandations de l'ICAO pour les futurs standards des communications des drones par satellite et la diffusion de vidéo numérique DVB-RCS2, et par l'OTAN pour le STANAG 4606. Cette classe de modulations forme un excellent candidat pour ce contexte, non seulement pour son enveloppe constante et sa très bonne occupation spectrale, mais aussi pour sa structure facilement adaptable pour les schémas concaténés en série. L'objectif de cette thèse a été d'étudier les récepteurs de CPM et d'optimiser d'autres codes basés sur des graphes creux. Pour les applications ciblées, nous nous sommes intéressés à des paquets relativement grands et nous avons ciblés de bonnes performances à des taux d'erreur paquet à 10^{-3}.

Les premiers codes qui ont été explorés dans la littérature pour les CPM sont les codes blocs courts convolutifs binaires et non binaires. Les codes LDPC, eux, ont été rejetés parce que il a été stipulé que la concaténation série avec des codes LDPC implique un système doublement itérative difficile à analyser et donc à optimiser. Par conséquent, aucune étude réelle complète n'a été menée dans ce sens, sinon dans quelque cas où les approches proposées manquent de généralité.

Le premier chapitre 1 a introduit la modulation à phase continue et a revu les majeures décompositions et les principales architectures des récepteurs. Ensuite, nous avons introduit les principaux codes basés sur des graphes creux qui ont été explorés tout au long de cette thèse.

Dans le deuxième chapitre 2, nous avons analysé et optimisé les performances asymptotiques de la concaténation en série de la CPM avec des codes LDPC non structurés. La méthode présentée est basée sur une approche d'ajustement de courbe EXIT Chart et peut être généralisée à n'importe quel autre détecteur. Grâce au fait que la courbe EXIT de la CPM atteint le point $(1, 1)$, nous avons

autorisé des noeuds de variables de degré 1 afin d'améliorer le seuil de décodage. Cette proportion est toutefois soumise à une condition de stabilité que nous avons dérivée à partir d'une analyse EXIT Chart. Dans le cas général, *i.e.* avec tout autre détecteur, notre condition de stabilité contraint les proportions de degrés- 1 et 2. Les résultats de simulation montre que nous sommes capable de concevoir des codes qui opèrent à des seuils très proches du seul minimal théorique.

Dans le troisième chapitre 3, nous avons étudié le décodage itératif avec des codes plus pratiques dans le sens où ils sont facilement encodables, ont une représentation plus compacte ou peuvent être implémentés dans des architectures parallélisables. Dans un premier temps, nous avons proposé une méthode d'optimisation des codes GIRA. Nous avons choisi d'utiliser des codes systématiques afin d'éviter une complexité d'optimisation supplémentaire liée aux noeuds de dopage. Pour ce, nous avons considéré un scheduling de décodage particulier qui a permis de concevoir des codes qui fonctionnent à seulement $0.2 - 0.5$dB des codes LDPC non structurées. Deuxièmement, nous avons étudié les codes protographes. En définissant convenablement une procédure d'optimisation, nous avons conçu des codes qui fonctionnent à 0.5dB des codes LDPC non structurées. Enfin, pour obtenir de bons protographes dans les deux régions de plancher d'erreur et *waterfall*, nous nous sommes penchés sur les codes LDPC spatialement couplés basés sur des protographes. Nous avons comparé les performances du couplage de protographes et du couplage des protograhes optimisés pour la CPM. Puis nous avons proposé une nouvelle méthode de terminaison qui donne de très bons seuils sans aucune perte de rendement en limitant le gain de convolution à une seul *vague*.

Dans le chapitre 4, nous avons étudié certains aspects de réception de la CPM et optimisé des codes LDPC pour les récepteurs à faible complexité basés sur la décomposition de Laurent. Contrairement aux détections CPM existantes du MAP, nous avons calculé un nouveau récepteur qui prend en compte les termes de l'ISI induits par la représentation de Laurent. Les résultats des simulations montrent que ce nouveau récepteur surpasse le classique aussi bien dans le cas des CPM codées que non codées. Finalement, nous avons démontrer que les codes LDPC optimisés pour les récepteurs optimaux restent très bons pour les récepteurs à faible complexité tant qu'un nombre suffisent de composantes est pris en compte.

Dans le dernier chapitre 5, nous avons présenté des résultats de simulation dans le cadre de certaines applications. Tout d'abord, nous avons comparé nos résultats avec le standard DVB-RCS2. Ensuite, nous avons étudié le comportement des schémas CPM codées et non codées dans le contexte du canal aéronautique. Enfin, nous avons prouvé qu'une procédure simple d'égalisation de type MMSE conduit à de très bons résultats avec une CPM sur un canal ISI général et sur les canaux

aéronautiques.

Perspectives

Beaucoup de perspectives peuvent être proposées pour des travaux futurs. Certaines d'entre elles ont été entamées au cours de cette thèse et ont montré des résultats prometteurs.

1 Turbo-égalisation

Les nouveaux schémas de décodage itératifs des CPM sur des canaux sélectifs en temps/fréquence comme le canal aéronautique peuvent prévoir une turbo-égalisation de type SISO MMSE. L'une des premières études ont été menées par [Ozg08] où l'auteur a proposé une égalisation et un décodage combinés pour les CPM binaires et a analysé les aspects liés à la complexité de calcul. Dans cette étude, une parfaite connaissance du canal a été supposée. Les travaux futurs peuvent étendre les résultats à des configurations non binaire de la CMP et explorer des algorithmes adaptatifs de turbo-égalisation sans estimation de canal [Sch04, RBL05]. D'autre part, de nouveaux algorithmes d'égalisation pourraient être proposés pour le récepteur Laurent MAP exact.

2 Synchronisation en temps et en fréquence et la détection non cohérente

Dans nos travaux, nous avons supposé une parfaite synchronisation en fréquence/temps et nous avons négligé l'effet Doppler. Afin de finaliser l'analyse de notre système, nous devons étudier la capacité de synchronisation et d'égalisation de la CPM sur les canaux à évanouissement avec l'effet Doppler, une configuration que l'on rencontre dans le canal aéronautique. D'autre part, suivant des travaux dans [VCT10] sur la détection non-cohérente, étendre les résultats à des schémas génériques de CPM et à la turbo détection non cohérente peut être envisagé. Ces recherches aideront à concevoir des systèmes de CPM robustes pour des applications qui opèrent dans de très mauvaises conditions de vol comme les véhicules de lancement spatial.

3 Antennes mutiples

Nous pouvons envisager l'extension de nos résultats de l'égalisation MMSE simple du chapitre 5 à des configurations simple input multiple outputs (SIMO) et étudier leur faisabilité dans le contexte de la CPM. En supposant que les réalisations du canal aéronautiques sont indépendantes par antenne, nous

pouvons lancer deux processus d'égalisation disjoints. Par conséquent, à la sortie des égaliseurs, nous bénéficierons d'une diversité spatiale qui peut être facilement prise en compte dans les métriques de branche du récepteur SISO CPM. Une analyse plus poussée peut également envisager un récepteur conjoint égalisation/décodage. Ces résultats peuvent être comparés aux travaux dans [HK98, WZ07] qui ont exploré les systèmes à entrées multiples-sorties multiples (MIMO) pour la CPM.

4 L'optimisation du mapping

Les modulations codées à bits entrelacés (BICM) [iFMC08] est une approche puissante qui tire profit des différents niveaux de protection de bits dans les modulations d'ordres élevés pour améliorer le seuil de décodage. L'optimisation de la BICM dans les schémas concaténés a été bien étudiée dans la littérature et plusieurs considérations ont été proposées pour améliorer le seuil comme l'optimisation de la configuration d'allocation de bits ou précodage [PS06, SB04, tB01b]. Les CPM M-aires présentent également différents niveaux de protections des différents canaux de bits comme illustré par Fig. 5.21

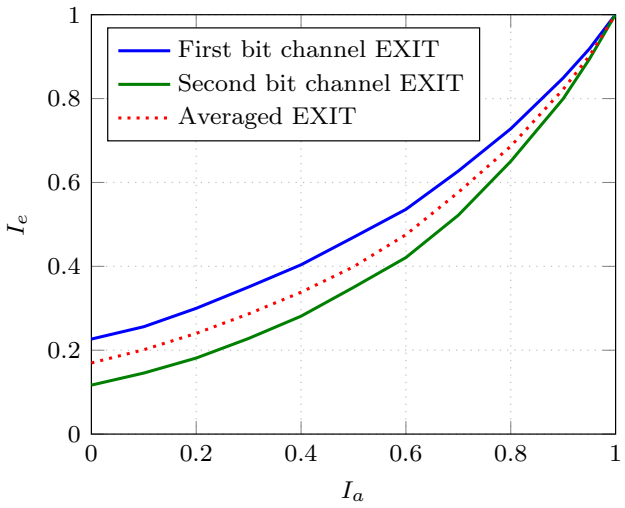

Figure 5.20: EXIT chart des différents canaux bits pour la CPM ($M = 4, L = 2, h = 1/3$, mapping naturel) à $E_s/N_0 = -0.5$dB

En s'inspirant de la méthode dans [HGiAB+14] et dans le contexte de la CPM, nous pouvons optimiser le mapping afin d'améliorer les seuils des codes optimisés ou de compenser la dégradation de seuil lorsque nous considérons la terminaison par troncature directe des codes LDPC couplés.

Des travaux préliminaires dans le cadre des modulations linéaires ont été menés en annexe D et promettent des résultats encourageants pour le CPM.

5 LDPC non binaires et adaptation de rendement

Dans cette thèse, nous avons exploré différents codes LDPC binaires. Cependant les codes LDPC non binaires peuvent également être envisagés. Ces codes montrent d'excellents résultats dans diverses applications après l'introduction d'un décodeur à faible complexité efficace dans le milieu de l'année 2000 [DF07]. En s'inspirant de l'étude [XA06], des aspects similaires peuvent être imaginés pour les codes LDPC non binaires concaténés avec des CPM M-aires. En outre, dans [LZM15], les auteurs ont étudié la complexité des algorithmes de décodage pour les codes LDPC non binaires concaténés avec les CPM. Plusieurs techniques peuvent être envisagées: la représentation de Rimoldi, la décomposition de Mengali [MM95], les récepteurs à faible complexité, les EXIT Charts non binaires [SMB01] .... Enfin, l'adaptabilité du rendement n'a pas été considérée pour concevoir les familles de codes à rendement adaptable comme dans [NND12] pour le cas du canal AWGN binaire.

6 Analyse à taille finie

Les énumerateurs de poids entrées/sorties sont un outil utile pour déterminer la performance des codes à longueur finie dans les schémas concaténés [RL09]. En utilisant la borne de l'union du taux d'erreurs binaires, on peut analyser la performance des schémas concaténés en série dans la région du plancher d'erreur.

6.1 Énumérateurs de la CPM

Comme la CPM peut être assimilée à un code non linéaire, la définition des événements d'erreurs est différente de codes convolutifs, puisque nous ne pouvons pas supposer le mot de code zéro. Pour cela, nous considérons la représentation de l'arbre de la différence de phase[AAS86]. Dans les configurations générales de la CPM, le spectre poids entrée/sorties est pas simple car les coefficients de pondération de sortie sont plus ou moins continue. Une extension de la méthode dans [AAS86, MA01] pour la taille finie des CPM reste un problème ouvert. Dans [MA01, GiAND09], les différents auteurs ont étudié la borne de l'union liée aux schémas CPM+codes convolutifs. Afin d'alléger les calculs, les auteurs ont considérés de grands entrelaceurs. Il est intéressant d'appliquer leur méthode à des shémas LDPC+CPM.

6.2 Les énumérateurs de poids pour les protographes

Pour les systèmes de codage avancés, il est généralement très complexe de calculer ls énumérateurs de poids en raison de la haute complexité combinatoire des calculs. Pour cela, on peut calculer les énumérateurs de poids asymptotiques (AWE), *i.e.* quand la longueur du mot de code tend vers l'infini. Les AWE nous permettent de calculer la distance minimale d'un code spécifique: les bons ensembles de codes sont ceux qui présentent une distance minimale qui croît linéairement avec la longueur du code. Inspiré des schémas concaténés [BDMP98], la dérivation des énumérateurs de poids des codes LDPC basés sur des protographes est bien expliquée dans [DJM98, FMT05]. Cependant, les simulations deviennent rapidement irréalisables lorsque l'on traite des grands mots de code. Le goulot d'étranglement dans ces calculs est l'évaluation des énumérateurs de poids des noeuds de variables, en particulier pour les codes à rendement élevé (noeuds de parité fortement connectés) ou pour les noeuds de parité généralisés. Afin d'alléger les calculs, [ASDR11] a proposé une conjecture fondée sur une approche *types de branches*.

Dans l'annexe C, nous passons en revue les principales méthodes pour calculer les énumérateurs de poids des codes propographes. Ensuite nous fournissons une preuve de la conjecture d'Abu Surra. D'autre part, nous introduisons une nouvelle méthode qui calcule de manière plus efficaces les énumérateurs de poids des noeuds de parité. Basée sur une relaxation continue du problème d'optimisation, cette méthode donne des résultats très précis et réduit considérablement la complexité même pour de très grandes longueurs de code ou de noeuds de parité de grand degré. Cette approche peut être appliquée notamment afin d'alléger les calculs pour les codes à haut rendement, les codes protographes généralisés ou les codes protographes spatialement couplés. Les résultats de cette annexe sont aussi utiles pour le dénombrement d'autres objets comme les ensembles de piégeage, les ensembles d'arrêt et les pseudo mots de code. Finalement, le calcul des énumérateurs asymptotiques pour les espaces euclidiens n'a pas encore été considéré et serait utile pour les schémas de modulation linéaire et non linéaire.

Pour les énumérateur de poids à taille finis ou pour les énumérateurs des codes LDPC non binaires, la méthode mentionnée ci-dessus n'est pas adaptée et engendre des calculs de très haute complexité. Dans ce cas, l'approche proposée dans [GDF15] serait plus adaptée.

Conclusions and perspectives

Conclusions

In this thesis, we were interested in the challenges related to the increasing demand of the frequency allocations for the civil UAVs applications. Indeed, thanks to their very good properties, continuous phase modulations were prescribed by the ITU and the ICAO recommendations for future UAV to satellite communications, digital video broadcasting DVB-RCS2 and by the NATO for STANAG 4606. This class of modulations is an excellent candidate for this context not only for its constant envelope and very good spectral occupancy, but also for its structure easily adaptable for serially concatenated schemes. The objective of this thesis was to study the CPM receivers and to design LDPC and other sparse graph-based codes for CPM as close as possible to the channel capacity. For the targeted applications, we are interested in relatively large frames and good performance at frame error rates of 10^{-3}.

The first investigated channel codes for CPM in the literature were based on the binary and non-binary short block convolutional codes. However, LDPC codes were dismissed because it has been widely argued that serial concatenation with LDPC codes implies a doubly iterative system which is difficult to analyse and thus to optimize. Consequently, no real complete studies have been conducted in that direction, and in most of the cases, the proposed approaches lack generality.

The first chapter 1 introduced continuous phase modulation and reviewed its main decompositions and receiver architectures. Then, we introduced the main sparse graph codes that have been investigate throughout the dissertation.

The second chapter 2 analysed and optimized the asymptotic performance for the serial concatenation of the CPM with unstructured LDPC codes. The presented framework is based on an EXIT curve fitting approach and can be generalized to any other detector. Thanks to the fact that the EXIT chart of the CPM reaches the point $(1, 1)$, we allowed some degree-1 variable nodes to improve

the decoding threshold. This proportion is subject to a stability condition that we derived from an EXIT chart point of view. In the general case, *i.e.* with any other detector, our stability condition constraints the proportions of degree-1 and degree-2 variable nodes in order to insure successful decoding. Simulation results where we were able to design LDPC codes very close to the capacity are also given.

In the third chapter 3, we studied the iterative decoding with more practical sparse graph based codes in the sense that they are easily encodable, have compact representations and can be implemented in parallel architectures. Firstly, we provide an optimization method to design GIRA codes. Since we proposed to use of systematic codes in order to avoid a supplementary optimization complexity of the doping check nodes, we considered an uncommon iterative decoding that allows to design codes that operate between $0.2 - 0.5$dB from the unstructured LDPC codes. Secondly, we studied protograph codes. By suitably defining an optimization procedure we were able to design codes that operate at 0.5dB from the unstructured LDPC codes. Finally, to obtain good protographs in both the error floor and water fall regions, we focused on protograph based spatially coupled LDPC codes. We compared the performance of coupling simple protograph and coupling CPM optimized protograhs. Moreover, we proposed a new termination method that gives very good thresholds without any rate loss by restricting the convolution gain to one *wave* only.

In the chapter 4, we studied some receiver aspects of the CPM and designed LDPC codes for low complexity receiver based on Laurent's decomposition. Unlike the existing CPM MAP detections, we derived a new receiver that takes into account the ISI terms induced by the Laurent's representation. The simulation results show that this new receiver outperforms the classical one by up to 2dB for both coded and uncoded CPM schemes. Finally, we demonstrate that the performance of the optimized LDPC codes for full complexity receivers remain very good for the low complexity implementation as long as enough components are taken into account.

The last chapter 5 gave simulation results in the context of some applications. Firstly, we compared our design results to the DVB-RCS2 standard. Then, we investigated the behaviour of the coded and uncoded CPM systems in the context of aeronautical channel. Finally, we proved that a simple equalization procedure of type MMSE leads to very good results with CPM over a general ISI and over the aeronautical channels.

Perspectives

Many perspectives can be suggested for future works as enumerated in the following non exhaustive propositions. Some of them have been initiated during this thesis and have shown promising results.

1 Turbo equalization

Novel iterative CPM decoding schemes over frequency/time fading channels as the aeronautical channel can include turbo equalizations of type SISO MMSE equalization. One of the first studies were conducted by [Ozg08] where the author proposed a combined equalization and decoding for binary CPMs and analysed related computational complexity aspects assuming perfect channel state information knowledge. Future works can extend the results to non binary CPM configurations and investigate adaptive turbo equalization algorithms without channel estimation functions [Sch04, RBL05]. Moreover, new equalization algorithms could be proposed for the new Laurent-based receiver.

2 Frequency/time synchronization and non-coherent detection

In our works, we assumed perfect frequency/time synchronizations and neglect the Doppler effect. In order to finalize the analysis of our system, we need to investigate the synchronization and mitigation capacity of the CPM over time and frequency fading channels with Doppler effect, a configuration that is encountered in the aeronautical channel. On the other hand, following the works in [VCT10] on non-coherent detection, extending the results to general CPM schemes and to non-coherent turbo detection can be envisaged. These research will help design robust CPM schemes for applications that can run across very bad flight conditions such as space launching vehicles.

3 Multiple antennas

We can consider the extension of our results of the simple MMSE equalization in chapter 5 to simple input multiple output (SIMO) schemes and their feasibility in the context of the CPM. By assuming that the aeronautical channel realizations are independent per antennas, we can run two disjoint equalization processes at the receiver side. As a result, at the output of the equalizers, we benefit from a spatial diversity that can be easily combined in the branch metrics of the SISO CPM receiver. Further analysis can consider also a joint equalization/decoding receiver. These results can be compared to the [HK98, WZ07] who investigate multiple input multiple output (MIMO) systems for the CPM.

4 Mapping optimization

Bit-interleaved coded modulation (BICM) technique [iFMC08] is a powerful approach that takes advantage of the different protection levels of bit channels in high modulation orders to improve the decoding threshold. The optimization of BICM in concatenated schemes has been well studied in the literature and several considerations have been proposed to improve the threshold such as the bit allocation mapping optimization or the precoding [PS06, SB04, tB01b].

M-ary CPM schemes also exhibits different bit protection levels of the different bit channels as depicted by Fig. 5.21

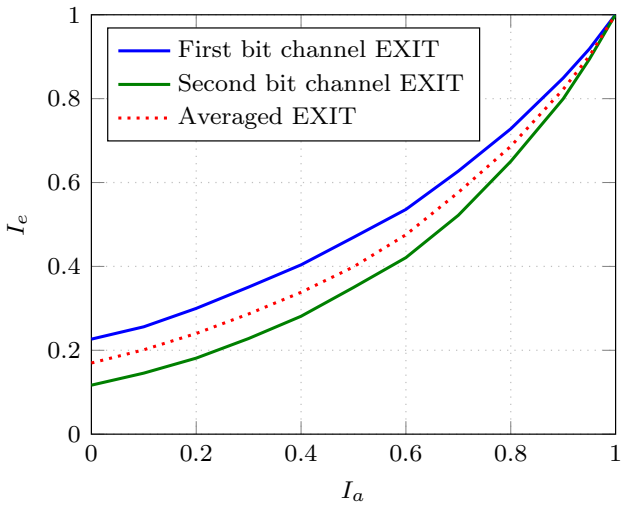

Figure 5.21: EXIT chart of different bit channels for the CPM scheme ($M = 4, L = 2, h = 1/3$, natural mapping) at $E_s/N_0 = -0.5$dB

Inspired by the method in [HGiAB+14] and in the context of the CPM, we can optimize the mapping in order to improve the design codes thresholds or in order to compensate the threshold degradation when we consider the direct truncation termination for spatially coupled LDPC codes. Preliminary works in the context of linear modulations were investigated in appendix D and promise encouraging results for the CPM.

5 Non-binary LDPC codes and rate compatible schemes

In this thesis, we analysed different binary LDPC codes. However non binary LDPC codes can also be of interest. These codes shows excellent results in various applications after the introduction

of an efficient low complexity decoder in the middle of 2000 [DF07]. Inspired by the study in [XA06], similar aspects can be investigate for non binary LDPC codes concatenated with M-ary CPM schemes. Moreover, in [LZM15], authors studied low complexity decoding algorithm for non binary LDPC codes and CPM concatenations. One can go further by designing non binary LDPC codes for CPM schemes. Several techniques can be considered: Rimoldi's representations, Mengali's decomposition [MM95], low complexity receivers, non binary EXIT charts [SMB01] ... Moreover, rate compatibility was not considered to design families of rate compatible protograph codes as conducted in [NND12] for the binary input AWGN channel , and thus could be considered in the context of the CPM.

6 Finite length analysis

Codeword input output weight enumerators are a useful tool to determine the finite length performance of concatenated schemes [RL09]. Using the union bound on the bit error probability, one can analyse the performance of serially concatenated schemes in the error floor region.

6.1 CPM enumerator

Because the CPM can be assimilated to an non-linear code, the definition of error events is different from convolutional codes since we cannot assume all-zero information word. Instead, we consider the difference phase tree representation [AAS86]. In general CPM configurations, the input output weight spectrum is not straightforward because the output weights are more or less continuous. Extending the method in [AAS86, MA01] to finite length CPM enumerators remains an open problem. In [MA01, GiAND09], authors studied the union bound for CPM+convolutional codes. In order to alleviate the computations, authors considered large interleaver lengths. It is interesting to apply their method to LDPC+CPM coded schemes.

6.2 Protograph-based LDPC enumerators

For advanced coding schemes, it generally impractical to compute weight enumerators due to the high combinatorial and computation complexity. Instead, one can compute asymptotic weight enumerators (AWE), *i.e.* when codeword length tends to infinity. The AWE allows us to compute the minimum distance of a specific code: good code ensembles are those which have a minimum distance that grows linearly with the code length. Inspired from concatenated schemes [BDMP98], the

derivation of the ensemble weight enumerators for protograph-based LDPC codes are well explained [DJM98, FMT05]. However, the simulations become quickly unfeasible when dealing with large code lengths. The bottleneck is the evaluation of the check node enumerators, especially for high rate codes (highly connected check nodes) and for generalized check nodes. In order to alleviate the computations, [ASDR11] proposed a conjecture based on an edge types approach.

In Appendix C, we review the main methods for the propograph code ensemble weight enumerators. We then provide a proof of the Abu Surra's conjecture. Additionally, we introduce a new method that computes more efficiently the enumerator of the check nodes. Based on a continuous relaxation optimization, this method gives very accurate results and reduces greatly the complexity even for very large code lengths or large degree check nodes. This approach can be applied particularly to lighten the computations for high rate codes, generalized protograph LDPC codes or protograph-based spatially coupled LDPC codes. The results of this appendix are also useful for the enumeration of other non-codeword objects such as trapping sets, stopping sets and pseudocodewords. Moreover, extension of the asymptotic weight enumerators for euclidean spaces has never been considered and could be useful for linear and non-linear high order modulation-based schemes.

For finite input output weight enumerators or for non binary protograph-based LDPC codes, the method mentioned here is inadapted and engender high complexity computations. Instead, the method proposed in [GDF15] must be investigated.

Appendices

Appendix A

A detailed proof of the Laurent's decomposition

In this appendix, we provide a detailed demonstration of the Laurent's decomposition in [Lau86].

Let us consider a CPM phase function $\varphi(t)$ defined as:

$$\varphi(t) = \begin{cases} 0 & t \leq 0 \\ h\pi & t \geq LT \end{cases} \tag{A.1}$$

Consider the complex notation of a CPM signal:

$$s(t) = \exp j \left[\theta_0 + \sum_{-\infty}^{+\infty} a_n . \varphi \left(t - nT \right) \right], \quad \text{where} \quad a_n = \pm 1 \tag{A.2}$$

For simplicity reasons, let us use the following notations, where T is the bit duration duration:

$$\begin{aligned} M &= 2^{L-1} \\ \phi &= h\pi \\ C &= \cos(\phi) \\ S &= \sin(\phi) \\ J &= \exp j\phi \\ t &= NT + \tau, \quad with \;\; 0 \leq \tau < T \end{aligned} \tag{A.3}$$

A baseband CPM signal is written as (see chapter 1 for more details):

$$\begin{aligned} s(t) &= \exp j \left[\theta_0 + \sum_{-\infty}^{+\infty} a_n . \varphi(t - nT)) \right] \\ &= \exp j \left[\theta_0 + \sum_{-\infty}^{N-L} a_n . \varphi(t - nT) + \sum_{N-L+1}^{+\infty} . \varphi(t - nT) \right] \end{aligned}$$

$$= \exp j\left[\theta_0\right] \times \exp j\left[\sum_{-\infty}^{N-L} a_n.\varphi(t-nT)\right] \times \exp j\left[\sum_{N-L+1}^{+\infty} a_n.\varphi(t-nT)\right]$$

$$\textbf{(A)} \qquad\qquad \textbf{(B)}$$

Without loss of generality, we can consider $\theta_0 = 0$. The time instant of **(A)** is:

$$\begin{aligned} n \leq N-L &\Rightarrow t - nT \geq t - (N-L)T \\ &\Rightarrow t - nT \geq NT + \tau - NT + LT, \quad \forall \tau \in [\![0, T[\![\\ &\Rightarrow t - nT \geq LT + \tau \\ &\Rightarrow t - nT \geq LT \end{aligned}$$

Then, using Eq. (A.1), we get:

$$\textbf{(A)} = \exp j\left[\sum_{-\infty}^{N-L} a_n \phi\right] = (\exp j\phi)^{\sum_{-\infty}^{N-L} a_n} = J^{\sum_{-\infty}^{N-L} a_n}$$

For term **(B)**, since we are at instant $t = NT + \tau$, all symbols a_k when $k > N$ are equal to 0. Then:

$$\begin{aligned} \textbf{(B)} &= \exp j\left[\sum_{N-L+1}^{+\infty} a_n.\varphi(t-nT)\right] \\ &= \exp j\left[\sum_{N-L+1}^{N} a_n.\varphi(t-nT)\right] \\ &= \exp j\left[\sum_{-L+1}^{0} a_{N+n}.\varphi(t-(N+n)T)\right] \\ &= \exp j\left[\sum_{0}^{L-1} a_{N-n}.\varphi(t-(N-n)T)\right] \end{aligned}$$

Finally, we can rewrite expression (A.2) to find expression in [Lau86, Eq. (4)] as:

$$s(t) = \exp j\theta_0 \times J^{\sum_{-\infty}^{N-L} a_n} \times \prod_{i=0}^{L-1} \exp j\left[a_{N-i}.\varphi(t-(N-i)T)\right] \tag{A.4}$$

[Lau86] shows that it is possible to see the complex exponential in (A.4) as sum of two terms where the second one is data independent. In the following, we provide a detailed derivation of such expression. For simplification reasons, we take $\varphi(t - nT) = \varphi$.

- If $a_n = +1$, we have

$$\begin{aligned} e^{ja_n\varphi} &= e^{j\varphi} \\ &= e^{j\varphi} \times \frac{e^{j\phi} - e^{-j\phi}}{e^{j\phi} - e^{-j\phi}} \\ &= \frac{e^{j\varphi}e^{j\phi} - e^{j\varphi}e^{-j\phi}}{e^{j\phi} - e^{-j\phi}} \\ &= \frac{e^{j\varphi}e^{j\phi} - e^{-j\varphi}e^{j\phi} + e^{-j\varphi}e^{j\phi} - e^{j\varphi}e^{-j\phi}}{e^{j\phi} - e^{-j\phi}} \\ &= \frac{e^{j\phi}\left(e^{j\varphi} - e^{-j\varphi}\right) + e^{j(\phi-\varphi)} - e^{-j(\phi-\varphi)}}{e^{j\phi} - e^{-j\phi}} \\ &= e^{j\phi} \times \frac{\sin\varphi}{\sin\phi} + \frac{\sin\left(\phi - \varphi\right)}{\sin\phi} \end{aligned}$$

- Otherwise if $a_n = -1$, we have:

$$\begin{aligned} e^{ja_n\varphi} &= e^{-j\varphi} \\ &= e^{-j\varphi} \times \frac{e^{j\phi} - e^{-j\phi}}{e^{j\phi} - e^{-j\phi}} \\ &= \frac{e^{-j\varphi}e^{j\phi} - e^{-j\varphi}e^{-j\phi}}{e^{j\phi} - e^{-j\phi}} \\ &= \frac{e^{-j\varphi}e^{j\phi} - e^{j\varphi}e^{-j\phi} + e^{j\varphi}e^{-j\phi} - e^{-j\varphi}e^{-j\phi}}{e^{j\phi} - e^{-j\phi}} \\ &= \frac{e^{j(\phi-\varphi)} - e^{-j(\phi-\varphi)} + e^{-j\phi}\left(e^{j\varphi} - e^{-j\varphi}\right)}{e^{j\phi} - e^{-j\phi}} \\ &= \frac{\sin\left(\phi - \varphi\right)}{\sin\phi} + e^{-j\phi} \times \frac{\sin\varphi}{\sin\phi} \end{aligned}$$

In both cases, we deduce that

$$e^{ja_n\varphi(t-nT)} = \frac{\sin\left(\phi - \varphi(t - nT)\right)}{\sin\phi} + e^{-j\phi}\frac{\sin\varphi}{\sin\phi}$$

Using notations in (A.3), we finally get the equality in [Lau86, Eq. (5)]:

$$e^{ja_n\varphi(t-nT)} = \frac{\sin\left(\phi - \varphi(t - nT)\right)}{\sin\phi} + J^{a_n}\frac{\sin\left(\varphi(t - nT)\right)}{\sin\phi} \tag{A.5}$$

At this stage, we define a generalized phase pulse function $\psi(t)$ as:

$$\psi(t) = \begin{cases} \varphi(t) & t < LT \\ \phi - \varphi(t - LT) & LT \leq t \end{cases} \tag{A.6}$$

This definition allows us to introduce the following sequence, which plays an important role in the Laurent's decomposition:

$$S_n(t) = \frac{\sin\left(\psi(t + nT)\right)}{S} = S_0(t + nT) \tag{A.7}$$

From Eqs. (A.4) and (A.5), we conclude:

$$\begin{aligned} S(t) &= J^{\sum_{-\infty}^{N-L} a_n} \times \prod_{i=0}^{L-1} \exp j \left[a_{N_i}.\varphi(t - (N-i)T)\right] \\ &= J^{\sum_{-\infty}^{N-L} a_n} \times \prod_{i=0}^{L-1} \left[\frac{\sin\left[\phi - \varphi(t - (N-i)T)\right]}{S} + J^{a_{N-i}} \frac{\sin\left[\varphi(t - (N-i)T)\right]}{S}\right] \end{aligned}$$

One can easily show that:

$$\begin{aligned} &\forall i \in [\![0, L-1]\!], \quad t - (N-i)T < LT \\ &\forall i \in [\![0, L-1]\!], \quad t - (N-i-L)T \geq LT \end{aligned}$$

This leads to the simplified expression:

$$S(t) = J^{\sum_{-\infty}^{N-L} a_n} \prod_{i=0}^{L-1} \left[S_{i+L-N}(t) + J^{a_{N-i}} S_{i-N}(t)\right] \tag{A.8}$$

Since the sum indexes considered in this equation vary as :

$$\begin{aligned} &(i + L - N) \in [\![L - N, 2L - N - 1]\!] \\ &(i - N) \in [\![-N, L - N - 1]\!] \end{aligned}$$

we conclude that:

$$\{S_i\}_{i \in [\![L-N, 2L-N-1]\!]} \cap \{S_n\}_{i \in [\![-N, L-N-1]\!]} = \emptyset$$

Consequently, the product in (A.8) can be written as a sum of 2^L different terms, where each of them is a product of L functions of the set $\{S_i\}_{i \in [\![-N, 2L-N-1]\!]}$

In the following example, we identify these terms. Let us consider the case where $N = 0$ and $L = 4$. Then we have:

$$S(t) = (S_4 + J^{a_0} S_0)(S_5 + J^{a_1} S_1)(S_6 + J^{a_2} S_2)(S_7 + J^{a_3} S_3)$$

After expanding this product, $S(t)$ contains 16 different terms. Those that contain $S_0(t)$ are:

$$F_1(t) = S_0.S_1.S_6.S_7 \qquad F_2(t) = S_0.S_1.S_2.S_7 \qquad F_3(t) = S_0.S_2.S_5.S_7 \qquad F_4(t) = S_0.S_1.S_3.S_6$$
$$F_5(t) = S_0.S_3.S_5.S_6 \qquad F_6(t) = S_0.S_2.S_3.S_5 \qquad F_7(t) = S_0.S_5.S_6.S_7 \qquad F_8(t) = S_0.S_1.S_2.S_3$$

From these 8 functions and their time-translated versions, we can derive all the 16 terms taking place in $S(t)$ as:

$$\begin{aligned} S(t) = {} & F_1(t) + F_2(t) + F_3(t) + F_4(t) + F_4(t+T) + F_5(t) + F_5(t+T) + F_6(t) + F_6(t+T) \\ & + F_6(t+2T) + F_7(t) + F_8(t) + F_8(t+T) + F_8(t+2T) + F_8(t+3T) + F_8(t+4T) \end{aligned}$$

Generalizing to any value of N and L, one can always construct such 2^{L-1} functions, noted $\{C_k\}_{k \in [\![0, 2^{L-1}-1]\!]}$, which generate, by time translations of $aT/a \in \mathbb{N}$, all the 2^L terms of S(t).

Compute the module of C_k

Let us now consider the new expression of S(t):

$$\begin{aligned} S(t) = & \prod_{i=0}^{L-1} S_{i+L-N} + S_{i-N} \\ = & (S_{L-N} + S_{-N})(S_{L-N+1} + S_{-N+1})...(S_{L-N+i} + S_{i-N})(S_{L-N+i+1} + S_{-N+i+1})... \\ & (S_{2L-N-1} + S_{-N+L-1}) \end{aligned}$$

i.e.:

$$S(t - NT) = (S_L + S_0)(S_{L+1} + S_1)...(S_{L+i} + S_i)(S_{L+i+1} + S_{i+1})...(S_{2L-1} + S_{L-1})$$

By definition, C_k are terms of $S(t)$ where $S_0(t)$ appears. It is clear from by expanding the above factorization that there are exactly 2^{L-1}. They are found when expending the product:

$$S_0 \times (S_{L+1} + S_1) \times (S_{L+2} + S_2) \times ... \times (S_{L+i} + S_i) \times ... \times (S_{2L-1} + S_{L-1})$$

Each C_k can then be redefined by the fact that it is S_0 times the sum of the elements of a pair chosen in $\{(S_{L+i}, S_i)\}_{i\in[\![1,L-1]\!]}$.

On the other hand, let us introduce the notation:

$$\{S_{L+i}, S_i\}_{i\in[\![1,L-1]\!]} = \{S_{i+L\alpha_{i,k}} / \alpha_{i,k} \in \{0,1\}\}$$

This leads to the new expression of C_k:

$$C_k(t) = S_0 \times \prod_{i=1}^{L-1} S_{i+L\alpha_{i,k}} \quad \text{where } \boldsymbol{\alpha_k} = (\alpha_{1,k}, \alpha_{2,k}, ..., \alpha_{L-1,k}) \in \{0,1\}^{L-1}$$

Therefore, each C_k can be characterized by a unique vector $\boldsymbol{\alpha_k}$. Since there are 2^{L-1} of them, all values of $\boldsymbol{\alpha_k}$ can be exhaustively enumerated by taking the binary representation on $L-1$ bits of the integers $\{0, 1, \ldots, 2^{L-1}-1\}$.

Finally, [Lau86, Eq. (10)] is obtained by reordering the C_k's as following:

$$C_k(t) = S_0(t-NT) \times \prod_{i=1}^{L-1} S_{i+L\alpha_{i,k}}(t-NT), \quad k = \sum_{i=1}^{L-1} 2^{i-1}\alpha_{i,k} \tag{A.9}$$

Compute the duration of C_k

According to Eq. (A.5):

$$t > 2LT, S_0(t) = 0$$

When applied to C_k, this leads to:

$$t + [i + L\alpha_{k,i}]T \geq 2LT \Rightarrow t \geq [(2-\alpha_{k,i})L - i]T$$

Consequently, $C_k(t)$ is different from the null function if $t \leq [(2-\alpha_{k,i})L - i]T$. From Eq. (A.9), we conclude:

$$0 \leq t \leq T \times \min_{i\in[\![1,L-1]\!]} [(2-\alpha_{i,k})L - i]$$

which gives the duration of C_k

Compute the module of $C_k(t)$

The pseudo symbol corresponding to $C_k(t)$ is given by Eq. (A.8) and (A.9):

$$\sum_{-\infty}^{N-L} a_n + a_N + \sum_{1}^{L-1} (1-\alpha_{k,i}) a_{N-i}$$

By introducing the following recursion, one can derive the phase of C_k:

$$\begin{aligned}
A_{k,N} &= \sum_{-\infty}^{N-L} a_n + a_N + \sum_{1}^{L-1} (1-\alpha_{k,i}) a_{N-i} \\
&= \sum_{-\infty}^{N-L} a_n + \sum_{N-L+1}^{N} a_n - \sum_{N-L+1}^{N} a_n + a_N + \sum_{1}^{L-1} (1-\alpha_{k,i}) a_{N-i} \\
&= \sum_{-\infty}^{N} a_n - \sum_{-L+1}^{0} a_{N+n} + a_N + \sum_{1}^{L-1} (1-\alpha_{k,i}) a_{N-i} \\
&= \sum_{-\infty}^{N} a_n - \sum_{1}^{L-1} a_{N-n} + \sum_{1}^{L-1} (1-\alpha_{k,i}) a_{N-i} \\
&= \sum_{-\infty}^{N} a_n - \sum_{1}^{L-1} \alpha_{k,i}.a_{N-i} \\
&= A_{0,N} - \sum_{1}^{L-1} \alpha_{k,i}.a_{N-i}
\end{aligned}$$

Finally, we form the Laurent's decomposition of a CPM signal as:

$$S(t) = \sum_{-\infty}^{+\infty} \sum_{k=0}^{M-1} J^{A_{k,N}}.C_k(t-NT) \tag{A.10}$$

By abuse of notations, C_k here refer to the module of C_k.

Appendix B

Proof of the stability condition

EXIT chart recursions are given by:

$$
\begin{aligned}
I_{v-c}^{\ell} &= \sum_{i=1}^{d_v} \lambda_i J\left[\sqrt{(i-1)\left[J^{-1}\left(I_{c-v}^{\ell-1}\right)\right]^2 + \left[J^{-1}\left(I_{cpm-v}^{\ell}\right)\right]^2}\right] \\
I_{cpm-v}^{\ell} &= T_\sigma\left(J\left(\sqrt{i}J^{-1}\left(I_{c-v}^{\ell-1}\right)\right)\right) \\
I_{c-v}^{\ell-1} &= \sum_{j=2}^{d_c} \rho_j I_{c-v}^{\ell-1}(j) \\
I_{c-v}^{\ell-1}(j) &= 1 - J\left(\sqrt{i-1}J^{-1}\left(1 - I_{v-c}^{\ell-1}\right)\right)
\end{aligned}
$$

Notations:

$$
\begin{aligned}
x^{\ell} &= I_{v-c}^{\ell} \\
J(x) &:= J(x^2/2) \\
f\left(x^{\ell-1}\right) &= I_{c-v}^{\ell-1} = 1 - \sum_{j=2}^{d_c} \rho_j J\left((j-1)J^{-1}\left(1 - x^{\ell-1}\right)\right)
\end{aligned} \tag{B.1}
$$

Then:

$$
x^{\ell} = \sum_{i=1}^{d_v} \lambda_i J\left[(i-1)J^{-1} \circ f\left(x^{\ell-1}\right) + J^{-1} \circ T_\sigma \circ J\left(iJ^{-1} \circ f\left(x^{\ell-1}\right)\right)\right]
$$

Define the recursion function:

$$
x^{\ell} = \Psi\left(x^{\ell-1}\right) = \sum_{i=1}^{d_v} \lambda_i J\left[(i-1)J^{-1} \circ f\left(x^{\ell-1}\right) + J^{-1} \circ T_\sigma \circ J\left(iJ^{-1} \circ f\left(x^{\ell-1}\right)\right)\right] \tag{B.2}
$$

Introduce the notations:

$$
\mu = J^{-1} \circ f \qquad \eta = J^{-1} \circ T_\sigma \circ J \tag{B.3}
$$

where $f(.)$ is defined in Eq. (B.1).

We get:

$$\Psi(x) = \sum_{i=1}^{d_v} \lambda_i J\left[(i-1)\,\mu(x) + \eta\left(i\mu(x)\right)\right] \tag{B.4}$$

Suppose T_σ is differentiable arround 1^- (slope of the tangent at 1^- is finite). We have:

$$\begin{aligned}
\frac{d\Psi}{dx}(x) &= \left[\sum_{i=1}^{d_v} \lambda_i J\left[(i-1)\,\mu(x) + \eta\left(i\mu(x)\right)\right]\right]' \\
&= \sum_{i=1}^{d_v} \lambda_i \left[(i-1)\,\mu(x) + \eta\left(i\mu(x)\right)\right]' J'\left[(i-1)\,\mu(x) + \eta\left(i\mu(x)\right)\right] \\
&= \sum_{i} \lambda_i \left[(i-1)\,\mu'(x) + i\mu'(x)\eta'(i\mu(x))\right] J'\left[(i-1)\,\mu(x) + \eta(i\mu(x))\right]
\end{aligned} \tag{B.5}$$

First we have:

$$\begin{aligned}
\mu'(x) &= \left(J^{-1} \circ f\right)'(x) \\
&= f'(x)\left(J^{-1}\right)' \circ f(x) \\
&= f'(x)\frac{1}{J' \circ J^{-1}} \circ f(x) \\
&= f'(x)\frac{1}{J' \circ J^{-1} \circ f}(x) \\
&= f'(x)\frac{1}{J'\left(\mu(x)\right)}
\end{aligned} \tag{B.6}$$

Let us find f'. From Eq. (B.1) we obtain:

$$\begin{aligned}
f'(x) &= \left[1 - \sum_j \rho_j J\left((j-1)J^{-1}(1-x)\right)\right]' \\
&= -\sum_j \rho_j (j-1)\left(J^{-1}(1-x)\right)' J'\left((j-1)J^{-1}(1-x)\right) \\
&= -\sum_j \rho_j (j-1)\frac{-1}{J' \circ J^{-1}(1-x)} J'\left((j-1)J^{-1}(1-x)\right) \\
&= \sum_j \rho_j (j-1)\frac{1}{J' \circ J^{-1}(1-x)} J'\left((j-1)J^{-1}(1-x)\right)
\end{aligned} \tag{B.7}$$

Finally, η' is equal to:

$$\eta'(x) = \left(J^{-1} \circ T_\sigma \circ J\right)'(x)$$

$$
\begin{aligned}
&= J'(x) \times \left(J^{-1} \circ T_\sigma\right)' \circ J(x) \\
&= J'(x) \times T'_\sigma \circ J(x) \times \left(J^{-1}\right)' \circ T_\sigma \circ J(x) \\
&= J'(x) \times T'_\sigma \circ J(x) \times \frac{1}{J' \circ J^{-1} \circ T_\sigma \circ J(x)} \\
&= J'(x) \times T'_\sigma(J(x)) \times \frac{1}{J'(\eta(x))} \qquad \text{(B.8)}
\end{aligned}
$$

From Eqs. (B.5), (B.6), (B.8) and (B.7)

$$
\begin{aligned}
\frac{d\Psi}{dx}(x) &= \sum_i \lambda_i \left[(i-1)\mu'(x) + i\mu'(x)\eta'(i\mu(x))\right] J'\left[(i-1)\,\mu(x) + \eta(i\mu(x))\right] \\
&= \sum_i \lambda_i \left[(i-1) + i\eta'(i\mu(x))\right] \mu'(x) J'\left[(i-1)\,\mu(x) + \eta(i\mu(x))\right] \\
&= \sum_i \lambda_i \left[(i-1) + iJ'(i\mu(x)) \times T'_\sigma(J(i\mu(x))) \times \frac{1}{J'(\eta(i\mu(x)))}\right] \\
&\qquad \times f'(x) \frac{1}{J'\left(\mu(x)\right)} \\
&\qquad \times J'\left[(i-1)\,\mu(x) + \eta(i\mu(x))\right] \\
&= \sum_i \lambda_i \left[(i-1) + iT'_\sigma(J(i\mu(x))) \times \frac{J'(i\mu(x))}{J'(\eta(i\mu(x)))}\right] \\
&\qquad \times \sum_j \rho_j(j-1) \frac{1}{J' \circ J^{-1}(1-x)} J'\left((j-1)J^{-1}(1-x)\right) \frac{1}{J'\left(\mu(x)\right)} \\
&\qquad \times J'\left[(i-1)\,\mu(x) + \eta(i\mu(x))\right] \\
&= \sum_i \lambda_i \left[(i-1) + iT'_\sigma(J(i\mu(x))) \times \frac{J'(i\mu(x))}{J'(\eta(i\mu(x)))}\right] \frac{J'\left[(i-1)\,\mu(x) + \eta(i\mu(x))\right]}{J'\left(\mu(x)\right)} \\
&\qquad \times \sum_j \rho_j(j-1) \frac{J'\left((j-1)J^{-1}(1-x)\right)}{J'(J^{-1}(1-x))} \\
&= \lambda_1 T'_\sigma(J(\mu(x))) \times \frac{J'(\mu(x))}{J'(\eta(\mu(x)))} \frac{J'\left[\eta(\mu(x))\right]}{J'\left(\mu(x)\right)} \sum_j \rho_j(j-1) \frac{J'\left((j-1)J^{-1}(1-x)\right)}{J'(J^{-1}(1-x))} \\
&\quad + \sum_{i \geq 2} \lambda_i \left[(i-1) + iT'_\sigma(J(i\mu(x))) \times \frac{J'(i\mu(x))}{J'(\eta(i\mu(x)))}\right] \frac{J'\left[(i-1)\,\mu(x) + \eta(i\mu(x))\right]}{J'\left(\mu(x)\right)} \\
&\qquad \times \sum_j \rho_j(j-1) \frac{J'\left((j-1)J^{-1}(1-x)\right)}{J'(J^{-1}(1-x))} \\
&= \lambda_1 T'_\sigma(J(\mu(x))) \sum_j \rho_j(j-1) \frac{J'\left((j-1)J^{-1}(1-x)\right)}{J'(J^{-1}(1-x))}
\end{aligned}
$$

$$+\sum_{i\geq 2}\lambda_i\left[(i-1)+iT'_\sigma(J(i\mu(x)))\times\frac{J'(i\mu(x))}{J'(\eta(i\mu(x)))}\right]\frac{J'\left[(i-1)\,\mu(x)+\eta(i\mu(x))\right]}{J'\left(\mu(x)\right)}$$
$$\times\sum_j\rho_j(j-1)\frac{J'\left((j-1)J^{-1}(1-x)\right)}{J'(J^{-1}(1-x))}$$

$$=\lambda_1T'_\sigma(J(\mu(x)))\sum_j\rho_j(j-1)\frac{J'\left((j-1)J^{-1}(1-x)\right)}{J'(J^{-1}(1-x))} \tag{B.9}$$

$$+\sum_{i\geq 2}(i-1)\lambda_i\frac{J'\left[(i-1)\,\mu(x)+\eta(i\mu(x))\right]}{J'\left(\mu(x)\right)}\times\sum_j\rho_j(j-1)\frac{J'\left((j-1)J^{-1}(1-x)\right)}{J'(J^{-1}(1-x))} \tag{B.10}$$

$$+\sum_{i\geq 2}i\lambda_iT'_\sigma(J(i\mu(x)))\times\frac{J'(i\mu(x))}{J'(\eta(i\mu(x)))}\times\frac{J'\left[(i-1)\,\mu(x)+\eta(i\mu(x))\right]}{J'\left(\mu(x)\right)}$$
$$\times\sum_j\rho_j(j-1)\frac{J'\left((j-1)J^{-1}(1-x)\right)}{J'(J^{-1}(1-x))} \tag{B.11}$$

Useful limits

• From the definition of the function $J(.)$ [tB01d], we have:

$$J(0)=0\quad,\quad J^{-1}(0)=0\quad,\quad\lim_{x\to+\infty}J(x)=1\quad\text{and}\quad\lim_{x\to1^-}J^{-1}(x)=+\infty \tag{B.12}$$

• Using the continuity of $J^{-1}(.)$ and $f(.)$, Eq. (B.3) gives:

$$\lim_{x\to1^-}\mu(x)=\lim_{x\to1^-}J^{-1}\circ f(x)$$
$$=\lim_{x\to1^-}J^{-1}\left(1-\sum_{j=2}^{d_c}\rho_jJ\left((j-1)\,J^{-1}\,(1-x)\right)\right)=+\infty \tag{B.13}$$

• From different observations, let us assume that the derivative of the EXIT transfer function of the detector T_σ is defined at 1, *i.e.*:

$$T'_\sigma(1)\in\mathbb{R} \tag{B.14}$$

• In [RU08], for small x, the Taylor expansion of J around 0 is given by:

$$J(x)=\frac{x}{4}-\frac{x^2}{16}+\frac{x^3}{48}+O(x^4)$$

which leads to:

$$J'(0)=\frac{1}{4} \tag{B.15}$$

- Using the result in [RU08] for very large x:

$$J(x) = 1 - \frac{\sqrt{\pi}}{\ln(2)} e^{-\frac{x}{4}} \left(m^{-\frac{-1}{2}} - \frac{8+\pi^2}{4} x^{\frac{-3}{2}} + O(x^{\frac{-5}{2}}) \right)$$

By deriving this Taylor expansion and taking the first order only, we get:

$$J'(x) \underset{+\infty}{\sim} \frac{\sqrt{\pi}}{4\ln(2)} \frac{e^{-\frac{x}{4}}}{\sqrt{x}} \tag{B.16}$$

Limit of the term in Eq. (B.9)

- From Eq. (B.15), and since $J'(.)$ is not null around 0, when $x \to 1$, we have:

$$\lim_{x \to 1^-} \frac{J'\left((j-1)J^{-1}(1-x)\right)}{J'(J^{-1}(1-x))} = \frac{J'(0)}{J'(0)} = 1 \quad \forall j \in \mathbb{N} \setminus \{0,1\} \tag{B.17}$$

- We then have from Eqs. (B.17) and (B.14):

$$\lim_{x \to 1^-} \lambda_1 T'_\sigma(J(\mu(x))) \sum_j \rho_j(j-1) \frac{J'\left((j-1)J^{-1}(1-x)\right)}{J'(J^{-1}(1-x))} = \lambda_1 T'_\sigma(1) \sum_j \rho_j(j-1) \tag{B.18}$$

Limit of the term in Eq. (B.10)

- From Eq. (B.16), and since $J'(.)$ is not null at high values, we can write:

$$\begin{aligned} \frac{J'\left[(i-1)\mu(x) + \eta(i\mu(x))\right]}{J'\left(\mu(x)\right)} &\sim \frac{e^{-\frac{(i-1)\mu(x)+\eta(i\mu(x))}{4}}}{\sqrt{(i-1)\mu(x)+\eta(i\mu(x))}} \frac{\sqrt{\mu(x)}}{e^{-\frac{\mu(x)}{4}}} \\ &\sim \sqrt{\frac{\mu(x)}{(i-1)\mu(x)+\eta(i\mu(x))}} \exp - \frac{(i-1)\mu(x)+\eta(i\mu(x))-\mu(x)}{4} \\ &\sim \sqrt{\frac{\mu(x)}{(i-1)\mu(x)+\eta(i\mu(x))}} \exp - \frac{(i-2)\mu(x)+\eta(i\mu(x))}{4} \end{aligned} \tag{B.19}$$

- if $i = 2$, then Eq. (B.19) becomes:

$$\frac{J'\left[(i-1)\mu(x) + \eta(i\mu(x))\right]}{J'\left(\mu(x)\right)} \sim \sqrt{\frac{\mu(x)}{\mu(x)+\eta(2\mu(x))}} \exp - \frac{\eta(2\mu(x))}{4}$$

If $\lim_{x \to 1^-} T_\sigma(x) < 1$:

$$\lim_{x \to 1^-} \sqrt{\frac{\mu(x)}{\mu(x)+\eta(i\mu(x))}} \exp - \frac{\eta(2\mu(x))}{4} = \exp - \frac{J^{-1}(T_\sigma(1))}{4}$$

Else if $\lim_{x\to 1^-} T_\sigma(x) = 1$: Since $\mu(.)$ and $\eta(.)$ are positive functions, we can write:

$$0 \leq \sqrt{\frac{\mu(x)}{\mu(x)+\eta(i\mu(x))}} \exp -\frac{\eta(2\mu(x))}{4} \leq \exp -\frac{\eta(2\mu(x))}{4}$$

Using the Sandwich theorem [Wei05], we conclude:

$$\lim_{x\to 1^-} \sqrt{\frac{\mu(x)}{\mu(x)+\eta(i\mu(x))}} \exp -\frac{\eta(2\mu(x))}{4} = 0$$

To summarize:

$$\lim_{x\to 1^-} \sqrt{\frac{\mu(x)}{\mu(x)+\eta(i\mu(x))}} \exp -\frac{\eta(2\mu(x))}{4} = \delta(T_\sigma(1)) \tag{B.20}$$

where $\delta(x)$ is defined as:

$$\delta(x) = \begin{cases} 0, \text{if } x = 1 \\ \exp\left(-\frac{J^{-1}(x)}{4}\right), \text{otherwise} \end{cases}$$

• Else if $i > 2$, in order to compute the limit of the left function in Eq. (B.19), we can simplify the right expression, using the fact that $\mu(.)$ is not null at high values:

$$\frac{J'\left[(i-1)\mu(x)+\eta(i\mu(x))\right]}{J'\left(\mu(x)\right)} \sim \sqrt{\frac{1}{(i-1)+i\frac{\eta(i\mu(x))}{i\mu(x)}}} \exp\left(-\frac{(i-2)+i\frac{\eta(i\mu(x))}{i\mu(x)}}{4}\mu(x)\right) \tag{B.21}$$

Since, by the definition of $\eta(.)$, $\mu(.)$, Eq. (B.3), and the positivity of $J(.)$ [tB01d]:

$$\frac{\eta(i\mu(x))}{i\mu(x)} = \frac{J^{-1}\circ T_\sigma \circ J(i\mu(x))}{iJ^{-1}\circ f(x)} \geq 0$$

then

$$0 \leq \sqrt{\frac{1}{(i-1)+i\frac{\eta(i\mu(x))}{i\mu(x)}}} \exp\left(-\frac{(i-2)+i\frac{\eta(i\mu(x))}{i\mu(x)}}{4}\mu(x)\right) \leq \sqrt{\frac{1}{i-1}} \exp\left(-\frac{i-2}{4}\mu(x)\right) \tag{B.22}$$

From Eq. (B.13), we deduce that:

$$\lim_{x\to 1^-} \sqrt{\frac{1}{i-1}} \exp\left(-\frac{i-2}{4}\mu(x)\right) = 0, \quad \forall i \in \mathbb{N}\setminus\{0,1\}$$

Using the sandwich theorem in Eq. (B.22), we find out:

$$\lim_{x\to 1^-}\sqrt{\frac{1}{(i-1)+i\frac{\eta(i\mu(x))}{i\mu(x)}}}\exp\left(-\frac{(i-2)+i\frac{\eta(i\mu(x))}{i\mu(x)}}{4}\mu(x)\right)=0$$

We conclude, from the equivalence in Eq. (B.21), that:

$$\lim_{x\to 1^-}\frac{J'\left[(i-1)\mu(x)+\eta(i\mu(x))\right]}{J'\left(\mu(x)\right)}=0 \tag{B.23}$$

- Finally, from Eqs. (B.17) and (B.23):

$$\lim_{x\to 1^-}\sum_{i\geq 2}(i-1)\lambda_i\frac{J'\left[(i-1)\,\mu(x)+\eta(i\mu(x))\right]}{J'\left(\mu(x)\right)}\times\sum_j\rho_j(j-1)\frac{J'\left((j-1)J^{-1}(1-x)\right)}{J'(J^{-1}(1-x))}=$$
$$\lambda_2\delta(T_\sigma(1))\sum_j\rho_j(j-1) \tag{B.24}$$

Limit of the term in Eq. (B.11)

- Let us compute $\lim_{x\to 1^-}\frac{J'(i\mu(x))}{J'(\eta(i\mu(x)))}\times\frac{J'[(i-1)\mu(x)+\eta(i\mu(x))]}{J'(\mu(x))}$
  - Because $J'(.),\mu(.)$ and $\eta(.)$ are not null for large x and using Eq. (B.16), we get then:

$$\begin{aligned}\frac{J'(i\mu(x))}{J'(\eta(i\mu(x)))}&\sim\frac{e^{-\frac{i\mu(x)}{4}}}{\sqrt{i\mu(x)}}\frac{\sqrt{\eta(i\mu(x))}}{e^{-\frac{\eta(i\mu(x))}{4}}}\\&\sim\sqrt{\frac{\eta(i\mu(x))}{i\mu(x)}}\exp-\frac{i\mu(x)-\eta(i\mu(x))}{4}\end{aligned} \tag{B.25}$$

  - By Multiplying Eq. (B.25) and (B.19) to form the term in Eq. (B.11), we get:

$$\begin{aligned}\frac{J'(i\mu(x))}{J'(\eta(i\mu(x)))}\frac{J'\left[(i-1)\,\mu(x)+\eta(i\mu(x))\right]}{J'\left(\mu(x)\right)}&\sim\sqrt{\frac{\eta(i\mu(x))}{i\mu(x)}}\exp-\frac{i\mu(x)-\eta(i\mu(x))}{4}\\&\times\sqrt{\frac{\mu(x)}{(i-1)\mu(x)+\eta(i\mu(x))}}\exp-\frac{(i-2)\mu(x)+\eta(i\mu(x))}{4}\\&\sim\sqrt{\frac{\eta(i\mu(x))}{(i-1)i\mu(x)+i\eta(i\mu(x))}}\exp-\frac{(2i-2)\mu(x)}{4}\\&\sim\sqrt{\frac{\eta(i\mu(x))}{(i-1)i\mu(x)+i\eta(i\mu(x))}}\exp-\frac{(i-1)}{2i}i\mu(x)\end{aligned}$$

Since $(i-1)i\mu(x) \geq 0$, We have:

$$0 \leq \sqrt{\frac{\eta(i\mu(x))}{(i-1)i\mu(x)+i\eta(i\mu(x))}} \exp -\frac{(i-1)}{2i} i\mu(x) \leq \sqrt{\frac{1}{i}} \exp -\frac{(i-1)}{2i} i\mu(x) \leq \exp -\frac{(i-1)}{2i} i\mu(x)$$

Finally, using Sandwich theorem, we compute:

$$\lim_{x\to 1^-} \frac{J'(i\mu(x))}{J'(\eta(i\mu(x)))} \frac{J'\left[(i-1)\,\mu(x)+\eta(i\mu(x))\right]}{J'\left(\mu(x)\right)} = 0 \tag{B.26}$$

- Finally, from Eqs. (B.14), (B.17) and (B.26), the limit in Eq. (B.11) is:

$$\lim_{x\to 1^-} \sum_{i\geq 2} i\lambda_i T'_\sigma(J(i\mu(x))) \frac{J'(i\mu(x))}{J'(\eta(i\mu(x)))} \frac{J'\left[(i-1)\,\mu(x)+\eta(i\mu(x))\right]}{J'\left(\mu(x)\right)} \sum_j \rho_j(j-1) \frac{J'\left((j-1)J^{-1}(1-x)\right)}{J'(J^{-1}(1-x))} = 0 \tag{B.27}$$

Conclusion

From Eqs. (B.18), (B.24) and (B.27), we conclude that:

$$\frac{d\Psi}{dx}(1) = \lim_{x\to 1^-} \frac{d\Psi}{dx}(x) = \left[\lambda_1 T'_\sigma(1) + \lambda_2 \delta(T_\sigma(1))\right] \sum_j \rho_j(j-1) \tag{B.28}$$

Attractive point

The recursion Eq. (B.2) is continuously differentiable in any neighborhood of 1^-, that attraction at the point 1 is guaranteed if $|\frac{d\Psi}{dx}(1)| < 1$, *i.e.* from Eq. (B.28):

Theorem 2 (Stability condition)**.**

$$\lambda_1 T'_\sigma(1) + \lambda_2 \delta(T_\sigma(1)) < \frac{1}{\sum_j \rho_j(j-1)} \tag{B.29}$$

where:

$$\delta(x) = \begin{cases} 0, \textit{ if } x = 1 \\ \exp\left(-\frac{J^{-1}(x)}{4}\right), \textit{ otherwise} \end{cases}$$

Appendix C

Ensemble weight enumerators for protographs: a proof of Abu Surra's conjecture and a continuous relaxation for a faster enumeration

C.1 Protograph ensemble weight enumerators

C.1.1 Notations

A *protograph* [Tho03] is a relatively small bipartite graph described by the tuple (V, C, E). The set of variable nodes V (of cardinality n_v) is connected to the set of check nodes C (of cardinality n_c) through edges in E (the set of edges with cardinality $|E|$). The protograph is usually described by its protomatrix $\boldsymbol{B}$ where $B(j,i) \geq 0$ is the number of connections between the variable node (VN) v_i and the check node (CN) c_j.

Let q_{v_i} (q_{c_j}) be the degree of the VN v_i (resp. CN c_j). The corresponding protograph based LDPC code is constructed by "copy-and-permute" operations [Tho03]: it consists of making a certain number of copies of the protograph, say N times, and merging them by permuting the endpoints of each edge copies. Fig. C.1 depicts the 'vectorized' protograph code associated with the following base matrix:

$$\boldsymbol{B} = \begin{pmatrix} 2 & 1 \\ 1 & 1 \end{pmatrix}$$

Let Ω_t (reps. Ω_p) denote the set of transmitted (resp. punctured) VNs of cardinality n_t (resp. n_p). The set operator $|.|$ returns the number of elements of an ensemble, the matrix operator $.^T$ denotes the transposition and the vector function $\|.\|_1$ (resp. $\|.\|_2$) is the L^1 (resp. L^2) norm.

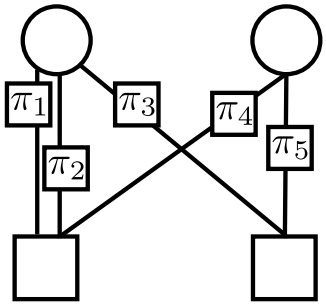

Figure C.1: The 'vectorized' protograph ldpc code generated by "copy-and-permute" operations. Each interleaver $\pi_i|_{1\leq i\leq 5}$ permutes the bundle of the N replicas of each edge.

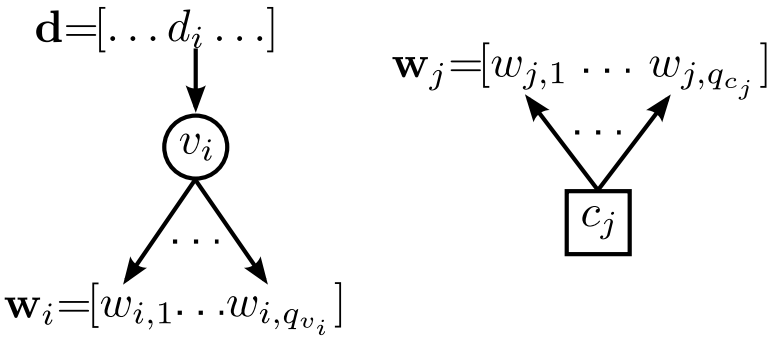

Figure C.2: Main notations considered for VNs and CNs

The overall input weight vector is denoted by $\boldsymbol{d} = [d_i]_i$: *i.e.*, to each VN v_i, we associate its input weight d_i $(0 \leq d_i \leq N)$ and output weight vector $\boldsymbol{w}_i = [w_{i,1}, \ldots, w_{i,q_{v_i}}]^T$. For CNs, we denote by $\boldsymbol{w}_j = [w_{j,1}, \ldots, w_{j,q_{c_j}}]^T$ the input weight vector of a CN c_j,and a fictitious edge output with weight 0. Observe that $\boldsymbol{w}_j$ is directly deduced from $\boldsymbol{d}$ and the graph connectivity, *i.e.* $w_{i,k} = w_{j,l}$ if $B(l,k) \neq 0$. Also, note that each component of the vector $\boldsymbol{w}_j$ is equal to a component d_i of the vector $\boldsymbol{d}$ if v_i is a neighbor of c_j for some i.

Eq. (C.2) summarizes the main notations. In the following, for ease of notations, we omit the subscripts i and j as long as it is clear from the context that we refer to an arbitrary VN or CN.

C.1.2 Weight enumerators

To derive the expression of the ensemble weight enumerator of protograph-based LDPC codes, we consider that the size-N interleavers $\{\pi_e\}_{1\leq e\leq |E|}$ are uniform. Hence, based on the result for serially concatenated codes [BDMP98], the average weight enumerator can be obtained when we reinterpret

the protograph LDPC code as a serial concatenation of VNs constituent codes and CNs constituent codes. It is shown in [ASDR11] that the average number of codewords of weight-vector $\boldsymbol{d} = [d_i]_i$ is written as:

$$A(\boldsymbol{d}) = \frac{\prod_{j=1}^{n_c} A^{c_j}(\boldsymbol{w}_j)}{\prod_{i=1}^{n_v} \binom{N}{d_i}^{q_{v_i}-1}} \tag{C.1}$$

where $A^{c_j}(\boldsymbol{w}_j)$ denotes the input weight-vector-$\boldsymbol{w}_j$ enumerator for the c_j constituent CN code. Writing Eq. (C.1) in the log-domain gives:

$$\log A(\boldsymbol{d}) = \sum_{j=1}^{n_c} \log A^{c_j}(\boldsymbol{w}_j) - \sum_{i=1}^{n_v} (q_{v_i} - 1) \log \binom{N}{d_i} \tag{C.2}$$

For sufficiently large N, using Stirling's approximation ($N! \approx (N/e)^N$) and denoting $\delta_i = d_i/N$, we get:

$$\log \binom{N}{d_i} \approx N.H(\delta_i) \tag{C.3}$$

where $H(.)$ is the binary entropy function.

In order to derive the expression of $a^{c_j}(\boldsymbol{w}_j)$, [Div06] derived the explicit expression of $a^{c_j}(\boldsymbol{w}_j)$ when $q_{c_j} = 3$. For higher degree CNs, one can perform a check splitting operation to write $a^{c_j}(\boldsymbol{w}_j)$ as the maximization over $q_{c_j} - 3$ variables of the sum of $q_{c_j} - 2$ degree-3 constituent CNs code weight enumerators [Div06, Eq. 14]. For highly connected CNs or for generalized CNs, this method introduces many dummy VNs and the maximization becomes complex. Therefore,[ASDR11] proposed a more efficient method for generalized CNs.

Consider a degree-q_c constituent CN code c. We want to compute $A^c(\boldsymbol{w})$ where $\boldsymbol{w} = \{w_1, ..., w_{q_c}\}^T$. We have:

$$A^c(\boldsymbol{w}) = \sum_{\{\mathscr{C}\}} C(N; \mathscr{C}) \tag{C.4}$$

where $\{\mathscr{C}\}$ is the family of sets $\mathscr{C}$, each contains N valid codewords of the CN constituent code c, such that the i^{th} component, $\forall i \in [\![1, q_c]\!]$, of all these codewords constitute a partition of the input weight w_i. $C(N; \mathscr{C})$ is the number of distinct permutations of the elements in $\mathscr{C}$.

Let $\boldsymbol{M}^c$ be the $q_c \times K$ matrix formed by the codewords of the CN c, denoted $\{C_1, \ldots, C_K\}$, as its columns ($K = 2^{q_c-1}$). Eq. (C.4) can be rewritten as:

$$A^c(\boldsymbol{w}) = \sum_{\{\boldsymbol{n}\}} C(N; \boldsymbol{n}) \tag{C.5}$$

where $\{\boldsymbol{n}\} = \{(n_1, \ldots, n_K)\}^T$ is the set of solutions of $\boldsymbol{w} = \boldsymbol{M}^c.\boldsymbol{n}$ such that $n_i \geq 0$ and $\sum_{i=1}^{K} n_i = N$. $C(N; \boldsymbol{n})$ is the multinomial coefficient [AS09].

Rewriting $A^c(\boldsymbol{w})$ in the logarithm domain gives:

$$\begin{aligned} \log\left(A^c(\boldsymbol{w})\right) &= \log\left(\sum_{\{\boldsymbol{n}\}} C(N;\boldsymbol{n})\right) \\ &= \max_{\{\boldsymbol{n}\}}{}^{*}\left(\log C(N;\boldsymbol{n})\right) \end{aligned} \tag{C.6}$$

where the pairwise $\max^*$ operator is defined as $\max^*(x, y) = \max(x, y) + \log\left(1 + e^{-|x-y|}\right)$.

As the number of combinations $C(N; \boldsymbol{n})$ can be very large, Eq. (C.6) can be approximated by:

$$\log\left(A^c(\boldsymbol{w})\right) = \max_{\{\boldsymbol{n}\}}\left(\log C(N;\boldsymbol{n})\right) \tag{C.7}$$

inducing an error of at most $\max_{x,y} \log\left(1 + e^{-|x-y|}\right) = \log 2$.

Lemma 1. *For sufficiently large N:*

$$\log C(N;\boldsymbol{n}) \approx N.H\left(\frac{n_1}{N}, \ldots, \frac{n_K}{N}\right)$$

where $H(.)$ is the multivariate entropy function.

Inserting Eq. (1) in Eq. (C.7) gives:

$$\log\left(A^c(\boldsymbol{w})\right) = N \max_{\{\boldsymbol{n}\}}\left(H\left(\frac{n_1}{N}, \ldots, \frac{n_K}{N}\right)\right)$$

Thus, the generic enumerator of the constituent CN code c with the N-normalized input weight vector $\boldsymbol{\delta} = \frac{\boldsymbol{w}}{N}$ can be written as

$$a^c(\boldsymbol{\delta}) = \limsup_{N\to\infty} \frac{\log\left(A^c(\boldsymbol{w})\right)}{N} \approx \max_{\{\boldsymbol{p}\}}\left(H(p_1, \ldots, p_K)\right) \tag{C.8}$$

under the constraints $\|\boldsymbol{p}\|_1 = 1$ and $\boldsymbol{\delta} = \boldsymbol{M}^c.\boldsymbol{p}$, where $\boldsymbol{p} = \{p_i\}_i$ and $p_i = \frac{n_i}{N}$.

C.2 A proof of Abu Surra's conjecture

The average number of the protograph's codewords of weight d is given by

$$A_d = \sum_{\{d_i/v_i \in \Omega_t\}} \sum_{\{d_k/v_k \in \Omega_p\}} A(\boldsymbol{d})$$

where $\sum_{d_i/v_i \in \Omega_t} d_i = d$. Let n be the number of transmitted VNs in the code (*i.e.* $n_t.N$). The n-normalized logarithmic asymptotic weight enumerator can be then written as [ASDR11]:

$$r\left(\frac{d}{n}\right) = \frac{1}{n_t}\tilde{r}(\delta)$$

where $\delta = d/N$ and

$$\begin{aligned}\tilde{r}(\delta) &= \limsup_{N\to+\infty} \frac{A_d}{N} \\ &= \max_{\delta_t : v_t \in \Omega_t} \max_{\delta_p : v_p \in \Omega_p} \left\{ \sum_{j=1}^{n_c} a_j^c(\boldsymbol{\delta}_j) - \sum_{i=1}^{n_v} (q_{v_i} - 1) H(\delta_i) \right\}\end{aligned} \tag{C.9}$$

The computation complexity of $\tilde{r}(\delta)$ is limited by the complexity of spanning all partitions of size n_t of the weight d, combined with all possible input weights of the punctured VNs. To alleviate this difficulty, [ASDR11] proposed the following steps: the protograph's VNs are partitioned into subsets according to their types. Two VNs are of the same type when their neighborhoods are identical, in other words, if one switches the input weights between the VNs of the same type, the resulting input weight vector forms a valid codeword and no difference is noticed from all CNs point of view. By labeling each edge of the protograph by its adjacent VN type, each CN's adjacent edge can be labeled with its weight and its type. The *subset-weight vector* (SWV) of a CN codeword is defined as the vector whose entries are the weights of bit subsets of the CN codeword.

[ASDR11] conjectured that *"in the maximization of Eq. (C.8), the optimal point occurs when codewords of equal SWV have the same proportion of occurence"*. This is equivalent to say that the maximum is reached when edges that belongs to the same type carry the same weight. In general, this is not always possible since the total weight carried by the edges of the same type is not necessarily a multiple of the number of edges of this type. In the following we will prove the generalized form of this conjecture:

Theorem 3. *The maximization of Eq. (C.8) occurs when the weights number of occurrences $\{p_i\}_i$ of the check node codewords, that belongs to the same VNs type composition are as uniform as possible.*

C.2.1 Proof when CN has 3 edges of the same type

Without loss of generality, let us consider a degree-q_c CN where 3 edges, $\alpha < \beta < \gamma$ are of the same type. The corresponding N-normalized input weight vector is $\boldsymbol{\delta} = (\delta_1 \dots \delta_\alpha \dots \delta_\beta \dots \delta_\gamma \dots \delta_{q_c})^T$ such that $\delta_\alpha, \delta_\beta$ and δ_γ are not all equal.

A triplet (f_1, f_2, f_3), of total weight $s = Nf_1 + Nf_2 + Nf_3$ is called as *as-uniform-as-possible* (AUAP) if a permutation of (Nf_1, Nf_2, Nf_3) has the form:

$$\begin{cases} (k,k,k) \text{ if } s = 3k \\ (k,k,k+1) \text{ if } s = 3k+1 \\ (k+1,k+1,k) \text{ if } s = 3k+2 \end{cases} \tag{C.10}$$

N.B.: In the asymptotic case, *i.e.* as N goes to infinity, the weights will be equal (dealing with normalized weights k/N asymptotically equals $(k+1)/N$, when N goes to infinity), *as-uniform-as-possible* could then be substituted simply with *uniform*.

Since $\boldsymbol{M}^c$ is not necessarily unimodular [HP94], $\boldsymbol{M}^c.\boldsymbol{p} = \boldsymbol{\delta}$ does exist only for some $\boldsymbol{\delta}$.

Definition 1. *$\boldsymbol{\delta}$ is called* admissible *if $\boldsymbol{M}^c.\boldsymbol{p} = \boldsymbol{\delta}$ admits a solution .*

Theorem 4. *If $\boldsymbol{\delta}$ is admissible, then the related AUAP version $\boldsymbol{\delta}^*$ is also admissible*

Proof

By circular permutation of the weights $\delta_\alpha, \delta_\beta$ and δ_γ, we form the following vectors:

$$\begin{aligned} \boldsymbol{\delta}_1^T &= (\delta_1 \dots \delta_\alpha \dots \delta_\beta \dots \delta_\gamma \dots \delta_{q_c}) \\ \boldsymbol{\delta}_2^T &= (\delta_1 \dots \delta_\gamma \dots \delta_\alpha \dots \delta_\beta \dots \delta_{q_c}) \\ \boldsymbol{\delta}_3^T &= (\delta_1 \dots \delta_\beta \dots \delta_\gamma \dots \delta_\alpha \dots \delta_{q_c}) \end{aligned}$$

Because of the symmetry of VNs of the same type, it is clear that $\boldsymbol{\delta}_1^T, \boldsymbol{\delta}_2^T$ and $\boldsymbol{\delta}_3^T$ are also valid CN input weight-vector (see introduction of Eq. (C)). Let $\boldsymbol{p}_1, \boldsymbol{p}_2$ and $\boldsymbol{p}_3$ be solutions of the equality contraint of Eq. (C.8) such that :

$$\boldsymbol{M}^c.\boldsymbol{p}_1 = \boldsymbol{\delta}_1 \tag{C.11}$$

$$\boldsymbol{M}^c.\boldsymbol{p}_2 = \boldsymbol{\delta}_2 \tag{C.12}$$

$$\boldsymbol{M}^c.\boldsymbol{p}_3 = \boldsymbol{\delta}_3 \tag{C.13}$$

$$\|\boldsymbol{p}_1\|_1 = \|\boldsymbol{p}_2\|_1 = \|\boldsymbol{p}_3\|_1 = 1$$

Let us find three variables a, b and c such that $a\boldsymbol{\delta}_1 + b\boldsymbol{\delta}_2 + c\boldsymbol{\delta}_3$ is AUAP wih respect to $\delta_\alpha, \delta_\beta$ and δ_γ. To this end, we have to solve the system:

$$\underbrace{\begin{pmatrix} \delta_\alpha & \delta_\gamma & \delta_\beta \\ \delta_\beta & \delta_\alpha & \delta_\gamma \\ \delta_\gamma & \delta_\beta & \delta_\alpha \end{pmatrix}}_{\boldsymbol{\Delta}} \begin{pmatrix} a \\ b \\ c \end{pmatrix} = \begin{pmatrix} f_1 \\ f_2 \\ f_3 \end{pmatrix} \tag{C.14}$$

Lemma 2. *Δ is invertible $\forall(\delta_\alpha, \delta_\beta, \delta_\gamma)$*

Proof

The determinant of $\boldsymbol{\Delta}$ is:

$$\begin{aligned} |\boldsymbol{\Delta}| &= \frac{1}{2}(\delta_\alpha + \delta_\beta + \delta_\gamma)\left((\delta_\alpha - \delta_\beta)^2 + (\delta_\alpha - \delta_\gamma)^2 + (\delta_\beta - \delta_\gamma)^2\right) \\ &\neq 0 \qquad (\delta_\alpha, \delta_\beta \text{ and } \delta_\gamma \text{ are not all null by definition}) \end{aligned}$$

□

The determinant of Eq. (C.14) is not null, it exists then a unique solution (a, b, c).

Lemma 3. *$(a, b, c) \in [0, 1]^3$ and $a + b + c = 1$*

Proof • By summing the three equations of the system Eq. (C.14), we obtain:

$$(\delta_\alpha + \delta_\beta + \delta_\gamma)(a + b + c) = f_1 + f_2 + f_3$$

Since $f_1 + f_2 + f_3 = \delta_\alpha + \delta_\beta + \delta_\gamma \neq 0$, then $a + b + c = 1$.

• Since $|\boldsymbol{\Delta}| > 0$, by Cramer's rule we have $a = |\boldsymbol{\Delta}_{\boldsymbol{a}}|/|\boldsymbol{\Delta}|$, where $\boldsymbol{\Delta}_{\boldsymbol{a}}$ is formed by replacing the first column of $\boldsymbol{\Delta}$ by $(f_1, f_2, f_3)^T$. By studying the sign of $|\boldsymbol{\Delta}_{\boldsymbol{a}}|$ in the cases depicted in Eq. (C.10), one can show that $a > 0$. Similar result can be shown for b and c.

So far, we have shown that a, b and c are positive and $a+b+c = 1$, which lead to $(a, b, c) \in [0, 1]^3$. □

Summing Eqs. (C.11),(C.12) and (C.13) weighted by (a, b, c) gives:

$$\boldsymbol{M}^c.(a\boldsymbol{p}_1 + b\boldsymbol{p}_2 + c\boldsymbol{p}_3) = a\boldsymbol{\delta}_1 + b\boldsymbol{\delta}_2 + c\boldsymbol{\delta}_3$$

$$= \left(\; \delta_1 \dots f_1 \dots f_2 \dots f_3 \dots \delta_{q_c} \; \right)^T \tag{C.15}$$
$$\triangleq \boldsymbol{\delta}^*$$

From Eq. (3), we get $\boldsymbol{p}^* \triangleq a\boldsymbol{p}_1 + b\boldsymbol{p}_2 + c\boldsymbol{p}_3 \in [0,1]^K$ and by construction:

$$\sum_{i:v_i \in \Omega_t} \boldsymbol{\delta}^*(i) = \sum_{i:v_i \in \Omega_t} \boldsymbol{\delta}_1(i) = \sum_{i:v_i \in \Omega_t} \boldsymbol{\delta}_2(i) = \sum_{i:v_i \in \Omega_t} \boldsymbol{\delta}_3(i) = \delta$$

i.e $\boldsymbol{\delta}^*$ is within the same search space in Eq. (C.9) as $\boldsymbol{\delta}_1$, $\boldsymbol{\delta}_2$ and $\boldsymbol{\delta}_3$. □

Theorem 5. *$H(\boldsymbol{p}_1) = H(\boldsymbol{p}_2) = H(\boldsymbol{p}_3)$ and $H(\boldsymbol{p}^*) \geq H(\boldsymbol{p}_1)$*

Proof Recall $\boldsymbol{M}^c = (C_1, \dots C_K)$ where $\{C_i\}_i$ are all CN codewords. Let L_j be the j^{th} row of the q_c rows of $\boldsymbol{M}^c$. Substituting the rows of Eq. (C.12) gives:

$$\boldsymbol{M}^c.\boldsymbol{p}_2 = \boldsymbol{\delta}_2 \Rightarrow \begin{pmatrix} L_1 \\ \vdots \\ L_\alpha \\ \vdots \\ L_\beta \\ \vdots \\ L_\gamma \\ \vdots \\ L_{q_c} \end{pmatrix} .\boldsymbol{p}_2 = \begin{pmatrix} \delta_1 \\ \vdots \\ \delta_\gamma \\ \vdots \\ \delta_\alpha \\ \vdots \\ \delta_\beta \\ \vdots \\ \delta_{q_c} \end{pmatrix}$$
$$\Rightarrow \begin{pmatrix} L_1 \\ \vdots \\ L_\beta \\ \vdots \\ L_\gamma \\ \vdots \\ L_\alpha \\ \vdots \\ L_{q_c} \end{pmatrix} .\boldsymbol{p}_2 = \begin{pmatrix} \delta_1 \\ \vdots \\ \delta_\alpha \\ \vdots \\ \delta_\beta \\ \vdots \\ \delta_\gamma \\ \vdots \\ \delta_{q_c} \end{pmatrix} \tag{C.16}$$

Concerning single parity check codes, notice that the necessary and sufficient condition of any CN codeword C_i is that it must have an even number of $'1's$. Permuting the rows of $\boldsymbol{M}^c$ clearly preserves the number of $'1's$ in each column (for general parity check nodes, particular attention must be given to the form of the matrix $\boldsymbol{M}^c$ and to the potential edges of the same type). Hence, the most left hand matrix in Eq. (C.16) is just a column-wise permuted version of $\boldsymbol{M}^c$. It exists then a permutation matrix Π_2 such that:

$$\Big(\; L_1 \dots L_\beta \dots L_\gamma \dots L_\alpha \dots L_{q_c} \; \Big)^T = \boldsymbol{M}^c.\Pi_2$$

Consequently, Eq. (C.16) becomes:

$$\boldsymbol{M}^c.\Pi_2.\boldsymbol{p}_2 = \boldsymbol{\delta}_1$$

By definition of $\boldsymbol{p}_1$ and the symmetry of the entropy function:

$$H(\boldsymbol{p}_1) \geq H(\Pi_2 \boldsymbol{p}_2) = H(\boldsymbol{p}_2)$$

Similarly, we can show that $H(\boldsymbol{p}_2) \geq H(\boldsymbol{p}_1)$. This leads to $H(\boldsymbol{p}_1) = H(\boldsymbol{p}_2)$. Same conclusion can be drawn for $\boldsymbol{p}_3$. Consequently:

$$H(\boldsymbol{p}_1) = H(\boldsymbol{p}_2) = H(\boldsymbol{p}_3)$$

Using Eq. (3) and the concavity of H, Jensen's inequality gives:

$$\begin{aligned} H(\boldsymbol{p}^*) &= H(a\boldsymbol{p}_1 + b\boldsymbol{p}_2 + c\boldsymbol{p}_3) \\ &\geq aH(\boldsymbol{p}_1) + bH(\boldsymbol{p}_2) + cH(\boldsymbol{p}_3) \\ &\geq (a+b+c)H(\boldsymbol{p}_1) \\ &\geq H(\boldsymbol{p}_1) \end{aligned}$$

□

To summarize, for a fixed δ, from an admissible input-weight vector $\boldsymbol{\delta}$, we built an admissible input-weigth vector $\boldsymbol{\delta}^*$ which is AUAP such that $a^c(\boldsymbol{\delta}^*) \geq a^c(\boldsymbol{\delta})$. Therefore, solutions of the maximization in Eq. (C.9) belongs to the set of AUAP $\boldsymbol{\delta}$ weight-vectors. Eq. (3) and the conjecture in [ASDR11] are hence proved. Q.E.D.

N.B.:A similar proof, with great simplifications, can be made for CN with only 2 edges of the same type.

C.2.2 CN has more than three edges of the same type

As in the previous section, let us consider the normalized CN input-weight vector $\boldsymbol{\delta} = (\delta_i)_i^T$. In this case, the corresponding vector $\boldsymbol{\delta}^* = (\zeta_1, ...\zeta_n)$ is said to be AUAP when the weights of all the edges that belong to the same type, *i.e.* a subset of $\{\zeta_i\}_i$, are as uniformly distributed as possible.

Consider first the particular case when the CN has 4 edges of the same type. $\boldsymbol{\Delta}$ in Eq. (C.14) is a size-4 right-hand circulant matrix. Consider its *associated polynomial* [Dav79]:

$$f(x) = \delta_\alpha + \delta_\beta x + \delta_\gamma x^2 + \delta_\kappa x^3$$

It follows that the 4 eigenvalues of $\boldsymbol{\Delta}$ are given by [Dav79]:

$$\lambda_1 = f(1),\ \lambda_2 = f(z),\ \lambda_3 = f(z^2),\ \lambda_4 = f(z^3)$$

where $z = exp(\frac{2\pi i}{4})$ is the 4-th root of unity and i the imaginary unit. We have:

$$\lambda_2 = f(z) = (\delta_\alpha - \delta_\gamma) + i(\delta_\beta - \delta_\kappa)$$

If $\delta_\alpha = \delta_\gamma$ and $\delta_\beta = \delta_\kappa$, then $\lambda_2 = 0$, therefore, $\boldsymbol{\Delta}$ is not invertible. Consequently the previous proof cannot be applied. A strategy to generalize our approach when more than 3 edges of the same type exist is as follows:

1. Pick the first leftmost edge, say edge i, whose weight δ_i is different from its AUAP value ζ_i.
2. Select two adequate edges j and k within the same type such that: $\delta_i + \delta_j + \delta_k \geq \zeta_i$.
3. Give to δ_i its final value ζ_i by putting $f_1 = \zeta_i$.
4. Form the new vector $\boldsymbol{\delta}$, where $\delta_i = \zeta_i$, and its corresponding $\boldsymbol{p}$.
5. Go back to step 1 if $\boldsymbol{\delta} \neq \boldsymbol{\delta}^*$.

At the end, we obtain the configuration $\boldsymbol{\delta}^*$ and its corresponding $\boldsymbol{p}^*$ that maximizes H.

C.3 Efficient computation of $\tilde{r}(\delta)$ through countinuous relaxation

In order to solve Eq. (C.8), [AS09] enumerates all the solutions of the equality $\boldsymbol{M}^c.\boldsymbol{p} = \boldsymbol{\delta}$ where $N.p_i \in \mathbb{N}$. Even if some reduction of the search space can be made (cf. [AS09, Appendix A]), Eq. (3) does not simplify necessarily the computation of Eq. (C.8) for protographs where not much VNs

can be gathered as belonging to the same type. If besides that, we have a generalized or a highly connected CN, the computation of Eq. (C.8) becomes very complex. Moreover, for convolutional LDPC codes [MLCJ14], this simplification cannot be applied since the VNs belongs to different time instants [MLC13].

C.3.1 Continuous relaxation

The constituent CN c weight vector enumerator in Eq. (C.8) is computed by solving the following optimization:

$$\begin{aligned} \underset{x}{\text{maximize}} \quad & H(\boldsymbol{x}) \\ \text{subject to:} \quad & \boldsymbol{M}^c.\boldsymbol{x} = \boldsymbol{\delta} \\ & \sum_{i=0}^{K} x_i = 1 \\ & x_i \in \{\frac{k}{N}/k \in [\![0, N]\!]\}, \quad \forall i \in [\![1, K]\!] \end{aligned}$$

By putting together the equality constraints, which defines $\boldsymbol{M'^c}.\boldsymbol{x} = \boldsymbol{b}$, and noting $\mathscr{L} = \{\frac{k}{N}/k \in [\![0, N]\!]\}$, we get the following discrete optimization programming:

$$\begin{aligned} \underset{x}{\text{maximize}} \quad & H(\boldsymbol{x}) \\ \text{subject to:} \quad & \boldsymbol{M'^c}.\boldsymbol{x} = \boldsymbol{b} \\ & \boldsymbol{x} \in \mathscr{L}^K \end{aligned} \tag{C.17}$$

Eq. (C.17) is a concave but nonlinear discrete optimization with equality constraints. To our knowledge, no method is given to solve efficiently this kind of problems. Consequently, we have to enumerate all possible solutions in the search space, which grows in exponential time with the CN degree q_c and polynomial time with the lifting factor N.

By relaxing Eq. (C.17), let us consider the following concave nonlinear continuous programming:

$$\begin{aligned} \underset{x}{\text{maximize}} \quad & H(\boldsymbol{y}) \\ \text{subject to:} \quad & \boldsymbol{M'^c}.\boldsymbol{y} = \boldsymbol{b} \\ & \boldsymbol{y} \in [0, 1]^K \end{aligned} \tag{C.18}$$

Eq. (C.18) can be solved easily and efficiently with different well-known optimization methods [Ber99], even for large values of K. Moreover, the solution, when it exists, is optimal.

Theorem 6. *Given a solution of Eq. (C.18), one can construct a solution in $\mathscr{L}^K$ of Eq. (C.17) given any arbitrary small penalty ε on the maximum value of $H(\boldsymbol{x})$ and the constraint equality in Eq. (C.17).*

Proof It is easy to show that $\mathscr{L}^K$ is dense in $[0,1]^K$, in other words, for any element $\boldsymbol{y}$ in $[0,1]^K$, we can form a sequence with elements $\boldsymbol{x}_N$ in $\mathscr{L}^K$ such that $\boldsymbol{x}_N \xrightarrow[N\to\infty]{\|.\|_2} \boldsymbol{y}$. As an example, one can take $\boldsymbol{x}_N = (\frac{\lfloor N y_i \rfloor}{N})_{1\leq i\leq K}$.

Let $\boldsymbol{y}^{opt} = (y_i^{opt})_{1\leq i\leq K}$ be the solution of Eq. (C.18) and $\boldsymbol{x}_N^{opt}$ the sequence of elements in $\mathscr{L}^K$ that tends to $\boldsymbol{y}^{opt}$. Using the formal definition of the limit and the continuity of the entropy function H, we have, $\forall \varepsilon \geq 0$:

$$\begin{aligned}
&\exists N_1 \in \mathbb{N}, \forall N \geq N_1, \|\boldsymbol{x}_N^{opt} - \boldsymbol{y}^{opt}\|_2 \leq \varepsilon \\
&\exists N_2 \in \mathbb{N}, \forall N \geq N_2, |H(\boldsymbol{x}_N^{opt}) - H(\boldsymbol{y}^{opt})| \leq \varepsilon \\
&\exists N_3 \in \mathbb{N}, \forall N \geq N_3, \|\boldsymbol{M'}^c.\boldsymbol{x}_N^{opt} - \boldsymbol{b}\|_2 \leq \varepsilon
\end{aligned}$$

Taking $N_0 = \max(N_1, N_2, N_3)$, we get:

$$\forall \varepsilon \geq 0, \exists N_0 \in \mathbb{N}, \forall N \geq N_0, \quad \begin{cases} \|\boldsymbol{x}_N^{opt} - \boldsymbol{y}^{opt}\|_2 \leq \varepsilon \\ |H(\boldsymbol{x}_N^{opt}) - H(\boldsymbol{y}^{opt})| \leq \varepsilon \\ \|\boldsymbol{M'}^c.\boldsymbol{x}_N^{opt} - \boldsymbol{b}\|_2 \leq \varepsilon \end{cases}$$

Consequently, $\boldsymbol{x}_N^{opt} \in \mathscr{L}^K$ is a solution to the optimization in Eq. (C.17) that satisfies both the maximization of H and the equality constraints for an arbitrarily small correction term ε as $N \to \infty$. □

C.3.2 On numerical implementations

To solve Eq. (C.18), we can apply different iterative optimization methods such as internal point (IP) or sequential quadratic programming (SQP) [Ber99]. For this king of algorithms, we need to provide an initial guess, denoted $\boldsymbol{y}_0$, that satisfies the constraints (here $\boldsymbol{M'}^c.\boldsymbol{y} = \boldsymbol{b}$), and is within the feasible region (here, $[0,1]^K$).

First, let us put aside the feasible region and try to find at least one solution in the following affine space:

$$\boldsymbol{M'^c}.\boldsymbol{y} = \boldsymbol{b}$$

One can compute the Moore−Penrose pseudoinverse [Pen55] (not necessarily unique) of $\boldsymbol{M'^c}$, denoted $\boldsymbol{M'^{c+}}$. Hence, $\boldsymbol{y}_0 = \boldsymbol{M'^{c+}}\boldsymbol{b}$.

In Eq. (C.17), since $\boldsymbol{M'^c}$ is not necessarily unimodular [Sch98], $\boldsymbol{M'^c}.\boldsymbol{x} = \boldsymbol{b}$ does not have a solution $\forall \boldsymbol{b}$, *i.e.* for any value of the CN input-weight vector $\boldsymbol{w}$. When it is not possible, it means that $\mathscr{C}$ is an empty set and no codeword of the protograph with such Hamming weight exists.

When the system is solvable, Moore−Penrose pseudoinverse does not provide necessarily a solution that remains within the domain of the multivariate entropy function H, (some entries of $\boldsymbol{y}_0$ may be < 0 or > 1). We can solve this problem by considering an adequate analytic continuation of H. Since H is concave, it has one global maximum, then substituting in Eq. (C.18) $H(.)$ with any analytic continuation $H^*(.)$ which does not induce local maxima in the regions $]-\infty,\ 0]$ and $[1,\ +\infty[$ is transparent for the optimization routines.

C.4 Numerical results

Fig. C.3 gives the asymptotic codeword weight enumerator for different regular LDPC codes and their corresponding d_{min}. The numerical results are obtained using $N = 10^5$.

C.5 Open problem

Eq. (3) proves that in order to maximize $\sum_{j=1}^{n_c} a_j^c(\boldsymbol{\delta}_j)$, the VNs of the same type should have weights as uniformly as possible. However, at the contrary of what was assumed in [ASDR11], this configuration does not necessarily maximize $r(\delta)$, since the second right hand term in Eq. (C.9), $\sum_{i=1}^{n_v} (q_{v_i} - 1)H(\delta_i)$, is also positive and is not minimized by the the above configuration of input weights.

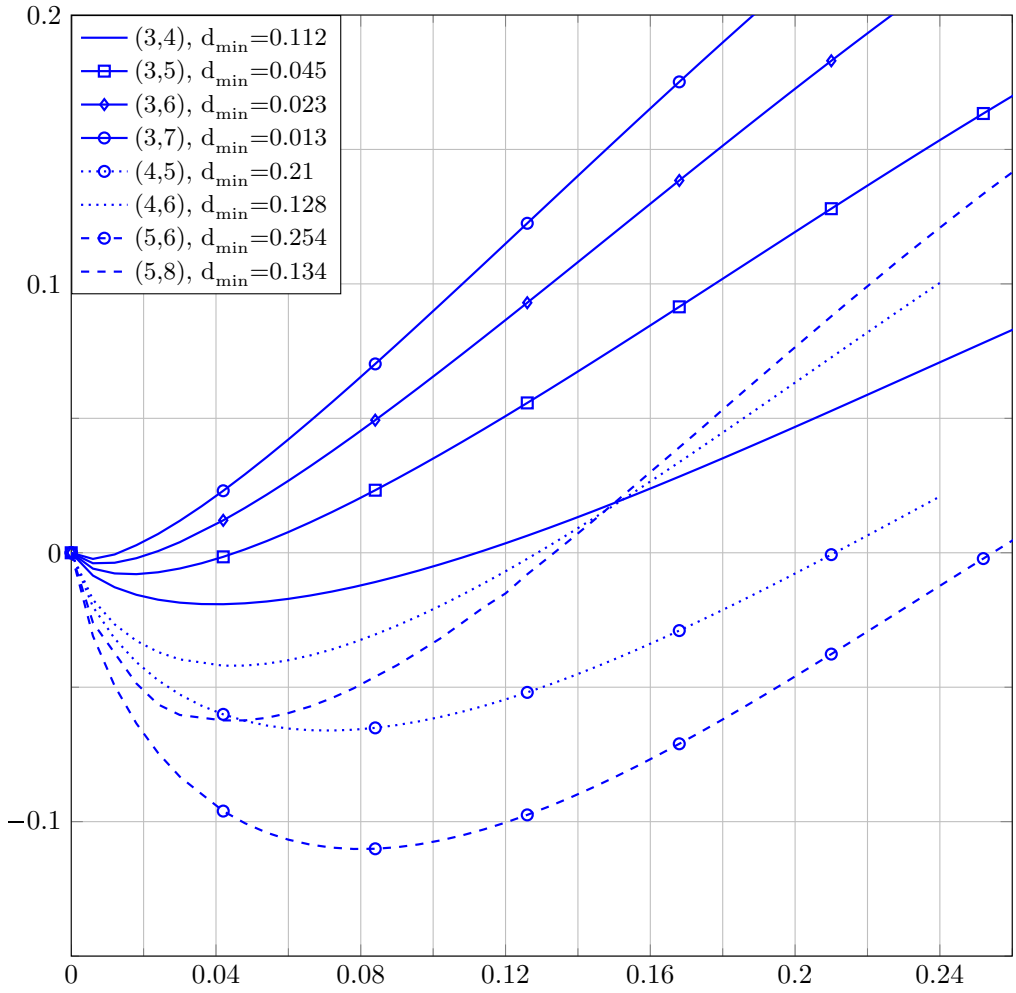

Figure C.3: Asymptotic weight enumerators for different protograph codes

Appendix: Proof of Eq. (1)

[ASDR11] proved Eq. (1) using the method of types [CT12, Thm. 12.1.3]. An alternative proof is as follows: For sufficiently large N and even if some particular n_i are not large we have:

$$\begin{aligned}
C(N;\boldsymbol{n}) &= C(N;n_1,\ldots,n_K) \\
&= \frac{N!}{n_1!n_2!\ldots n_K!} \\
&\approx \frac{\left(\frac{N}{e}\right)^N}{\left(\frac{n_1}{e}\right)^{n_1}\ldots\left(\frac{n_K}{e}\right)^{n_K}} \quad \text{(Striling: } n! \approx \left(\tfrac{n}{e}\right)^n \text{)} \\
&= \frac{\left(\frac{N}{e}\right)^{n_1}\cdots\left(\frac{N}{e}\right)^{n_K}}{\left(\frac{n_1}{e}\right)^{n_1}\ldots\left(\frac{n_K}{e}\right)^{n_K}} \quad \left(\textstyle\sum_{i=1}^K n_i = N\right) \\
&= \prod_{i=1}^K \left(\frac{N}{n_i}\right)^{n_i} \\
&= \exp\left(\sum_{i=1}^K n_i \log\left(\frac{N}{n_i}\right)\right) \\
&= \exp\left(N.H(\frac{n_1}{N},\ldots,\frac{n_K}{N})\right)
\end{aligned}$$

Appendix: Proof of Eq. (3)

$$\begin{aligned}
|\boldsymbol{\Delta}| &= \begin{vmatrix} \delta_\alpha & \delta_\gamma & \delta_\beta \\ \delta_\beta & \delta_\alpha & \delta_\gamma \\ \delta_\gamma & \delta_\beta & \delta_\alpha \end{vmatrix} \\
&= \delta_\alpha^3 + \delta_\beta^3 + \delta_\gamma^3 - 3\delta_\alpha\delta_\beta\delta_\gamma \\
&= (\delta_\alpha + \delta_\beta + \delta_\gamma)\left(\delta_\alpha^2 + \delta_\beta^2 + \delta_\gamma^2\right. \\
&\qquad\qquad \left. -\delta_\alpha\delta_\beta - \delta_\alpha\delta_\gamma - \delta_\beta\delta_\gamma\right) \\
&= \frac{1}{2}(\delta_\alpha + \delta_\beta + \delta_\gamma)\left((\delta_\alpha - \delta_\beta)^2 + (\delta_\alpha - \delta_\gamma)^2\right. \\
&\qquad\qquad \left. + (\delta_\beta - \delta_\gamma)^2\right) \\
&\neq 0 \qquad (\delta_\alpha, \delta_\beta \text{ and } \delta_\gamma \text{ are not all null by definition})
\end{aligned}$$

Appendix: Proof of Eq. (C.15)

$$
\begin{aligned}
\boldsymbol{M}^c.(a\boldsymbol{p}_1 + b\boldsymbol{p}_2 + c\boldsymbol{p}_3) &= a\boldsymbol{\delta}_1 + b\boldsymbol{\delta}_2 + c\boldsymbol{\delta}_3 \\
&= \begin{pmatrix} (a+b+c)\delta_1 \\ \vdots \\ a\delta_\alpha + b\delta_\gamma + c\delta_\beta \\ \vdots \\ a\delta_\beta + b\delta_\alpha + c\delta_\gamma \\ \vdots \\ a\delta_\gamma + b\delta_\beta + c\delta_\alpha \\ \vdots \\ (a+b+c)\delta_{q_c} \end{pmatrix} \\
&= \begin{pmatrix} \delta_1 \dots f_1 \dots f_2 \dots f_3 \dots \delta_{q_c} \end{pmatrix}^T \\
&\triangleq \boldsymbol{\delta}^*
\end{aligned}
$$

Appendix D

Protograph-based LDPC convolutional codes for BICM

D.1 Introduction

Bit-interleaved coded modulation (BICM) technique [iFMC08] is a powerful approach that takes advantage of the different protection levels of bit channels in high modulation orders to improve the decoding threshold. The optimization of BICM in concatenated schemes has been well studied in the literature and several considerations have been proposed to improve the threshold such as the bit allocation mapping optimization or the precoding [PS06, SB04, tB01b]. For instance for Gray mapping, [JJZ10] proposed a variable degree matched mapping to improve the threshold of accumulate repeat jagged accumulate (ARJA) codes [DJDT05]. For other mappings, BICM with iterative decoding (BICM-ID) such in [tBKA04].

In this section, we focus on protograph LDPC-C codes [MLCJ14]. For these codes, some studies have been made to analyse their convergence is BICM-ID schemes. In [YEKLK13], authors studied the performance of LDPC-C codes with different modulations. [SB13] analyzed the performance of terminated LDPC-C codes combined with 16-QAM with Gray, set partitioning [Ung82] and M16^{a} [SGHB03] mappings. In [HAB^{+}13], it is shown that, thanks to their bit mapping design, the threshold of the terminated LDPC-C code can be improved and that the 'wave effect' can be retrieved for tail-biting LDPC-C codes. In general, this optimization is complex especially for LDPC-C codes with relatively large coupling lengths [HBA^{+}14]. Concerning precoding, no work have been done to our knowledge in order to analyze the performance of LDPC-C codes with precoded modulations.

In concatenation schemes, several considerations can be taken into account to improve the thresholds of BICM in iterative decoding (BICM-ID). First we find the modulator mapping. In [SB13], authors analyzed the performance of terminated LDPC-C codes combined with 16-QAM with Gray,

set partitioning [Ung82] and M16[a] [SGHB03] mappings. An other technique is bit mapping optimization. The main challenge is to find good assignments of different bit channels to variable nodes in order to achieve better threshold. Authors in [HAB+13] have shown that, thanks to their bit mapping design, the threshold of the terminated LDPC convolutional (LDPC-C) code can be improved and that the 'wave effect' can be retrieved for tail-biting LDPC-C codes. In general, this optimization is complex especially for LDPC-C codes with relatively large coupling lengths [HBA+14]. Finally, code doping [PS06, SB04, tB01b] can be considered: it consists in introducing an additional rate-1 convolutional recursive code before the mapper. To our knowledge, no work have been done to analyze the performance of percoding with LDPC-C codes.

In this section, we analyse the performance of LDPC-C codes in BICM and BICM-ID systems when bit mapping or precoding are used. Also, we introduce a simple procedure to design bit mapping for LDPC-C codes based on their underlying protograph code. By taking advantage from the fact that accumulate repeat jagged accumulate (ARJA) codes behave very good in additive white Gaussian noised (AWGN) channels [DJDT05], and the optimal variable degree matched mapping of ARJA codes proposed in [JJZ10], we construct a bit mapping for spatially coupled ARJA codes that operates at only 0.1dB from the capacity. Also, we introduce a new termination method for LDPC-C codes without rate loss and that leads to better performance than the underlying LDPC code. Finally, we show that we can meliorate the performance of this new terminated LDPC-C codes by considering precoding. With this new consideration, we are able to design protograph-based LDPC codes described by small protographs, whose threshold does not depend on the coupling factor and that benefit from the convolutional gain.

D.2 Spatially coupled BICM

D.2.1 System model

Recall from chapiter 3 that a protograph-based LDPC-C code can be obtained by replicating the graph $\boldsymbol{B}$ L times, then each VNs bundle is connected to its pairing CNs bundle through a permutation of the corresponding edges bundle only in the forward direction, *i.e.* from the protograph at time t to the protographs at time $t' > t$. The manner of connecting these different graphs is driven by the components base matrices $\{\boldsymbol{B}_i\}_i$. Note that $\sum_{i=0}^{i=m_s} \boldsymbol{B_i} = \boldsymbol{B}$ and that the design rate can be written as $R = 1 - c/v$.

In our study, we will consider as a reference only terminated time-invariant subfamily of LDPC

Figure D.1: Transmitter

convolutional codes [MLC11]. The corresponding base matrix of size $(L+m_s)c \times Lv$ is denoted by $\boldsymbol{B}_{[0,L-1]}$ where L is called the coupling length or the termination factor.

$$\boldsymbol{B}^T_{[0,L-1]} = \begin{bmatrix} \boldsymbol{B}^T_0 & \cdots & \boldsymbol{B}^T_{m_s} & & \\ & \ddots & & \ddots & \\ & & \boldsymbol{B}^T_0 & \cdots & \boldsymbol{B}^T_{m_s} \end{bmatrix} \tag{D.1}$$

For ease of notation, $\boldsymbol{B}_{[0,L-1]}$ is simply written $\boldsymbol{B}_L$.

Let us consider a serial concatenation of a binary LDPC convolutional code and a mapper as depicted in Fig. D.1. Recall that the design rate of terminated LDPC-C codes without puncturing is given by:

$$R_L = R - \frac{m_s}{L}(1-R) \tag{D.2}$$

Note that with increasing L, the rate loss penalty, $\frac{m_s}{L}(1-R)$, vanishes to 0 and the design rate R_L tends to the effective code rate R.

Without loss of generality, we will consider the quadrature amplitude modulation (QAM). The coded bits $\boldsymbol{c}$ in Fig. D.1 are interleaved, into $\boldsymbol{\alpha}$, grouped by tuples of m consecutive bits, $\boldsymbol{\alpha_k} = \{\alpha_{k,q} = \alpha_{m(k-1)+q}\}_{1\leq q\leq m}$, and mapped to QAM symbols s_k. Each symbol $s_k = \mu(\boldsymbol{\alpha_k})$ is picked from a constellation of M-ary complex symbols $\chi = \{a_1, \ldots, a_M\}$ $(M = 2^m)$. Different mappings were proposed in the literature for BICM systems (Gray, Set partitioning (SP) [Ung82], Modified SP (MSP) [CR01], M16$^{\text{r}}$ [SGHB03], Maximum squared Euclidean weight (MSEW) [TS02], ...).

Symbol energy is defined as $E[|a_i|^2]$. The transmitted signal $\boldsymbol{s}$ is sent over a memoryless AWGN channel having a double-sided power spectral density $\sigma^2_{noise} = N_0/2$.

D.2.2 BICM receiver

At the receiver, several strategies can be considered. The classical tandem decoding consists in the serial soft decoding of both the modulator and the LDPC code. The receiver structure is depicted in Fig. D.2 At the decoder side, the soft demapper processes the channel observations $\boldsymbol{y} = \{y_k\}_k$ and the apriori log-likelihood ratio (LLRs) values of the bits $\boldsymbol{\alpha}$, $\boldsymbol{L^M_a} = \{\boldsymbol{L^M_a(k)}\}_k$, to calculate the

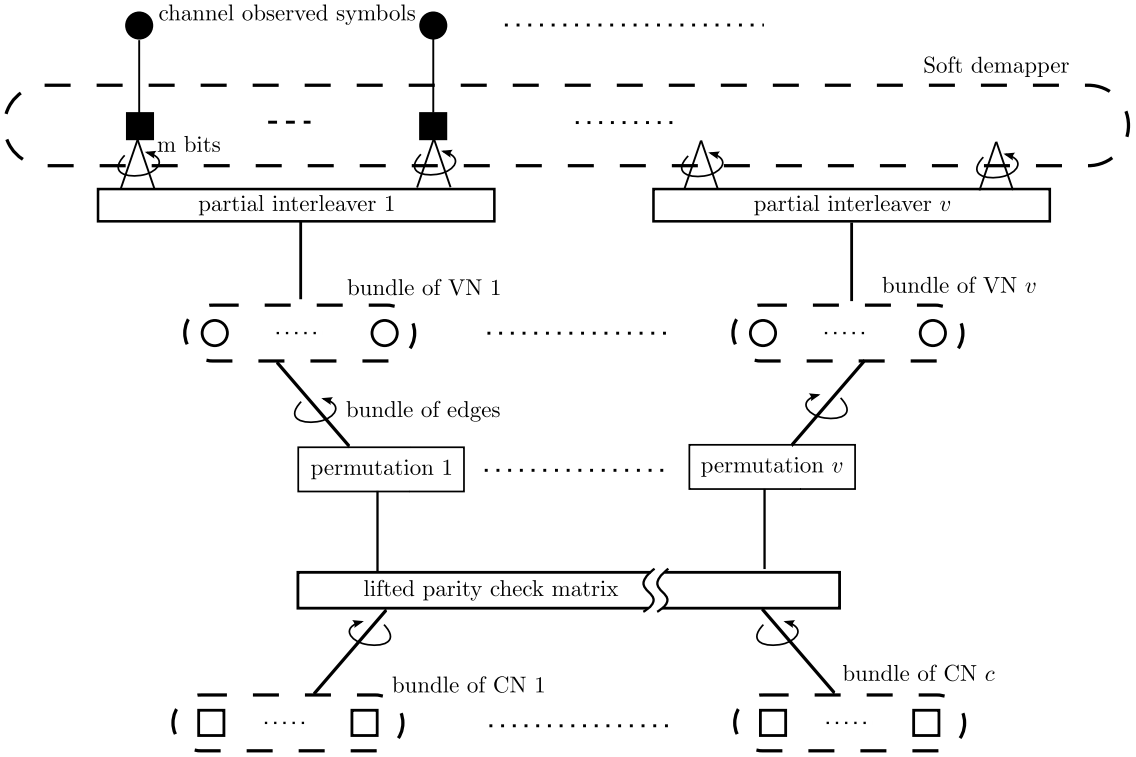

Figure D.2: Factor graph of the receiver

aposteriori $\boldsymbol{L}^{\boldsymbol{M}}_{\boldsymbol{app}} = \{\boldsymbol{L}^{\boldsymbol{M}}_{\boldsymbol{app}}(\boldsymbol{k})\}_k$ and extrinsic $\boldsymbol{L}^{\boldsymbol{M}}_{\boldsymbol{e}} = \{\boldsymbol{L}^{\boldsymbol{M}}_{\boldsymbol{e}}(\boldsymbol{k})\}_k$ LLRs. We introduce the following notations for different LLRs:

$$\begin{aligned}
\boldsymbol{L}^{\boldsymbol{M}}_{\boldsymbol{a}}(\boldsymbol{k}) &= \{L^M_a(k,q) = L^M_a(\alpha_{m(k-1)+q})\}_{1\leq q\leq m} \\
\boldsymbol{L}^{\boldsymbol{M}}_{\boldsymbol{app}}(\boldsymbol{k}) &= \{L^M_{app}(k,q) = L^M_{app}(\alpha_{m(k-1)+q})\}_{1\leq q\leq m} \\
\boldsymbol{L}^{\boldsymbol{M}}_{\boldsymbol{e}}(\boldsymbol{k}) &= \{L^M_e(k,q) = L^M_e(\alpha_{m(k-1)+q})\}_{1\leq q\leq m}
\end{aligned}$$

The demapper computes the aposteriori and the extrinsic LLRs of the q^{th} bit of the k^{th} symbol as following:

$$\begin{aligned}
L^M_{app}(k,q) &= \ln \sum_{\hat{\boldsymbol{\alpha}}_{\boldsymbol{k}} \in \chi^q_{+1}} \gamma(\hat{\boldsymbol{\alpha}}_{\boldsymbol{k}}) - \ln \sum_{\hat{\boldsymbol{\alpha}}_{\boldsymbol{k}} \in \chi^q_{-1}} \gamma(\hat{\boldsymbol{\alpha}}_{\boldsymbol{k}}) \\
\gamma(\hat{\boldsymbol{\alpha}}_{\boldsymbol{k}}) &= \exp\left(\frac{-|y_k - \mu(\hat{\boldsymbol{\alpha}}_{\boldsymbol{k}})|^2}{2\sigma^2} + \frac{\hat{\boldsymbol{\alpha}}_{\boldsymbol{k}}{}^T . \boldsymbol{L}^{\boldsymbol{M}}_{\boldsymbol{a}}(\boldsymbol{k})}{2}\right) \\
L^M_e(k,q) &= L^M_{app}(k,q) - L^M_a(k,q)
\end{aligned} \tag{D.3}$$

where $\chi_{\pm 1}^{q} = \{\hat{\boldsymbol{\alpha}}_{\boldsymbol{k}}/\alpha_{m(k-1)+q} = \pm 1\}$

For LDPC decoder, we consider the belief propagation (BP) decoding algorithm [RU01].

D.3 Convergence Analysis

In this section, we study the convergence of different protograph-based LDPC-C codes over the AWGN channel using EXIT chart analysis. We consider the following scheduling: the ℓ^{th} iteration consists in one soft demapping step given by Eq. (D.3), followed by one BP iteration for the LDPC-C code. We further assume partial interleavers between the soft demapper module and each VN bundle [BPB+14b, BPB+14a]. Let us consider hereafter the following notations relative to the ℓ^{th} iteration:

- $I_v^{\ell}(q,r)$: extrinsic mutual information (eMI) between the code bits associated with VN r and the LLRs sent from this VN to the CN q.
- $I_c^{\ell}(q,r)$: eMI associated with messages sent from CN q to VN r.
- $I_{app}^{\ell}(r)$: *a posteriori* MI associated with the VN r.
- $I_{a,M}^{\ell}(r)$: *a priori* MI associated with messages sent from the VN r to the soft demapper.
- $I_M^{\ell}(r)$: eMI associated with messages sent from soft demapper to the VN r.
- $T_M(.)$: input-output EXIT transfer function of the detector. It is inherently a function of the noise variance σ_{noise}^2. Analytic expression is not always available, alternatively, we compute it by Monte Carlo simulations.

Let $\boldsymbol{B}$ be the original protograh, of size $c \times v$, that gives the terminated LDPC-C code $\boldsymbol{B}_L$ of size $Lv \times (L+m_s)c$. As discussed in chapter 3, the decoding update equations are given by:

$$I_M^{\ell}(r) = T_M(I_{a,M}^{\ell-1}(r)) \tag{D.4}$$

where

$$I_{a,M}^{\ell}(r) = J\left(\sqrt{\sum_s B_L(s,r)\left[J^{-1}(I_v^{\ell-1}(s,r))\right]^2}\right) \tag{D.5}$$

If $B_L(q,r) \neq 0$:

$$I_v^{\ell}(q,r) = J\left(\sqrt{\sum_s B_L(s,r)\left[J^{-1}(I_c^{\ell-1}(s,r))\right]^2 -}\right.$$

$$\overline{\left[J^{-1}(I_c^{\ell-1}(q,r))\right]^2 + \left[J^{-1}(I_M^{\ell}(r))\right]^2}\Bigg) \tag{D.6}$$

otherwise, $I_v^{\ell}(q,r) = 0$.

Similarly, using reciprocal channel approximation, if $B_L(q,r) \neq 0$:

$$I_c^{\ell}(q,r) = 1 - J\left(\sqrt{\sum_s B_L(q,s)\left[J^{-1}(1 - I_v^{\ell}(q,s))\right]^2 - \overline{\left[J^{-1}(1 - I_v^{\ell}(q,r))\right]^2}}\right) \tag{D.7}$$

otherwise, $I_c^{\ell}(q,r) = 0$.

At the end of each iteration, thanks to the partial interleavers [BPB+14c], we are allowed to write:

$$I_{app}^{\ell}(r) = J\left(\sqrt{\sum_s B_L(s,r)\left[J^{-1}(I_c^{\ell-1}(s,r))\right]^2 + \overline{\left[J^{-1}(I_M^{\ell}(r))\right]^2}}\right) \tag{D.8}$$

Combining Eqs. (D.8),(D.7),(D.6),(D.4) and (D.5), we can evaluate the convergence of the receiver by tracking I_{app}^{ℓ} for each VN through iterations. The threshold is then defined as the smallest E_b/N_0 such that $\forall r: \; I_{app}^{\ell}(r) = 1$.

D.4 BICM design rules

ARJA codes [DJDT05] are good codes both in terms of threshold and minimum distance growth rate for AWGN channels. Their base matrix is given by:

$$\boldsymbol{B}_{ARJA} = \begin{pmatrix} 1 & 2 & 0 & 0 & 0 \\ 0 & 3 & 1 & 1 & 1 \\ 0 & 1 & 2 & 1 & 2 \end{pmatrix}$$

where the second VN is punctured.

When used with 16-QAM with Gray mapping, the EXIT chart analysis gives a threshold of $E_b/N_0 = 3$dB. In comparison, the $(3,6)$-regular protograph code threshold is 3.59dB.

D.4.1 Bit mapping optimization

For BICM modulation with high modulation order, each bit channel has generally unequal error protection. One way to improve the decoding threshold in concatenated schemes is to assign different

bit channels to different VNs. [JJZ10] pointed out a mapping that allows a threshold of $E_b/N_0 = 2.85$dB, *i.e.* a gain of about 0.25dB. In the next sections, we will see how one can improve these results.

For this scheme, Gray mapping without iterative decoding between the demapper and the decoder is assumed. The other approach, referred to as BICM-ID, consists in applying iterative soft decoding between the soft demapper and the LDPC code. Note that BICM-ID is not usefull when Gray mapping is considered. For other mapping, BICM-ID allows to achieve better thresholds.

D.4.2 Spatial coupling: terminated truncation

In this section, we will investigate the convergence of some examples of LDPC-C serially concatenated with the 16-QAM modulator using MSEW and Gray mappings. The proposed LDPC-C codes were chosen for simplicity to illustrate the convergence behavior of the proposed methods.

Tail-bitting (TB) method [MLC13] has been introduced to avoid the rate loss. The parity check matrix tail-biting protograph-based LDPC-C codes $\boldsymbol{B}_L^{tb}$ can be found in [LMFC10]. Because the most right-hand and left-hand CNs are no more 'irregular', there is no coupling gain and the threshold will remain the same as $\boldsymbol{B}$. Generally, TB LDPC-C codes are used to obtain some bounds (free distance, trapping set, ...) of the T termination LDPC-C codes [MLC13].

D.4.2.1 Spatially coupled ARJA with Gray mapping

Consider the spatially coupled ARJA code with constraint length $\nu_s = 2$ that is described by the two component matrices:

$$\boldsymbol{B}_0 = \begin{pmatrix} 1 & 2 & 0 & 0 & 0 \\ 0 & 1 & 1 & 1 & 0 \\ 0 & 0 & 1 & 0 & 2 \end{pmatrix}, \boldsymbol{B}_1 = \begin{pmatrix} 0 & 0 & 0 & 0 & 0 \\ 0 & 2 & 0 & 0 & 1 \\ 0 & 1 & 1 & 1 & 0 \end{pmatrix}$$

Note that in this scheme, there is no need to iterate between the demapper and the decoder since the EXIT chart of the demapper is flat. In this scheduling, a threshold of $E_b/N_0 = 2.57$dB was found for $L = 100$ (rate $R = 0.495$). The decoding threshold of the 16-QAM over AWGN channel is at $E_b/N_0 = 2.286$dB [VNND11, YEKLK13].

D.4.2.2 $(3, 6)$-regular protograph and MSEW mapping

Here we will consider a BICM-ID decoding with one BP data pass check pass in each iteration. Moreover, we will consider the $(3, 6)$-regular protograph spatial coupling given by $\mathrm{B}_0 = \mathrm{B}_1 = \mathrm{B}_2 =$ [1 1]. We observe a threshold at $E_b/N_0 = 2.97$dB when $L = 100$ (rate $R = 0.495$).

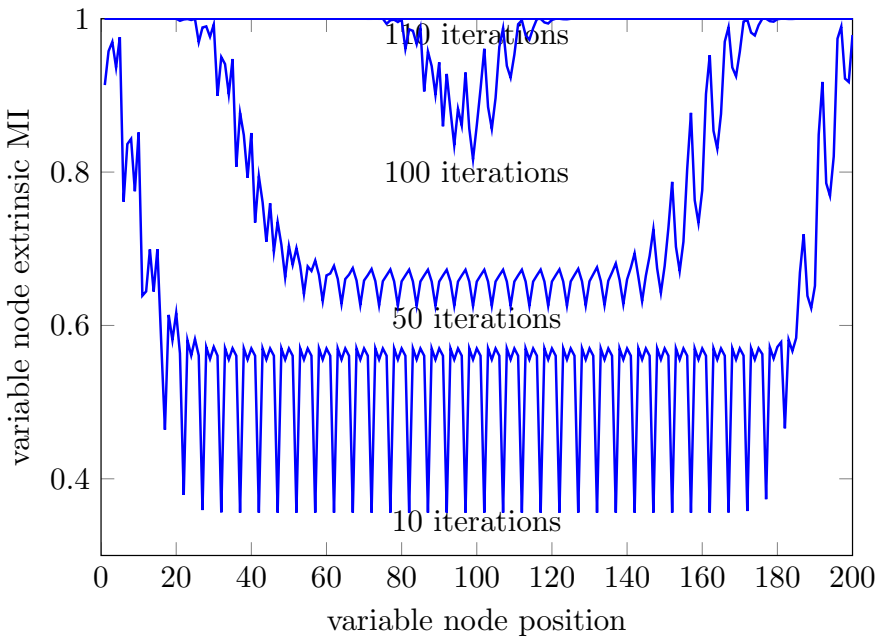

Figure D.3: VNs' MI evolution through iterations for convolutional ARJA with Gray at $E_b/N_0 = 3.1$dB and $L = 40$

Figure D.3 depicts the evolution the MI of different VNs through iterations for the schemes.

D.4.3 Combining spatial coupling with bit mapping

As discussed before, [DJDT05] shows that the ARJA code has a very good threshold over AWGN channel, with 16-QAM and Gray mapping, it allows a threshold of $E_b/N_0 = 3$dB. Authors in [JJZ10] reduced this threshold to $E_b/N_0 = 2.85$dB by optimizing the bit mapping. For the spatially coupled version of ARJA, instead of optimizing the bit mapping for the spatially coupled code as in [HBA+15, HAB+13], we will re-use the optimal mapping of the underlying protograph: *i.e.*, the VNs within each bundle are connected to the same bit channel as their corresponding VN in $\boldsymbol{B}_{ARJA}$. Taking advantage of the performance of the ARJA code, the coupling gain and the mapping optimization of the underlying protograph, the threshold is considerably improved: now $E_b/N_0 = 2.39$dB when $L = 100$ (*i.e.* a rate of 0.495).

D.4.4 Spatial coupling: direct truncation

Recall form chapter 3 the corresponding parity check matrix for the direct truncated LDPC-C code $\boldsymbol{B}_L^{DT}$ has the form:

$$\boldsymbol{B}_L^{DT} = \begin{bmatrix} \boldsymbol{B}_0 & & & \\ \vdots & \boldsymbol{B}_0 & & \\ \boldsymbol{B}_{m_s} & \vdots & \ddots & \\ & \boldsymbol{B}_{m_s} & \dots & \boldsymbol{B}_0 \end{bmatrix} \tag{D.9}$$

As discussed in chapter 3, the main advantage here is that, since the rate R does not depend on L, the threshold is now fixed and independent of L. Consequently, taking small L is satisfactory and the code ensemble $\boldsymbol{B}_L^{DT}$ becomes particularly interesting for finite length design. Furthermore, another advantage is the conservation of the design rate $R_{DT} = R$ with an only a relatively small loss in the threshold depending on the chosen coupling. This loss can be explained as following: as the most left protograph of $\boldsymbol{B}_L^{DT}$ configuration is similar to $\boldsymbol{B}_L$, the convolutional gain induced by these nodes remains intact, which leads to a better threshold than $\boldsymbol{B}$. However, since the most right VNs are less connected in comparison to their counterparts in $\boldsymbol{B}_L$, they will deteriorate the threshold. Figure D.4 depicts the convergence of different VNs through iterations. As expected, the extrinsic MI of the last VNs is slightly worse than the other VNs and, through iterations, we observe only the convolution gain induced by the most left CNs. This single *wave* propagates over all VNs and is sufficient to decode perfectly all the bit nodes.

D.4.4.1 $(3, 6)$ direct truncation protograph and MSEW mapping

Concatenation with 16−QAM gives a threshold of $E_b/N_0 = 4.92$dB. Even if it is better than the $(3, 6)$-regular LDPC code (threshold at $E_b/N_0 = 5.21$dB), it remains very far from the threshold of the classical termination (threshold at $E_b/N_0 = 2.72$dB).

D.4.4.2 Direct truncation with precoded mapper

For BICM modulations with high modulation order, beside bit channels mapping, a second way to improve the decoding threshold is to use precoding or doping [PS06, SB04, tB01b]. By adding a recursive inner rate-1 convolutinal code, the modulated bits are no more independent. Figure D.5 depicts the new transmitter and receiver when an accumulator is used as a precoder. When $P = 1$, all bits are precoded before being mapped. When P is greater than the message length, we retrieve the previous receiver in Fig. D.1. In the in-between values, only 1 bit among P is precoded.

Figure D.6 shows the EXIT curves of the precoded MSEW mapping. One has to be careful when computing different MI and different LLRs (see [PS06] for more details).

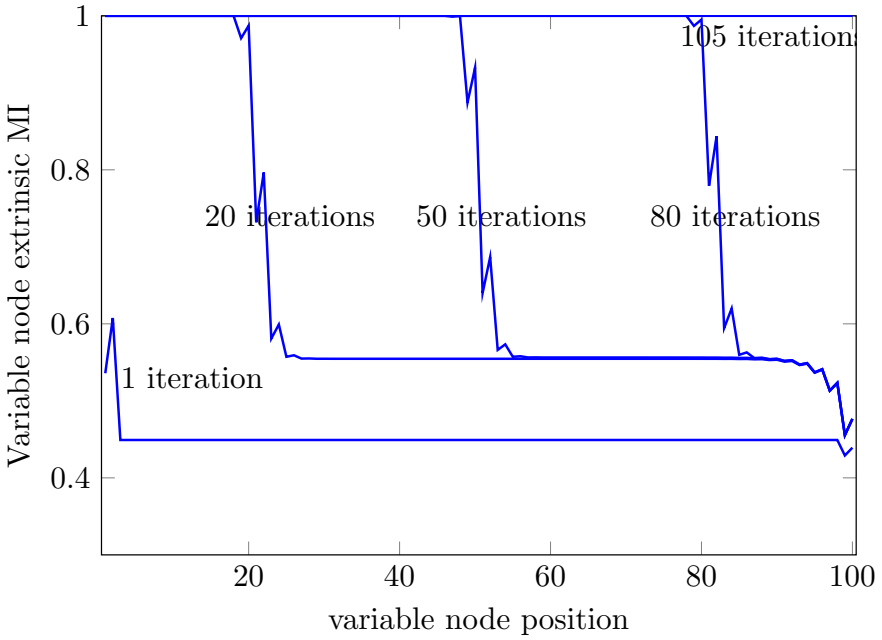

Figure D.4: VNs' MI evolution through iterations for DT $(3, 6)$-regular LDPC code with MSEW mapping at $E_b/N_0 = 5.18$dB and $L = 50$

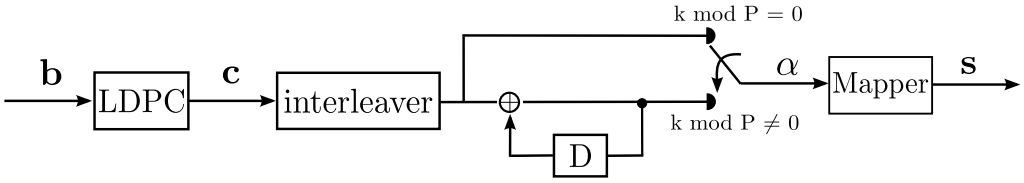

Figure D.5: Modified transmitter when precoding is used

When doped, all EXIT curves, $\forall P$, now join the point $(1, 1)$. Figure D.6 also illustrates that, at a fixed E_b/N_0, the bigger P is, the less the extrinsic MI will decrease at low *a priori* MI and the more abrupt the convergence to the point $(1, 1)$ will be at high *a priori* MI. From different experiments, it has been noticed that when concatenated with LDPC-C codes, in order to improve the threshold, a trade-off must be made between the extrinsic MI loss at lower *a priori* MI and extrinsic MI convergence 'smoothness' to the point $(1, 1)$. Furthermore, for the different spatially coupled LDPC codes with classical termination no real threshold improvement have been noticed compared to no doped mapping, however, a gain of 2.17dB has been observed for the $(3, 6)$ DT

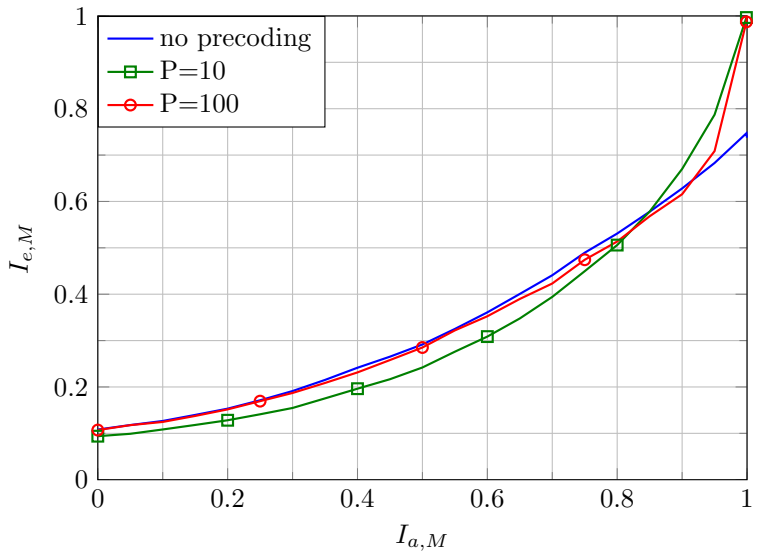

Figure D.6: MSEW demapper EXIT charts at $E_s/N_0 = 2$dB with precoding

protograph code, the new threshold is at $E_b/N_0 = 2.95$dB.

Figure D.7 summarizes the thresholds of different configurations studied so far. Coupled ARJA with optimized mapping for the underlying protograph for Gray outperforms all other codes and is at 0.1dB from the capacity. $(3, 6)$ with MSEW mapping does not perform very well, but when used with direct truncation and doping with (P=300), a gain of 2.17dB is observed. This code outperforms the optimized ARJA code with Gray [JJZ10] and has an exact rate of 0.5 with $L = 5$ only.

D.5 Conclusion

In this appendix, we investigated to performance of spatially coupled LDPC codes in BICM schemes and we showed, thanks to the spatial coupling and to bit mapping, we were able to design codes that operate at only 0.1dB from the capacity. Finally we introduced a new termination method that leads, when combined with precoding, to competitive trade-offs between rate loss and threshold with their terminated LDPC-C counterparts.

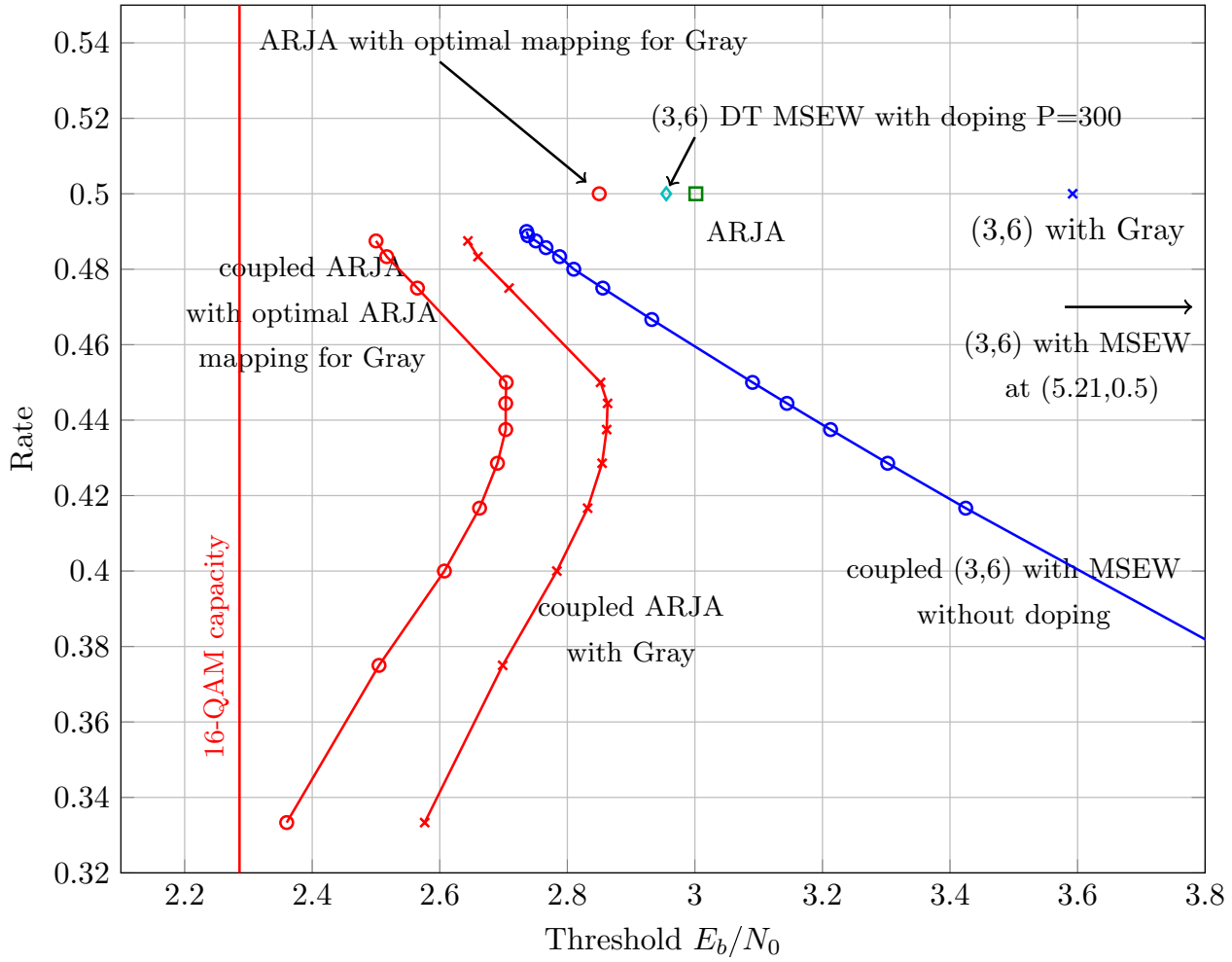

Figure D.7: Threshold vs rate of different codes

Bibliography

[AAS86] John B Anderson, Tor Aulin, and Carl-Erik Sundberg. *Digital phase modulation*. Springer, 1986.

[ADY07] Aliazam Abbasfar, Dariush Divsalar, and Kung Yao. Accumulate-repeat-accumulate codes. *IEEE Transactions on Communications*, 55(4):692–702, 2007.

[AKtB04] Alexei Ashikhmin, Gerhard Kramer, and Stephan ten Brink. Extrinsic information transfer functions: model and erasure channel properties. *IEEE Trans. Inf. Theory*, 50(11):2657–2673, 2004.

[ao61] and others. Minimum-shift data communication system, March 28 1961. US Patent 2,977,417.

[ARS81a] Tor Aulin, Nils Rydbeck, and Carl-Erik W Sundberg. Continuous phase modulation–part i: Full response signaling. *IEEE Transactions on Communications*, 29(3):196–209, 1981.

[ARS81b] Tor Aulin, Nils Rydbeck, and Carl-Erik W Sundberg. Continuous phase modulation–part ii: partial response signaling. *IEEE Transactions on Communications*, 29(3):210–225, 1981.

[AS03] John B Anderson and Arne Svensson. *Coded modulation systems*. Springer Science & Business Media, 2003.

[AS09] Shadi Ali Abu-Surra. *Protograph-based Generalized LDPC codes: Enumerators, Design, and Applications*. PhD thesis, The University of Arizona, 2009.

[ASDR11] Shadi Abu-Surra, Dariush Divsalar, and William E Ryan. Enumerators for protograph-based ensembles of ldpc and generalized ldpc codes. *IEEE Transactions on Information Theory*, 57(2):858–886, 2011.

[B+63] Philip Bello et al. Characterization of randomly time-variant linear channels. *IEEE transactions on Communications Systems*, 11(4):360–393, 1963.

[B+73] Phillip Bello et al. Aeronautical channel characterization. *IEEE Transactions on Communications*, 21(5):548–563, 1973.

[BB83] Sergio Benedetto and Ezio Biglieri. Nonlinear equalization of digital satellite channels. *IEEE Journal on Selected Areas in Communications*, 1(1):57–62, 1983.

[BBD79] Sergio Benedetto, Ezio Biglieri, and Riccardo Daffara. Modeling and performance evaluation of nonlinear satellite links-a volterra series approach. *IEEE Transactions on Aerospace and Electronic Systems*, (4):494–507, 1979.

[BCDB+13] Bassel F Beidas, Stefano Cioni, U De Bie, Alberto Ginesi, R Iyer-Seshadri, P Kim, LN Lee, D Oh, A Noerpel, Marco Papaleo, et al. Continuous phase modulation for broadband satellite communications: design and trade-offs. *International Journal of Satellite Communications and Networking*, 31(5):249–262, 2013.

[BCJR74] LR Bahl, J Cocke, F Jelinek, and J Raviv. Optimal decoding of linear codes for minimizing symbol error rate (corresp.). *IEEE Trans. Inf. Theory*, 20:284–287, 1974.

[BDMP98] Sergio Benedetto, Dariush Divsalar, Guido Montorsi, and Fabrizio Pollara. Serial concatenation of interleaved codes: Performance analysis, design, and iterative decoding. *IEEE Transactions on Information Theory*, 44(3):909–926, 1998.

[BE97] Jürgen Bierbrauer and Yves Edel. Extending and lengthening bch codes. *Finite Fields and Their Applications*, 3(4):314–333, 1997.

[Ber99] Dimitri P Bertsekas. *Nonlinear programming*. Athena Scientific, 1999.

[BFC09] Alan Barbieri, Dario Fertonani, and Giulio Colavolpe. Spectrally-efficient continuous phase modulations. *IEEE Trans. Wireless Commun*, 8(3):1564–1572, 2009.

[BG96] Claude Berrou and Alain Glavieux. Near optimum error correcting coding and decoding: Turbo-codes. *IEEE Trans. Commun.*, 44(10):1261–1271, 1996.

[BPB+14a] Tarik Benaddi, Charly Poulliat, Marie-Laure Boucheret, Benjamin Gadat, and Guy Lesthievent. Design of systematic gira codes for cpm. *Proc. of ISTC*, 2014.

[BPB+14b] Tarik Benaddi, Charly Poulliat, Marie-Laure Boucheret, Benjamin Gadat, and Guy Lesthievent. Design of unstructured and protograph-based ldpc coded continuous phase modulation. In *2014 IEEE International Symposium on Information Theory (ISIT)*, pages 1982–1986, 2014.

[BPB+14c] Tarik Benaddi, Charly Poulliat, Marie-Laure Boucheret, Benjamin Gadat, and Guy Lesthievent. Protograph-based ldpc convolutional codes for continuous phase modulation. In *2014 IEEE International conference on Communications, (ICC)*, pages 1982–1986. IEEE, 2014.

[BRC60] Raj Chandra Bose and Dwijendra K Ray-Chaudhuri. On a class of error correcting binary group codes. *Information and control*, 3(1):68–79, 1960.

[BT72] S Butman and Uzi Timor. Interplex–an efficient multichannel psk/pm telemetry system. *IEEE Transactions on Communications*, 20(3):415–419, 1972.

[BTP+13] Bouchra Benammar, Nathan Thomas, Charly Poulliat, Marie-Laure Boucheret, and Mathieu Dervin. On linear mmse based turbo-equalization of nonlinear volterra channels. In *IEEE International Conference on Acoustics, Speech and Signal Processing (ICASSP)*, pages 4703–4707, 2013.

[CB05] Giulio Colavolpe and Alan Barbieri. Simplified iterative detection of serially concatenated cpm signals. In *IEEE Global Telecommunications Conference, 2005. GLOBECOM'05*, volume 3, pages 5–pp, 2005.

[CBB+04] R Chaggara, ML Boucheret, C Bazile, E Bouisson, A Ducasse, and JD Gayrard. Continuous phase modulation for future satellite communication systems in ka band. In *2004 International Conference on Information and Communication Technologies: From Theory to Applications, 2004. Proceedings.*, pages 269–270. IEEE, 2004.

[CFC10] Enrico Casini, Dario Fertonani, and Giulio Colavolpe. Advanced cpm receiver for the nato tactical narrowband waveform. In *Military Communications Conference Proceedings MILCOM 2010*, pages 1725–1730, 2010.

[CFJRU01] Sae-Young Chung, G David Forney Jr, Thomas J Richardson, and Rüdiger Urbanke. On the design of low-density parity-check codes within 0.0045 db of the shannon limit. *IEEE Communications Letters*, 5(2):58–60, 2001.

[Chu00] Sae-Young Chung. *On the construction of some capacity-approaching coding schemes*. PhD thesis, Citeseer, 2000.

[CNE12] CNES. Analyse des communications avec les drones en bande 5ghz. *R & T study*, 2012.

[CR97] Giulio Colavolpe and Riccardo Raheli. Reduced-complexity detection and phase synchronization of cpm signals. *Communications, IEEE Transactions on*, 45(9):1070–1079, 1997.

[CR01] Aik Chindapol and James A Ritcey. Design, analysis, and performance evaluation for bicm-id with square qam constellations in rayleigh fading channels. *IEEE Journal on Selected Areas in Communications*, 19(5):944–957, 2001.

[CS94] Joseph Cheung and Raymond Steele. Soft-decision feedback equalizer for continuous phase modulated signals in wideband mobile radio channels. *IEEE Transactions on Communications*, 42(234):1628–1638, 1994.

[CT12] Thomas M Cover and Joy A Thomas. *Elements of information theory*. John Wiley & Sons, 2012.

[CVT09] Shi Cheng, Matthew C Valenti, and Don Torrieri. Coherent continuous-phase frequency-shift keying: parameter optimization and code design. *IEEE Trans. Wireless Commun*, 8(4):1792–1802, 2009.

[Dav79] Philip J Davis. *Circulant matrices*. American Mathematical Soc., 1979.

[DB72] Rudi De Buda. Coherent demodulation of frequency-shift keying with low deviation ratio. *Communications, IEEE Transactions on*, 20(3):429–435, 1972.

[DDJ06] Dariush Divsalar, Sam Dolinar, and Christopher Jones. Construction of protograph ldpc codes with linear minimum distance. In *IEEE International Symposium on Information Theory, 2006*, pages 664–668, 2006.

[DDJA09] Dariush Divsalar, Samuel Dolinar, Christopher R Jones, and Kenneth Andrews. Capacity-approaching protograph codes. *IEEE J. Sel. Areas Commun.*, 27(6):876–888, 2009.

[DDP01] Dariush Divsalar, Samuel Dolinar, and Fabrizio Pollara. Iterative turbo decoder analysis based on density evolution. *IEEE Journal on Selected Areas in Communications*, 19(5):891–907, 2001.

[Det11] Thomas Frederick Detwiler. *Continuous Phase Modulation for High Speed Fiber Optic Links*. PhD thesis, Georgia Institute of Technilogy, 2011.

[DF07] David Declercq and Marc Fossorier. Decoding algorithms for nonbinary ldpc codes over gf. *IEEE Transactions on Communications*, 55(4):633–643, 2007.

[Div06] Dariush Divsalar. Ensemble weight enumerators for protograph ldpc codes. In *IEEE International Symposium on Information Theory, 2006*, pages 1554–1558. IEEE, 2006.

[DJDT05] Dariush Divsalar, Christopher Jones, Sam Dolinar, and Jeremy Thorpe. Protograph based ldpc codes with minimum distance linearly growing with block size. In *IEEE Global Telecommunications Conference (GLOBECOM)*, volume 3, pages 5–pp, 2005.

[DJM98] Dariush Divsalar, Hui Jin, and Robert J McEliece. Coding theorems for" turbo-like" codes. In *Proceedings of the annual Allerton Conference on Communication control and Computing*, volume 36, pages 201–210. UNIVERSITY OF ILLINOIS, 1998.

[DL12] Luc Deneire and Jerome Lebrun. Continuous phase modulation and space-time coding: A candidate for wireless robotics. *Wireless Personal Communications*, 64(3):473–487, 2012.

[ETS05] EBU ETSI. Digital video broadcasting (dvb); second generation framing structure, channel coding and modulation systems for broadcasting, interactive services, news gathering and other broadband satellite applications. Technical report, Tech. rep., ETSI, 2005.

[ETS06] EN ETSI. 302 307 v1. 1.2 digital video broadcasting (dvb). *Second generation framing structure, channel coding and modulation systems for Broadcasting, Interactive Services, News Gathering and other broadband satellite applications*, 2006.

[FMT05] SL Fogal, Robert McEliece, and Jeremy Thorpe. Enumerators for protograph ensembles of ldpc codes. In *International Symposium on Information Theory, 2005. ISIT 2005.*, pages 2156–2160. IEEE, 2005.

[Gal62] Robert G Gallager. Low-density parity-check codes. *IRE Transactions on Information Theory*, 8(1):21–28, 1962.

[Gan03] Aravind Ganesan. *Capacity estimation and code design principles for continuous phase modulation (CPM).* PhD thesis, Texas A&M University, 2003.

[GDF15] Giuliano Garrammone, David Declercq, and Marc PC Fossorier. Weight distributions of non-binary multi-edge type ldpc code ensembles. In *IEEE International Symposium on Information Theory (ISIT)*, pages 2875–2879, 2015.

[Geo00] Mark Geoghegan. Description and performance results for a multi-h cpm telemetry waveform. In *21st Century Military Communications Conference Proceedings MILCOM 2000*, volume 1, pages 353–357, 2000.

[GH88] David E Goldberg and John H Holland. Genetic algorithms and machine learning. *Machine learning*, 3(2):95–99, 1988.

[GHGZ12] Benjamin Gadat, Erwan Ho, Hugo Gozalez, and Frank Zeppenfeldt. Satellite communications : a key enabler for uav insertion into civil airspace. *Toulouse Space Show*, 2012.

[GiAND09] Alexandre Graell i Amat, Charbel Abdel Nour, and Catherine Douillard. Serially concatenated continuous phase modulation for satellite communications. *IEEE Trans. Wireless Commun*, 8(6):3260–3269, 2009.

[HAB+13] Christian Häger, Alex Alvarado, Fredrik Brännström, Erik Agrell, et al. Optimized bit mappings for spatially coupled ldpc codes over parallel binary erasure channels. *arXiv preprint arXiv:1309.7583*, 2013.

[Hag04] Joachim Hagenauer. The exit chart-introduction to extrinsic information transfer in iterative processing. In *Proc. 12th European Signal Processing Conference (EUSIPCO)*, pages 1541–1548, 2004.

[HBA+14] Christian Häger, Fredrik Brännström, Alex Alvarado, Erik Agrell, et al. Improving soft fec performance for higher-order modulations via optimized bit channel mappings. *Optics Express*, 22(12):14544–14558, 2014.

[HBA+15] Christian Häger, Fredrik Brännström, Alex Alvarado, Erik Agrell, et al. Terminated and tailbiting spatially coupled codes with optimized bit mappings for spectrally efficient fiber-optical systems. *Journal of Lightwave Technology*, 33(7):1275–1285, 2015.

[HEA01] Xiao-Yu Hu, Evangelos Eleftheriou, and D-M Arnold. Progressive edge-growth tanner graphs. 2:995–1001, 2001.

[HGiAB+14] C Hager, A Graell i Amat, F Brannstrom, A Alvarado, and E Agrell. Terminated and tailbiting spatially-coupled codes with optimized bit mappings for spectrally efficient fiber-optical systems. 2014.

[HK98] Paul KM Ho and Jae Hyung Kim. Pilot-symbol aided continuous phase modulation system, January 27 1998. US Patent 5,712,877.

[HNP+86] J Hagenauer, A Neul, W Papke, et al. The aeronautical satellite channel. *Draft Final Report, DFVLR*, 1986.

[Hoc59] Alexis Hocquenghem. Codes correcteurs d'erreurs. *Chiffres (paris)*, 2(147-156):116, 1959.

[HP94] Dorit S Hochbaum and Anu Pathria. Can a system of linear diophantine equations be solved in strongly polynomial time? *Citeseer*, 1994.

[HSMP03] Jilei Hou, Paul H Siegel, Laurence B Milstein, and Henry D Pfister. Capacity-approaching bandwidth-efficient coded modulation schemes based on low-density parity-check codes. *IEEE Transactions on Information Theory*, 49(9):2141–2155, 2003.

[iFMC08] Albert Guillén i Fàbregas, Alfonso Martinez, and Giuseppe Caire. *Bit-interleaved coded modulation*. Now Publishers Inc, 2008.

[IR10] ITU-R. Results of studies of the am(r)s allocation in the band 960-1 164 mhz and of the ams(r)s allocation in the band 5 030-5 091 mhz to support control and non-payload communications links for unmanned aircraft systems. *Report M.2205*, 2010.

[IR11] ITU-R. Frequency band study to support the line-of-sight control and non-payload communications (cnpc) link(s) for unmanned aircraft systems (uas) within new allocations in the band 5 030-5 091 mhz,. *Draft New Report ITU-R M.[UAS-BANDS-NEW-ALLOC-5030- 5091 MHz], document 5/269*, 2011.

[JFZ99] A Jimenez Felstrom and Kamil Sh Zigangirov. Time-varying periodic convolutional codes with low-density parity-check matrix. *IEEE Trans. Inf. Theory*, 45(6):2181–2191, 1999.

[Jin01] Hui Jin. *Analysis and design of turbo-like codes*. PhD thesis, California Institute of Technology, 2001.

[JJZ10] Yi Jin, Ming Jiang, and Chunming Zhao. Optimized variable degree matched mapping for protograph ldpc coded modulation with 16qam. In *th International Symposium on Turbo Codes and Iterative Information Processing (ISTC), 2010 6*, pages 161–165. IEEE, 2010.

[JK05] Sudhanshu John and Hyuck M Kwon. Approximate cycle extrinsic message degree regular quasi circulant ldpc codes. In *IEEE Military Communications Conference, 2005. MILCOM 2005.*, pages 2877–2881, 2005.

[JW05] Sarah J Johnson and Steven R Weller. Constructions for irregular repeat-accumulate codes. In *Proceedings. International Symposium on Information Theory, ISIT*, pages 179–183, 2005.

[JW08] Sarah J Johnson and Steven R Weller. Combinatorial interleavers for systematic regular repeat-accumulate codes [transactions letters]. *IEEE Trans. Commun.*, 56(8):1201–1206, 2008.

[Kal89] Ghassan Kawas Kaleh. Simple coherent receivers for partial response continuous phase modulation. *IEEE J. Sel. Areas Commun.*, 7(9):1427–1436, 1989.

[KC04] C Kuo and Keith M Chugg. On the bandwidth efficiency of cpm signals. In *MILCOM*, volume 1, page 218, 2004.

[KFL01] Frank R Kschischang, Brendan J Frey, and Hans-Andrea Loeliger. Factor graphs and the sum-product algorithm. *IEEE Transactions on Information Theory*, 47(2):498–519, 2001.

[KMM03] Aleksandar Kavčić, Xiao Ma, and Michael Mitzenmacher. Binary intersymbol interference channels: Gallager codes, density evolution, and code performance bounds. *IEEE Transactions on Information Theory*, 49(7):1636–1652, 2003.

[KP83] Jin Kim and Judea Pearl. A computational model for causal and diagnostic reasoning in inference systems. 1983.

[KRU11] Shrinivas Kudekar, Thomas J Richardson, and Rüdiger L Urbanke. Threshold saturation via spatial coupling: Why convolutional ldpc ensembles perform so well over the bec. *IEEE Trans. Inf. Theory*, 57(2):803–834, 2011.

[KRU12] Shrinivas Kudekar, Tom Richardson, and Rüdiger Urbanke. Spatially coupled ensembles universally achieve capacity under belief propagation. In *2012 IEEE International Symposium on Information Theory Proceedings (ISIT)*, pages 453–457. IEEE, 2012.

[Lau86] Pierre Laurent. Exact and approximate construction of digital phase modulations by superposition of amplitude modulated pulses (amp). *IEEE Trans. Commun.*, 34(2):150–160, 1986.

[LC07] Gianluigi Liva and Marco Chiani. Protograph ldpc codes design based on exit analysis. In *IEEE Global Telecommunications Conference, 2007. GLOBECOM'07*, pages 3250–3254, 2007.

[Liv06] Gianluigi Liva. *Block codes based on sparse graphs for wireless communication systems.* PhD thesis, University of Bologna, 2006.

[LMFC10] Michael Lentmaier, David GM Mitchell, Gerhard Fettweis, and Daniel J Costello. Asymptotically good ldpc convolutional codes with awgn channel thresholds close to the shannon limit. In *2010 6th International Symposium on Turbo Codes and Iterative Information Processing (ISTC)*, pages 324–328. IEEE, 2010.

[LNF81] Tho Le-Ngoc and K Feher. Power and bandwidth efficient isi and jitter free/ijf/transmission techniques for linear and nonlinear channels. In *International Conference on Communications (ICC)*, volume 2, page 33, 1981.

[LSL06] Gottfried Lechner, Jossy Sayir, and Ingmar Land. Optimization of ldpc codes for receiver frontends. In *IEEE International Symposium on Information Theory, 2006*, pages 2388–2392. IEEE, 2006.

[LTHS03] LH-J Lampe, Roman Tzschoppe, Johannes B Huber, and Robert Schober. Noncoherent continuous-phase modulation for ds-cdma. In *IEEE International Conference on Communications, 2003. ICC'03*, volume 5, pages 3282–3286, 2003.

[LZM15] Xiying Liu, Shancheng Zhao, and Xiao Ma. A low complexity detection/decoding algorithm for nb-ldpc coded prcpm system. *Physical Communication*, 2015.

[MA00] Pär Moqvist and T Aulin. Trellis termination in cpm. *Electronics Letters*, 36(23):1940–1941, 2000.

[MA01] Pär Moqvist and Tor M Aulin. Serially concatenated continuous phase modulation with iterative decoding. In *IEEE Trans. Commun.*, volume 49, pages 1901–1915, 2001.

[MFG97] Peter A Murphy, Gary E Ford, and Michael Golanbari. Map symbol detection of cpm bursts. *Kluwer Iinternational Series in Engineering and Computer Science*, pages 199–210, 1997.

[MH] A Montazeri and J Haddadnia. Mcm and cpm combination as compared to the use of fde for cpm. Citeseer.

[MIL99] Department of defense interface standard. interoperablility standard for single-acess 5-khz and 25-khz uhf satellite communications channels. In *MIL-STD188-181B*, Mar. 1999.

[MLC11] David GM Mitchell, Michael Lentmaier, and Daniel J Costello. Awgn channel analysis of terminated ldpc convolutional codes. In *Information Theory and Applications Workshop (ITA), 2011*, pages 1–5. IEEE, 2011.

[MLC13] David GM Mitchell, Michael Lentmaier, and Daniel J Costello. On the minimum distance of generalized spatially coupled ldpc codes. In *IEEE International Symposium on Information Theory Proceedings (ISIT), 2013*, pages 1874–1878. IEEE, 2013.

[MLCJ14] David GM Mitchell, Michael Lentmaier, and Daniel J Costello Jr. Spatially coupled ldpc codes constructed from protographs. *arXiv preprint arXiv:1407.5366*, 2014.

[MM95] Umberto Mengali and Michele Morelli. Decomposition of m-ary cpm signals into pam waveforms. *IEEE Trans. Inf. Theory*, 41(5):1265–1275, 1995.

[MMC98] Robert J McEliece, David JC MacKay, and Jung-Fu Cheng. Turbo decoding as an instance of pearl's belief propagation algorithm. *IEEE Journal on Selected Areas in Communications*, 16(2):140–152, 1998.

[MN96] David JC MacKay and Radford M Neal. Near shannon limit performance of low density parity check codes. *IEEE Electronics letters*, 32(18):1645–1646, 1996.

[MPFBH92] Michel Mouly, Marie-Bernadette Pautet, and Thomas Foreword By-Haug. *The GSM system for mobile communications*. Telecom publishing, 1992.

[MW86] Howard H Ma and Jack K Wolf. On tail biting convolutional codes. *IEEE Trans. Commun.*, 34:104–111, 1986.

[NAN01] Krishna R Narayanan, Ibrahim Altunbas, and R Narayanaswami. On the design of ldpc codes for msk. In *IEEE Global Telecommunications Conference, 2001. GLOBECOM'01*, volume 2, pages 1011–1015. IEEE, 2001.

[NAN03] Krishna R Narayanan, Ibrahim Altunbas, and R Sekhar Narayanaswami. Design of serial concatenated msk schemes based on density evolution. *IEEE Trans. Commun.*, 51(8):1283–1295, 2003.

[NHP+87] Andreas Neul, Joachim Hagenauer, Wolfgang Papke, Frank Dolainsky, and Franz Edbauer. Propagation measurements for the aeronautical satellite channel. In *37th IEEE Vehicular Technology Conference*, volume 37, pages 90–97, 1987.

[NND12] Troy V Nguyen, Aria Nosratinia, and Dariush Divsalar. The design of rate-compatible protograph ldpc codes. *IEEE Transactions on Communications*, 60(10):2841–2850, 2012.

[NS99] Krishna R Narayanan and Gordon L Stuber. A serial concatenation approach to iterative demodulation and decoding. *IEEE Trans. Commun.*, 47(7):956–961, 1999.

[NS01] Antonio Napolitano and Chad M Spooner. Cyclic spectral analysis of continuous-phase modulated signals. *IEEE Transactions on Signal Processing*, 49(1):30–44, 2001.

[NYPN11] Phong S Nguyen, Arvind Yedla, Henry D Pfister, and Krishna R Narayanan. Spatially-coupled codes and threshold saturation on intersymbol-interference channels. *arXiv preprint arXiv:1107.3253*, 2011.

[OL74] William P Osborne and Michael B Luntz. Coherent and noncoherent detection cpfsk. *IEEE Transactions on Communications*, 22(8):1023–1036, 1974.

[Ozg08] Baris Ozgul. *Advanced transceiver design for continuous phase modulation*. PhD thesis, Bogazici University, 2008.

[Par10] Cheol Hee Park. Frequency domain processing techniques for continuous phase modulation. 2010.

[PDL71] MG Pelchat, RC Davis, and MB Luntz. Coherent demodulation of continuous phase binary fsk signals(coherent demodulation of continuous phase binary fsk signals in additive white noise, determining error probability). In *International Telemetering Conference, Washington, D. C*, pages 181–190, 1971.

[Pea82] Judea Pearl. Reverend bayes on inference engines: A distributed hierarchical approach. In *AAAI*, pages 133–136, 1982.

[Pea14] Judea Pearl. *Probabilistic reasoning in intelligent systems: networks of plausible inference*. Morgan Kaufmann, 2014.

[Pen55] Roger Penrose. A generalized inverse for matrices. In *Mathematical proceedings of the Cambridge philosophical society*, volume 51, pages 406–413. Cambridge Univ Press, 1955.

[PR04] Erik Perrins and Michael Rice. Optimal and reduced complexity receivers for m-ary multi-h cpm. In *IEEE Wireless Communications and Networking Conference, 2004. WCNC*, volume 2, pages 1165–1170, 2004.

[PS06] Stephan Pfletschinger and Frieder Sanzi. Error floor removal for bit-interleaved coded modulation with iterative detection. *Wireless Communications, IEEE Transactions on*, 5(11):3174–3181, 2006.

[PS07] John Proakis and Masoud Salehi. *Digital communications*. McGraw-Hill Education; 5th edition, 2007.

[PT87] Al-Nasir Premji and Desmond P Taylor. A practical receiver structure for multi-h cpm signals. *IEEE Transactions on Communications*, 35(9):901–908, 1987.

[PV06] Fabrizio Pancaldi and Giorgio M Vitetta. Equalization algorithms in the frequency domain for continuous phase modulations. *IEEE Transactions on Communications*, 54(4):648–658, 2006.

[RBL05] Luca Rugini, Paolo Banelli, and Geert Leus. Simple equalization of time-varying channels for ofdm. *IEEE Communications Letters*, 9(7):619–621, 2005.

[Rim88] Bixio E Rimoldi. A decomposition approach to cpm. *IEEE Trans. Inf. Theory*, 34(2):260–270, 1988.

[RL09] William Ryan and Shu Lin. *Channel codes: classical and modern*. Cambridge University Press, 2009.

[RSU01] Thomas J Richardson, Mohammad Amin Shokrollahi, and Rüdiger L Urbanke. Design of capacity-approaching irregular low-density parity-check codes. *IEEE Trans. Inf. Theory*, 47(2):619–637, 2001.

[RU01] Thomas J Richardson and Rüdiger L Urbanke. The capacity of low-density parity-check codes under message-passing decoding. *IEEE Trans. Inf. Theory*, 47(2):599–618, 2001.

[RU08] Tom Richardson and Ruediger Urbanke. *Modern coding theory*. Cambridge University Press, 2008.

[S+76] Thomas Schonhoff et al. Symbol error probabilities for m-ary cpfsk: coherent and noncoherent detection. *IEEE Transactions on Communications*, 24(6):644–652, 1976.

[SB04] Frank Schreckenbach and Gerhard Bauch. Irregular signal constellations, mappings and precoder. In *International Symposium on Information Theory and its Applications (ISITA)*, pages 1332–1336. Citeseer, 2004.

[SB13] Laurent Schmalen and Stephan ten Brink. Combining spatially coupled ldpc codes with modulation and detection. In *Proceedings of 2013 9th International ITG Conference on Systems, Communication and Coding (SCC)*, pages 1–6. VDE, 2013.

[Sch98] Alexander Schrijver. *Theory of linear and integer programming.* John Wiley & Sons, 1998.

[Sch04] Philip Schniter. Low-complexity equalization of ofdm in doubly selective channels. *IEEE Transactions on Signal Processing*, 52(4):1002–1011, 2004.

[SDPR+10] Andrea Scorzolini, Veronica De Perini, Elena Razzano, Giulio Colavolpe, Susana Mendes, Pierluigi Fiori, and Angelo Sorbo. European enhanced space-based ais system study. In *Advanced satellite multimedia systems conference (ASMA) and the 11th signal processing for space communications workshop (SPSC), 2010 5th*, pages 9–16, 2010.

[ser09] Propagation data required for the design of earth-space maritime mobile telecommunication systems. *Recommendation ITU-R P. 680-3*, 2009.

[SGHB03] Frank Schreckenbach, N Gortz, Joachim Hagenauer, and Gerhard Bauch. Optimized symbol mappings for bit-interleaved coded modulation with iterative decoding. In *Global Telecommunications Conference, 2003. GLOBECOM'03. IEEE*, volume 6, pages 3316–3320. IEEE, 2003.

[Sha01] Claude Elwood Shannon. A mathematical theory of communication. *ACM SIGMOBILE Mobile Computing and Communications Review*, 5(1):3–55, 2001.

[Sim05] Marvin K Simon. *Bandwidth-efficient digital modulation with application to deep-space communications*, volume 2. John Wiley & Sons, 2005.

[SLPF+08] Alexander Steingass, Andreas Lehner, Fernando Pérez-Fontán, Erwin Kubista, and Bertram Arbesser-Rastburg. Characterization of the aeronautical satellite navigation

channel through high-resolution measurement and physical optics simulation. *International Journal of Satellite Communications and Networking*, 26(1):1–30, 2008.

[SMB01] Bartolo Scanavino, Guido Montorsi, and Sergio Benedetto. Convergence properties of iterative decoders working at bit and symbol level. In *IEEE Global Telecommunications Conference, (GLOBECOM'01)*, volume 2, pages 1037–1041, 2001.

[SP97] Rainer Storn and Kenneth Price. Differential evolution–a simple and efficient heuristic for global optimization over continuous spaces. *Journal of global optimization*, 11(4):341–359, 1997.

[SS83] AAM Saleh and J Salz. Adaptive linearization of power amplifiers in digital radio systems. *Bell System Technical Journal*, 62(4):1019–1033, 1983.

[SS05] Amin Shokrollahi and Rainer Storn. Design of efficient erasure codes with differential evolution. In *Differential Evolution*, pages 413–427. Springer, 2005.

[StBLL12] Laurent Schmalen, Stephan ten Brink, Gottfried Lechner, and Andreas Leven. On threshold prediction of low-density parity-check codes with structure. In *2012 46th Annual Conference on Information Sciences and Systems (CISS)*, pages 1–5. IEEE, 2012.

[Tan81] Robert Michael Tanner. A recursive approach to low complexity codes. *IEEE Trans. Inf. Theory*, 27(5):533–547, 1981.

[tB01a] Stephan ten Brink. Code characteristic matching for iterative decoding of serially concatenated codes. In *Annales des télécommunications*, volume 56, pages 394–408. Springer, 2001.

[tB01b] Stephan ten Brink. Code doping for triggering iterative decoding convergence. In *2001 IEEE International Symposium on Information Theory, 2001*, page 235, 2001.

[tB01c] Stephan ten Brink. Convergence behavior of iteratively decoded parallel concatenated codes. *IEEE Trans. Commun.*, 49(10):1727–1737, 2001.

[tB01d] Stephan ten Brink. *Design of concatenated coding schemes based on iterative decoding convergence*. PhD thesis, University of Stuttgart, 2001.

[tBK03] Stephan ten Brink and Gerhard Kramer. Design of repeat-accumulate codes for iterative detection and decoding. *IEEE Transactions on Signal Processing*, 51(11):2764–2772, 2003.

[tBKA04] Stephan ten Brink, Gerhard Kramer, and Alexei Ashikhmin. Design of low-density parity-check codes for modulation and detection. *IEEE Trans. Commun.*, 52(4):670–678, 2004.

[Tho03] JC Thorpe. Low-density parity-checks codes (ldpc) constructed from protographs. *IPN Progress Report*, pages 42–154, 2003.

[TS02] Jun Tan and Gordon L Stuber. Analysis and design of interleaver mappings for iteratively decoded bicm. In *IEEE International Conference on Communications, 2002. ICC 2002*, volume 3, pages 1403–1407. IEEE, 2002.

[TS05] Jun Tan and Gordon L Stuber. Frequency-domain equalization for continuous phase modulation. In *IEEE Trans. Wireless Commun.*, volume 4, pages 2479–2490, 2005.

[Ung82] Gottfried Ungerboeck. Channel coding with multilevel/phase signals. *IEEE Transactions on Information Theory*, 28(1):55–67, 1982.

[V1.13] ETSI EN 301 545-2 V1.1.1. Digital video broadcasting (dvb); second generation dvb interactive satellite system (dvb-rcs2); part 2: Lower layers for satellite standard. 2013.

[VCT10] Matthew C Valenti, Shi Cheng, and Don Torrieri. Iterative multisymbol noncoherent reception of coded cpfsk. *IEEE Transactions on Communications*, 58(7):2046–2054, 2010.

[Vit67] Andrew J Viterbi. Error bounds for convolutional codes and an asymptotically optimum decoding algorithm. *IEEE Transactions on Information Theory*, 13(2):260–269, 1967.

[VNND11] Thuy Van Nguyen, Aria Nosratinia, and Dariush Divsalar. Threshold of protograph-based ldpc coded bicm for rayleigh fading. In *IEEE Global Telecommunications Conference (GLOBECOM 2011), 2011*, pages 1–5. IEEE, 2011.

[VNND12] Thuy Van Nguyen, Aria Nosratinia, and Dariush Divsalar. Protograph-based ldpc codes for partial response channels. In *IEEE International Conference on Communications (ICC), 2012*, pages 2166–2170, 2012.

[Wei05] Eric W Weisstein. Ham sandwich theorem. 2005.

[WG06] Marilynn P Wylie-Green. A new pam decomposition for continuous phase modulation. In *40th Annual Conference on Information Sciences and Systems, 2006*, pages 705–710, 2006.

[Wib96] Niclas Wiberg. *Codes and decoding on general graphs*. Citeseer, 1996.

[WS01] Andrew P Worthen and Wayne E Stark. Unified design of iterative receivers using factor graphs. *IEEE Transactions on Information Theory*, 47(2):843–849, 2001.

[WZ07] Oomke Weikert and Udo Zölzer. A wireless mimo cpm system with incoherent demodulation. In *SIP*, pages 353–358, 2007.

[XA05] Ming Xiao and Tor Aulin. Irregular repeat continuous phase modulation. *IEEE communications letters*, 9(8):722–725, 2005.

[XA06] Ming Xiao and Tor M Aulin. Serially concatenated continuous phase modulation with convolutional codes over rings. *IEEE Transactions on Communications*, 54(8):1387–1396, 2006.

[XA07] Ming Xiao and Tor M Aulin. On analysis and design of low density generator matrix codes for continuous phase modulation. *IEEE Trans. Wireless Commun*, 6(9):3440–3449, 2007.

[YEKLK13] Arvind Yedla, Mostafa El-Khamy, Jungwon Lee, and Inyup Kang. Performance of spatially-coupled ldpc codes and threshold saturation over bicm channels. *arXiv preprint arXiv:1303.0296*, 2013.

[YRL04] Michael Yang, William E Ryan, and Yan Li. Design of efficiently encodable moderate-length high-rate irregular ldpc codes. *IEEE Transactions on Communications*, 52(4):564–571, 2004.

[YS97] Lihbor Yiin and Gordon L Stuber. Mlse and soft-output equalization for trellis-coded continuous phase modulation. *IEEE Transactions on Communications*, 45(6):651–659, 1997.

[ZGKK12] Shahram Zarei, Wolfgang Gerstacker, Gerd Kilian, and Wolfgang Koch. An iterative detection algorithm for coded cpfsk signals with irrational modulation index. In *Proceedings of the 20th European Signal Processing Conference (EUSIPCO)*, pages 2541–2545, 2012.